UNIVERSITÉ DU QUÉBEC À CHICOUTIMI

THESIS SUBMITTED TO THE
UNIVERSITY OF QUEBEC AT CHICOUTIMI
IN PARTIAL FULFILLMENT OF THE
REQUIREMENT FOR THE DEGREE OF
DOCTOR OF PHILOSOPHY IN ENGINEERING

BY

EMAD-ELDIN MOHAMED ELGALLAD

EFFECT OF ADDITIVES ON THE MECHANICAL PROPERTIES AND MACHINABILITY OF A NEW ALUMINUM-COPPER BASE ALLOY

JUNE 2010

UNIVERSITÉ DU QUÉBEC À CHICOUTIMI

THÈSE PRÉSENTÉ À

L'UNIVERSITÉ DU QUÉBEC À CHICOUTIMI

COMME EXIGENCE PARTIELLE

DU DOCTORAT EN INGÉNIERIE

PAR

EMAD-ELDIN MOHAMED ELGALLAD

EFFETS DES ADDITIFS SUR LES PROPRIÉTÉS MÉCANIQUES ET L'USINABILITÉ D'UN NOUVEL ALLIAGE DE BASE Al-Cu

JUIN 2010

Dedicated to my parents,
Sahar, Engy, and Karim

RÉSUMÉ

Le présent travail vise à étudier les effets des additifs sur les propriétés mécaniques ainsi que sur l'usinabilité d'un nouvel alliage de fonderie, le 220 (Al-2%Cu-1.3%Si-0.4%Mg), destinés à des applications automobiles. Ce travail de recherche a été accompli à travers deux types d'étude : (i) l'étude des propriétés mécaniques (ii) et l'étude de l'usinabilité. L'étude des propriétés mécaniques visait à examiner les effets du Sr, Ti, Zr, Fe, Mn et Ag en plus des éléments de décolletage, Sn et Bi, sur les propriétés mécaniques de l'alliage 220 aux conditions tel que coulée et traitée thermiquement. Les propriétés mécaniques en question incluant la traction, la dureté et la résilience lesquelles ont tous été évaluées à la température ambiante. L'étude de l'usinabilité a été consacrée à l'examen des performances de perçage et de taraudage de quatre alliages basés sur le 220 ainsi que sur l'alliage A206 qui a été sélectionné dans le but d'une étude comparative sur l'usinabilité sur celui-ci et celle du 220. Les quatre alliages sélectionnés parmi les alliages préparés pour la première étude incluent : (i) l'alliage 220, (ii) l'alliage 220 + Ti + Zr, (iii) l'alliage 220 + Ti + Zr + Sn et (iv) l'alliage 220 + Ti + Zr + Bi. Les performances d'usinage ont été évaluées en terme de force de coupe, de moment de coupe et de durée de vie de l'outil aussi bien que par la caractérisation des copeaux. La durée de vie de l'outil est exprimée en termes de nombre de trous percés ou taraudés avant que l'outil ne cède.

Une évaluation microstructurale révèle que les phases Al_2Cu, $Al_5Mg_8Si_6Cu_2$, et le script chinois α-$Al_{15}(Fe,Mn)_3Si_2$ sont les principaux constituants de la microstructure de l'alliage 220. L'absence de particule libre de Si dans la microstructure implique que le silicium a été consommé sous forme de phases intermétalliques Al-Fe-Si et Al-Cu-Mg-Si. Les plaquettes de la phase β-Al_5FeSi ne sont pas en évidence en raison du haut ratio Mn: Fe (~ 1) de l'alliage 220 qui favorise la formation de la phase α-Fe au dépend de la phase β-Fe. L'ajout de Sr affine la morphologie de la phase de script chinois α-Fe dans une certaine mesure, résultant à une distribution égale des particules de cette phase dans la matrice d'aluminium. L'ajout combiné de Ti et Zr provoque une diminution de la taille des grains de 68% par rapport à l'alliage de base 220 non-affiné. Cette réduction peut-être attribuable à la formation de particules Zr-Ti qui agissent comme sites de nucléation pour les petits grains équiaxes de α-Al. Les précipités d'étain formant les particules β-Sn qui apparaissent sous forme de petites grappes réparties aléatoirement, se solidifient habituellement au sein du réseau de phase Al_2Cu. Après le traitement thermique, des particules de Bi et de β-Sn ont été trouvés non dissoutes dans la matrice d'aluminium, rendant ainsi possible leur action de décolletage pendant l'usinage.

L'évaluation des propriétés mécaniques montrent que l'effet du Sr sur les propriétés mécaniques à l'égard de la modification du silicium eutectique n'entre pas en jeu et ce en raison de la faible teneur en Si. Le rôle du Sr d'affiner la morphologie de la phase de script chinois α-Fe contribue à une légère amélioration de la ductilité et la ténacité. L'ajout de zirconium produit une amélioration marquée des propriétés mécaniques dans la condition telle que coulée et après traitement thermique en raison de son action d'affinage de grains.

Une quantité excessive de Fe augmente la précipitation des particules de script chinois α-Fe réduisant ainsi les propriétés de traction et de résilience. L'ajout subséquent de Mn augmente légèrement la limite élastique et la limite ultime sans créer de changement observable pour la ductilité et la ténacité. Contrairement aux attentes, l'ajout d'argent ne produit pas d'augmentation considérable dans les propriétés de résistance (YS et UTS) ou dans les valeurs de dureté pour les conditions traitées. Ces résultats sont attribuable à la présence de Si qui favorise la formation de la phase Mg-Si au début du vieillissement, qui à son tour réduit le nombre de co-amas Mg-Ag, appelés à servir de sites de nucléation efficaces pour les précipités de durcissement. L'addition de Sn diminue les propriétés de résistance et les valeurs de dureté mais augmente la ductilité et la ténacité dans l'état tel que coulé en raison de l'effet d'adoucissement de la phase Sn. Dans les conditions de traitement, la réduction causés aux propriétés de résistance et de dureté est principalement attribuable à la formation de porosité associée à la fonte de Sn pendant le traitement de mise en solution et le remplacement du Si par le Sn dans les composés de Mg, ce qui à son tour, entrave la précipitation de la phase de Mg lors du durcissement. La présence de Bi sous forme de particules fragiles non dissoutes réduit mécaniquement les propriétés de traction et de résilience dans l'état tel que coulé. Ces particules, en liaison avec l'interaction Bi-Mg qui consomme le Mg libre disponible pour former la phase de durcissement Mg, sont responsables de la réduction causée aux propriétés mécaniques dans les conditions traitées.

Les caractéristiques de vieillissement révèlent qu'un traitement à 180°C entraîne un durcissement de l'alliage pour des temps allant de 2 à 16 heures, alors qu'un traitement à 220°C cause un sur-revenu qui occasionne un adoucissement après 2 heures de vieillissement. La présence de plusieurs phases de durcissement dans le système d'alliage Al-Cu-Si-Mg, y compris θ (Al_2Cu), β (Mg_2Si), et Q ($Al_5Mg_8Si_6Cu_2$), qui ne doivent pas céder à tous croissance simultanément, conserve les propriétés de résistance et les valeurs de dureté à des niveaux élevés, sans aucun recul pour un vieillissement à 180°C allant jusqu'à 16 heures. Basé sur cette enquête, afin de maintenir un compromis satisfaisant entre la résistance et la ductilité, un traitement T6, réalisé à 180°C pour des temps de vieillissement allant de 2 à 8 heures, est recommandé pour le nouvel alliage Al-Cu.

Pour les essais d'usinage, les résultats montrent que tous les alliages étudiés ont atteint un taux d'usinabilité supérieur tout en respectant la durée de vie de l'outil qui peut dépasser 2500 trous. Ces résultats pour la durée de vie de l'outil sont compatibles avec le fait qu'il n'y a pas eu d'usure importante sur le foret ou de changement observable dans la largeur de la l'arête (BUE) pendant le processus de forage. L'addition de Sn et Bi améliore considérablement l'usinabilité en diminuant la force totale de forage pendant la période d'évaluation par des valeurs moyennes de 14% et 25%, respectivement, par rapport à l'alliage de base 220. Le moment total de forage a été réduit d'à peu près les mêmes valeurs. Une inspection des copeaux de forage révèle que les alliages de base 220 produits des copeaux en forme d'éventail à l'exception des alliages contenant du Bi, les copeaux ont tendance à prendre une forme d'aiguille. L'ajout de Bi augmente la fragmentation des copeaux de 70% par rapport à l'alliage de base 220, alors qu'aucun changement pour les

caractéristiques des copeaux a été causé par l'addition de Sn. De par sa ductilité supérieure, l'alliage A206 est apte à produire des copeaux coniques longs et continus et affiche une fragmentation qui est 32% inférieure à celle de l'alliage 220. Les résultats de taraudage montrent que les additifs ont le même effet sur la force et le moment de taraudage que celle observée pour les essais de forage. Le taraud, cependant, affiche une durée de vie plus courte par rapport à le foret pour toutes les conditions d'alliage étudiées. Une telle diminution de la durée de vie peut être attribuable à une plus grande sensibilité du taraud en acier rapide à l'effort de coupe par rapport au foret en carbure. Une étude comparative menée sur le comportement d'usinage de l'alliage 220 et celui des alliages A206, 356, B319, A319 révèle que l'alliage 220 peut être proposé comme une alternative moins dispendieuse et plus légère pour une utilisation dans les applications d'usinage des alliages A206. Cette conclusion est solidement fondée sur la convergence des résultats pour les deux alliages à l'égard des forces et des moments de forage, ainsi que sur l'amélioration relative des caractéristiques des copeaux obtenus de l'alliage 220. La comparaison montre également que l'usinabilité de l'alliage 220 peut être un compromis acceptable entre ceux des alliages 356 et B319, d'une part, et celle de l'alliage A319 de l'autre.

ABSTRACT

The present dissertation is aimed at investigating the effects of additives on the mechanical properties and machinability of the 220 alloy which is a new Al-2%Cu-1.3%Si-0.4%Mg casting alloy intended for automotive applications. The research involved here was accomplished through two types of study: (i) study of mechanical properties; (ii) and study of machinability. The study of mechanical properties was proposed to examine the effects of Sr, Ti, Zr, Fe, Mn, and Ag as well as of free-cutting elements, specifically Sn and Bi, on the mechanical properties of the 220 alloy in both the as-cast and heat-treated conditions. The mechanical properties in question include tensile, hardness, and impact properties which were all evaluated at room temperature. The study of machinability was devoted to examining the drilling and tapping performance of four 220 based-alloys as well as of A206 alloy which was selected for a comparative study on the machinability of this particular alloy and that of 220 alloy. The four 220 based-alloys were selected from amongst the alloys prepared in the first study and include: (i) 220 alloy; (ii) 220 alloy + Ti + Zr; (iii) 220 alloy + Ti + Zr + Sn; and (iv) 220 alloy + Ti + Zr + Bi. The machining performance was evaluated based on the calculation of the cutting force, cutting moment, and tool life, as well as on the investigation of chip characteristics. Tool life was expressed as the number of holes drilled/tapped up to the point of tool breakage.

An assessment of the microstructure reveals that Al_2Cu, $Al_5Mg_8Si_6Cu_2$, and the Chinese script-like α-$Al_{15}(Fe,Mn)_3Si_2$ phases are the main microstructural constituents of the 220 alloy. The absence of free Si in the microstructure implies that the Si-content was consumed in the formation of the Al-Fe-Si and Al-Cu-Mg-Si intermetallic phases. The platelet-like β-Al_5FeSi phase was not in evidence because of the higher Mn:Fe ratio (~1) of the 220 alloy which promotes the formation of the α-Fe phase at the expense of the β-Fe phase. The addition of Sr refines the morphology of the α-Fe Chinese script phase to a certain extent, resulting in the even distribution of the particles of this phase within the aluminum matrix. The combined addition of Ti and Zr causes a reduction in the grain size by about 68% compared to the non-grain-refined base 220 alloy. This reduction may be ascribed to the formation of Zr-Ti particles which act as nucleation sites for small equiaxed grains of α-Al. Tin precipitates in the form of β-Sn particles which appear as small non-uniformly distributed clusters usually solidified within the Al_2Cu phase network. Bismuth and β-Sn particles were found undissolved in the Al-matrix after heat treatment, thereby making it possible to induce their free-cutting action during machining.

Results from the evaluation of the mechanical properties show that, because of the low Si content, the effects of Sr on the mechanical properties with respect to the modification of silicon eutectic do not come into play. The role of Sr in refining the morphology of the α-Fe Chinese script phase, however, contributes to a slight improvement in ductility and toughness. The addition of zirconium produces a

significant improvement in the mechanical properties in the as-cast and heat-treated conditions as a result of its grain-refining action. An excess amount of Fe increases the precipitation of α-Fe Chinese script particles thereby reducing the tensile and impact properties. The subsequent addition of Mn marginally increases the YS and UTS without creating any observable change in ductility and toughness. Contrary to expectations, the addition of silver does not produce any considerable increase in the strength properties (YS and UTS) or in the hardness values in the heat-treated conditions. Such results may be ascribed to the presence of Si which favors the formation of the Mg-Si phases during the early stages of aging, in turn reducing the number of Mg-Ag co-clusters known to act as effective nucleation sites for hardening precipitates. The addition of Sn lessens the strength properties and hardness values but raises the ductility and toughness in the as-cast condition as a result of the softening effect of the soft Sn-bearing phases. In the heat-treated conditions, the reduction caused in the strength properties and hardness is attributed mainly to the formation of porosity associated with the melting of Sn during solution heat treatment and the replacement of Si with Sn in Mg compounds; this in turn hinders the precipitation of Mg-hardening phases. The presence of Bi as undissolved brittle particles mechanically reduces the tensile and impact properties in the as-cast condition. These particles, in conjunction with the Bi-Mg interaction which consumes the amount of free Mg available to form the Mg-hardening phases, are responsible for the reduction caused in the mechanical properties in the heat-treated conditions.

Aging characteristics reveal that age-hardening at 180°C results in alloy-hardening with aging for times ranging from 2 to 16 hours, whereas age-hardening at 220°C causes overaging and alloy-softening after 2 hours of aging. The presence of several hardening phases in the Al-Cu-Si-Mg alloy system, including θ (Al_2Cu), β (Mg_2Si), and Q ($Al_5Mg_8Si_6Cu_2$), which need not all yield to coarsening simultaneously, maintains strength properties and hardness values at high levels without any significant decline for up to 16 hours of aging at 180°C. These results suggest that a T6-temper, carried out at 180°C for aging times ranging from 2 to 8 hours, may be recommended for the new Al-Cu based alloys under investigation in order to maintain a satisfactory compromise between strength and ductility.

As regards the machinability trials, the results show that all alloys studied attained a *superior rate of machinability with respect to the drill life* which may exceed 2500 holes. This record of tool life is consistent with the fact that there is no significant drill wear or any outstanding change in the width of the built-up edge (BUE) observed with the progress of the drilling process. The addition of Sn and Bi improves the machinability considerably by decreasing the total drilling force over the evaluation period by average values of 14% and 25%, respectively, compared to the base 220 alloy. The total drilling moment was reduced by almost the same values. An inspection of drilling chips reveals that all 220 based-alloys produce fan-shaped chips except for the Bi-containing alloy, chips from which tend to assume a needlelike form. The addition of Bi increases chip breakability by about 70% compared to the base 220 alloy,

whereas no distinct change in chip characteristics was caused by the addition of Sn. In the light of its higher ductility, the A206 alloy is apt to produce long continuous conical chips and displays a chip breakability which is about 32% less than that of the 220 alloy. Tapping results show that the additives have the same effect on the tapping force and moment as that observed for the drilling tests. The tap, however, displays a shorter tool life compared to the drill for all the alloy conditions studied. Such a shorter tool life may be ascribed to the higher sensitivity of the high-speed steel tap to the cutting force compared to the carbide drill. A comparative study carried out on the machining behavior of the 220 alloy and that of the A206, 356, B319, and A319 alloys reveals that the 220 alloy may confidently be proposed as a promising cheaper and lighter alternative for use in the machining applications of A206 alloy. This conclusion is solidly based on the convergence found in the results for both alloys with respect to the drilling forces and moments, as well as on the relatively improved chip characteristics displayed by the 220 alloy. The comparison also shows that the machinability of the 220 alloy may be deemed an acceptable compromise between that of the 356 and B319 alloys, on the one hand, and that of the A319 alloy on the other.

ACKNOWLEDGMENTS

First of all, I would like to express my sincere gratitude to my supervisor, Dr. Fawzy H. Samuel, Professor at Université du Québec à Chicoutimi (Canada) and visiting Professor at King Saud University (Saudi Arabia) for motivating me to complete my Ph.D. degree; without his continuous guidance and support it would have been impossible to do so. I am much indebted to him for helping me so generously over the last four years. I feel privileged to have been able to work with someone whose dedication and contribution to the field of science will be a constant inspiration to me throughout my life.

I would also like to express my sincere thanks to Dr. Agnes Marie Samuel, Research Professor at Université du Québec à Chicoutimi (Canada) for her invaluable guidance and help during different stages of my research work.

Financial support in the form of scholarships received from the Natural Sciences and Engineering Research Council of Canada (NSERC), the Fondation de l'Université du Québec à Chicoutimi (FUQAC), General Motors Powertrain Group (U.S.A), and Corporativo Nemak (Mexico) is gratefully acknowledged.

I would like to extend my appreciation to Mr. Alain Bérubé of the TAMLA group, at UQAC, for his assistance with the castings and sample preparation, as well as to Mr. Lang Shi of the Microanalysis Laboratory, Earth and Planetary Sciences, McGill University for carrying out EPMA analyses.

Thanks are also due to Madame Marion Sinclair for her patience and painstaking efforts in editing my thesis.

Credit goes to the members of my family, especially to my parents and my wife, Sahar, as well as to my brothers and sister for their sound advice and unfailing encouragement during the time it took to write my thesis.

PUBLICATIONS

Journal Papers

1 - Machinability Aspects of New Al-Cu Alloys Intended for Automotive Castings,
E.M. Elgallad, F.H. Samuel, A.M. Samuel and H.W. Doty,
Journal of Materials Processing Technology, Accepted (6 June 2010).

2 - Effects of Additives on the Microstructures and Tensile Properties of a New Al-Cu Based Alloy Intended for Automotive Castings,
E.M. Elgallad, F.H. Samuel, A.M. Samuel and H.W. Doty,
AFS Transactions, 2010, Vol. 118, Paper 10-042, pp 39-56.

3 - Development of New Al-Cu Based Alloys Aimed at Improving the Machinability of Automotive Castings,
E.M. Elgallad, F.H. Samuel, A.M. Samuel and H.W. Doty,
International Journal of Metalcasting, 2009, Vol. 3, Issue 2 (Spring 2009), pp 29-41.

4 - Development of New Al-Cu Based Alloys Aimed at Improving the Machinability of Automotive Castings,
E.M. Elgallad, F.H. Samuel, A.M. Samuel and H.W. Doty,
AFS Transactions, 2008, Vol. 116, Paper 08-007, pp 31-45.

Conference and Presentations

5 - Effects of Additives on the Microstructures and Tensile Properties of a New Al-Cu Based Alloy Intended for Automotive Castings,
114th AFS Metalcasting Congress, Orlando, FL, USA, 20-23 March 2010.

6 - Effects of the Addition of Free-Cutting Elements on the Machinability of a new Al-Cu Base Alloy Intended for Automotive Castings,
Annual conference of General Motors Corporation, Detroit, MI, USA, 17 April 2009

7 - Development of New Al-Cu Based Alloys Aimed at Improving the Machinability of Automotive Castings,
112th AFS Metalcasting Congress, Atlanta, GA, USA, 17-20 May 2008.

8 - Development of New Al-Cu Based Alloys for Improving the Machinability of Automotive Castings,
Poster: Axis II – New Aluminium Products and Materials, *The Encyclopaedia of Research on Aluminium in Quebec – 2007 Edition*, Les Presses de l'Aluminium (PRAL), Chicoutimi, Canada, 2008, p. 43.

TABLE OF CONTENTS

LIST OF TABLES

CHAPTER 2: REVIEW OF THE LITERATURE

CHAPTER 3: EXPERIMENTAL PROCEDURES

CHAPTER 4: MICROSTRUCTURAL CHARACTERIZATION

CHAPTER 6: MACHINABILITY EVALUATION

LIST OF FIGURES

CHAPTER 2: REVIEW OF THE LITERATURE

CHAPTER 3: EXPERIMENTAL PROCEDURES

CHAPTER 4: MICROSTRUCTURAL CHARACTERIZATION

CHAPTER 5: INVESTIGATION OF THE MECHANICAL PROPERTIES

CHAPTER 6: MACHINABILITY EVALUATION

CHAPTER 1

DEFINING THE PROBLEM

CHAPTER 1

DEFINING THE PROBLEM

1.1 INTRODUCTION

This study was undertaken to examine the effects of certain additives on the mechanical properties and machinability of a new Al-2%Cu-1.3%Si-0.4%Mg casting alloy intended for automotive applications; this is known as the 220 alloy. This alloy may be proposed as a potentially promising companion to the notable alloys of both the Al-Cu and Al-Cu-Si-Mg systems based on the following considerations:

- The alloy can be produced easily by recycling aluminum scrap.
- The alloy composition makes it possible for the same phases found in the A319 alloy to form, except for the Al-Si eutectic phase, which ensures a significant response to the precipitation-hardening process.
- The Si content is sufficient to tie up the Fe and Mg in the form of intermetallics. There would, thus, be no free Si in the matrix to cause problems from the machinability point of view.
- The lower copper content in the 220 alloy of only 2%, compared to 5 % in the 206 alloy, improves the corrosion resistance, as well as reduces the density and cost of this category of alloys.

Aluminum-copper alloys represent a significant category of aluminum alloys based on their distinctive age-hardening response which is attributed to the precipitation of the effective hardening phase *θ* (Al_2Cu) in such alloys. Poor casting properties, however, restrict the application of high strength binary Al-Cu casting alloys. These alloys are therefore usually inoculated with Si in order to increase their fluidity and to curtail their tendency to hot tearing. Magnesium may also be added to Al-Cu casting alloys to stimulate the aging process and to form the *S* (Al_2CuMg) hardening phase as well as *β* (Mg_2Si) and/or *Q* ($Al_5Mg_8Si_6Cu_2$) hardening phases in the presence of Si.

Addition of alloying elements is one of the major techniques used to improve the quality of aluminum casting alloys in the form of better structure and mechanical properties. Traces of Sr are added to Al casting alloys containing Si to modify the morphology of Si particles from coarse flakes to a finer spherical morphology. In addition, recent studies show that the absorption of Sr by iron intermetallics will refine their morphology considerably.[1-3] Titanium and boron are added either individually or in combination to refine the grain structure of *α*-Al by providing large numbers of nuclei in the melt; this in turn induces the formation of small equiaxed grains of *α*-Al which otherwise solidifies with a coarse, columnar grain structure. Zirconium is used as a grain refiner and can also be used to form the fine coherent Al_3Zr dispersoids. These coherent particles are observably stable at high aging temperatures and they resist coarsening due to the low solubility and diffusivity of Zr in the Al matrix.[4, 5] Silver is added to Al-Cu-Mg alloys to enhance their age-hardening response. It has been reported that Ag and Mg atoms attract each other forming atom clusters which serve as nucleation sites for the Ω phase.[6,7] This phase is a variant of the equilibrium θ (Al_2Cu) phase and substantially improves high-temperature strength values because of its considerable thermal stability.[8,9]

All elements which are not classified as alloying additives are termed impurities. The percentage of such impurities must be controlled carefully to avoid their negative effects on the castability and mechanical properties of aluminum alloys. Iron is the most common impurity to be found in aluminum alloys appearing in the form of intermetallic second phases in combination with aluminum as well as other elements. The most deleterious Fe-rich intermetallic phase is the brittle platelet-like β-Al_5FeSi.[10-12] It has been reported that the presence of Mn promotes the development of a more compact, less harmful α-$Al_{15}(Fe,Mn)_3Si_2$ phase at the expense of the β-Al_5FeSi phase.[12-15]

Heat-treatment is of major importance since it is commonly used to alter the mechanical properties of cast aluminum alloys. Heat-treatment improves the strength properties and dimensional stability of aluminum alloys through a process known as precipitation-hardening in which precipitates are formed in the aluminum matrix. These second-phase particles impede the motion of the dislocations which in turn increases strength. When an alloy is heated above the solvus temperature of the secondary phases in the matrix, the hardening alloying elements dissolve in the aluminum matrix to form a solid solution. Following a quench or rapid cooling, the alloying elements precipitate out of the solution during the next step called aging, which may be carried out either naturally at room temperature or artificially at elevated temperatures to increase the kinetics of the process. The T6 and T7 tempers are the most frequently applied heat treatments for the improvement of the mechanical properties of Al casting alloys. The T6-temper is applied to obtain the best compromise between strength and ductility,[16,17] whereas the stabilizing T7-temper is usually carried out to increase dimensional stability and performance at elevated temperatures.[18]

Machinability can be defined, simply, as a measure of the ease with which a particular material can be machined satisfactorily. The most commonly used criteria for assessing machinability are the cutting force, or power consumption, chip form, and tool-wear rate.[19-21] Machinability increases as the cutting force and power consumption decrease for the cutting conditions of interest. Lower cutting forces imply lower tool-wear rates, better dimensional accuracy, and increased machine tool life. Based on the chip form criterion, materials producing short chips which are easily managed and disposed of are more machinable than those which produce long unbroken chips or small, powder-like chips. Chip form is often used to assess the machinability of soft, ductile alloys, especially aluminum alloys. Chip control involving chip breaking and removal are of great importance in drilling, since the allowable penetration rate of the drill is often limited by the chip-breaking characteristics.

The development of *free-cutting* aluminum alloys is the most common metallurgical technique used to improve the machinability of this type of alloys. The terms *free cutting* or *free machining* mean that the chips should flow freely from the cast specimen being cut, and that they should also be short and breakable to prevent fouling of the cutting tool or other operating parts of the machine. Free-cutting aluminum alloys were prepared through the addition of free-cutting elements such as tin, lead, and bismuth, which remain as separate phases dispersed in the matrix due to their very limited solubility in the aluminum matrix.[22] During the machining operation, the temperature generated in the cutting zone is believed to be sufficient enough to melt these dispersed phases. This melting leads to a local loss in material strength and ductility which in turn promotes the formation of short, discontinuous chips. Also, these elements act as a lubricant during machining, thereby decreasing the friction between chip and tool edge which again leads to lower cutting forces, less tool wear, a low tendency to form built-up edge (BUE), and a smooth surface finish.

1.2 OBJECTIVES

This research study was planned with the aim of understanding how alloying elements affect the mechanical properties and machinability of an Al-2%Cu-1.3%Si-0.4%Mg casting alloy (the 220 alloy). In keeping with this aim, the objectives of the proposed research are as follows:

1. Determining the effects of certain additives, namely Sr, TiB_2, Zr, Ag, Fe, and Mn, as well as certain free-cutting elements, specifically Sn and Bi, on the mechanical properties (*i.e.* tensile, hardness, and impact properties) of the base 220 alloy in the as-cast and different aging conditions.
2. Using quality index maps to correlate the tensile properties, *i.e.* YS, UTS, and %EL, and to evaluate the quality of the alloys corresponding to the abovementioned additives.

3. Assessing the machinability of selected compositions (4 or 5 alloys) in the drilling and tapping processes through the measurement of the cutting force, cutting moment, and tool life, as well as through the investigation of chip characteristics.

In addition, introducing the 220 alloy for industrial applications relevant to machining processes imposes the need for:

4. Ranking the machinability of the 220 alloy against that of the most significant Al-Cu and Al-Si-Mg-(Cu) alloys, namely the A206, 356, and 319 alloys.

CHAPTER 2

REVIEW OF THE LITERATURE

CHAPTER 2

REVIEW OF THE LITERATURE

2.1 ALUMINUM ALLOYS

The unique combination of properties provided by aluminum and its alloys makes aluminum one of the most adaptable, economical and attractive metallic materials for a broad array of uses ranging from soft, highly ductile wrapping foil to applications in the automobile and aircraft industries.

Aluminum alloys are divided into two main groups: aluminum wrought alloys and aluminum casting alloys.[23] Aluminum wrought alloys are available primarily in the form of worked products which have been subjected to plastic deformation by cold and hot working processes such as rolling, extrusion, and drawing either singly or in combination, so as to transform cast aluminum ingots into the desired product form. The microstructural changes associated with the working and with any accompanying thermal treatments are used to control certain properties and characteristics of the worked, or wrought, product or alloy. Typical examples of wrought products include plates or sheets, household foil, extruded shapes such as window frames, and forged automotive and airframe components.

Aluminum casting alloys are the most versatile of all common foundry alloys and possess the following favorable characteristics: excellent castability, low melting temperature, low gas solubility, and high strength-to-weight ratio, all of which are accompanied by good machinability and satisfactory thermal and electrical conductivity. Worldwide, the use of aluminum casting alloys for automotive applications is increasing; these alloys are thus used primarily for engine components, including engine blocks, cylinder heads, pistons, intake manifolds, and housings. Aluminum alloy castings are routinely produced by means of high-pressure die, permanent-mold, green-and dry-sand, investment, and plaster casting. They are also readily cast with vacuum, low pressure, centrifugal, and pattern-related processes such as lost foam.

Aluminum wrought alloys and aluminum casting alloys are most commonly identified according to the Aluminum Association (AA) using a four digit designation xxxx and a three-digit-plus decimal designation xxx.x, respectively.[18] For both wrought and casting alloys the first digit indicates the alloy series. The second digit in the wrought alloys designation, if different from 0, indicates a modification of the specific alloy. The last two digits for wrought alloys and the second and third digits for casting alloys are arbitrary numbers given to identify a specific alloy in the series or to identify aluminum purity for 1xxx and 1xx.x pure aluminum series. For casting alloys, the digit following the decimal indicates the form of the product so that the alloys are registered by the AA as xxx.0 to represent the chemical composition limit for castings and as xxx.1 and xxx.2 to represent the chemical composition limits for ingots. Several casting alloys designations also include a capital letter prefix indicating certain composition modifications to a specific alloy, for example 356 and A356, or 380, A380, and B380, and so forth.

~~Aluminum alloys may be further classified as heat-treatable and non-heat-treatable~~ alloys, based on the primary mechanism of property development.[23,24] Heat-treatable alloys are strengthened by precipitation hardening involving solution heat treatment, quenching, and controlled aging. Non-heat-treatable alloys are those which derive strength from solid solution or dispersion hardening and are further strengthened by strain hardening. The major heat-treatable aluminum alloy systems include Al-Cu(-Mg), Al-Mg-Si, and Al-Zn-Mg(-Cu) systems while the non-heat-treatable aluminum alloy systems include Al-Si, Al-Mg, and Al-Mn systems. Heat-treatable alloys are used for manufacturing aircraft and automotive parts and structures, screw machine parts, and welded structures. Non-heat-treatable alloys are used for manufacturing deep drawn parts, sheets, foil, tubes, wire, extruded parts, and pressure vessels.

Aluminum alloys usually contain several alloying elements in order to achieve the best combination between mechanical, physical, and processing properties. The major alloying elements are Si, Cu, Mg, and Zn.[18,24] Silicon provides excellent castability, good wear resistance, low specific gravity, high thermal conductivity, and a low thermal expansion coefficient and contributes to the age-hardening process in the presence of Mg by forming the precipitation hardening β (Mg_2Si) phase precipitates. Copper imparts substantial precipitation-hardening characteristics through the precipitation of the θ' (Al_2Cu) phase. Magnesium is used in combination with copper to accelerate and intensify the age-hardening process, particularly at room temperature. Zinc and magnesium form $MgZn_2$, which produces a considerable response to heat treatment. The addition of minor alloying elements such as Sr, Ti, Sn, Pb, and Bi are also important because of their specific effects.[18] Traces of Sr are added to Al-Si casting alloys to modify the morphology of Si particles from coarse flakes to a finer spherical morphology. Titanium is added at concentrations of 0.1 to 0.2% to refine the primary aluminum grain structure for aluminum alloy castings and ingots. The low melting-point metals such as Sn, Pb, and Bi are introduced either individually or together to improve the machinability of both wrought and casting aluminum alloys. Some elements may frequently be present in aluminum alloys in small quantities as impurities. Iron is the most common impurity to be found in aluminum alloys appearing in the form of intermetallic second phases in combination with aluminum as well as other elements. Despite the fact that small amounts of Fe occurring in aluminum may reduce soldering during die casting, its presence in Al-Si casting alloys is generally undesirable since it forms coarse iron-rich phases which adversely affect the mechanical properties and machinability of these alloys.

2.2 ALUMINUM-COPPER CASTING ALLOYS

Copper is one of the most important alloying ingredients for aluminum alloys because of its appreciable solubility in solid aluminum with a maximum value of approximately 5.7 wt% at the eutectic temperature of 548°C, as depicted in Figure 2.1.[25] The aluminum rich α-Al phase forms initially during the solidification of hypoeutectic alloys containing less than 33.2% Cu; subsequently the remaining liquid separates at the eutectic temperature into α-Al and the Al_2Cu intermetallic phase designated θ. The composition of the θ (Al_2Cu) phase ranges from 52.5 to 54.1% Cu corresponding to the eutectic temperature and room temperature, respectively.

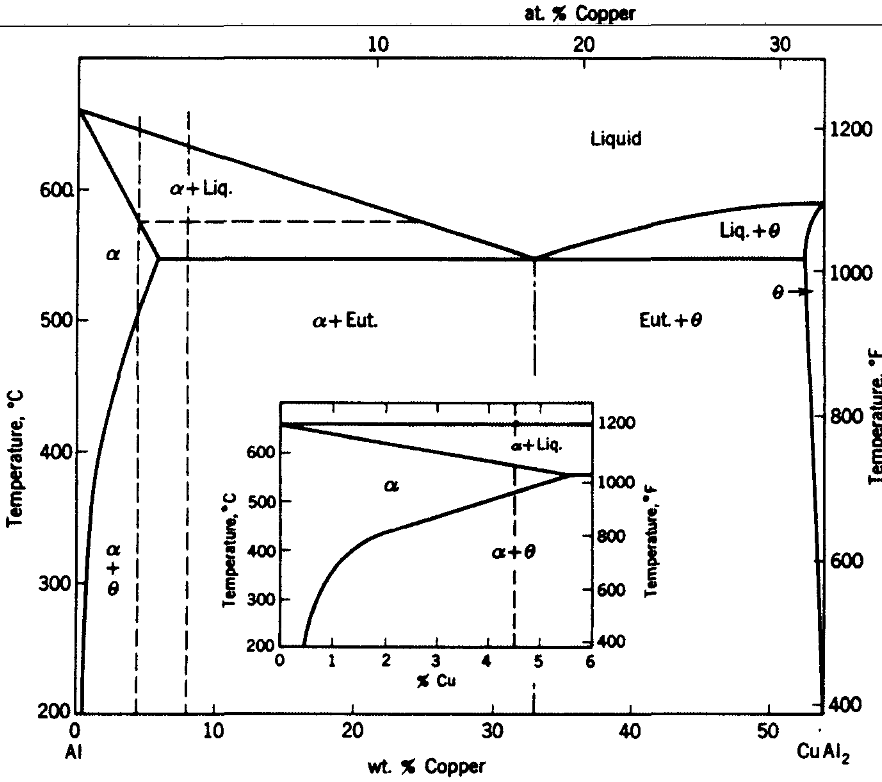

Figure 2.1 Phase diagram of the Al-Cu alloy system, from 0 to 54% Cu.[25]

Owing to their distinctive precipitation-hardening response, Al-Cu alloys have contributed more than any other alloy system to the growth of the aluminum industry. A significant expansion of the use of aluminum castings occurred with the development of the heat-treatable Al-Cu alloy 295 which offered much higher mechanical properties than were available in previous alloys. Later, another variation of this 4.5% Cu alloy was developed for use in permanent mold castings, namely alloy 296 containing 0.5% Si, which improves resistance to hot cracking. Alloys 240, 242, A242, and 243 also possess high strength and hardness values at elevated temperatures and are used for diesel engine pistons and air-cooled cylinder heads for aircraft engines. The more recently developed 201, A206, 224, and 249 alloys have revealed higher tensile properties which are comparable to those of any previous aluminum casting alloys, and they are consequently being used to cast premium-quality aerospace parts.[18, 24]

Aluminum-copper alloys, however, have marginal castability relative to almost any of the alloys containing Si. These alloys have limited fluidity and require careful gating and generous riser feeding during solidification to ensure casting soundness. In addition, it should be kept in mind that pressure-tight parts of intricate design are difficult to obtain, and their resistance to hot cracking is relatively poor; they are also susceptible to stress-corrosion cracking in the fully-hardened condition. As a result, the binary Al-Cu casting alloys are infrequently used, in actual fact, while most commercial alloys are alloyed with other additives, mainly Si and Mg.

The addition of Si and Mg to Al-Cu based alloys results in the formation of a family of Al-Cu-Si-Mg alloys which has widespread applications, especially in the automotive and aerospace industries based on the superiority of their mechanical properties, castability, weldability and machinability. The metallurgical parameters controlling the quality and mechanical properties of these alloys, namely, melt treatment, heat treatment, iron-intermetallics, and the addition of alloying elements, will all be discussed in the following subsections.

2.2.1 Melt Treatment

Melt treatment is carried out with the aim of obtaining a preliminary improvement in both the casting and mechanical properties of the cast alloy. The melt treatment of aluminum cast alloys involves three main tasks: (i) melt degassing; (ii) modification of Al-Si eutectic; and (iii) refining the grain structure of α-Al.

2.2.1.1 Melt Degassing

Melt cleanliness is one of the major concerns in the aluminum casting processes due to the desirable high quality of cast products.[26,27] The unwanted inclusions and impurities that could be present in the melt include dissolved gases such as hydrogen, and solid particles such as oxides, carbides, and intermetallic compounds. A high level of these constituents is detrimental to the fluidity, mechanical properties, and machinability of the cast product. Therefore, melt-cleaning practices are routinely used in aluminum casting processes. Rotary degassing is one of the most common techniques that are used for removing unwanted solid particles and dissolved hydrogen from molten aluminum alloys. In this technique an inert gas is injected into the melt through a rotating impeller. The most commonly used inert gas is argon. Figure 2.2 shows a schematic representation of the

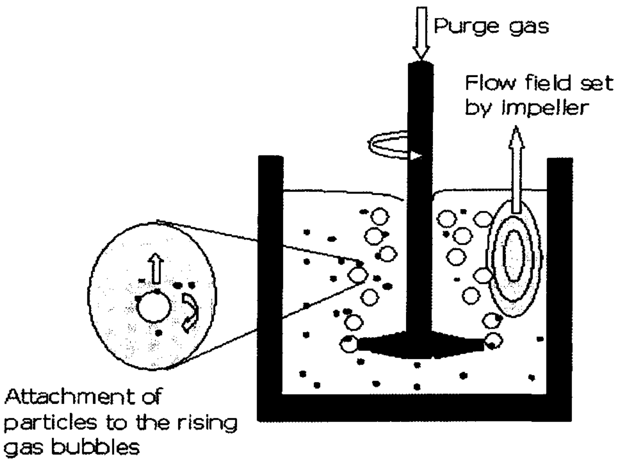

Figure 2.2 Schematic representation of rotary degassing process.

rotary degassing process. The mechanism of hydrogen removal is by diffusion of hydrogen across the metal/gas interface, and the unwanted solid particles are attached to the rising gas bubbles, and may subsequently be removed by carefully skimming the surface layer of the melt.

2.2.1.2 Modification of Al-Si Eutectic

The morphology of eutectic silicon, that is to say, particle size and shape, plays an important role in determining the mechanical properties of Si-containing aluminum cast alloys. The silicon particles appear in the form of coarse acicular plates, and they therefore act as internal stress raisers leading to a lowering in the mechanical properties particularly ductility and impact strength. Changing this morphology, with its deleterious aspect, into a finer and more interconnected fibrous one is known as *eutectic modification.*[28-31] Typical examples for the microstructure of unmodified and modified alloys are provided in Figure 2.3.[31] Chemical modification is the most commonly applied method of modification which produces a fine fibrous silicon structure through the addition of trace levels of

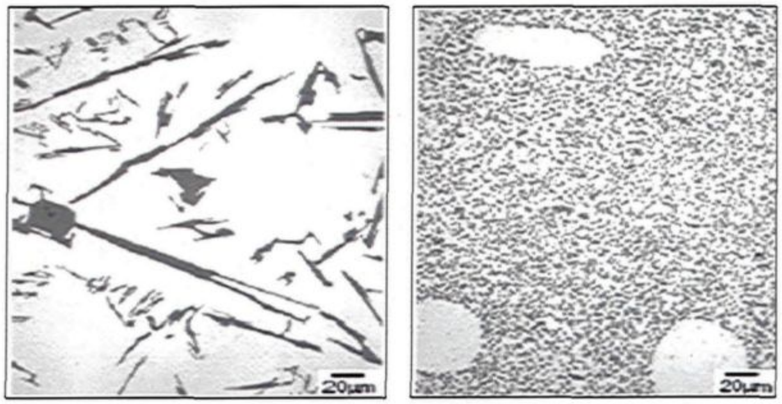

(a) (b)

Figure 2.3 Silicon morphology in (a) unmodified; and (b) Sr-modified hypoeutectic Al-Si alloys.[31]

certain modifying elements, such as strontium, sodium, and antimony. Strontium is preferred as a modifying agent in the light of the rapid fading of sodium and the toxic effects associated with antimony.[30]

This modification of Si morphology reduces the stress-raising capacity of the silicon particles and significantly improves the mechanical properties. Hafiz *et al.*[32] reported that, for steel mold-cast Al-Si alloys, the UTS improved from 177.2 MPa for the non-modified alloy to 225.6 MPa for the modified one using 240 ppm Sr. Fat-Halla[33] also reported that the addition of 200 ppm Sr to Al-13% Si type alloys increases the percentage elongation and the tensile strength without significantly changing the yield strength.

Unfortunately, eutectic modification has also been associated with undesirable changes in porosity characteristics. Modification causes a redistribution of the porosity, which is sometimes accompanied by an increase in porosity levels. It has been observed that the redistribution of porosity is a fundamental characteristic of modification, whereas the effects of modification on the amount of porosity may depend on the casting design and the casting condition.[34,35]

2.2.1.3 Grain Refining

The quality of aluminum cast alloys can be improved by grain refining which reduces the grain size of primary α-Al which otherwise solidifies with a coarse, columnar grain structure. The addition of grain refiners produces large numbers of nuclei in the melt which, in turn, induces the formation of small equiaxed grains of α-Al, as may be seen in

Figure 2.4.[36] A fine equiaxed grain structure leads to several advantages in cast alloys such as upgraded mechanical properties, improved machinability and heightened surface finish. In addition, the fine grains promote adequate feeding during solidification, thereby eliminating shrinkage porosity, and ensuring the even distribution of second phase constituents and microporosity.[37, 38]

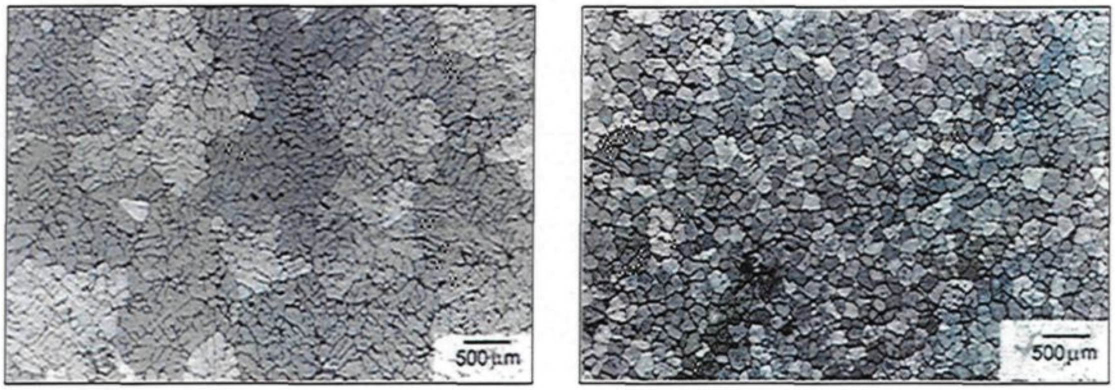

(a) (b)

Figure 2.4 Micrographs of Al-3%Si: (a) unrefined; and (b) refined with 0.15%Ti.[36]

The best grain refiner is that which possesses the same crystal structure as α-Al and which can be effective in small quantities without harming the melt properties. Generally speaking, Al-Ti, Al-B, and Al-Ti-B master alloys are efficient grain refiners for cast aluminum alloys.[39-42] The master alloy Al-5%Ti-1%B is most often used in Al-Si cast alloys to obtain fine equiaxed grains. The grain refining power of Al-5%Ti-1%B master alloy appears to be less than that of Al-3%B and Al-3%Ti-3%B master alloys, however, in Al-Si alloys containing high levels of Si. This occurrence may be attributed to the formation of titanium silicide over the surface of $TiAl_3$ particles in the melt which poisons the nucleating action of the latter.[43]

2.2.2 Heat Treatment of Al-Cu-Si-Mg Alloys

Heat treatment is one of the major techniques applied to enhance the mechanical properties of aluminum casting alloys. The T6 treatment, which comprises solution heat treatment, quenching, and precipitation hardening through artificial aging, is the one most commonly used for Al-Cu-Si-Mg casting alloys with the intent of obtaining the best compromise between strength and ductility.[16,17,23] The stabilization T7 temper is conducted at higher aging temperatures (200-240°C) than is the T6 temper (150-180°C), causing overaging and a consequent reduction in the hardening effect. The T7 treatment is usually carried out to improve some specific characteristic such as corrosion resistance and/or to increase the stability and performance at elevated temperatures.[18] The three steps involved in both T6 and T7 tempers, *i.e.* solution heat-treatment, quenching, and precipitation hardening through artificial aging, are reviewed in the following sections in connection with Al-Cu-Si-Mg alloys.

2.2.2.1 Solution Heat Treatment

The solution heat treatment of Al-Cu-Si-Mg alloys is carried out mainly to dissolve the Al_2Cu and Mg_2Si hardening phases in the Al matrix thereby producing a supersaturated solid solution (S.S.S) of α-Al rich in hardening solutes. The process involves heating the alloy to a temperature which is sufficiently high for a duration of time long enough to achieve a nearly homogeneous solid solution. Under common foundry conditions, polynary Cu-rich eutectic phases with low melting points are often found at the grain boundaries of

Cu-containing Al casting alloys because of non-equilibrium solidification. Solution heat treatment at a higher temperature than the optimum can lead to the incipient melting of these phases at the grain boundaries, which in turn would affect the mechanical properties adversely. Solution heat treatment at low temperatures can also cause problems, however, by not allowing enough solute to go into solid solution. The temperature range of the solution heat treatment of binary Al-Cu alloys is shown in Figure 2.5.[18] It will be observed that the initial eutectic melting temperature is only a few degrees above the maximum recommended solution heat treatment temperature.

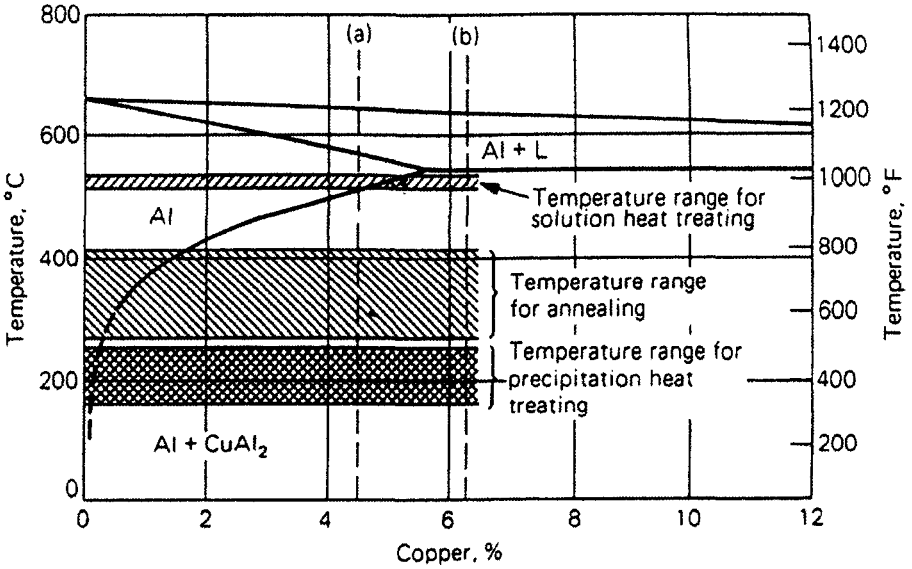

Figure 2.5 Partial equilibrium diagram for aluminum-copper alloys showing the temperature range of solution heat treatment.[18]

For Al-Cu-Si-Mg alloys containing high levels of Cu, such as the 319 alloys, three different copper-rich eutectic phases were reported together with their eutectic melting temperatures, namely, Al_2Cu blocklike eutectic (T_E = 540°C), Al-Al_2Cu eutectic (T_E = 520°C), and $Al_5Mg_8Si_6Cu_2$ fine eutectic (T_E = 507°C).[44] It was suggested that the solution heat treatment temperature of these Al-Cu-Si-Mg alloys should be restricted to below 495°C.[45-47] Wang *et al.*[48] studied the influence of Cu content on the solution heat treatment of Al-11%Si-x%Cu-0.3%Mg cast alloys. They found that an increase in Cu content increases the amount of polynary eutectic phases and consequently the restrictive solution temperature for avoiding incipient melting at the grain boundaries is lowered. For alloys containing 1 wt% Cu, this temperature should be 535°C whereas for alloys having more than 2 wt% Cu it should be 500°C. Crowell *et al.*[49] determined the optimum solution heat treatment for 319.1 alloy by studying the tensile properties at different solution heat treatment temperatures and times. They suggested that, at a temperature of 495°C, the strength properties improve with solution heat treatment time, attaining a peak value between 16 and 32 hours in sand castings and at about 16 hours in unmodified permanent-mold castings. The Sr-modified permanent-mold samples display higher peak values of tensile strength after only about 4 hours.

2.2.2.2 Quenching

The objective of quenching is to preserve the solid solution formed at the solution heat treatment temperature by rapidly cooling it to some lower temperature, usually close to room temperature. When castings are removed from the solution treatment furnace, they are usually quenched in warm or hot water. The best strength is attained when the time taken to place hot castings into water is less than five or six seconds. A high cooling rate after solution treatment significantly increases the hardness in the peak-aged condition.[50,51] Slow quenching rates result in precipitation during quenching, thus reducing the amount of the subsequent possible hardening. This outcome may be ascribed to the fact that, as solute is precipitated from the solid solution during quenching, it is unavailable for any further precipitation reactions. In addition, the slow quenching rates may reduce the corrosion resistance of the alloy at the grain boundaries.[18,52] Thus, many foundries prefer to build the heat treatment furnaces directly above the quenching tank so as to be able to drop the castings directly into the tank thereby obtaining rapid quenching.

2.2.2.3 Precipitation-Hardening Characteristics of Al-Cu-Si-Mg Alloys

The hardening of Al-Cu alloys is achieved by the precipitation of the hardening phase θ (Al_2Cu) out of the supersaturated solid solution (S.S.S), as shown in Table 2.1.[18]

Table 2.1 Precipitation-hardening system of Al-Cu alloys[18]

α-$Al_{s.s.s}$	→	Vacancy-Rich	→	θ''	→	θ'	→	θ
		GP Zones		Disk-Like Coherent		Disk-Like Semi-Coherent		Al_2Cu Equilibrium

The addition of Si and Mg to Al-Cu alloys alters the precipitation-hardening system of these alloys substantially. The precipitation-hardening characteristics of the resulting Al-Cu-Si-Mg alloys often appear to be relatively complex. This complexity may be attributed to the formation of several hardening phases including θ' (Al_2Cu), β'' (Mg_2Si), S' (Al_2CuMg), and the quaternary phase AlMgSiCu which is designated as Q ($Al_5Mg_8Si_6Cu_2$) or λ ($Al_5Mg_8Si_5Cu_2$).[53, 54] It is imperative to mention here that the precipitation-hardening characteristics of Al-Cu-Si-Mg alloys are sensitive to the Cu/Mg and Mg/Si ratios as well as to the total solute content of the alloy. The projection of tetrahedron phase fields, shown in Figure 2.6, was proposed for the identification of the equilibrium phases which may exist in Al-Si-Cu-Mg alloys.[24] When the Mg/Si ratio is greater than about 1, the compositions lie in Field I, having the coexisting phases (Al), *Q*, *θ*, and *β*. When the Mg/Si is less than 1, the compositions occupy Field II, having the coexisting phases (Al), *Q*, *θ*, and (Si). Field III is occupied when the Cu content is generally less than 0.2-0.5%, with variations in the Mg and Si levels.

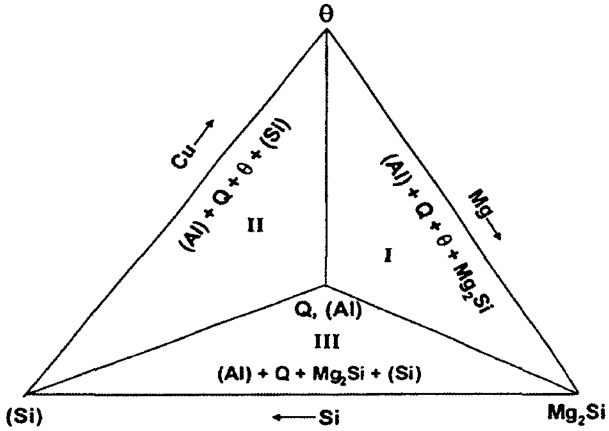

Figure 2.6 Projection of tetrahedron phase fields of Al-Si-Cu-Mg alloys.[24]

The precipitation-hardening characteristics of Al-Cu-Si-Mg alloys have been widely studied. Suzuki *et al.*[55] reported that the precipitation sequence of Al-2%Cu-0.9%Mg-0.25%Si results in the formation of *S′* (Al_2CuMg) and *β′* (Mg_2Si) phase precipitates. Increasing the Si content of up to 0.5%, however, promotes the precipitation of *θ′* (Al_2Cu) and *Q* ($Al_5Mg_8Si_6Cu_2$) while suppressing the formation of the *S′* and *β′* phase precipitates. According to Yao *et al.*,[56] the peak hardening of the Al-7.1%Si-3%Cu-0.39%Mg alloy is caused by the combined precipitation of plate-like *θ′* precipitates and needle-like precipitates. Some of these needles have the same crystal structure as the L and β'' phases where L phase has been reported as a precursor of the Q' phase.[57] In addition, small B' precipitates were observed to be present in the peak-aged specimens and were confirmed to be the lath-shaped transient Mg_2Si-phase, which differs from the rod shaped β'-phase.[58] Li *et al.*[59] concluded that the improvement observed in the mechanical properties of Al-7%Si-0.5%Mg foundry alloys through the addition of Cu may be attributed to the increase in the density of β'' precipitates and the precipitation of Q phase precursors in addition to the precipitation of the θ' phase at higher Cu contents.

A comparison of the age-hardening curves of Al-Si-Mg, Al-Si-Cu, and Al-Si-Cu-Mg alloys was made by Li *et al.*,[60] as shown in Figure 2.7. It was found that double aging peaks are present in the age-hardening curves of Al-Si-Cu-Mg alloys and that the first peak is higher than the second one, whereas a hardness plateau and single hardness peak are present in the age-hardening curves of Al-Si-Mg and Al-Si-Cu alloys, respectively. For the Al-Si-Cu-Mg alloy, the first aging peak is associated with the formation of GP II zones/θ''

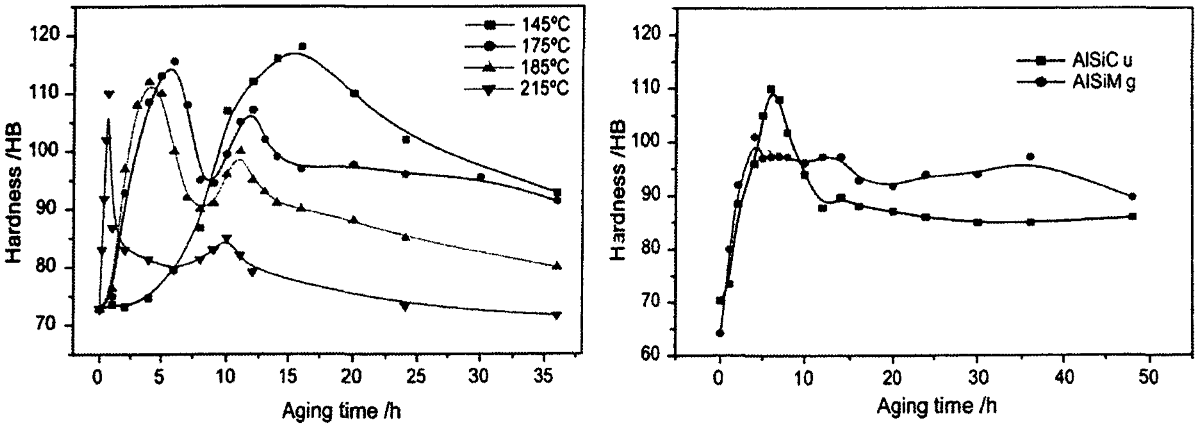

(a) (b)

Figure 2.7 (a) Age-hardening curves for Al-Si-Cu-Mg alloy aged at different temperature; and (b) age-hardening curves for the Al-Si-Mg and Al-Si-Cu alloys aged at 175°C.[60]

and β'' phase, while the second one is the result of the precipitation of metastable phases θ' and β'. The interval occurring between the transition from GP zones to metastable phases, caused by the dissolution of the GP zones and the nucleation of the metastable phases upon dislocation, may be the main reason of the formation of double aging peaks.

2.2.3 Effects of Iron Intermetallic Phases

Iron is one of the most common impurities found in aluminum alloys, frequently appearing as intermetallic second phases in combination with aluminum and other elements. The less common Fe-rich intermetallic phases are δ-Al_4FeSi_2 and π-$Al_8Mg_3FeSi_6$, while the more outstanding and commonly observed ones are α-$Al_{15}(Fe,Mn)_3Si_2$ and β-Al_5FeSi.[10, 61] On a metallographic section, the α-phase appears as Chinese script particles while the platelet-like β-phase appears as needles (Figure 2.8).[62]

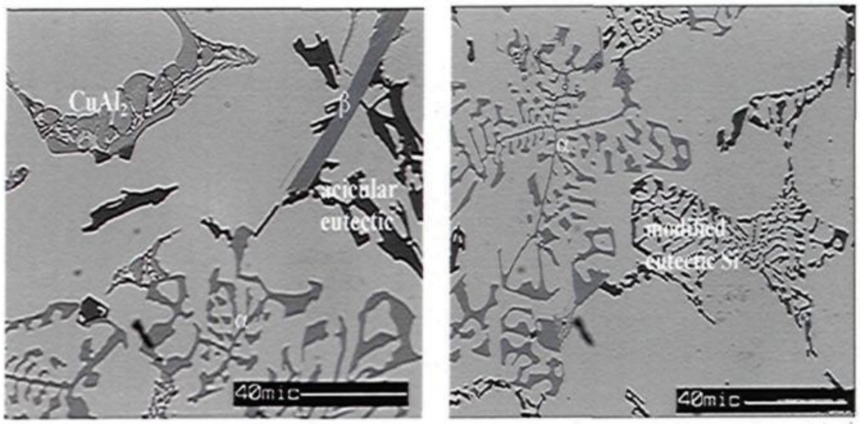

Figure 2.8 Optical micrographs obtained from an as-cast 319 alloy showing the morphology of β-Fe and α-Fe intermetallic phases.[62]

The brittle β-Fe intermetallic phase platelets act as stress raisers during service and adversely affect mechanical properties. It was reported that increasing the iron content from

0.5 to 1.2% in Al-Si casting alloys dramatically reduces the mechanical properties, particularly ductility, due to the formation of the β-Fe phase.[11] Bonsack[12] found that in Al-Si alloys with Fe contents higher than 0.5%, the formation of the β-Fe phase increases strength values and slightly decreases ductility; when the Fe content exceeds 0.8%, however, the ductility decreases significantly. In Al-Si-Cu alloys, increasing the Fe content continuously decreases ductility, and drastically so for Fe contents above 0.9%.[10] The coarse β-Fe phase platelets interfere with liquid flowing into interdendritic channels; this reduces feeding during solidification and consequently promotes the formation of porosity.[63,64] Increasing the Fe content also adversely affects machinability. It has been reported that the abrasive Fe-rich phases abrade cutting tools, even at Fe contents of less than 0.6%. Moreover, the dispersion hardening effect of iron is also likely to increase tool wear.[12]

The critical iron content at which the β-Fe phase appears has been the subject of much debate in the literature. The β-Fe phase is most associated with Fe content of more than 1%.[10] Backerud *et al.*[44] reported, however, that an iron content of 0.48% is sufficient to form the β-Fe phase during solidification of the 356 aluminum alloy. In fact, the critical iron content at which the β-Fe phase forms is strongly dependant on the cooling rate. A recent study states that, at low cooling rates (0.1°C/s), the β-Fe phase is favored, at high cooling rates (10°C/s), the β-Fe phase is inhibited, but at very high cooling rates (20°C/s), the β-Fe phase is strongly favored.[65]

Neutralization of Fe through the promotion of the less harmful α-Fe Chinese script phase is sought at the expense of the brittle needlelike β-Fe phase with the goal of improving strength, ductility and other properties. Small amounts of manganese (usually Mn:Fe = 0.5) play a positive role in combining with iron to form the less harmful α-Fe Chinese script phase instead of the brittle β-Fe phase.[12,13] At higher Mn:Fe ratios and/or in the presence of chromium, however, the iron, manganese and chromium form another version of the α-Fe phase, α-$Al_{15}(Fe,Mn,Cr)_3Si_2$, termed sludge, displaying a star-like morphology. These sludge particles are extremely hard and thus have a detrimental effect on mechanical properties and machinability. The formation of these particles may be controlled by calculating the sludge factor which correlates the %Fe, %Mn, and %Cr levels, as follows:[66, 67]

$$\text{Sludge Factor (S.F.)} = 1 \text{ x wt\% Fe} + 2 \text{ x wt\% Mn} + 3 \text{ x wt\% Cr} \tag{2.1}$$

The critical sludge factor beyond which sludge is formed equals 1.8 if a casting temperature of 650°C or more is maintained. However, for holding temperatures lower than this value, a critical sludge factor of 1.4 is recommended, since sludge formation is a temperature-dependent process in combination with the Fe, Mn, and Cr concentrations.

2.2.4 Effects of Alloying Elements

The addition of alloying elements is a further technique used in combination with heat treatment to improve the mechanical properties of aluminum alloys. The influence of the alloying elements, as used in this research, on heat treatment characteristics and hence on the mechanical properties of aluminum alloys is reviewed below. The alloying elements in question include, specifically, zirconium, silver, tin, and bismuth.

2.2.4.1 Effects of Zirconium

Only a few scattered studies are available to date on the subject of the effects of Zr on cast aluminum alloys. Zirconium is used as a grain refiner to reduce the as-cast grain size and consequently to improve strength and ductility.[18,24] Moreover, additions of Zr in the range of 0.1 to 0.3% are used to form fine coherent precipitates of Al_3Zr called dispersoids. These coherent particles are observably stable upon heating and they resist coarsening because of the low solubility and diffusivity of Zr in the Al matrix and also because of the low interface energy of the particles with the matrix.[4] As a result, these dispersoids effectively inhibit recovery and recrystallization during heat treatment due to their obstructive action thereby causing an increase in hardness and strength properties.[68,69]

It has been reported that a minor addition of Zr, in the amount of 0.15 wt%, can significantly improve the hardness and strength properties of A319 aluminum alloy in both the as-solutionized and age-hardened conditions. This hardening effect of Zr is ascribed to the precipitation of the coherent coarsening-resistant Al_3Zr dispersoids during solution heat treatment.[70] Sepehrband *et al.*[71] reported that small additions of Zr to A319 aluminum cast alloy improve the hardness of the material in both the as-solutionized and age-hardened conditions provided that the alloy is solutionizied for sufficiently long times; this is to allow the precipitation of Al_3Zr phase during solution heat treatment, which has very slow kinetic of precipitation. The same study showed that the aging curve of the Zr-containing A319 alloy exhibits almost constant behaviour after peak hardness has been attained, thereby confirming the resistance of the Al_3Zr dispersoids to coarsening. Yin *et al.*[72] found that the simultaneous addition of 0.1% Zr and 0.2% Sc to Al-5%Mg increases the strength by 150MPa, whereas the ductility remains at a high level. These authors attributed the increment in strength mainly to grain-refinement strengthening, to $Al_3(Zr,Sc)$ dispersive strengthening, and to substructure strengthening.

2.2.4.2 Effects of Silver

The addition of silver to Al-Cu-Mg alloys has been known to promote the formation of a hexagonal-shaped Ω-strengthening phase that forms as finely dispersed plates on the $\{111\}_\alpha$ habit planes replacing the precipitation sequence of Al-Cu based systems.[73-75] The Ω phase, believed to be a variant of the equilibrium θ (Al_2Cu) phase, is most commonly found in Al-Cu-Mg-(Ag) alloys and greatly improves high-temperature strength because of its considerable thermal stability. Based on its similarity with the structure of the θ (Al_2Cu) phase, Garg *et al.*[75] designated the Ω phase as θ_M, representing a modified θ phase.

Reich *et al.*[76] studied the evolution of the Ω phase in an Al-1.9%Cu-0.3%Mg-0.2%Ag alloy. They concluded that this phase evolves from Mg-Ag co-clusters to plate-like precipitates continuously, rather than precipitating directly by heterogeneous nucleation on their precursors. It was also found that neither Mg nor Ag is incorporated within the well-grown Ω plate and its chemical composition is Al-33wt%Cu. Zhu *et al.*[7] stated that, in ternary Al-Cu-Mg alloys with low Mg-to-Cu ratios, Mg-rich Mg-Cu co-clusters act as precursors for the plate-like Ω precipitates. In Al-Cu-Mg-Ag alloys, Ag has an overwhelming tendency to form co-clusters with Mg and this leads to Ag-Mg-Cu co-clusters which act as precursors for Ω precipitates.

The effects of Ag addition on the aging response and mechanical properties of Al-Mg-Si alloys has been discussed in a number of studies.[77,78] Zou *et al.*[77] compared the age-hardening behavior of Al-0.67%Mg-0.77%Si and Al-0.67%Mg-0.77%Si-0.5%Ag alloys. They found that the Ag-bearing alloy has higher aging-hardness than the Ag-free alloy under the same aging conditions. It was presumed that the Ag atoms can trap some moving Mg atoms forming Mg-Ag clusters which provide large number of nucleation sites for Mg-Si clusters or GP zones; this in turn refines and increases β'' phase precipitates. Matsuda *et al.*[78] investigated the effects of the addition of silver on the mechanical properties of two types of Al-Mg-Si alloys, namely a "balanced" alloy and an "excess Si" alloy with a Si-content in excess of that required for Mg_2Si precipitates. These authors found that the addition of Ag increases the peak hardness of the "balanced" alloy, whereas no obvious changes were observed in the hardness of the "excess Si" alloy. The same study indicated that the addition of silver significantly reduces the width of precipitates-free zones (PFZ) which suppresses the intergranular fracture and consequently improves the elongation of the alloy.

2.2.4.3 Effects of Tin

It has been reported that small quantities of Sn, of the order of 0.05 wt%, can have a definite influence on the course of the precipitation of copper in an Al-4%Cu-0.15%Ti alloy. The natural aging of the alloy becomes dampened, but during elevated temperature aging at 165°C and 190°C both the response to artificial aging and the absolute strength increase.[79]

Tin is one of the microalloying elements which is most effective at facilitating the nucleation of θ'. Silcock *et al.*[80] found that the hardening of the Sn-containing Al-Cu alloy proceeds through a single stage at aging temperatures of 130°C and 190°C as a result of the nucleation of the θ' phase at the expense of (GP) zones and θ''. Due to the high binding energy between Sn atoms and vacancies, it is likely that a high vacancy concentration is associated with the Sn clusters reducing the number of free vacancies available to promote the diffusion of Cu atoms for the formation of GP zones and θ'' precipitates.[81, 82] This interpretation was supported by research carried out by Bourgeois *et al.*[83] in which the response to natural aging and the width of the precipitate-free zone (PFZ) in Al-4%Cu and Al-4%Cu-0.05%Sn were compared. It was found that the strong interaction between Sn and vacancies causes a lowering of the diffusion rate of Cu atoms, which would explain the large reduction in the natural aging response and the narrowness of the PFZ observed in the Sn-containing alloy compared with the binary alloy.

To date, there are still a number of different conflicting explanations for the effectiveness of Sn in nucleating θ'. Ringer *et al.*[82] observed that β-Sn particles precipitated in an Al-4%Cu-0.05%Sn alloy after quenching created heterogeneous nucleation sites for fine and uniformly dispersed θ' phase precipitates. Silcock *et al.*[84] studied the role of the trace elements Cd, In or Sn, coded X, in the formation of θ' in Al-Cu alloys. They reported that the nucleation of θ' is considered to result from two possible mechanisms. Heterogeneous nucleation on pre-precipitated X particles is the main mechanism involved at high aging temperatures, at and above 200°C. At lower temperatures, the easier nucleation is due to the incorporation of X atoms into the θ' nuclei which reduces the misfit with the aluminum matrix and thereby reduces the interfacial energy of θ' nuclei.

On the other hand, an automotive parts manufacturing foundry recently reported that Sn reduces the hardness of the heat-treated 319 alloy, a phenomenon which is believed to be due to the softening of α-Al. Grebenkin *et al.*[85] found that Sn and Pb are the electronic analogs of silicon and replace it in magnesium compounds thereby preventing the formation of the Mg_2Si and $Al_xMg_5Si_4Cu_4$ hardening phases in Al-Cu-Si-Mg alloys.

2.2.4.4 Effects of Bismuth

Bismuth was used to improve the machinability of free cutting steel and aluminum alloys. Only a limited amount of research has been carried out on the effects of Bi on the mechanical properties of Al casting alloys. It was demonstrated that Bi could serve as an effective eutectic modifier in Al-Si casting alloys.[86, 87] Thai[88] concluded that Bi refines the eutectic silicon at a concentration of 0.005%, and that the refining ability diminishes beyond this level. It was reported, however, that increasing the amounts of added Bi may counteract the modification effect of Sr.[89, 90] Cho *et al.*[89] found that increasing the amounts of Bi addition to the Sr-modified A356.2 Al alloy decreases the Sr-modification effect and that at a concentration of 1000 ppm Bi, the Sr-modification effect is completely eliminated. It was also reported that Bi counteracts the modification effect of Sr in Al-Si-Cu 319 type casting alloy.[90] This negative effect of Bi was interpreted in terms of Bi-Sr or Bi-Mg-Sr interactions which reduce the amount of free Sr available for Si modification. Despite this marked influence of Bi on the microstructure of Al-Si alloys, it was observed that the addition of this element in proportions of up to 500 ppm to unmodified as well as Na- or Sr-modified A413 alloy does not bring about any significant deterioration in the hardness values or the tensile properties.[91]

Hardy[79] found that Bi has no influence on the aging behavior of an Al-4%Cu-0.15%Ti alloy. It was also suggested that the presence of undissolved Bi particles mechanically reduces the strength properties and elongation of the alloy studied. The effects of the addition of Zn and Bi on the precipitation process of Al-6%Mg alloy was investigated.[92] The results show that the addition of 0.3% Bi to Al-6%Mg-1%Zn alloy further improves the aging response. This effect is surprising since Bi is usually added to Al-Mg-Zn alloys to increase the stress-corrosion performance. It was suggested that the favorable effect produced by the addition of Bi may be explained in terms of an increase in the supersaturation of the alloy, despite the very small atomic fraction that goes into solution.

2.3 QUALITY OF CAST ALUMINUM ALLOYS

Quality in engineering applications will usually be governed by a combination of different factors which provide the minimum risk and maximum performance in conjunction with cost efficiency. The quality of a cast alloy is related to certain microstructural features such as porosity, inclusions, and intermetallic compounds; on the other hand, this quality can also be characterized in terms of its mechanical performance. From the design point of view, the quality of an alloy may be understood as a combination of mechanical properties which meet the design prerequisites of a given application. Thus, the quality of aluminum alloy castings may be defined using a unique numerical value called the quality index "*Q*" which is used to correlate specific mechanical properties. Based on the concept of the quality index, it is possible to generate quality maps for use in evaluating cast aluminum alloys thereby providing the designer a tool for selecting a particular material with properties tailored to suit the requirements of the specific application under consideration. The quality index was first proposed by Drouzy *et al.*[93] in 1980 to correlate the tensile strength and ductility values of Al-7%Si-Mg casting alloys, namely A356/357 alloys. It was then developed in different forms in order to evaluate and optimize the mechanical properties of various series of cast aluminum alloys used for automotive and aerospace applications. The most significant quality indices proposed for aluminum casting alloys together with the relevant quality maps will be explained in greater detail in the following subsections.

2.3.1 Quality Index (*Q*) Proposed by Drouzy *et al.*

The concept of the quality index, Q, was originally proposed by Drouzy *et al.*[93] from the observation that, as a batch of specimens of an Al-7%Si-Mg alloy is aged, a semilogarithmic plot of the tensile strength versus the tensile ductility follows a linear relationship as follows:

$$Q = UTS + d\log(s_f) \qquad (2.2)$$

This relationship implies that alloy quality with respect to the tensile strength, UTS (MPa), and the elongation-to-fracture, s_f (%), can be expressed by a single numeric quality index,

Q (MPa). The parameter d was empirically found to equal 150 MPa for Al-7%Si-Mg alloys.

On the other hand, the study of correlations between tensile strength, 0.2% yield strength, and percentage elongation-to-fracture in cast aluminum alloys[94] showed that the probable yield strength, YS (MPa), may be estimated using the following relationship:

$$YS = a\,UTS - b\log(s_f) + c \tag{2.3}$$

The coefficients a, b, and c depend upon the nature of the alloy. For the Al-7%Si-Mg alloy family,[93] they were determined as 1, 60 MPa, and -13 MPa, respectively. The two equations shown above are valid only for an elongation ≥ 1.

Drouzy and co-workers used Equations (2.2) and (2.3) to plot the "Quality Index Chart" for the A356 alloy (Al-7%Si-0.4%Mg) as shown in Figure 2.9. The chart has two main axes, UTS and s_f, and two auxiliary ones represented by the two sets of parallel lines.

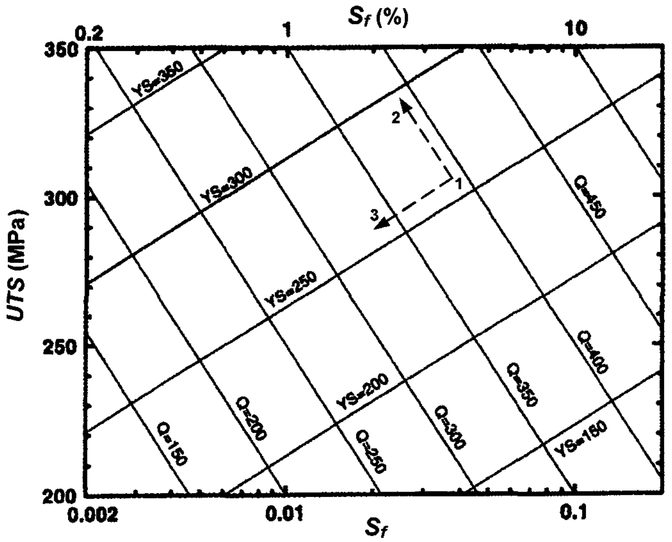

Figure 2.9 A quality index chart for heat-treated Al-7%Si-Mg alloys.[93]

The lines identified by the quality index value, Q, are generated by Equation (2.2) and are called "*iso-Q*" lines, while the lines identified by the probable yield strength value, YS, are generated by Equation (2.3) and are called "*iso-YS*" lines. The change in UTS and $\log(s_f)$ is then said to follow an "*iso-Q*" line or, in other words, the loss of ductility due to the increased strength does not reduce the "quality" of the alloy, as indicated by arrow 1-2 in Figure 2.9. On the other hand, if the ductility is reduced at constant yield strength, for instance by increasing either the dendrite arm spacing (DAS) or the Fe-content of the alloy (for a given aging and Mg content), the alloy quality is said to decrease, as indicated by arrow 1-3 in Figure 2.9. These observations mean that the quality index, Q, is practically independent of the degree of hardening of the alloy, *i.e.* of Mg content and aging conditions, but it depends essentially on the alloy quality, namely upon the soundness, compactness, and fineness of its structure and upon all the factors related to solidification conditions. On the other hand, the probable yield strength YS depends on the Mg-content and heat treatment conditions.

2.3.2 Quality Index (Q_C) Proposed by Cáceres

The drawback of the quality index concept proposed by Drouzy *et al.*[93] is that, it was given no proper theoretical grounding or explicit physical meaning. This gap in its physical basis has been bridged recently by the analytical model created by Cáceres[95-97] which allows calculation of the quality index from knowledge of the parameters of the deformation curve, namely, the strength coefficient of the material and the strain-hardening exponent. The analytical model by Cáceres is based on the assumption that the deformation curves of the material can be described with a constitutive equation of the following form

$$\sigma = K\varepsilon^n \tag{2.4}$$

where σ is the true flow stress, K is the strength coefficient of the material, ε is the true plastic strain, and n is the strain-hardening exponent, defined by

$$n = (\varepsilon / \sigma)(d\sigma / d\varepsilon) \tag{2.5}$$

The true stress σ and the engineering stress P are related by the equation

$$\sigma A_f = P A_o \tag{2.6}$$

where A_o and A_f are the cross sectional areas in the initial and strained conditions, respectively. Since the volume is assumed to be constant during deformation, the following equation can be obtained

$$A_o / A_f = e^{\varepsilon_t} \tag{2.7}$$

where ε_t is the total true strain which has elastic and plastic components. Combining Equations (2.4), (2.6), and (2.7) gives

$$P = K\varepsilon^n e^{-\varepsilon_t} \approx K s^n e^{-s} \tag{2.8}$$

where s is the engineering plastic strain. In Equation (2.8), the sign $\approx$ indicates that the elastic strain component as well as the difference between the engineering and true strain have been disregarded. The latter is a reasonable assumption for casting alloys due to their limited ductility.

Equation (2.8) has been used to draw the family of solid flow curves for the A356 alloy (Al-7%Si-0.4%Mg) with K = 430 MPa, as shown in Figure 2.10. The curves are identified by n-values which vary between 0.2 for as-quenched samples and 0.08 for samples aged 6 hours at 170°C. The values of the strength coefficient, K, and the strain-hardening exponent, n, were obtained from the true stress-true strain curves of Al-7%Si-Mg alloys.[95] The *YS*-values on the right hand side axis indicate the flow stress (MPa) at an offset strain of 0.2%. As reported by Cáceres,[95] for a given aging condition the flow curve of the most ductile samples represents the locus of the UTS/elongation-to-fracture points of the samples with the same yield stress but lower ductility. Thus, the solid flow curves in Figure 2.10 may be interpreted in terms of Drouzy *et al.*[93] as *"iso-YS"* lines relating *UTS* and elongation-to-fracture, each for a particular aging condition.

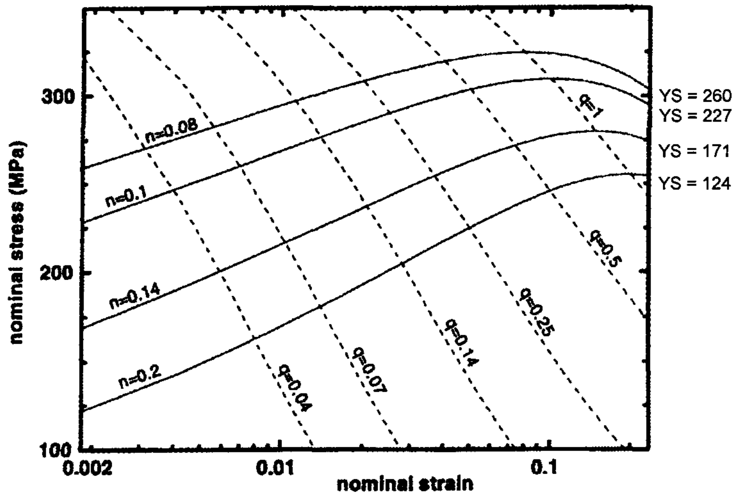

Figure 2.10 The quality index chart proposed by Cáceres for A356 alloy.[95]

In the case of high ductility castings, tensile failure involves some amount of necking. Necking begins when the Considère criterion is met, that is $\gamma = 1$, where γ is the strain-hardening parameter defined as

$$\gamma = (1/\sigma)(d\sigma/d\varepsilon) \tag{2.9}$$

By comparing Equations (2.5) and (2.9), it is obvious that $\gamma = n/\varepsilon$. Thus, when $\gamma = 1$, this implies that $\varepsilon^* = n$, where ε^* is the true plastic strain at the onset of necking. Assuming that $s^* \approx \varepsilon^* = n$, the relative ductility parameter q, defined as the ratio between the engineering plastic strain at failure, s_f, and the engineering plastic strain at the onset of necking, s^*, is given by

$$q = s_f/s^* = s_f/n \tag{2.10}$$

Combining Equations (2.8) and (2.10) gives

$$P = K s^{s/q} e^{-s} \tag{2.11}$$

Equation (2.11) can be used to generate the lines representing contours of constant relative ductility called "*iso-q*" lines, as shown in Figure 2.10, each identified by a q-value. The usefulness of q resides in the fact that it expresses how far a particular sample is from its maximum possible ductility. The samples which deform up to or beyond necking (*i.e.* $q \geq 1$) have the highest combination of elongation and *UTS* or be of the best quality possible, while the samples which fail before the onset of necking (*i.e.* $q < 1$) will be of a lesser quality. This concept provides a straightforward physical meaning for the quality index, *Q*, in terms of the relative ductility parameter; it implies that the "*iso-q*" lines are roughly equivalent to the "*iso-Q*" lines generated by Drouzy *et al.*[93]

The correlation between the models created by Cáceres, and Drouzy and co-workers can be understood from Figure 2.11 where the lines of Figure 2.10 (solid lines) are superimposed on those of Figure 2.9 (dashed lines). It will be observed that the flow curves identified by the *n*-value are nearly parallel to the *"iso-YS"* lines except where necking occurs, while the "*iso-q*" lines tend to run parallel to the "*iso-Q*" lines, especially at higher flow stress values. Thus, Figure 2.11 shows that the *"iso-YS"* are actually flow curves for a given aging condition, as was anticipated earlier, but more importantly, it shows that the *"iso-Q"* lines can be identified as lines of constant relative ductility, *i.e.* *"iso-q"* lines.

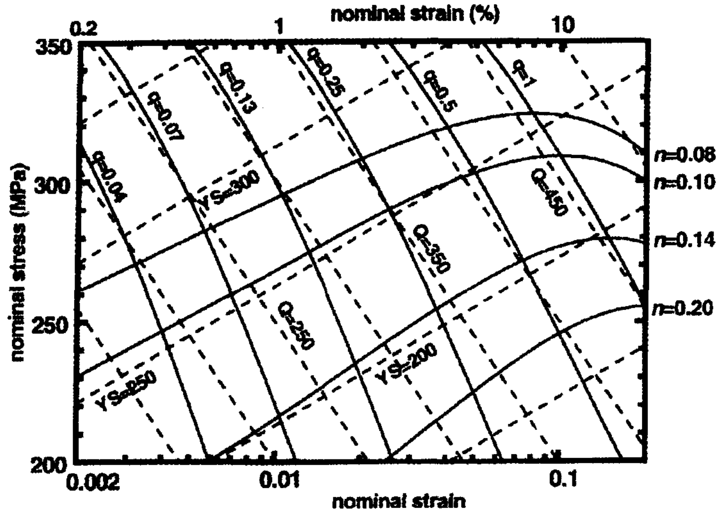

Figure 2.11 Curves of Figure 2.10 (solid lines) superimposed on Figure 2.9 (dashed lines). Note that the two sets of lines are nearly parallel to each other.[95]

2.4 MACHINING

Machining is a term applied to material removal processes in which excess metal is removed through a process of extensive plastic deformation or controlled fracture. The most common types of machining are: (i) traditional machining including turning, milling, drilling, *etc.*; and (ii) non- traditional machining including electrical discharge machining (EDM), electrochemical machining (ECM), *etc.* The drilling and tapping processes which were selected to study the machinability of the alloys introduced in this work are described in the following sections.

2.4.1 Drilling Process

Drilling is the standard process for producing holes and is known to be one of most common metal cutting processes. Drilling is often a bottleneck process in high volume manufacturing; in engine manufacture, for example, critical holes may be drilled in two or more passes, each penetrating to only a fraction of the final depth, so as to reduce cycle time. In drilling, the cutting tool used is the drill which has one or more cutting edges, and flutes to allow the cutting fluid to enter and chips to eject. There are many different types of drills including twist drills for general machining, laser drills for extremely small holes, and gun drills for deep holes. The most significant nomenclature pertaining to the twist drill, which is the most commonly used drill, is illustrated in Figure 2.12.[98]

An essential feature of drilling is the variation in the cutting speed along the cutting edge. The speed is at a maximum at the periphery of the drill and approaches zero near the center-line of the drill, the web, where the cutting edge is blended to a chisel shape.

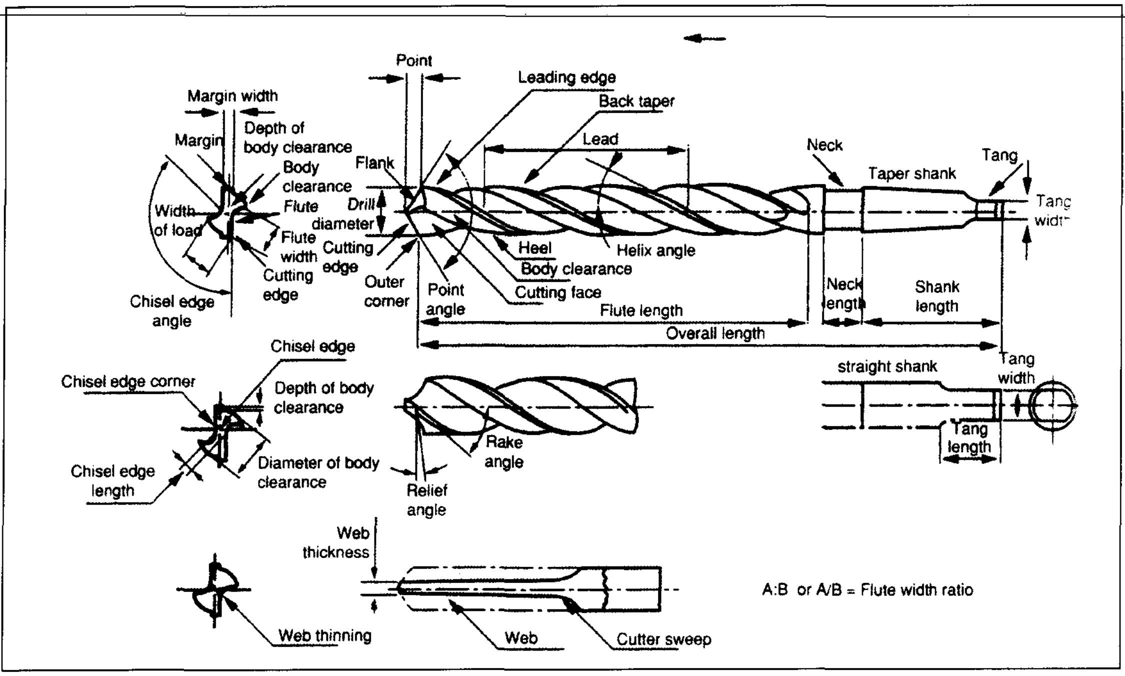

Figure 2.12 Nomenclature of the twist drill.[98]

Also, the cutting action on the cutting edge differs from one radius to another since the rake angle varies along the cutting edge. The variations in speed and rake angle along the cutting edge are responsible for many aspects of drilling which are peculiar to this cutting process.[98, 99]

The cutting forces, namely thrust (Th) and radial force (F_r), as well as cutting moment (*M*) acting on the drill during the drilling process together with the three cutting edges responsible for these forces and moment are shown in Figure 2.13.[98] The main cutting edges or cutting lips are of the greatest interest and account for most of moment and power consumption, a significant portion of axial thrust force, and the radial forces caused by cross holes, inclined exits and point asymmetry. The central chisel edge generally produces much of the axial thrust force and affects the centering accuracy and buckling behavior of the drill. Therefore, total thrust, Th, is the sum of the chisel-edge thrust and the main cutting-edge thrust. The marginal cutting edges form the machined surface of the hole and may contribute to the cutting moment.

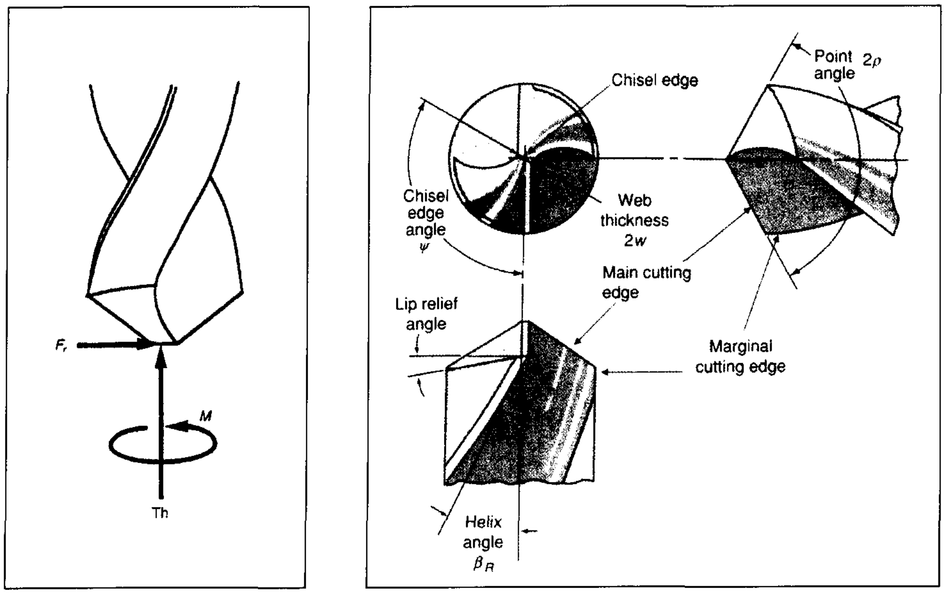

(a) (b)

Figure 2.13 (a) Forces and moment acting on the drill; and (b) cutting edges of a conventional drill.[98]

2.4.2 Tapping Process

Tapping is a common cutting process used for producing internal threads. In tapping, a specially formed threading tool called a tap is fed into a pre-drilled hole. The tap and thread nomenclature is provided in Figure 2.14.[98] The tap may either cut or plastically deform the hole wall material to form the thread. Size and geometric style are two of the major considerations in selecting the correct tap for a particular material and machine/part setup. The tap style is defined by the number of flutes, rake or hook angle, chamfer length, land, and helix angle.[100]

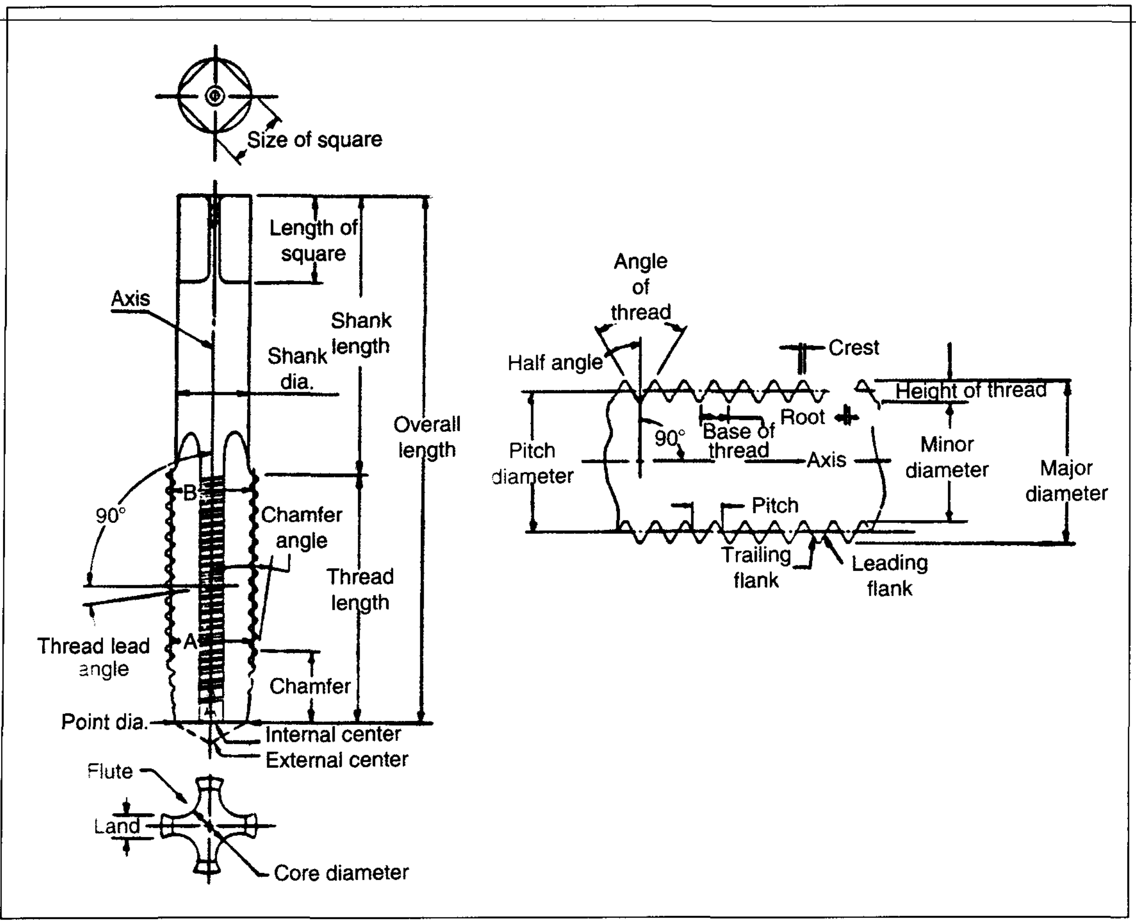

Figure 2.14 Tap and thread nomenclature.[98]

Cut tap, which cuts and removes metal to produce threads, is the major tap style used for internal threading. In cut tapping, only the chamfered teeth on the front end portion of the tap contribute to the cutting action, as shown in Figure 2.15(a), while the uniform threads behind the tapered portion guide the tap by bearing on the thread already generated. The chamfered teeth and the first full thread of the tap cut or deform the material. Each succeeding chamfered tooth makes a deeper cut until the full thread is generated. The chamfer is directly related to the chip load. It is therefore important to use the proper chamfer depending on the thread pitch, workpiece material, and the type of hole involved.

Commonly used chamfers include taper, plug, and bottoming, which are all illustrated in Figure 2.15(b).[98] The taper chamfer is designed for difficult-to-machine materials because it provides a better distribution of chip load per tooth, resulting in better thread quality. The plug chamfer is used for through holes in most materials to be tapped at conventional or higher speeds. The bottoming chamfer results in a large chip load, which requires less torque, and is used mainly for blind holes.

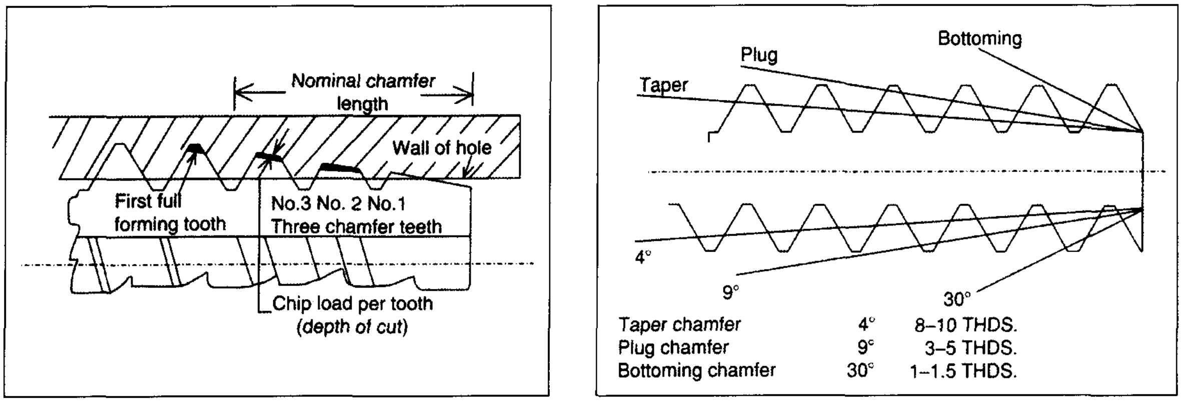

(a) (b)

Figure 2.15 (a) Chip load per individual tooth of a tap; and (b) Influence of chamfer on tap geometry.[98]

2.4.3 Machinability

The term *machinability* can refer either to the ease or difficulty of machining a material. When used in the first sense, machinability is often regarded as a material property and assigned a numerical rating. As shown schematically in Figure 2.16, however, the ease or difficulty of machining a particular part is affected by a variety of factors. These factors include the chemical composition, mechanical, and thermophysical properties of the work material, the rigidity of the machine tool and fixtures, the tool material, and such cutting variables as cutting speed, feed, and depth of cut. Machinability is thus in reality a property of both the workpiece material and the machining system operating under a given set of conditions.

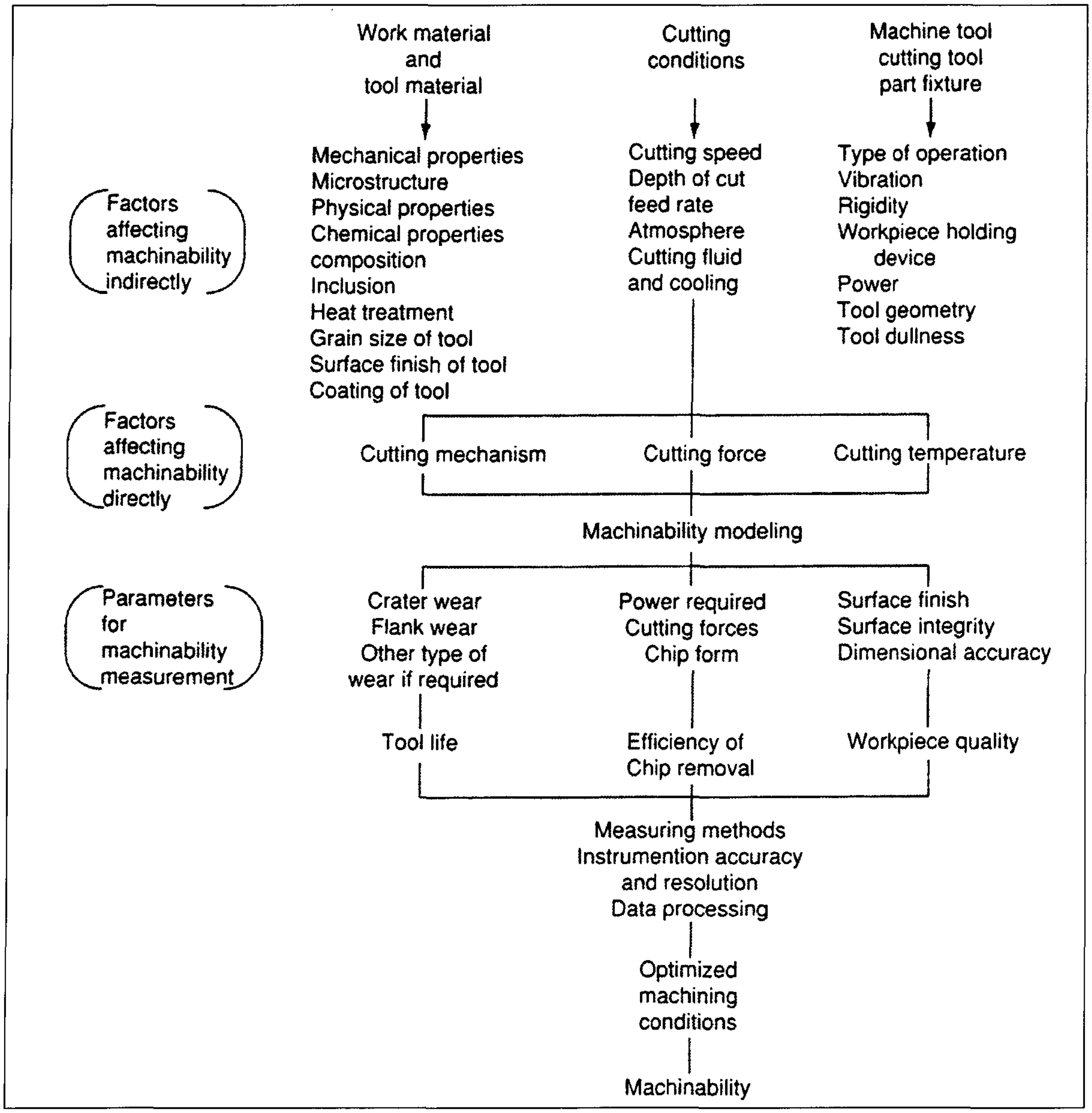

Figure 2.16 Factors affecting machinability.[98]

~~The most commonly used criteria for assessing machinability are:~~[19-21]

1) *Tool Life or Tool Wear Rates.* This is the most meaningful and common machinability criterion.[101] Tool wear affects both the quality and cost of the machined part. Machinability is said to increase when tool wear rates decrease, or tool life increases, under the machining conditions of interest. Ratings based on wear rates are generally applicable to a restricted range of cutting conditions; when conditions change, for example, when the cutting speed is substantially increased or decreased, the dominant tool wear mechanism and tool wear rate may change. This fact is particularly relevant when ranking the machinability of a group of materials under different cutting conditions.
2) *Chip Form.* Materials producing short chips which are easily managed and disposed of are more machinable than those which produce long unbroken chips or small powder-like chips. The chip form is particularly important for applications such as drilling for which chip-breaking and disposal concerns may limit production rates. Chip form is often used to assess the machinability of soft ductile alloys, especially aluminum alloys, since these materials are normally machined with diamond tools and do not generate a great deal of wear.

Tool wear and chip control issues will be discussed in the next sections particularly with regard to the drilling process since the drilling performance of a new Al-Cu base alloy will be evaluated in this study. Less commonly used machinability criteria include the following:[21]

3) *Cutting Force or Power Consumption.* Machinability increases as the cutting force and power consumption decrease for the cutting conditions of interest. Lower cutting forces imply lower tool wear rates, better dimensional accuracy as a result of decreased deflections, and increased machine tool life.

4) *Achievable Surface Finish.* Generally, machinability increases as the surface finish obtainable under a given set of cutting conditions improves. The average roughness is the most common parameter used to assess surface quality in machining tests. This criterion is most useful in ranking different classes of materials, for example, conventional versus powder metal steels.

5) *Cutting Temperature.* Cutting temperature measurements such as tool-work thermocouple measurements can be used to compare the machinability of materials under a given set of cutting conditions. Machinability increases as the cutting temperatures decrease because many tool wear mechanisms are temperature-activated. The average temperature is therefore correlated with tool life, and thus with machinability.

2.4.4 Tool Wear and Tool Life

Tool life is often the most important practical consideration when selecting cutting tools and cutting conditions. Tools which wear out or otherwise fail slowly have comparatively long service lives, resulting in reduced production costs and a more consistent dimensional and surface finish capability. For these reasons, tool life is the most common criterion used to rate cutting tool performance and the machinability of materials.

It is often possible to predict tool wear rates based on test data, but this does not translate into a prediction of tool life in a general sense, since tool life depends strongly on part requirements. In practice, tools are removed from service when they no longer produce an acceptable part. This may occur when the dimensional accuracy or surface finish of the part is out of tolerance or when there is an unacceptable probability of gross failure due to an increase in cutting forces or power. Tool wear may be classified by the region of the tool affected or by the physical mechanisms which produce it, as explained below.

2.4.4.1 Tool Wear Mechanisms

The physical mechanisms which produce the various types of wear depend on the materials involved, tool geometry, and the cutting conditions, especially the cutting speed. The most significant wear mechanisms are:[102-104]

1) *Adhesive* or *Attritional Wear*. This occurs when small particles of the tool adhere or weld to the chip due to friction and are then removed from the tool surface. It occurs primarily on the rake face of the tool and contributes to the formation of crater wear. Significant adhesive wear may accompany built-up edge (BUE) formation, since the BUE is also caused by adhesion, and can result in chipping of the tool. The problem of BUE is usually encountered in the drilling process of soft work materials. A full discussion of BUE formation will be found in Subsection 2.4.5.1.
2) *Abrasive Wear*. This occurs when hard particles abrade and remove material from the tool. The abrasive particles may be contained in the chip, as with free silicon particles in Al-Si alloys and fibers in metal matrix composites. Abrasion occurs

primarily on the flank surface of the cutting tool. Abrasive wear is usually the primary cause of flank wear and affects crater wear as well, as such it is often the mechanism of wear which controls tool life, especially at low to medium cutting speeds.

As the cutting speed is increased further, temperature-activated wear mechanisms become predominant; these include *diffusion*, *oxidation*, and *chemical* or *corrosion wear*. These mechanisms of wear depend on the chemical compatibility of the tool and workpiece materials, tool-chip interface temperature, and the melting temperature of the chip. Generally, these mechanisms of wear can be controlled by machining at lower speeds to reduce cutting temperatures, or by coating the tool with a hard layer of chemically inert material to act as a buffer between the tool substrate and the chip, cutting fluid, and the atmosphere.[105]

2.4.4.2 Types of Drill Wear

Characteristic wear patterns for conventional twist drills are shown in Figure 2.17. Four types of wear may commonly be observed:[106-109]

1) *Chisel Edge Wear*. This takes place at the central chisel edge of the drill and results from abrasion or plastic deformation. This form of wear may double or triple the thrust force on the drill and affects its centering accuracy.
2) *Lip* or *Flank Wear*. This occurs along the relief face of the cutting lips of the drill and results from abrasion, plastic deformation, insufficient flank relief caused by improper point grinding, or excessive dwelling at the bottom of blind holes. Lip

wear increases the thrust force, power consumption, and maximum lip temperature, which in turn leads to increased thermal softening and further wear. Lip wear also increases the size of the burr produced when drilling through holes. When lip wear becomes excessive, the drill may cease to cut and fail by chatter or breakage.

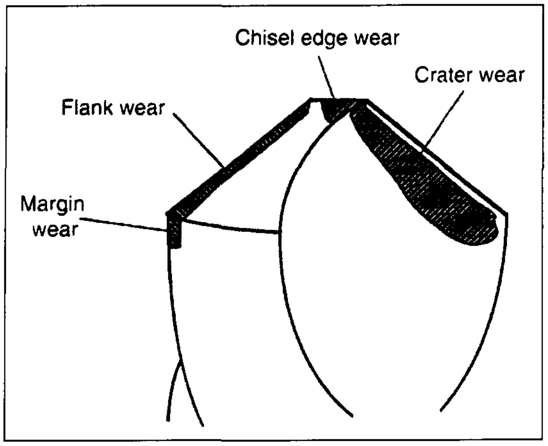

Figure 2.17 Types of drill wear.[98]

3) *Margin* or *Land Wear*. This occurs at the outer corner of the cutting lip or on the land which contacts the drilled surface. Margin wear results from abrasion, thermal softening, or diffusion wear. Excessive margin wear results in poor hole size control and surface finish. Generally, margin wear produces an undersized hole unless it is accompanied by built-up edge (BUE) formation or centering errors, in which case it produces an oversized hole.

4) *Crater Wear*. This occurs on the flute surface and results from thermal softening or diffusion wear. Moderate crater wear is usually not of concern, but excessive cratering weakens the cutting edge of the drill and can lead to edge deformation, chipping, or breakage.

When wear is caused primarily by abrasives in the work material, the number of holes to failure can be estimated from an abrasive wear model. In general, the number of holes to failure, *N*, depends directly on the feed, *f*, and is inversely proportional to the cutting speed, *V*, as follows:

$$N = C_1.\mathrm{VB}.f / V^a \tag{2.12}$$

The time to failure, *T*, should be independent of the feed and inversely proportional to the cutting speed:

$$T = C_2.\mathrm{VB} / V^{a+1} \tag{2.13}$$

In the above equations, C_1, C_2, and *a* are empirical constants whereas VB is the width of flank wear.[110]

2.4.5 Chip Formation

It is important to study the formation of chips during the machining process as this affects the surface finish, cutting forces, cutting temperature, tool life, and dimensional tolerance which in turn all affect machinabilty, as mentioned above. Understanding the chip formation of a specific material will make it possible to determine the machining speeds, feed rates, and depth of cuts for the creation of an efficient machining process. The significant aspects of chip issue are discussed in the following sections.

2.4.5.1 Types of Chip

The type of chip produced depends on the characteristics of the workpiece material and the geometry of the cutting tool. According to Ernst[111] and Merchant[112] chips formed during the machining process fall into three categories, as shown in Figure 2.18; these are:

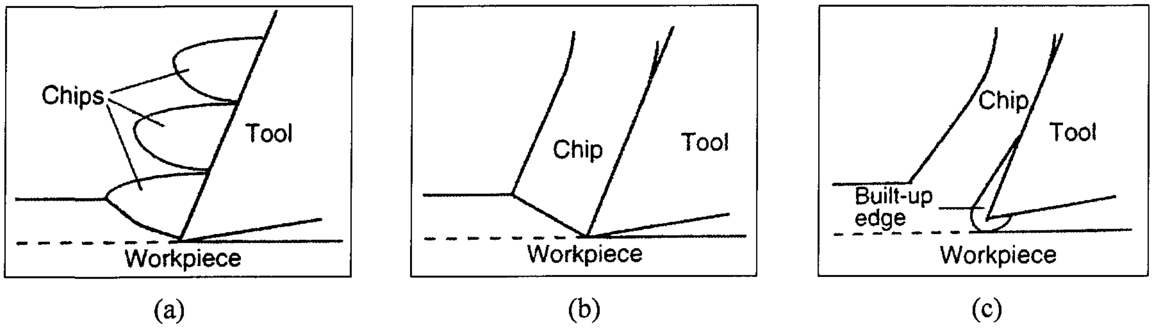

Figure 2.18 Three basic types of chips: (a) discontinuous; (b) continuous; and (c) continuous with built-up edge (BUE).[98]

1) *Discontinuous Chip.* This type of chip occurs during the machining of brittle work material such as grey cast iron, bronze, and cast brass. It also occurs when machining is carried out using cutting tools with small rake angles, coarse machining feeds, low cutting speeds and lack of lubricant or cutting fluid.
2) *Continuous Chip.* This is the long ribbon-like chip which is produced by tools with high positive rake angle when machining ductile materials such as low-carbon steels, copper, and aluminum. Continuous chips have razor-sharp and ragged edges which are extremely dangerous. These long ribbon-like chips tend to tangle with the tool and workpiece, and they are difficult to dispose of. Swarf removal is particularly important in high-production automatic and computer-controlled machine tools.

3) *Continuous Chip with Built-Up Edge*. This type of chip is basically the same as the continuous chip. When the friction between the continuous chip and the rake face of the tool increases, however, the metal particles from the chip become pressure welded to the rake face, and layer after layer of chip material is built up; this is called *built-up edge* (BUE). It occurs most often when cutting soft metals, such as aluminum alloys, at low cutting speeds. Heginbotham and Gogia[113] noted that BUE starts as an embryonic structure to which successive layers adhere as cutting progresses, until it eventually attains a size and shape characteristic of the cutting conditions. Ultimately the BUE breaks off and the process repeats itself continuously. The formation of BUE is undesirable because it changes the effective depth of cut (or hole diameter), and also because it is often unstable, leading to poor surface finish and tool chipping. Buildup is also a serious problem in drilling operations; it may occur at the outer corner of the spiral point drills because the chip becomes thin at this point. BUE formation can be minimized by using a more positive rake angle, higher cutting speeds, coolant with increased lubricity to reduce tool-chip friction, and by making the work material less ductile through the addition of inhomogeneities such as Sn, Bi, or Pd particles in free-cutting aluminum alloys.

Chip size in the drilling process is governed by its formation geometry at the cutting edge, namely thickness and curl, and the characteristic length. Nakayama[114] attributed chip curl to the following consideration as depicted in Figure 2.19:

1) The rake face is not flat and the rake angle varies along the cutting edge. The twisted, non-planer rake face gives the chip a rotation, ω_c, about the drill axis.

2) The cutting speed varies proportionally with the distance from the drill center, which cause a side-curl, shown by ω_z.
3) The side-curled chip is forced to curl in another direction by the obstruction of the web and flutes of the drill giving the chip the rotation ω_x.

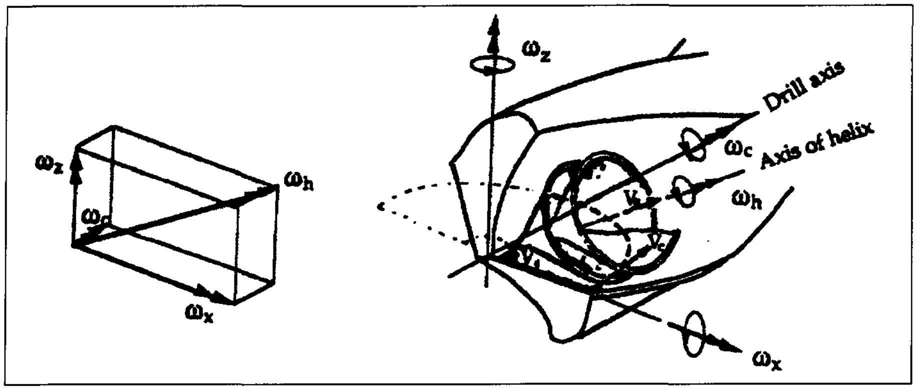

Figure 2.19 Drilling chip-curl components.[114]

Given the three components of angular velocity ω_c, ω_z, and ω_x, the chip experiences a helical motion with the angular velocity ω_h, which is the resultant of these three angular velocity components. The remaining dimensions required to fully describe the morphology of the chip are: the deformed chip thickness, which may vary along the lip, and the characteristic length, which is determined by the point at which the chip breaks in the generation cycle.

As the drilling process progresses, the weight of the chip increases constantly and the center of gravity moves away from the root of the chip. Chip flow then gradually becomes impeded by the web and the flutes, thereby imposing a resistance force on the chip. This force develops a bending moment at the root of the chip causing unstable or fragmented chips. The fragmentation acts to decrease the resistance force and consequently the bending moment. In other words, the chip changes its form to meet the external forces and constraints governing its flow. The resistance force acting on the chip contributes to the total thrust and torque on the drill.

Kahng and Koegler[115] studied the chip formation characteristics in twist drilling. It was concluded that chip curl formation in drilling is governed by the variation in the rake angle and the widely varied chip flow direction along the lip. Moreover, the first generated chip is generally larger than subsequent chips. The study also shown that, the effects of cutting conditions on the chip properties are closely related. This conclusion is based on the observation that increasing the cutting speed or feed rate remarkably increases the microhardness of the resulting chip, meaning that the chip was work hardened.

The effects of cutting variables on the chip morphology in the drilling of cast aluminum alloys were investigated.[116] The variables involved are workpiece material, speed, feed, hole depth, drill type, and cutting fluid. The feed and workpiece material were found to be the most significant variables affecting the chip size. As the feed increased, so did the mass of the chips produced. This was due to increased cutting edge engagement leading to a greater undeformed chip thickness which in turn increases the bending strength of the resulting chip, delaying chip fracture. The SAE 308 and SAE 390 cast aluminum alloys chosen for this study exhibited different chip characteristics. The SAE 390 alloy, having the greater Si content and therefore lower ductility, produced consistently smaller chips.

The chip forms which may be created during the drilling of cast aluminum alloys are shown in Figure 2.20; these include[116]

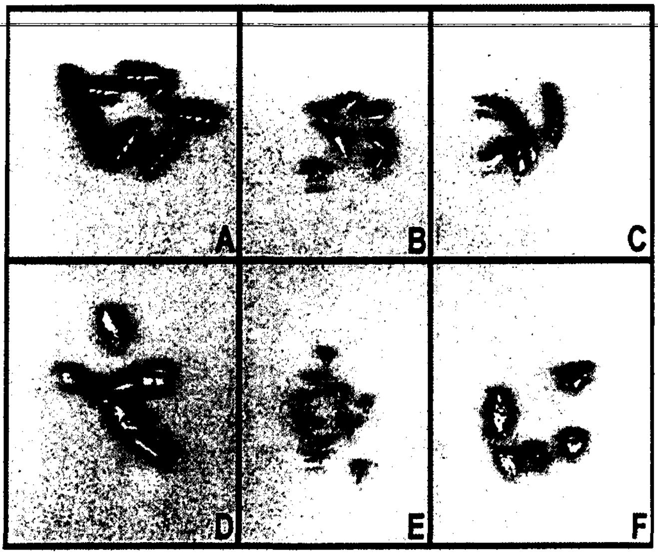

Figure 2.20 Generated chip forms: (A) conical; (B) fan shaped; (C) chisel edge; (D) amorphous; (E) needle; and (F) impacted.[116]

1) *Conical Chip.* The diameter of this chip must be small enough to allow it to move loosely through the flute/hole wall cavity.[117] The conical chip begins with a spiral form when the drill contacts the workpiece and grows as the entire lip becomes engaged. After several rotations, the chip fractures and all newly developed chips are fan shaped.
2) *Fan-Shaped Chip.* This chip is formed when a conical chip cannot curl sufficiently to follow the flute and fractures prior to a complete revolution. The fan shape is by far the predominant chip form and can be considered the ideal chip for most drilling applications.
3) *Chisel-Edge Chip.* It forms due to the extrusion of metal from the drill chisel edge.[118] This chip is long and narrow, streaming out of the drill along the interior of the flute at the web. To eliminate the chisel-edge chip, it may be necessary to decrease the feed and thereby the amount of metal extruded.

4) *Amorphous Chip.* This chip has a rather wrinkled, uncurled appearance. It does not have enough consistent curl to take a fan shape and are guided unbroken up the flutes. Apparently, the amorphous form is the heaviest chip form and the least desirable.

5) *Needle Chip.* It is caused by severe upcurling.[114] As can be shown there is no substantial difference between the needle and fan-shaped chips except for the marked change in the radius of the former about the lip axis which results in the needle shape. This change in radius occurs when the BUE alters the geometry of the drill cutting surface. In spite of the needle chip is the smallest chip observed, it may be undesirable, since it is associated with the formation of the unfavorable BUE.

6) *Impacted Chip.* This chip is the aggregation of primary smaller chips which have amalgamated while moving up the flute. It is thus heavier than the primary chip and takes on the shape of the flute. The impacted chip is undesirable since its formation results in the clogging of the flute. To avoid this chip, it may be necessary to reduce the feed, cutting speed or both, or to use a drill with a larger flute cavity.

2.4.5.2 Chip Control

Chip control is an important issue in many machining operations, especially turning and drilling operations involving ductile work materials such as low-carbon steel and aluminum alloys. Chip control usually involves two tasks; that of the breaking of chips to avoid the formation of long continuous chips which can become entangled in the machinery, and that of the removal of chips from the cutting zone to prevent damage to the machined surface.

Chip-breaking and removal are important in drilling, since the allowable penetration rate is often limited by chip-breaking characteristics. Chip-breaking can be facilitated by modifying the flute profile or drill point.[119] Common modifications to split the chip are shown in Figure 2.21; these include grooves in the flute or flank profiles, stepped cutting edges, and multi-faceted point geometries with cusps. Chip-breaking in drilling can also be promoted by adding the free-cutting elements, Sn, Bi, and Pb, to the work material, as will be explained later in greater detail.

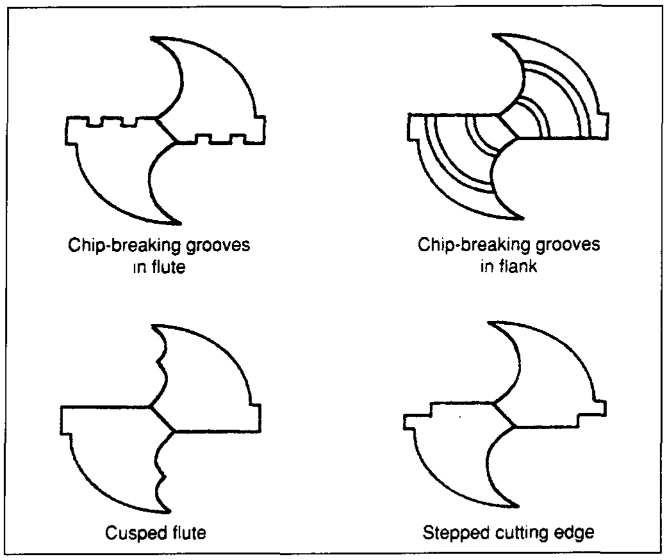

Figure 2.21 Drill point and flute modifications to improve chip breaking.[98]

Even if chips are broken, they may cause difficulties if they are not cleared from the machine tool or machined part. Chip-packing in drilling occurs when the chips become lodged in the flute, so that further chip evacuation is impossible; it occurs especially when drilling deep holes. Chip packing can be prevented (i) by changing the flute profile (*e.g.* to a parabolic flute), (ii) by increasing the helix angle, (iii) by decreasing the feed rate, and (iv) by changing the spindle orientation from vertical to horizontal.

2.4.6 Machinability of Aluminum Alloys

Machinability problems of aluminum alloys with respect to tool wear, chip disposal, cutting force and moment, and surface finish, depend to a large extent on the chemical composition of the alloy and the additives involved.

Jorstad[120] studied the effects of minor elements and impurities on the machinability of primary 380 die casting aluminum alloy. It was found that the addition of 0.3% Mg to the alloy improves its machinability. Magnesium hardens the alloy matrix leading to the formation of shorter and tighter chips and to a reduction in the coefficient of friction between tool and workpiece; this in turn decreases the tendency to form a BUE and it also provides a better surface finish. Although zinc, lead, and tin are often credited with producing improvements in the machinability of casting alloys, they were observed to be much less effective than Mg in altering the machining characteristics of the primary 380 alloy. The heavy elements, Mn and Cr, increase the abrasiveness of the alloy, and therefore detract from tool life.

The effects of metallurgical parameters, namely alloy chemistry, additives, and hardness, on the drilling and tapping performance of 319 and 356 aluminum alloys were investigated.[121,122] It was concluded that increasing the Mg content of 319 alloy results in a higher cutting force for the same level of hardness. This can be explained by the fact that a high volume fraction of Mg precipitates may be formed within the alloy matrix in the high Mg-content 319 alloy compared to the low Mg-content one. The high Mg-content 319 alloys, however exhibit a lower cutting force compared to 356 alloy having the same level of hardness. This may be explained by the improvement in the homogeneity of the alloy matrix hardness in high Mg-content 319 alloys caused by the cooperative precipitation of Al_2Cu and Mg_2Si hardening phase particles compared to the precipitation of only Mg_2Si particles in the 356 alloy. It was also observed that as the hardness increases both the cutting force and moment increase while the BUE on the cutting tool decreases.

The development of "free-cutting" aluminum alloys is the most common metallurgical technique used to improve the machinability of aluminum alloys. The term "free cutting" or "free machining" means that the chips should flow freely from the specimen being cut, and that they should also be short and breakable to prevent fouling of the cutting tool or other operating parts of the machine. Free-cutting aluminum alloys are prepared from standard heat-treatable alloys with the addition of free-cutting elements which form inhomogeneities in the aluminum matrix. Due to the very limited solubility of the free-cutting elements in the Al-matrix, they remain as separate entities dispersed in the matrix. During the machining operation, it is believed that the temperature generated in the cutting zone is great enough to melt these dispersed entities. This melting gives rise to a local loss of material strength and ductility which in turn leads to the formation of short, discontinuous chips. Also, these elements act as a lubricant during machining, thereby decreasing the friction between chip and tool edge which, again, in turn leads to lower cutting forces, less tool wear, a low tendency to form BUE, and a smooth surface finish. According to Smolej *et al.*,[22] free cutting elements should have the following properties:

1) No solubility in either liquid or solid aluminum
2) Low melting point compared to aluminum
3) Must not form intermetallic compounds with aluminum and other alloying elements
4) Lower hardness values with regard to the aluminum matrix.

The most common free-cutting elements fulfilling the above requirements include Pb, Bi, Sn, and In. Due to the harmful effect of Pb on the environment and the high price of In, both Bi and Sn are the most preferable choice as free-cutting elements.

The most significant application of Bi in aluminum alloys is its use as a chip breaker in free-machining alloys. It was used principally together with Pb in AA2011 alloy;[123] after solidification of this alloy, Bi and Pd were to be observed in the form of eutectic globules at the grain boundaries. These globules melt during machining thereby producing an internal notch effect and leading to fracture of the chip. Kim and Chung[124] concluded that as the Pb and Bi contents increase, the turning performance of Al-Cu alloys with regard to cutting forces and bite temperature is remarkably enhanced without any observable degradation of tensile properties. It was also found that the appropriate addition levels, beyond which Al-Cu alloys attain their optimum cutting properties, are 0.4% Pd and 0.4% Bi.

As mentioned earlier, the use of Pb as a free-cutting element is being discouraged in view of its potential for causing environmental problems. Also, the addition of Bi to Mg-containing alloys is not advantageous since this element has a strong affinity for Mg which increases the tendency towards the formation of Mg_3Bi_2 and thus hinders the hardening effect of Mg. The design strategy aimed at the replacement of Pb and Bi with Sn in the free-cutting aluminum alloys was, therefore, introduced. Smolej *et al.*[22,125] substituted Pb and Pb + Bi with Sn in the standard AlCuMgPb (AA2030) and AlCu5PbBi (AA2011) alloys. They found that Sn formed free-machining inclusions which were finely distributed on the grain boundaries together with the intermetallic compounds of other alloying elements. They also suggested that the machinability of Sn-containing alloys in terms of the size and shape of the chips was favorable at a Sn content of higher than 1 wt %. Sircar *et al.*[126] developed the AA6262 alloy by replacing the Pb-Bi eutectic with the In-Sn eutectic. It was found that, provided the In and Sn are added in the correct eutectic proportions, the addition of this eutectic improves chip-formation characteristics without significantly affecting other desirable properties. On the other hand, the replacement of the Pb-Bi eutectic with Bi-Sn eutectic in AA6262 did not bring about any improvement in the machinability of the alloy.

Faltus *et al.*[127] demonstrated that the Pb-containing machinable $AlCu_4PbMg(Mn)$ alloy can be successfully replaced with alternative Pb-free AlCuMgSnBi alloys. The distribution of Pb particles in the AlCu4PbMg(Mn) alloy was found to be rather irregular in comparison with the regular distribution of soft Sn phases in the experimental AlCu4MgSnBi alloy. This difference in phase distribution explains the relatively low chip quality in the reference Pb-containing alloy with a tendency to form continuous chips. Royset *et al.*[128] reported that an addition of 0.28% Sn is insufficient to improve the chip formation in the turning of extruded 6082 alloy; increasing the Sn content to 1%, however, produces excellent chip formation. Furthermore, the chip formation is observed to improve considerably when the hardness of the alloy is increased.

CHAPTER 3

EXPERIMENTAL PROCEDURES

CHAPTER 3

EXPERIMENTAL PROCEDURES

3.1 INTRODUCTION

This chapter will endeavor to shed light on the experimental procedures carried out for the purposes of the present study. Eleven alloys were prepared and classified into three groups according to the additives used. All of the alloys were mechanically tested in order to acquire an understanding of the effects of these additives on the mechanical properties. For machinability testing, only four alloys were selected from amongst the eleven alloys based on the selection considerations to be outlined in Chapter 6. The relevant experimental procedures, namely (i) preparation of the different alloy composition melts; (ii) pouring of the castings from these melts; (iii) heat treatment of the cast samples; (iv) investigation of the microstructure; (v) tensile testing; (vi) hardness testing; (vii) impact testing; and (viii) machinability testing, will all be discussed in the following subsections.

3.2 ALLOYS AND MATERIALS

The nominal level of the alloying elements added to the base alloy and the codes of the resulting alloys as well as their classification are shown in Table 3.1.

Table 3.1 Nominal composition and codes of the alloys prepared for the present study

Group I		Group II		Group III	
Alloy code	**Composition**	**Alloy code**	**Composition**	**Alloy code**	**Composition**
A	Base alloy	**A3**	A + Sr + 0.15%Ti	**A4**	A + 0.15%Ti + 0.20%Zr
A1	A + Sr	**A31**	A3 + 0.20%Fe	**A41**	A4 + 0.15%Sn
A2	A + 0.15%Ti	**A32**	A3 + 0.20%Fe + 0.2%Mn	**A42**	A4 + 0.50%Bi
A3	A + Sr + 0.15%Ti	**A33**	A3 + 0.50%Ag	**A43**	A4 + 0.15%Sn + 0.5%Bi
A4	A + 0.15%Ti + 0.20%Zr				

Note: Sr level = 100-150 ppm

It will be observed that the alloys were classified into three groups according to the alloying additions involved, namely, Groups I, II, and III.

- Group I was used to examine the effects of melt treatment through the addition of Sr, Ti, Sr + Ti, and Ti + Zr to the base A alloy (A1, A2, A3, and A4 alloys, respectively).
- Group II was used to examine the effects of iron intermetallics and hardening alloying elements by adding Fe, Fe + Mn, and Ag to the A3 alloy (A31, A32, and A33 alloys, respectively).
- Group III was used to examine the effects of free-cutting elements through the addition of Sn, Bi, and Sn + Bi to the A4 alloy (A41, A42, and A43 alloys, respectively).

Melts of the eleven alloys listed in Table 3.1 were prepared so as to obtain castings for mechanical test samples. Melts of alloys A, A4, A41, and A42 were subsequently prepared once again to obtain castings for machinability test blocks. The actual chemical composition for each of the alloys for the mechanical test samples and for the machinability test blocks was obtained by means of chemical analysis and is provided in Tables 3.2 and 3.3, respectively.

Table 3.2 Actual chemical compositions for the alloys of the mechanical test samples

Alloy code	**Chemical Composition (% wt)**											
	Cu	**Si**	**Mg**	**Fe**	**Mn**	**Sr**	**Ti**	**Zr**	**Ag**	**Sn**	**Bi**	**Al**
A	2.09	1.32	0.42	0.58	0.59	0.000	0.07	0.00	0.00	0.00	0.00	bal.
A1	2.13	1.28	0.42	0.58	0.60	0.013	0.08	0.00	0.00	0.00	0.00	bal.
A2	2.18	1.23	0.40	0.61	0.61	0.000	0.15	0.00	0.00	0.00	0.00	bal.
A3	2.11	1.23	0.40	0.52	0.60	0.011	0.16	0.00	0.00	0.00	0.00	bal.
A4	2.24	1.28	0.41	0.61	0.58	0.000	0.15	0.20	0.00	0.00	0.00	bal.
A31	2.17	1.22	0.40	0.84	0.59	0.014	0.16	0.00	0.00	0.00	0.00	bal.
A32	2.09	1.17	0.39	0.82	0.79	0.010	0.18	0.00	0.00	0.00	0.00	bal.
A33	2.09	1.21	0.39	0.57	0.60	0.010	0.16	0.00	0.50	0.00	0.00	bal.
A41	2.31	1.33	0.43	0.63	0.59	0.000	0.16	0.20	0.00	0.22	0.00	bal.
A42	2.31	1.26	0.45	0.52	0.61	0.000	0.18	0.20	0.00	0.00	0.51	bal.
A43	2.24	1.24	0.47	0.45	0.61	0.000	0.17	0.20	0.00	0.24	0.55	bal.

Table 3.3 Actual chemical compositions for the alloys of the machinability test blocks

Alloy code	**Chemical Composition (% wt)**											
	Cu	**Si**	**Mg**	**Fe**	**Mn**	**Sr**	**Ti**	**Zr**	**Ag**	**Sn**	**Bi**	**Al**
A	2.49	1.22	0.36	0.38	0.62	0.000	0.05	0.00	0.00	0.00	0.00	bal.
A4	2.41	1.10	0.33	0.37	0.59	0.000	0.17	0.19	0.00	0.00	0.00	bal.
A41	2.43	1.10	0.34	0.36	0.59	0.000	0.18	0.19	0.00	0.21	0.00	bal.
A42	2.42	1.10	0.36	0.37	0.60	0.000	0.19	0.18	0.00	0.00	0.52	bal.
A206	5.44	0.10	0.25	0.10	0.39	0.000	0.18	0.00	0.00	0.00	0.00	bal.

The actual chemical composition of the A206 alloy, which was selected here for a comparative study of the machinability of this particular alloy and that of 220 alloy, is also provided in Table 3.3. Each alloy composition listed in Tables 3.2 and 3.3 is the average of three different chemical analysis samples taken from the alloy melt. The chemical analysis was carried out at the GM facilities in Milford, NH using a Spectrolab Jr CCD Spark Analyzer. The actual chemical composition of each alloy was checked to make sure that it matched the corresponding nominal one.

3.3 MELTING AND CASTING PROCEDURES

The base alloy A used in this study was supplied in the form of 12.5-Kg ingots which were cut, dried, and then melted in a SiC crucible of 150-Kg capacity, using an electrical resistance furnace shown in Figure 3.1. The melting temperature was maintained at 750 ± 5°C. The melt was grain-refined and modified using Al-5%Ti-1%B and Al-10%Sr master alloys, respectively. Iron, manganese, silver, zirconium, and bismuth were added in the form of Al-25%Fe, Al-25%Mn, Al-50%Ag, Al-15%Zr, and Al-50%Bi master alloys, respectively, whereas Sn was introduced as a pure metal. Degassing was carried out using pure dry argon for 15 min, injected into the melt by means of a graphite impeller rotating at 150 rpm. The surface oxides/inclusions were skimmed thoroughly prior to pouring. The melt was poured at ~ 735°C into the following molds, which had been preheated to 450°C:

Figure 3.1 Electrical resistance melting furnace.

(i) an ASTM B-108 permanent mold to obtain castings for tensile test bars, as shown in Figure 3.2, (ii) an L-shaped rectangular graphite-coated metallic mold to obtain castings for hardness test blocks, as shown in Figure 3.3, and (iii) a starlike mild-steel mold to obtain castings for impact test bars, as shown in Figure 3.4. Each casting obtained by each one of these molds provides two ASTM tensile test bars, three rectangular (35 x 30 x 80 mm) hardness test blocks, and ten square (10 x 10 x 55 mm) impact test bars, respectively, as shown in Figure 3.5. The tensile test bars were subsequently cut from their castings with dimensions corresponding to the ASTM dimensions shown in Figure 3.6. Both the hardness test blocks and the impact test bars were subsequently cut from their castings and

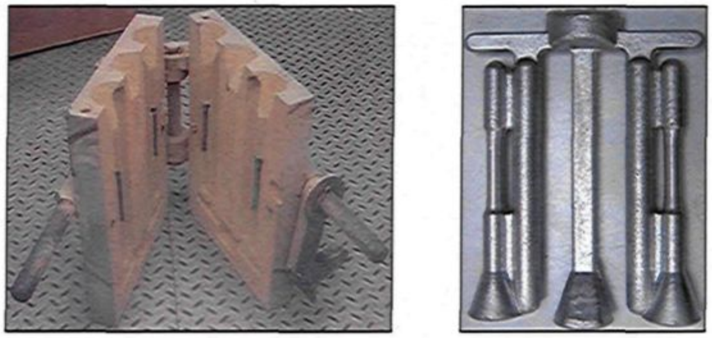
(a) (b)

Figure 3.2 (a) ASTM B-108 permanent mold; and (b) corresponding tensile test bar casting.

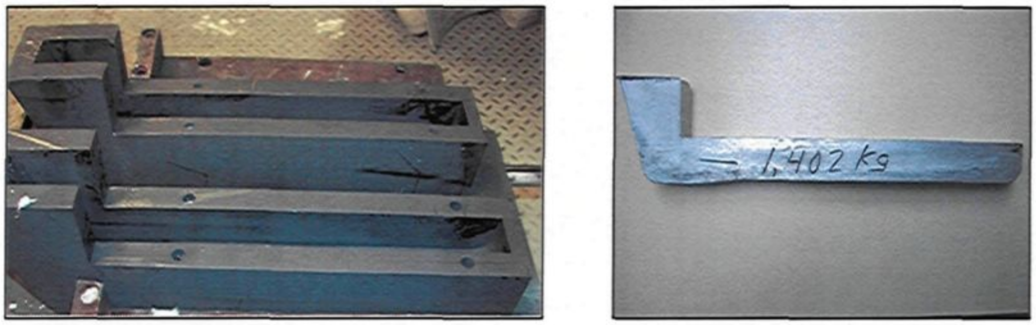

(a) (c)

Figure 3.3 (a) L-shaped metallic mold; and (b) corresponding hardness test block casting.

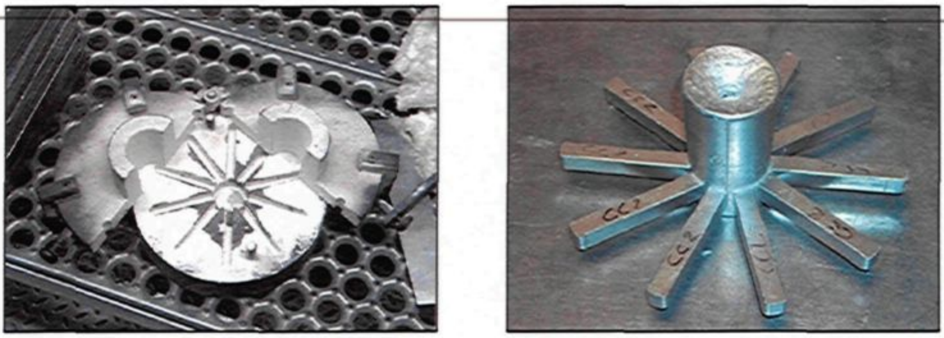

(a) (b)

Figure 3.4 (a) Starlike mild-steel mold; and (b) corresponding impact test bar casting.

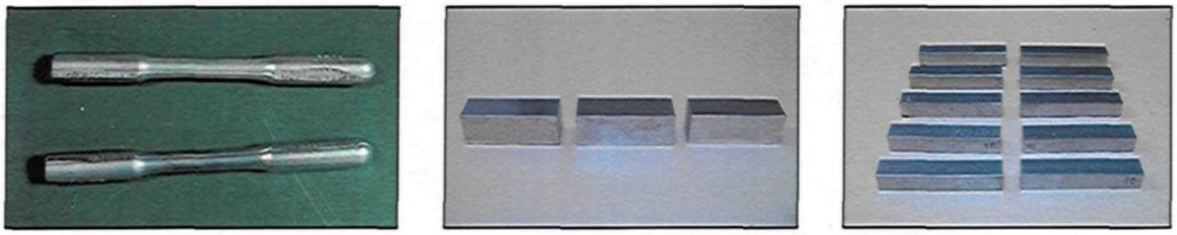

(a) (b) (c)

Figure 3.5 (a) 2 ASTM tensile test bars; (b) 3 rectangular (35 x 30 x 80 mm) hardness test blocks; and (c) 10 square (10 x 10 x 55 mm) impact test bars.

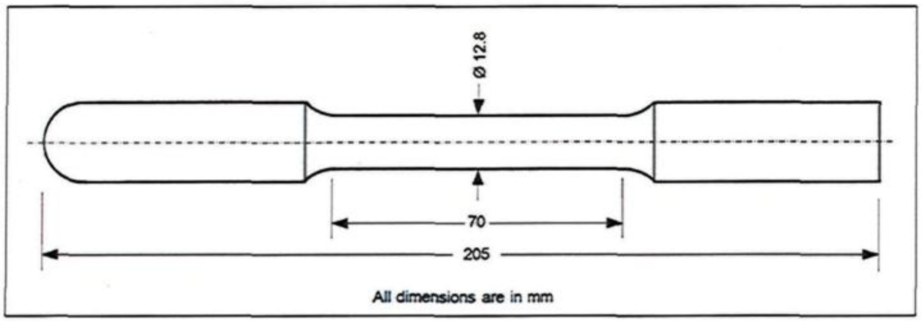

Figure 3.6 The dimensions of the tensile test bar used according to ASTM specifications.

further machined to the final testing dimensions of 35 x 30 x 80 mm and 10 x 10 x 55 mm, respectively. For each alloy composition listed in Table 3.2, one hundred tensile test bars, twenty hardness test blocks, and one hundred impact test bars were prepared from their respective castings. Samplings for metallographic observation and spectrochemical analysis were also taken simultaneously for each alloy melt composition during the casting of the mechanical test samples.

The machinability test blocks were later cast for the 220 based alloys assigned for machinability tests, namely A, A4, A41, and A42 alloys, as well as the A206 alloy. The melting procedures and the addition of alloying elements were carried out as explained above for the casting of mechanical test samples. A waffle-plate graphite-coated metallic mold was used to obtain the machinability test block castings, as shown in Figure 3.7. One test block was subsequently cut from each casting and then machined to the final testing form shown in Figure 3.8(a). A descriptive drawing for the machinability test block is provided in Figure 3.8(b). For each alloy composition listed in Table 3.3, eighteen test blocks were prepared. Samplings for spectrochemical analysis were also taken simultaneously for each alloy melt composition during the casting of these blocks.

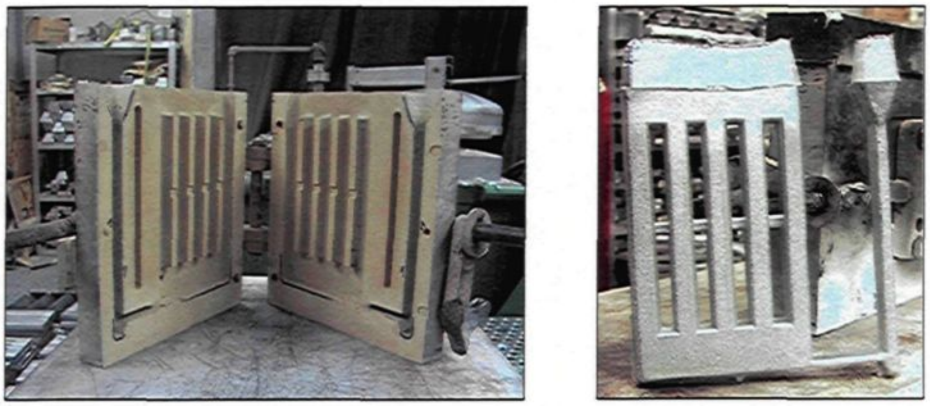

(a) (b)

Figure 3.7 (a) Waffle-plate mold; and (b) corresponding machinability test block casting.

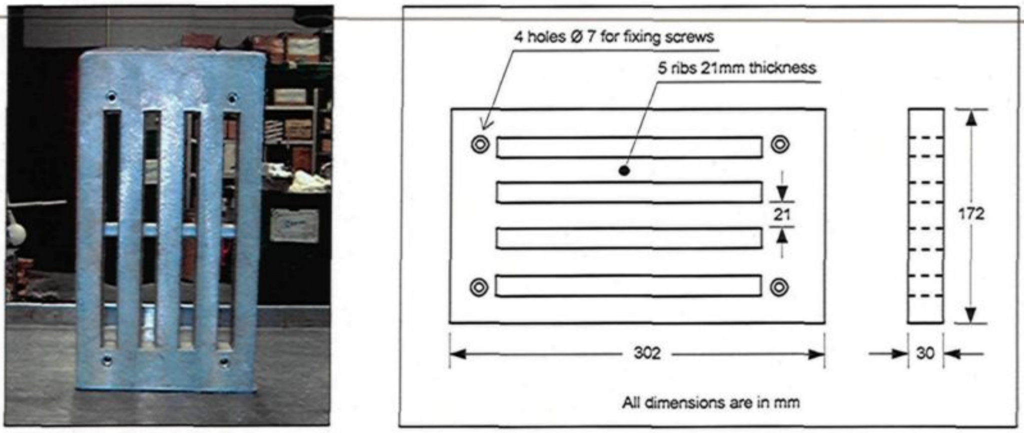

(a) (b)

Figure 3.8 (a) Machinability test block; and (b) dimensions of machinability test block.

3.4 HEAT TREATMENT

The mechanical test samples obtained for each alloy composition were divided into twenty sets. Each set contains five tensile test bars, one hardness test block, and ten impact test bars. The twenty sets were assigned to the following alloy conditions:

- as-cast condition;
- as-solutionized condition (solution heat treatment at 495°C for 8 h followed by quenching in warm water at 65°C);
- nine T6 heat-treated conditions corresponding to nine aging times;
- nine T7 heat-treated conditions corresponding to nine aging times.

In both T6 and T7 tempers, the samples were solution heat-treated at 495°C for 8 h, quenched in warm water at 65°C, and then artificially aged. The artificial aging was carried out at 180°C and 220°C for T6 and T7 tempers, respectively, for aging times of 2, 4, 6, 8, 12, 16, 20, 24, and 48 h.

The machinability test blocks of the 220 based alloys intended for machinability test, *i.e.* A, A4, A41, and A42 alloys, were all T6 tempered at 180°C for 4 h. This temper condition was most specifically selected from amongst the abovementioned heat treatment conditions, since it is able to deliver hardness values to within 100±10 HB for these alloys, as was observed from the hardness test results. This hardness range is to be desired since it conforms to most of the required hardness levels observed in the commercial application of aluminum alloys. The T71 temper was carried out in accordance with AMS (Aerospace Material Specifications) 4235A[129] for the A206 alloy machinability test blocks as a common heat treatment used for A206 alloy applications. Solid solution treatment was carried out at 515°C for 2 h then raised to 525°C for 8 h. The blocks were then quenched in warm water, followed by artificial aging at 185°C for 5 h. All heat treatments were conducted in a forced-air Blue M Electric furnace equipped with a programmable temperature controller (± 2°C), as shown in Figure 3.9.

3.5 METALLOGRAPHY-MICROSTRUCTURAL EXAMINATION

For metallographic observations, 25 x 25 mm samples were cut from the castings prepared for this purpose, and mounted in bakelite using a Struers Labopress-3 Mounting Press. The samples were then ground and polished to the desired fine finish by means of a Struers Tegrapol-35 Grinder-Polisher. The grinding was carried out using successively #120, # 240, # 320, # 400, # 600, # 800 grit SiC papers. The polishing was carried out by applying polycrystalline diamond powder suspended in water with particles of 6 μm and 3 μm for rough and fine polishing, respectively. Struers oil is used in both

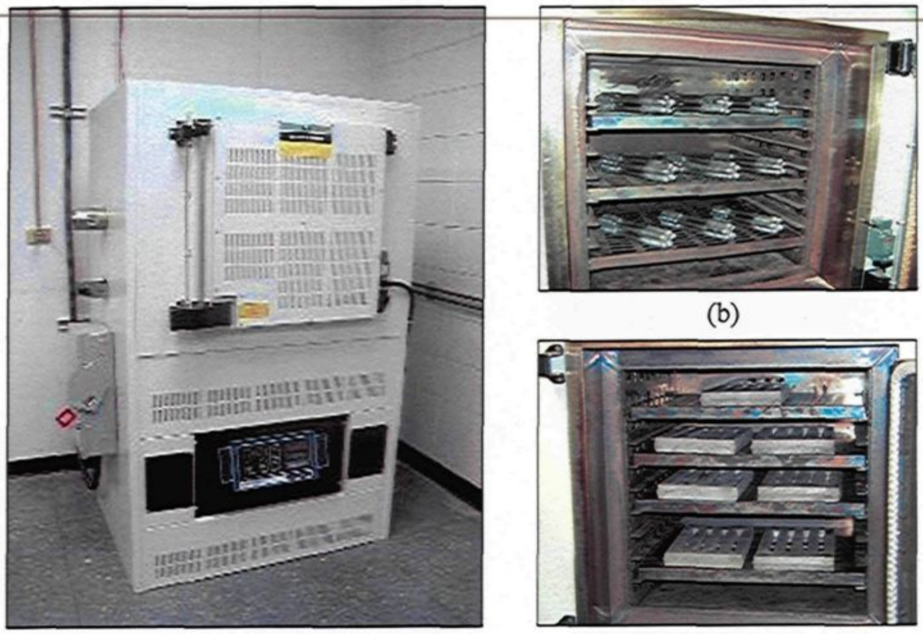

(b)

(a)

(c)

Figure 3.9 (a) Blue M Electric furnace; (b) furnace loaded with tensile test bars; and (c) furnace loaded with machinability test blocks.

polishing stages as a cooling and lubricating medium. Finally, to produce a mirror-like surface of the samples, the ultimate polishing stage was completed using 1 μm colloidal silica suspension with water as a coolant and lubricant. After polishing, the mounted samples were washed with a mix of soap and alcohol, and then dried using compressed air.

The microstructures were examined by means of a Leica DM LM optical microscope. The grain-size measurements were carried out using a Clemex image analyzer in conjunction with the optical microscope. The grain size was obtained from the average of 200 measurements taken over 20 fields (10 measurements per field) at 100x magnification for each alloy sample. Phase identification was carried out using an Electron Probe Micro-Analyzer (EPMA) in conjunction with energy dispersive X-ray analysis

(EDX) and wavelength dispersive spectroscopic analysis (WDS) where required, integrating a combined JEOL JXA-8900l WD/ED microanalyzer operating at 20 kV and 30 nA, where the size of the spot examined was ~ 2 μm. Figure 3.10 shows an illustration of the JEOL WD/ED combined microanalyzer setup as used for this purpose.

Figure 3.10 Electron probe microanalyzer used in the present work.

3.6 MECHANICAL TESTS

The mechanical tests carried out for the purposes of this study include tensile, hardness, and impact tests. The description of the samples prepared for these tests has been provided in subsection 3.1.2.

3.6.1 Tensile Test

The tensile test bars were pulled to fracture at room temperature at a strain rate of 4×10^{-4} s^{-1}, using a Servohydraulic MTS Mechanical Testing machine, shown in Figure 3.11. A strain gauge extensometer (with a 50.8 mm range) was attached to the test

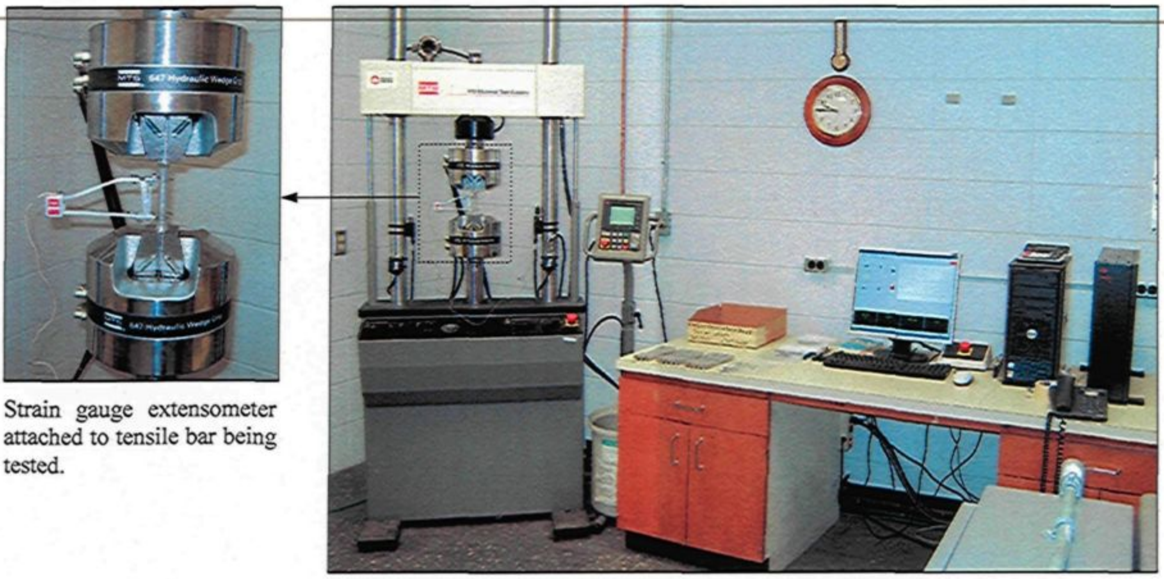

Strain gauge extensometer attached to tensile bar being tested.

Figure 3.11 Servohydraulic MTS mechanical testing machine with data-acquisition system.

bar to measure percentage elongation as the load was applied. The data were analyzed using the TestWorks 4 software designed for tensile testing. The tensile properties, namely yield stress (YS) at a 0.2% offset strain, ultimate tensile strength (UTS), and fracture elongation (%El), were derived from the data-acquisition and data-treatment systems of the software. The tensile properties of each alloy condition were represented by the average %El, YS, and UTS values which were calculated over the values obtained from the five tensile test bars assigned to that condition.

3.6.2 Hardness Test

The hardness measurements were carried out on both the hardness test blocks and the machinability test blocks using a Brinell hardness tester, as shown in Figure 3.12. For all hardness measurements, the Brinell hardness tester used a steel ball indenter of 10 mm

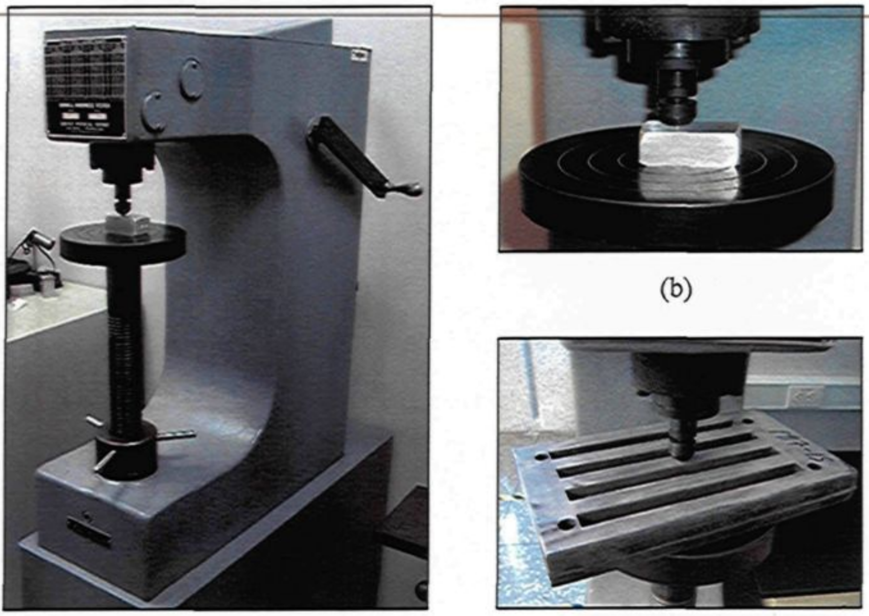

(b)

(a) (c)

Figure 3.12 (a) Brinell hardness tester; (b) hardness measurement for hardness test blocks; and (c) hardness measurement for machinability test block.

diameter. The indenter was pressed into the test block by an accurately controlled test force of 500 Kg for a dwell time of 30 s causing a round indentation in the test block, as shown in Figure 3.13. The diameter, d, of the indentation, which is inversely proportional to the block hardness, is the average of two diagonal diameters, d_1 and d_2, measured optically at right angles after removal of the applied test force, using a portable scaled microscope. The Brinell hardness number (BHN) corresponding to the resulting indentation was calculated by dividing the applied test force by the surface area of the indentation as follows:[130]

$$\mathrm{BHN} = 2F/[\pi D(D\text{-}(D^2 - d^2)^{1/2})] \tag{3.1}$$

where F is the applied force (kgf), D is the diameter of the ball indenter, and d is the diameter of the indentation left in the test block.

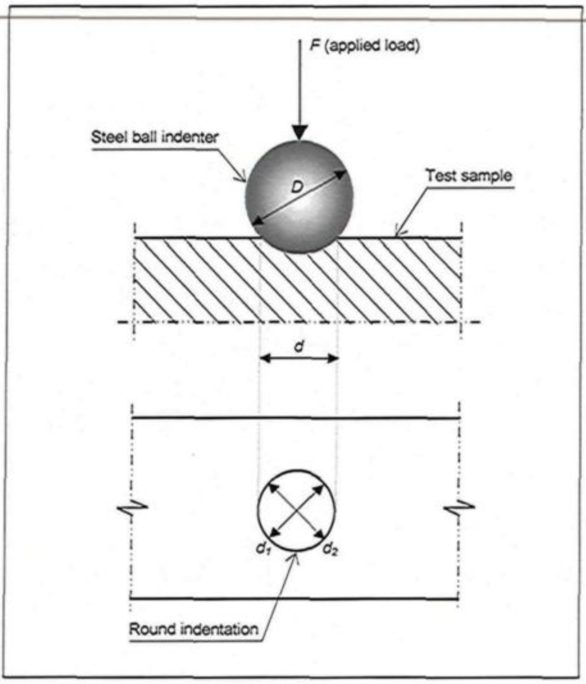

Figure 3.13 Brinell hardness test method.

The Brinell hardness value of each alloy condition is the average of eight determinations obtained from two perpendicular faces of the hardness test block (*i.e.* four indentations per face) corresponding to that condition. Hardness measurements were also carried out subsequently on the heat-treated machinability test blocks to make sure that the blocks acquired the desired hardness levels of 100±10 HB. Four blocks were randomly selected from among the eighteen machinability test blocks prepared for each alloy in order to carry out the hardness measurements. The Brinell hardness value of each block is the average of thirty determinations obtained from both faces of the five ribs (*i.e.* three indentations per rib face) of such a block. The average hardness of the four blocks was then calculated and taken to represent the hardness value of the eighteen machinability test blocks from which the four blocks were randomly selected.

3.6.3 Impact Test

A computer-aided instrumented SATEC SI-1 Universal Impact Testing Machine (SATEC System Inc., Model SI-1D3), shown in Figure 3.14, was used to carry out the impact test. The striking pendulum of the machine is latched in the *high latch* mode without additional weights to provide an operating capacity of 81.35 J. The pendulum then strikes the impact test bar in the direction shown in Figure 3.15. A Dynatup Impulse Data Acquisition and Analysis System had earlier been connected to the impact machine to

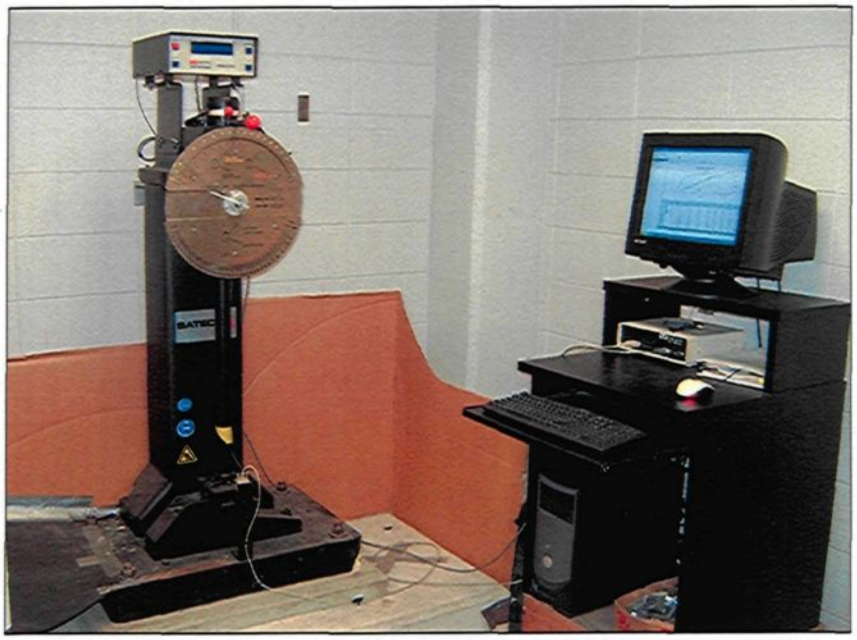

Figure 3.14 Computer-aided instrumented impact testing.

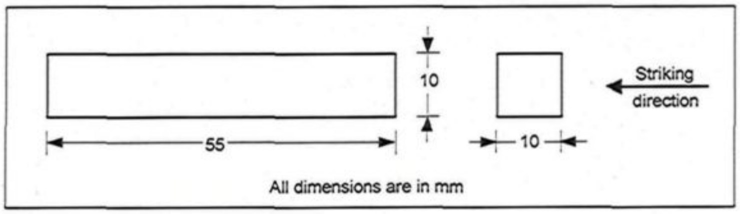

Figure 3.15 Striking direction taken by the pendulum.

determine the total absorbed energy during the test, the crack initiation and propagation energies, total time, and maximum load required to break the specimens. Furthermore, the load-time and energy-time curves were also obtained at the same time. The average values of the energies obtained from the five bars tested for each alloy condition were taken as the representative values for that particular condition.

3.7 MACHINABILITY TESTS

Drilling and tapping experiments were carried out on a HURON high speed 5-axis CNC vertical machining centre, as shown in Figure 3.16. The drilling of each test block was accomplished in such a way that 36 blind holes of 6.5 mm diameter arranged in two columns were drilled in each rib, giving a total of 180 holes per test block. Tapping was done simultaneously for the drilled holes of the full test block. A machinability test block, after drilling and tapping of 180 holes, is illustrated in Figure 3.17(a) while the dimensions of the resulting holes are provided in Figure 3.17(b).

(a) (b)

Figure 3.16 (a) HURON high speed machining center; (b) drilling of machinability test block (180 holes/block).

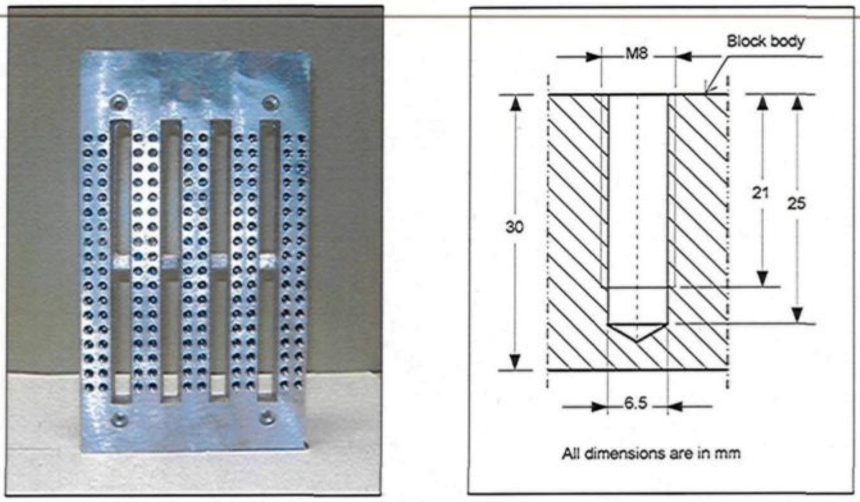

(a) (b)

Figure 3.17 (a) Machinability test block after drilling and tapping; (b) dimensions of the resulting holes.

Each alloy condition was tested with a new drill and new tap(s). A drill life of 2520 holes, *i.e.* 14 test blocks, was targeted for each alloy condition. If the drill broke during the drilling of the blocks of a particular alloy condition, two options could be followed: (i) if the drill broke because of the presence of a defect or a large inclusion, the test would be resumed for the remaining blocks of the same alloy condition using a new drill; otherwise (ii) drilling would be stopped and tapping would be continued up to the position where the drill had broken and then the test would be changed for that of the blocks of another alloy condition. If the tap broke during the tapping of the blocks of a particular alloy condition, it would be replaced by a new one as long as the drill used for such an alloy condition did not break.

All the alloy conditions were tested under the same drilling and tapping parameters listed in Table 3.4. Straight flute and coolant-fed carbide "G" type drills of 6.5 mm diameter and a minimum of 30 mm length were used to carry out the drilling process.

Titanium-nitride coated HSS cutting taps, M8x1.25-6H, with three spiral flutes were used for subsequent tapping processes. The dimensions of these cutting tools are provided in Figure 3.18 together with Table 3.5.

Table 3.4 Cutting parameters applied for machinability testing

Parameter	Drilling	Tapping
Speed (rpm)	11000	400
Hole diameter (mm)	6.5	M8 x 1.25
Hole depth (mm)	≤ 4.5xD (≈28)	≤ 3xD (≈21)
Feed rate (mm/s)	19.50	9.33
Coolant	Synthetic metalworking fluid concentrate CIMTECH® 310	

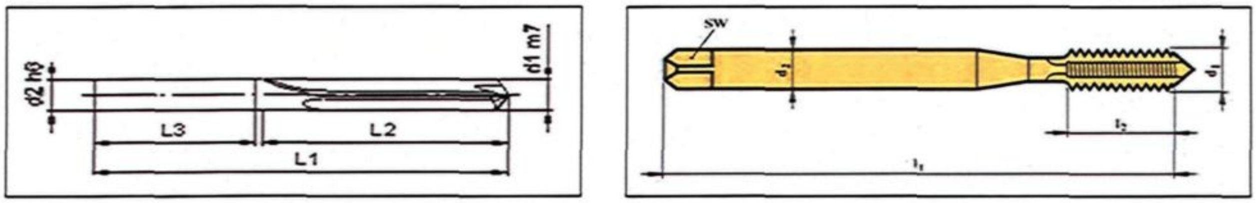

(a) (b)

Figure 3.18 (a) Straight flute and coolant-fed carbide "G" type drill; (b) TiN-coated HSS cutting tap.

Table 3.5 Cutting tool dimensions in mm

Tool	d1	d2	L1	L2	L3	SW	Point angle	Helix angle
Drill	6.5	8	90	53	36	-	120°	0°
Tap	7.9	8	90	-	-	6.2	-	40°

A Go/No-Go gauge test was executed after the drilling and after the tapping of each test block (180 holes) to verify the dimensional accuracy of both drilled and tapped holes. The reference diameters of Go/No-Go gauge test are 6.5024 and 6.5278 mm, respectively, for drilled holes while they are 7.02056 and 7.15518 mm, respectively, for tapped holes.

The drilling chips were collected and visually inspected at the end of the drilling of each test block. This examination was not made for tapping since there were no chips produced during the tapping test. After the drilling and tapping of each test block, the built-up edge (BUE) width of the drill was measured and the failure of the first and second teeth of the tap was checked using a TM-505 type Toolmaker's Microscope with a 30x magnification. All of these examinations were conducted periodically throughout the drilling and tapping tests for each alloy composition to monitor the condition of the cutting tools used, and to evaluate the cutting performance of the alloys tested.

A Kistler 6-component piezoelectric quartz crystal dynamometer of the type 9255B shown in Figure 3.19(a) was used for measuring the cutting force and moment during drilling and tapping tests. In such measuring systems, the force acting on the quartz crystal element is converted to a proportional electric charge. Thus, the four sensors of the dynamometer provide eight electric charges corresponding to the values of eight components of the cutting force measured in x, y, and z directions, namely Fx_{1+2}, Fx_{3+4}, Fy_{1+4}, Fy_{2+3}, Fz_1, Fz_2, Fz_3, and Fz_4, as shown in Figure 3.19(b). The sampling rate of these charges or force components is 1000 Hz which implies that each force component is measured at each 0.001 s of the drilling or tapping time of the test block. The charges were then fed directly into the eight charge amplifiers, shown in Figure 3.19(c), through the eight-core connecting cables, type 1677A5/1679A5. The charge amplifiers convert these charges into standardized voltage signals which are subsequently converted into force signals through an analog-to-digital (A/D) converter. It should be kept in mind that the eight force signals obtained for a particular test block (180 holes) give the values of the abovementioned eight drilling/tapping force components over the drilling/tapping time of such a block. These force signals were independently monitored and recorded for each test block into the Lab View program, as shown in Figure 3.20, where Cut Pro 8.0 software was used for cutting force measurements.

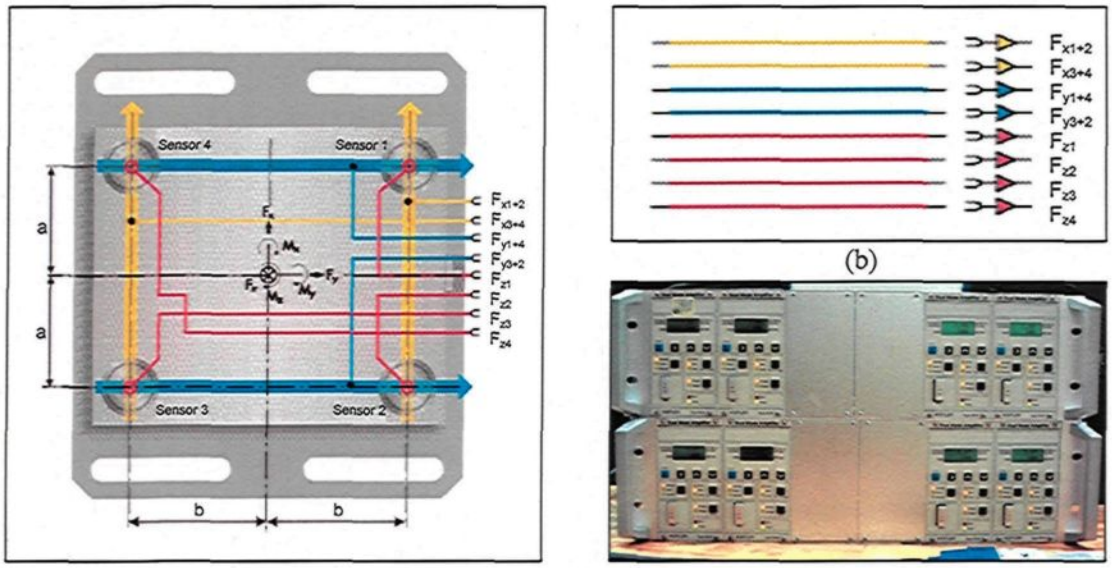

(a) (c)

Figure 3.19 (a) Kistler 6-component dynamometer; (b) 8 charge amplifier channels; and (c) 8 charge amplifiers.

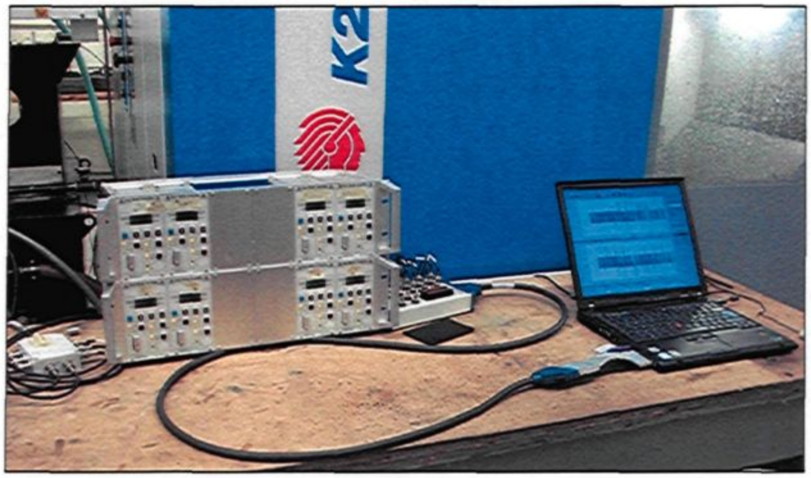

Figure 3.20 Monitoring and recording of drilling/tapping force signals.

CHAPTER 4

MICROSTRUCTURAL CHARACTERIZATION

CHAPTER 4

MICROSTRUCTURAL CHARACTERIZATION

4.1 INTRODUCTION

A metallographic study was carried out with the intention of identifying the phases contained in the microstructure of the base 220 alloy under investigation. In addition, the study also examined the specific microstructural changes associated with such melt treatment procedures as modification and grain refining, as well as the addition of alloying elements, and solution heat-treatment. The results obtained will be discussed in the following subsections.

4.2 MICROCONSTITUENTS OF THE BASE ALLOY

The optical micrograph and backscattered image obtained from the as-cast base A alloy and shown in Figures 4.1(a) and 4.1(b), respectively, reveal that θ-Al_2Cu, Q-$Al_5Mg_8Si_6Cu_2$, and Chinese script-like α-$Al_{15}(Fe,Mn)_3Si_2$ phases are the main constituents of the alloy microstructure. The Al_2Cu phase precipitates in both block-like and eutectic-like forms whereas the $Al_5Mg_8Si_6Cu_2$ phase appears as small particles growing out of the Al_2Cu phase. The absence of free Si in the microstructure implies that the Si content of the alloy was consumed in the formation of the Q-$Al_5Mg_8Si_6Cu_2$ and α-$Al_{15}(Fe,Mn)_3Si_2$ phases.

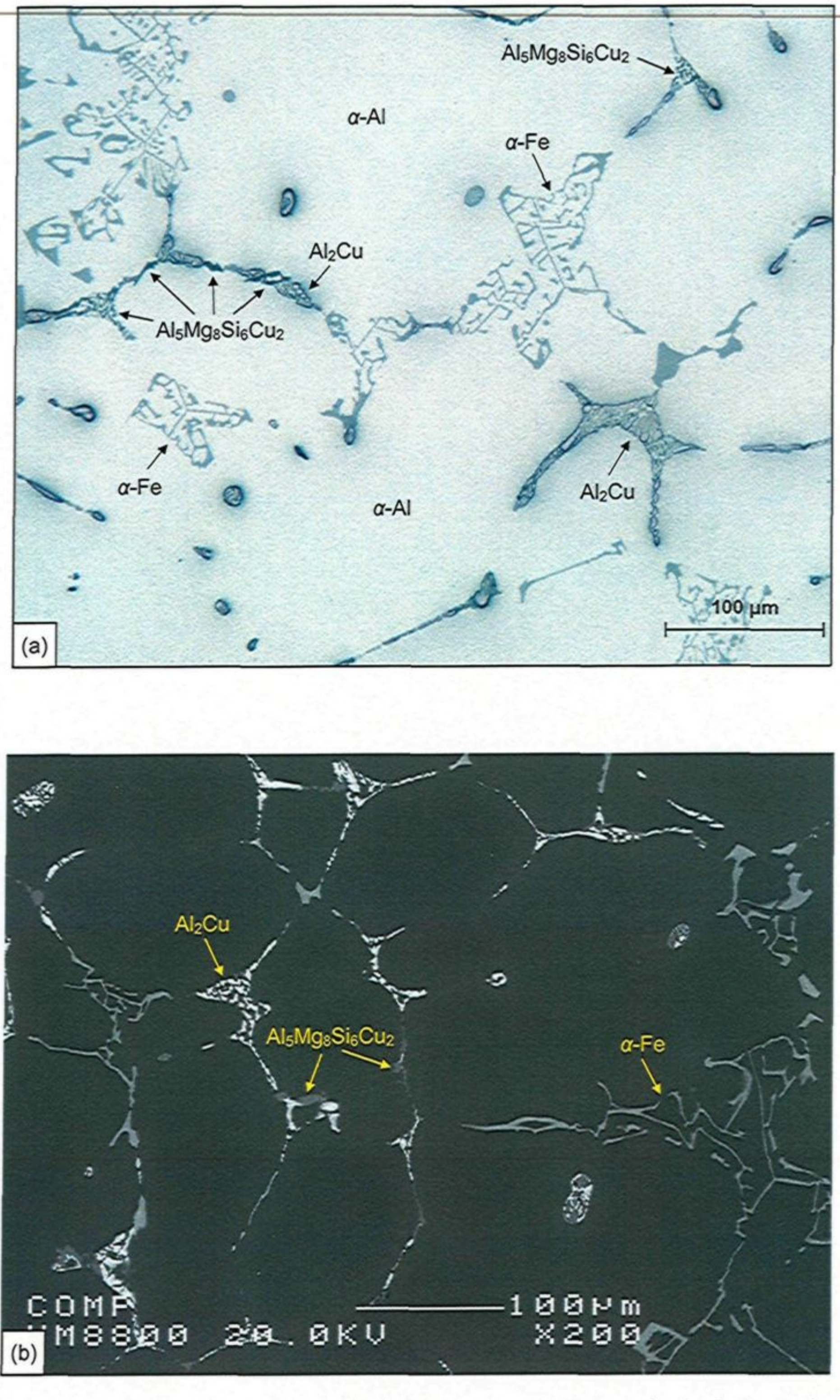

Figure 4.1 (a) Optical micrograph; and (b) backscattered image obtained from the as-cast base A alloy.

The platelet-like β-Al_5FeSi phase was not in evidence because of the high Mn/Fe ratio (~1) of the alloy which promotes the formation of the α-Fe phase at the expense of the β-Fe phase. The chemical compositions of the phases observed in the as-cast base A alloy, as identified by using wavelength dispersive spectroscopy (WDS), are listed in Table 4.1 together with the shape characteristics and suggested formulae for these phases.

Table 4.1 Chemical composition of the phases observed in the as-cast base A alloy

Phase	Element	Wt%	At%	Calculated formula	Shape characteristics	Suggested formula
Al-Cu	Al	48.17	68.48	$Al_{2.18}Cu$	Block-like / eutectic-like, white	Al_2Cu
	Cu	52.03	31.47			
	Total	100.2	99.95			
Al-Mg-Si-Cu	Al	15.83	16.78	$Al_{3.13}Mg_8Si_{5.7}Cu_{1.74}$	Small particles, grey	$Al_5Mg_8Si_6Cu_2$
	Mg	36.42	42.84			
	Si	29.96	30.51			
	Cu	20.74	9.33			
	Total	102.9	99.46			
α-Fe	Al	63.48	74.08	$Al_{13.9}(Fe,Mn)_3Si_{1.82}$	Chinese-script, grey	$Al_{15}(Fe,Mn)_3Si_2$
	Fe	14.92	8.48			
	Mn	13.22	7.51			
	Si	8.67	9.72			
	Total	100.3	99.79			

Thermal analysis techniques were also applied in order to monitor the reactions which take place during the solidification of the base A alloy producing the abovementioned alloy phases. A sample taken from the alloy melt was poured into a preheated (600°C) graphite crucible of diameter 50 mm and height 100 mm. The temperature was measured by means of a sheathed thermocouple inserted through the bottom of the crucible along its centre-line before pouring. A PC-based data acquisition system connected to the thermocouple was then used to analyze the data. The temperature of the metal was recorded as a function of time from the fully liquid state, through the solidification range, to the solid state. From the temperature-time curve obtained, the first derivative was determined and the resulting peaks corresponding to the main reactions were identified, as shown in Figure 4.2. These reactions, together with the temperatures at which they occurred, are summarized and presented in Table 4.2.

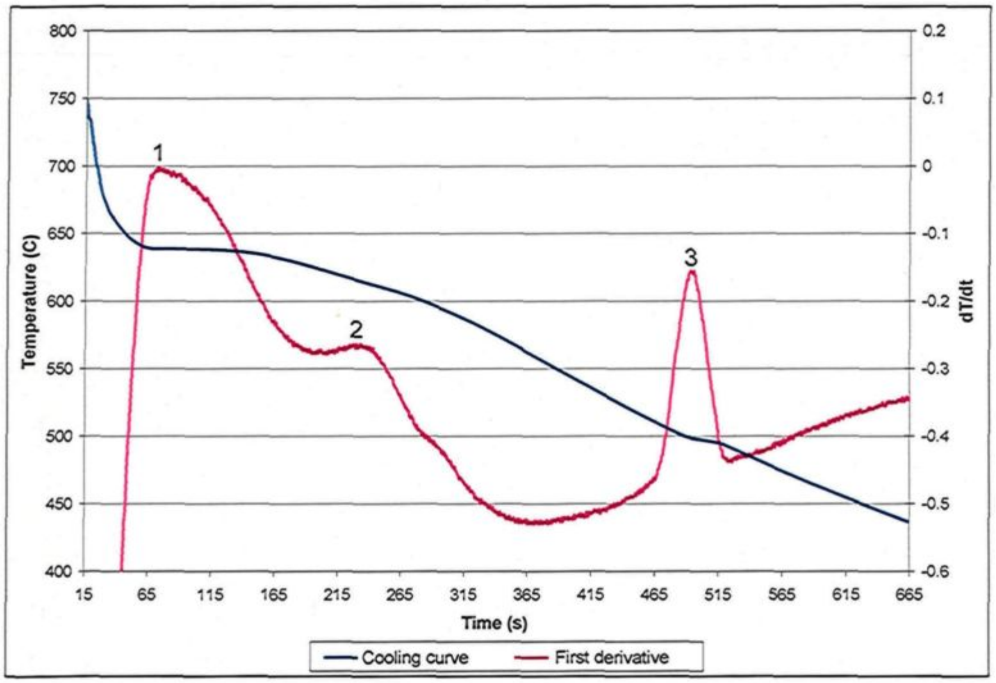

Figure 4.2 Temperature-time cooling curve and its first derivative obtained from the 220 (A) base alloy.

Table 4.2 Main reactions observed from the thermal analysis diagram shown in Figure 4.2

Peak Number	**Temperature (°C)**	**Reaction**
1	639	Formation of α-Al
2	615	Precipitation of α-$Al_{15}(Fe,Mn)_3Si_2$
3	497	Precipitation of θ-Al_2Cu and $\underline{Q}$-$Al_5Mg_8Si_6Cu_2$

4.3 EFFECTS OF MELT TREATMENT

Owing to the absence of free Si in the base A alloy, it might be expected that there would be no significant change in the alloy microstructure resulting from Sr addition as a chemical modifier for eutectic silicon. However, upon comparing the micrographs obtained from the unmodified A alloy and the Sr-modified A1 alloy, shown in Figures 4.3(a) and 4.3(b), respectively, it would be appear that the addition of Sr refines the morphology of the α-Fe Chinese-script phase to a certain extent in the A1 alloy, resulting in the even distribution of the particles of this phase within the aluminum matrix. The effects of Sr modification on the formation of iron intermetallics have recently been investigated.[1,3] Samuel *et al.*[1] demonstrated that the beneficial effects of Sr modification are manifested through the fragmentation and dissolution of the platelet-like β-Fe phase. Shabestari *et al.*[3] reported that the addition of 600 ppm Sr to the Al-12%Si alloys leads to a considerable reduction, of ~ 46%, in the particle size of the α-Fe Chinese-script phase.

The combined addition of Ti and Zr to the base A alloy, *i.e.* producing the A4 alloy, results in the formation of $Al_3(Zr,Ti)$ phase particles as may be seen in the backscattered image shown in Figure 4.4. It will be observed that these particles tend to assume a star-like morphology and are present within some of the α-aluminum grains as if they were crystallization nuclei. The $Al_3(Zr,Ti)$ phase particles are clearly depicted in the higher magnification backscattered image shown in Figure 4.5, whereas the distribution of Zr and Ti in these particles is provided in the corresponding X-ray images shown in Figures 4.6(a) and (b), respectively. In addition, the composition of the $Al_3(Zr,Ti)$ phase, as confirmed by WDS analysis, is also listed in Table 4.3.

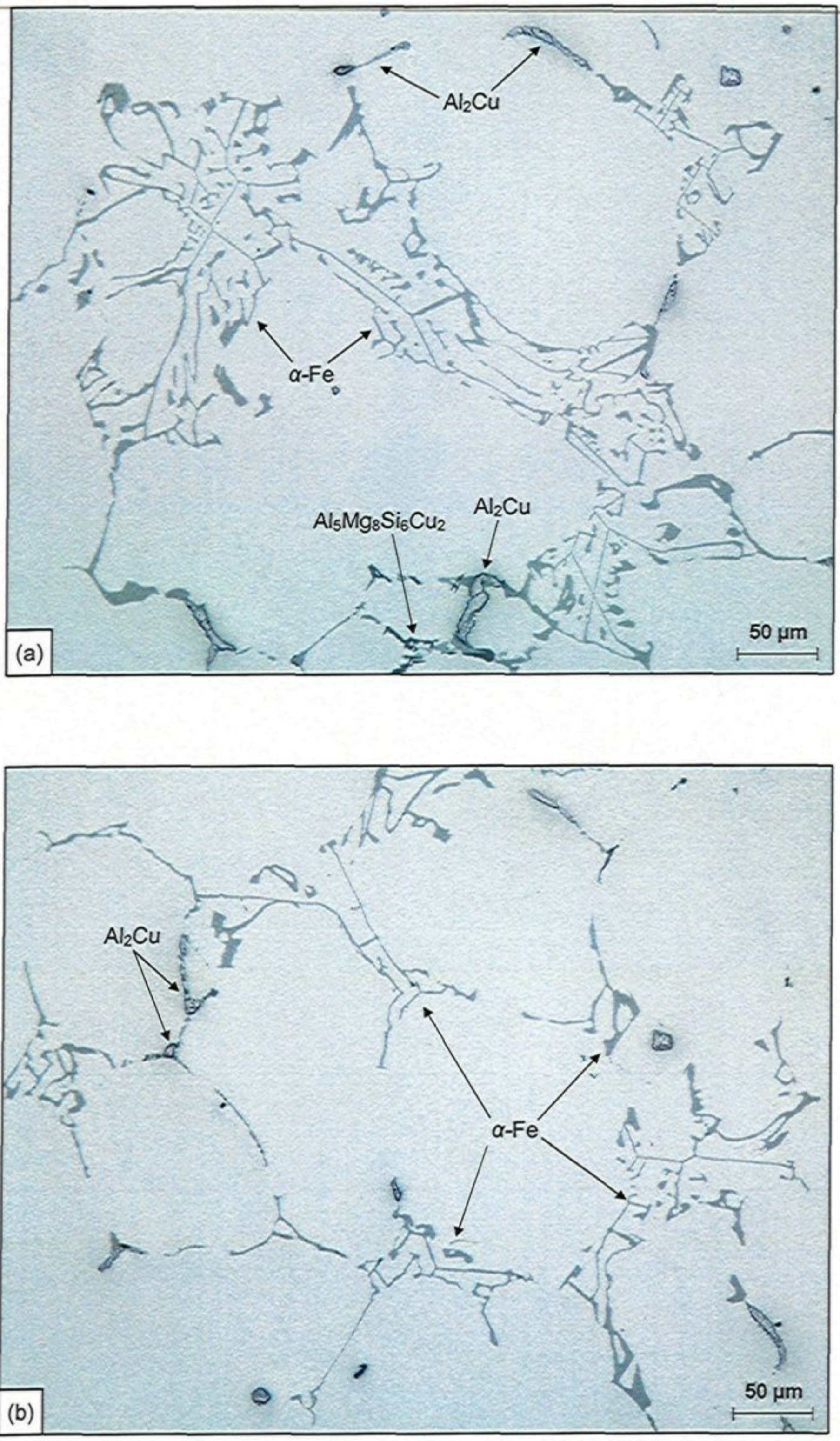

Figure 4.3 Optical micrographs obtained from: (a) the unmodified base A alloy; and (b) the Sr-modified A1 alloy in as-cast condition.

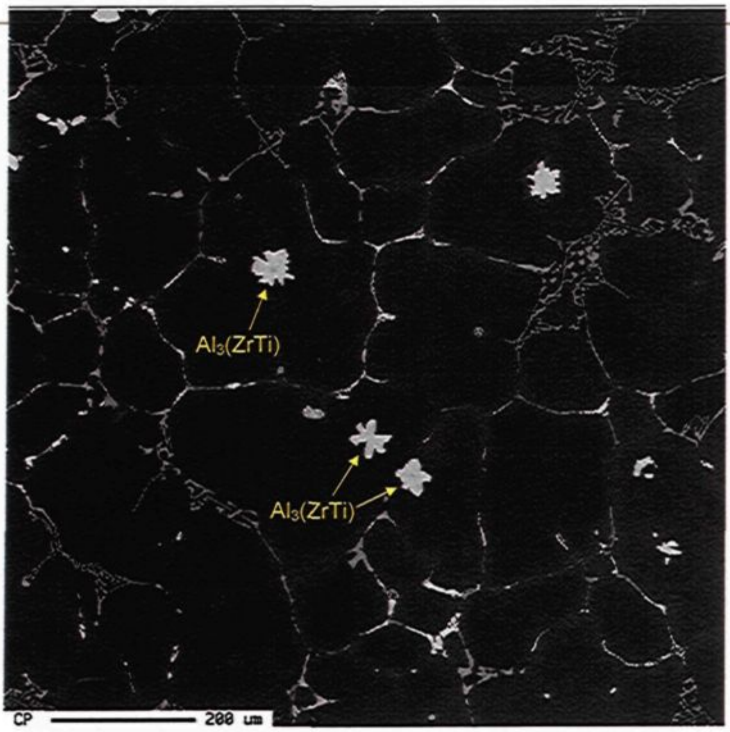

Figure 4.4 Backscattered image showing the precipitation of $Al_3(ZrTi)$ phase particles in A4 alloy in the as-cast condition.

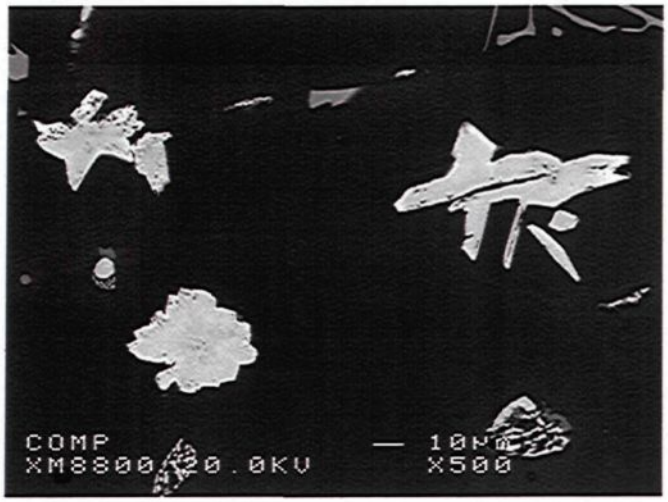

Figure 4.5 Higher magnification backscattered image showing the $Al_3(ZrTi)$ phase particles.

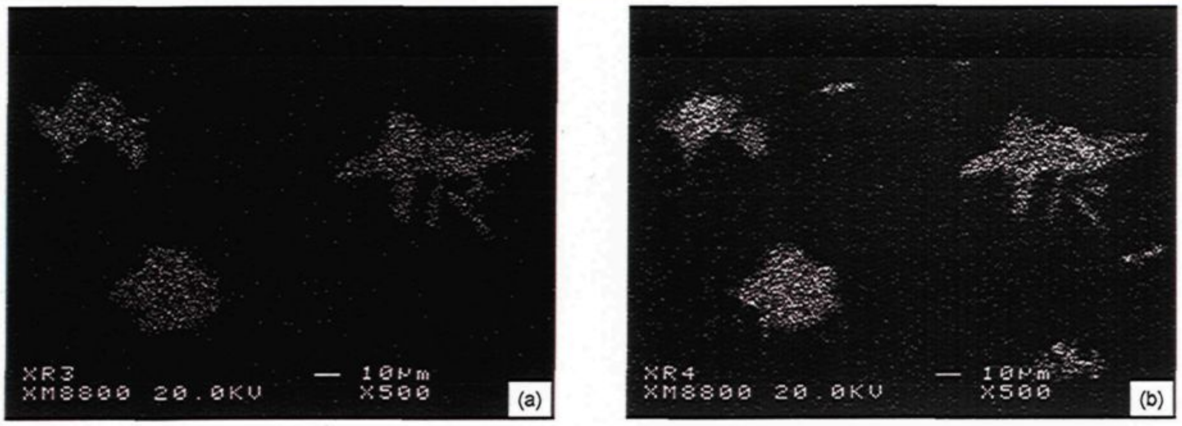

Figure 4.6 X-ray images of (a) Zr; and (b) Ti, corresponding to the backscattered image shown in Figure 4.5.

Table 4.3 Chemical composition of the Al-Zr-Ti phase observed in the as-cast A4 alloy

Phase	Element	Wt%	At%	Calculated formula	Shape characteristics	Suggested formula
Al-Zr-Ti	Al	49.87	74.10	$Al_3(ZrTi)$	Star-like,	$Al_3(ZrTi)$
	Zr	41.32	18.15		Light grey	
	Ti	7.18	6.32			
	Total	98.37	98.57			

In order to appreciate the importance of $Al_3(Zr,Ti)$ phase particles with regard to the nucleation of the α-aluminum grains, grain size measurements were carried out for both the non-grain-refined base A alloy and the grain-refined A4 alloy containing additions of Ti and Zr. It was found that the combined addition of Ti and Zr causes a decrease in the grain size from 500µm in the base A alloy to 160µm in the A4 alloy. This difference in grain size is clearly evident upon comparing the micrographs of both the alloys, as shown in Figures 4.7(a) and (b), respectively.

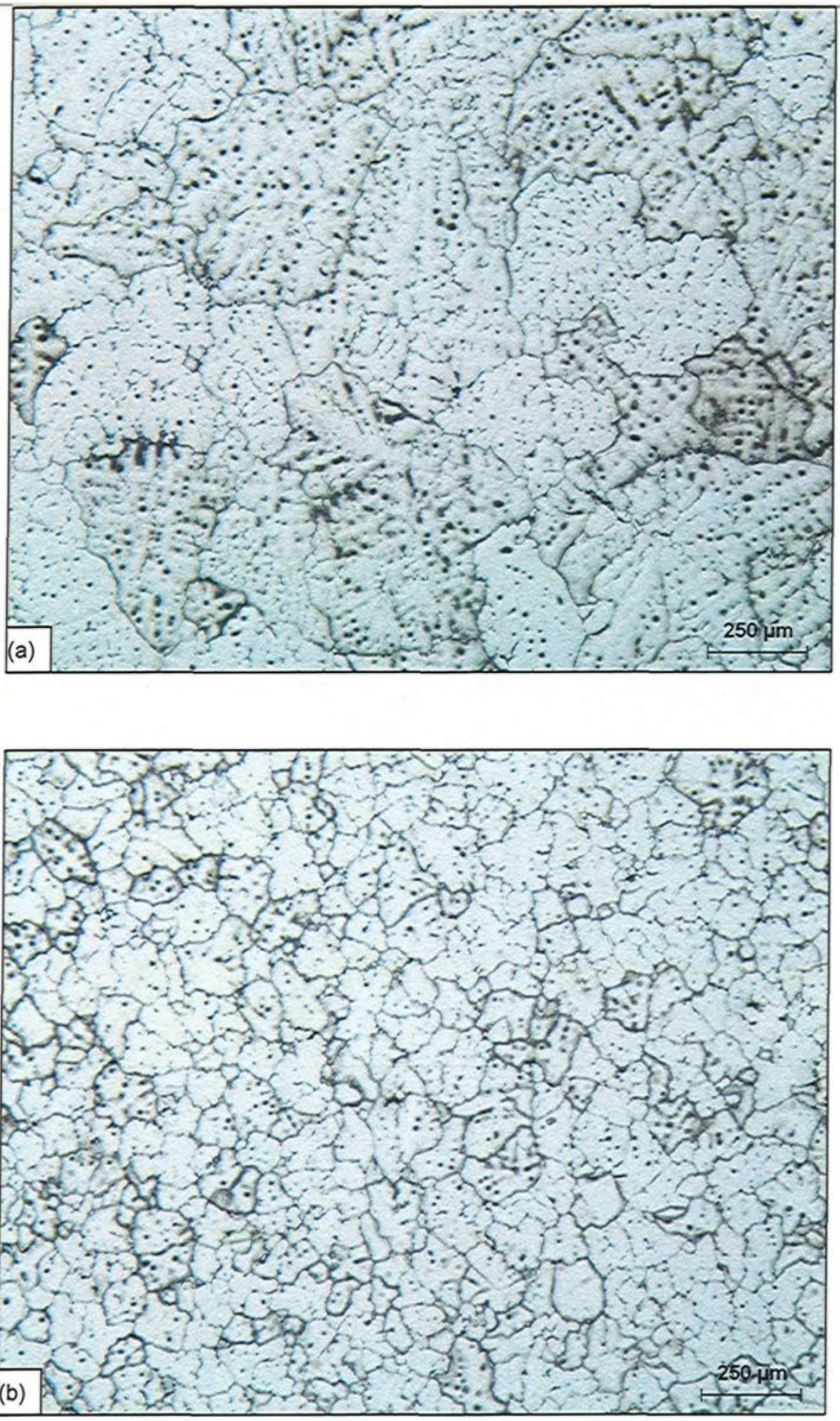

Figure 4.7 Micrographs obtained from: (a) non-grain-refined base A alloy; and (b) grain-refined A4 alloy containing Ti and Zr.

4.4 EFFECTS OF THE ADDITION OF IRON AND MANGANESE

The addition of 0.2% Fe to the A3 alloy, thereby producing the A31 alloy, was found to increase the precipitation of the α-Fe Chinese script phase particles, as illustrated by the optical micrograph shown in Figure 4.8. This finding was supported by further evidence from volume fraction measurements, as will be discussed in Section 4.6. The platelet-like β-Fe phase, however, did not form since the Mn/Fe ratio of the alloy was still high enough (~0.7) to promote the formation of the α-Fe phase rather than that of the β-Fe phase.

The further addition of 0.2% Mn to the A31 alloy, producing the A32 alloy, did not lead to the precipitation of undesirable sludge particles, which may form at higher Mn levels, as may be noted by their absence in the micrograph shown in Figure 4.9. The WDS analysis relating to both the A31 and A32 alloys did not detect any additional phases, namely platelet-like β-Fe and the star-like sludge phases, other than those found in the base A alloy; this in turn sustains the fact that increasing either the Fe level or the Fe and Mn level in these alloys, respectively, leads only to intensifying the precipitation of α-Fe Chinese-script phase particles.

4.5 EFFECTS OF THE ADDITION OF TIN AND BISMUTH

Figure 4.10 is a high magnification backscattered image obtained from the as-cast Sn-containing A41 alloy where the precipitation of Sn in the form of β-Sn particles may be observed as the white phase, based on its high atomic number. These particles appear as

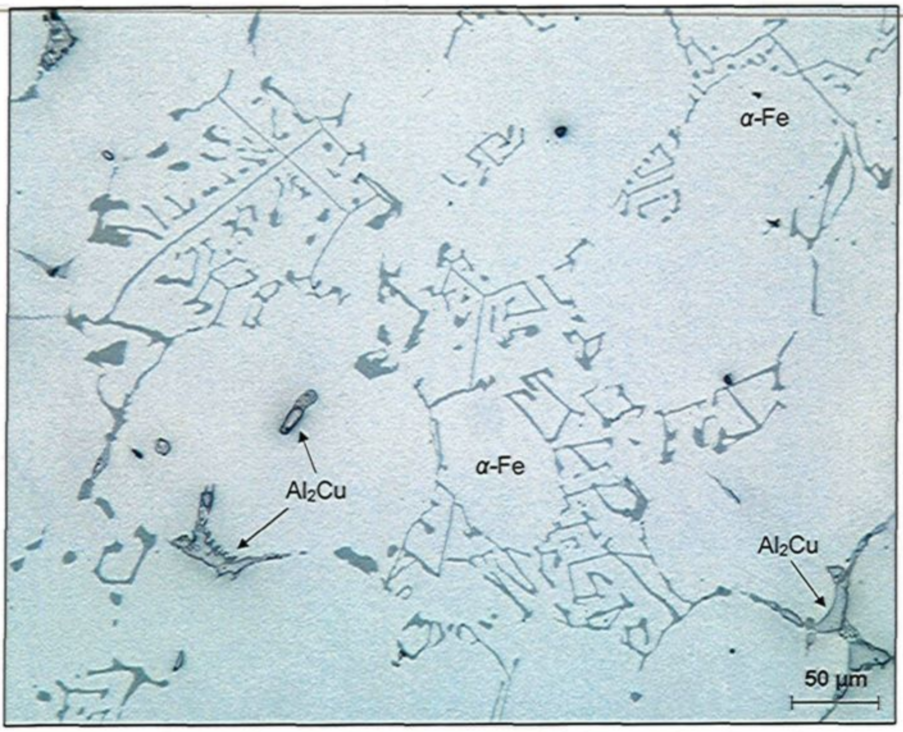

Figure 4.8 Micrograph obtained from the A31 alloy (A3 alloy + 0.2% Fe) in the as-cast condition.

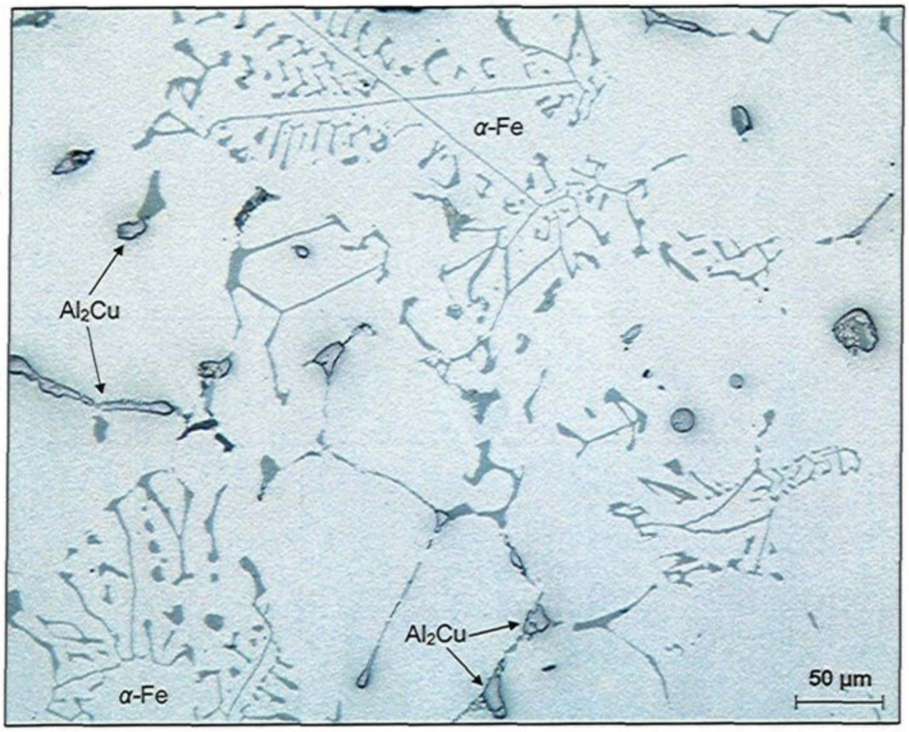

Figure 4.9 Micrograph obtained from the A32 alloy (A3 alloy + 0.2%Fe + 0.2%Mn) in the as-cast condition.

small non-uniformly distributed clusters usually solidified within the Al_2Cu phase network. The atomic composition of the β-Sn phase, as indicated by WDS analysis, is 97.93 ± 0.16% Sn and 2.10 ± 0.29% Cu.

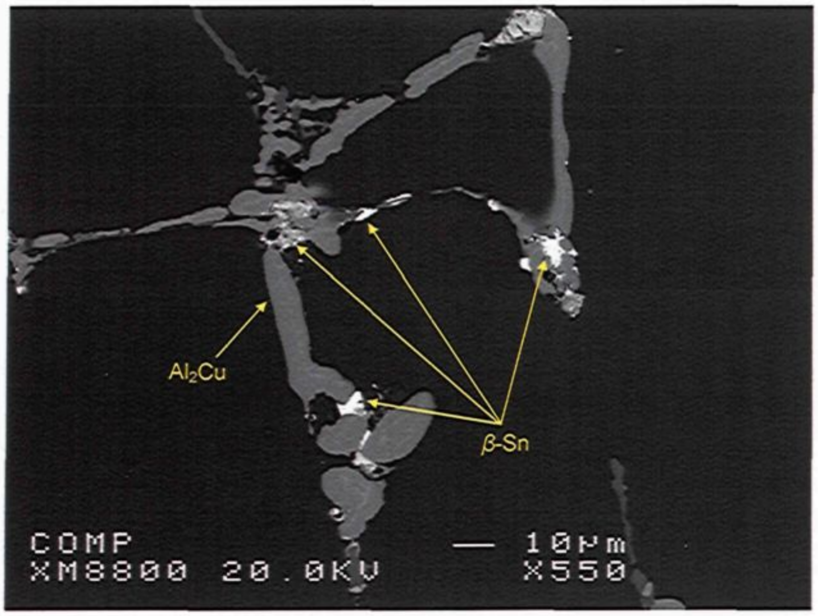

Figure 4.10 Backscattered image obtained from the A41 alloy (A4 alloy + 0.15%Sn) in the as-cast condition.

Considering that the melting point of Sn is ~231°C, the β-Sn particles would be subjected to melting during the solution heat treatment carried out at 495°C. Figure 4.11 is a higher magnification backscattered image obtained from the A41 alloy solutionized at 495°C for 8 h, followed by quenching in hot water at ~65°C and aging at 180°C for 2 h; it shows a resolidified β-Sn particle which had undergone incipient melting during the solution heat treatment.

Tiny Mg_2Sn phase particles were also found in the Sn-containing A41 alloy, as will be observed from the high magnification backscattered image shown in Figure 4.12.

Figure 4.11 Resolidified β-Sn particle which had undergone incipient melting during the solution heat treatment of A41 alloy.

Figure 4.12 Precipitation of Mg_2Sn phase in the Sn-containing A41 alloy.

The chemical composition of the Mg_2Sn phase found in the A41 alloy, as identified by WDS analysis, is provided in Table 4.4. The formation of the higher melting point Mg_2Sn phase consumes the amount of Mg present, thereby hindering the precipitation of such Mg-hardening phases as β-Mg_2Si and Q-$Al_5Mg_8Si_6Cu_2$. Grebenkin *et al.*[85] found that Sn and Pb are the electronic analogs of silicon and have been observed to replace it in magnesium compounds, this in turn impedes the formation of the Mg-hardening phases in Al-Cu-Si-Mg alloys.

Table 4.4 Chemical composition of the Mg-Sn phase observed in the as-cast A41 alloy

Phase	Element	Wt%	At%	Calculated formula	Shape characteristics	Suggested formula
Mg-Sn	Mg	30.05	68.01	$Mg_{2.1}Sn$	Tiny particles, grey	Mg_2Sn
	Sn	68.64	31.81			
	Total	98.69	99.82			

Figure 4.13 is a high magnification backscattered image obtained from the as-cast Bi-containing A42 alloy. It will be observed that Bi precipitates in the form of undissolved independently-distributed particles within the alloy microstructure. There is no evidence for the formation of any intermetallic compound between Bi and Al or any other alloying elements. The higher magnification backscattered image shown in Figure 4.14 illustrates

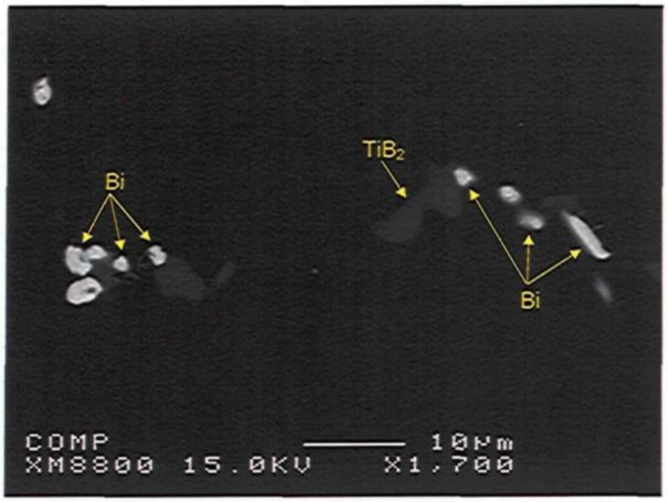

Figure 4.13 Backscattered image showing the precipitation of Bi particles in the A42 alloy.

the morphology of both Bi- and Sn-particles precipitated in the A43 alloy. Also, there is no intermetallic compound to be found in this alloy occurring between Sn and Bi, both of them having been precipitated independently. The X-ray images of the Sn and Bi particles shown in Figure 4.14 are displayed in Figures 4.15(a) and 4.15(b), respectively.

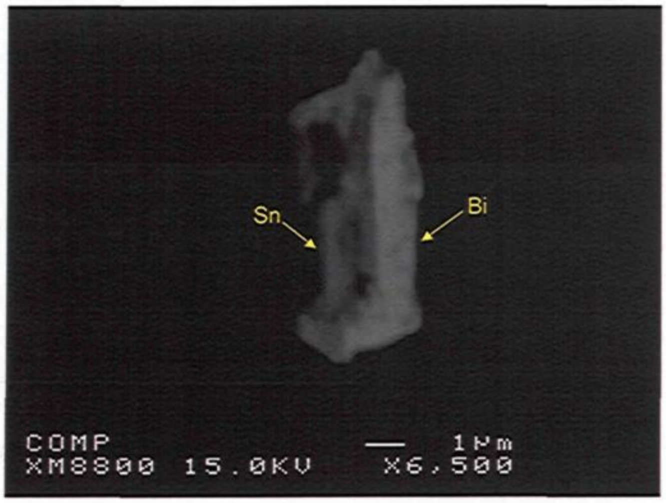

Figure 4.14 Backscattered image showing the precipitation of Sn and Bi particles in the A43 alloy.

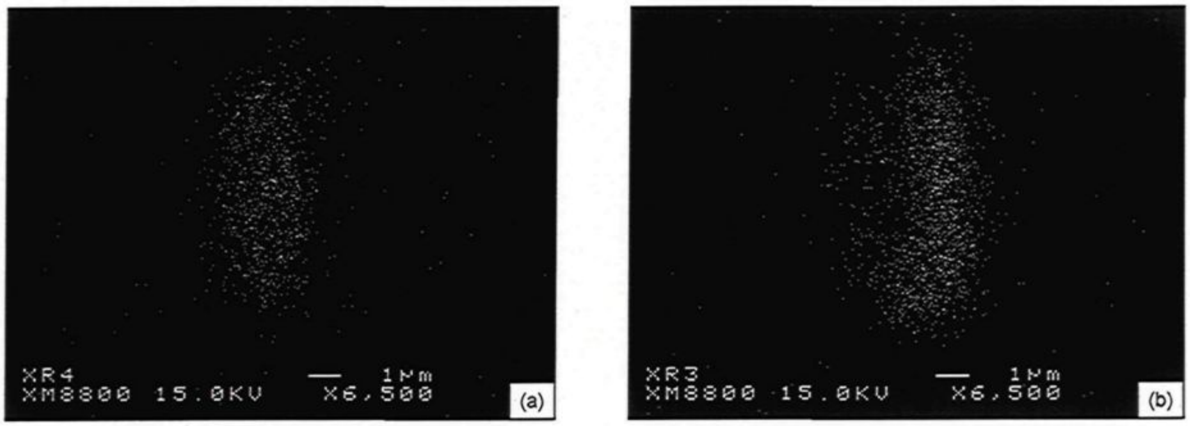

Figure 4.15 X-ray images of (a) Sn; and (b) Bi, corresponding to the backscattered image shown in Figure 4.14.

4.6 EFFECTS OF SOLUTION HEAT TREATMENT

Figure 4.16 shows the backscattered image obtained from the solutionized base A alloy. The rarity of the Cu-rich intermetallic phases in the microstructure shown implies that the solution heat treatment dissolved these phases almost completely into the solid solution. On the other hand, the α-Fe Chinese-script phase particles, clearly seen in the microstructure, were not habitually affected by the solution treatment.

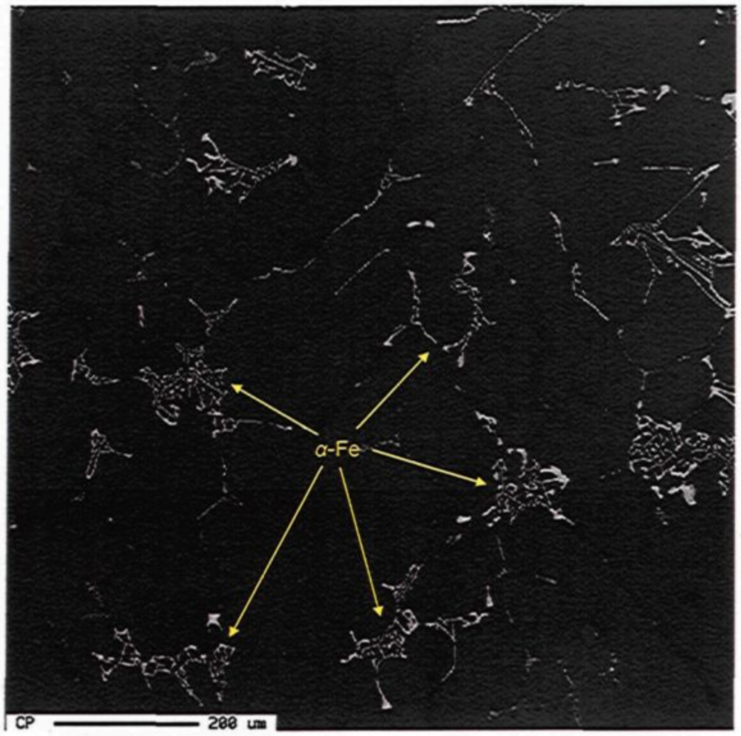

Figure 4.16 Backscattered image obtained from the solutionized base A alloy.

Figure 4.17 shows the effects of solution heat treatment on the volume fraction of the iron and copper intermetallics contained in the alloys studied. It will be seen that solution heat treatment reduces the volume fraction of these intermetallics by

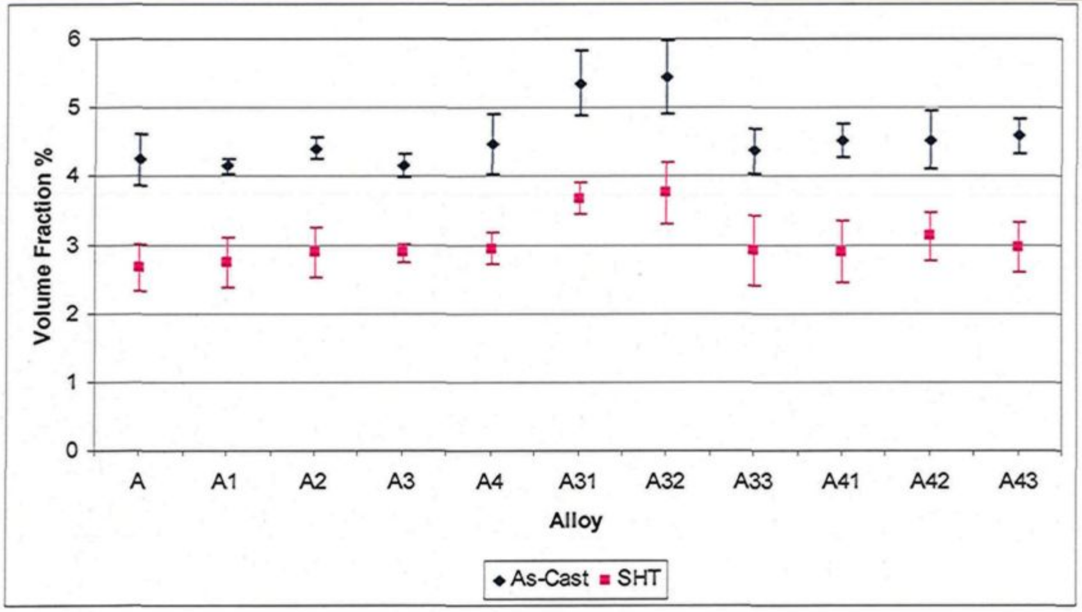

Figure 4.17 Effects of solution heat treatment on the volume fraction (%) of copper and iron intermetallic phases.

approximately 35%, corresponding to the dissolution of the Cu-rich intermetallic phases. Thus, the volume fractions of the α-Fe Chinese-script phase, which remained unaffected by the solution heat treatment, would correspond to the values plotted in the solution heat-treated condition. It will be observed that all the alloys, except for the A31 and A32 alloys, have almost the same volume fraction value with regard to this phase. As will be seen, both the A31 and A32 alloys exhibit an increase in the volume fraction of α-Fe Chinese-script phase by approximately 27% and 30%, respectively, compared to the other alloys because of the higher Fe content in the former and the higher Fe and Mn content in the latter. This increase in the volume fraction of α-Fe Chinese-script phase is clearly seen from a comparison of the backscattered image obtained from the solutionized A32 alloy (having the higher Fe and Mn content) shown in Figure 4.18 with the one obtained from the solutionized base A alloy, shown in Figure 4.16.

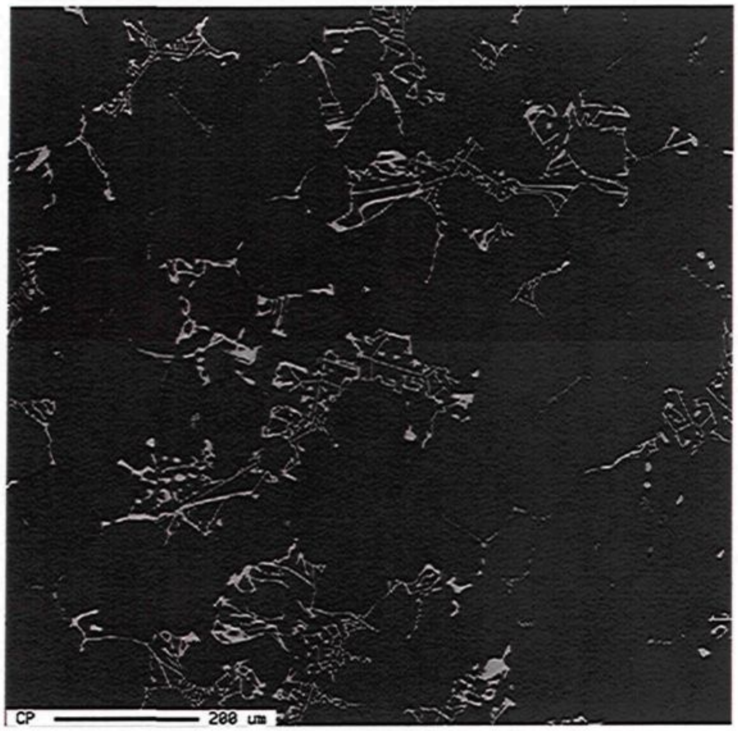

Figure 4.18 Backscattered image obtained from the solutionized A32 alloy.

CHAPTER 5

INVESTIGATION OF THE MECHANICAL PROPERTIES

CHAPTER 5

INVESTIGATION OF THE MECHANICAL PROPERTIES

5.1 INTRODUCTION

This chapter will focus on the mechanical properties, specifically tensile, hardness, and impact properties, of the alloys prepared for this study with the intention of identifying the effects of the additives and heat treatment regimes on the mechanical properties of the base alloy in question, namely the 220 alloy. Moreover, the quality index technique will be applied here as a trial to correlate the tensile properties YS, UTS, and %El, and to evaluate the quality of the alloys corresponding to the additives introduced.

5.2 EFFECTS OF ADDITIVES ON THE TENSILE PROPERTIES AND HARDNESS

The following subsections will discuss the effects of additives on the tensile properties and hardness of the base 220 alloy in both as-cast and heat-treated conditions. The results will be elaborated upon for the three alloying groups which, as described in Chapter 3, were separated in order to examine: (i) the effects of melt treatment: Alloying Group I; (ii) the effects of iron intermetallics and hardening alloying elements: Alloying Group II; and (iii) the effects of free-cutting elements: Alloying Group III.

5.2.1 Effects of Melt Treatment: Alloying Group I

The effects of melt treatment on the tensile properties and the hardness of the Alloying Group I are shown in Figures 5.1(a) and 5.1(b), respectively, for the as-cast condition. These effects are also shown in Figures 5.2 and 5.3 for the T6 and T7 heat-treated conditions, respectively.

It will be observed that, owing to the low Si content of the base A alloy, the effect of Sr with respect to the modification of silicon eutectic did not bring about any substantial change in the strength properties (YS and UTS) of the Sr-modified A1 alloy either in the as-cast or in the heat-treated conditions. The slight improvement caused in the ductility of the A1 alloy, especially in the as-cast condition, can most probably be ascribed to the role of Sr in refining the morphology of the α-Fe script phase observed in the alloy microstructure. This role may also be considered responsible for the reduction caused in the hardness values of the A1 alloy.

A comparison of the grain-refined A2 alloy with the base A alloy in the as-cast condition reveals that the A2 alloy shows improvement in the %El values, whereas neither the strength properties nor the hardness values appear to have been affected. In both T6 and T7 heat-treated conditions, the UTS, %El, and hardness values of the A2 alloy were observed to be higher than those of the base A alloy for most of the aging times applied.

In spite of the grain-refined A2 alloy displaying improvements in the tensile properties and hardness values, the modified grain-refined A3 alloy did not produce tensile properties or hardness values which were any better than those of the former alloy whether

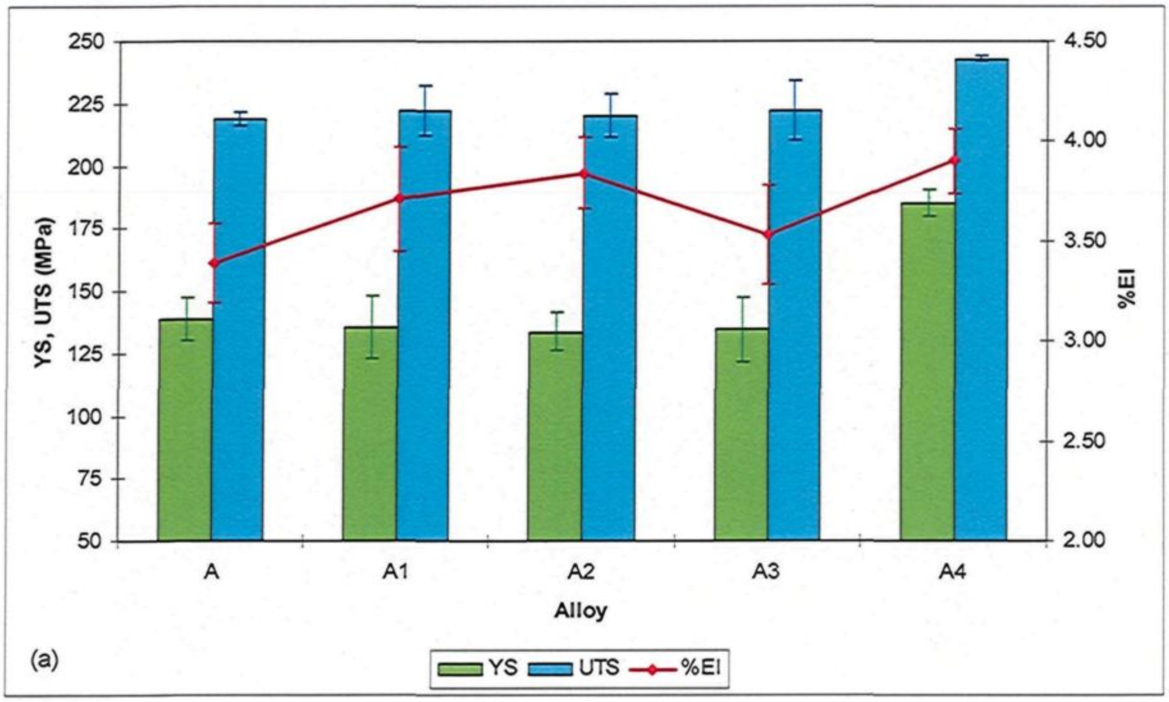

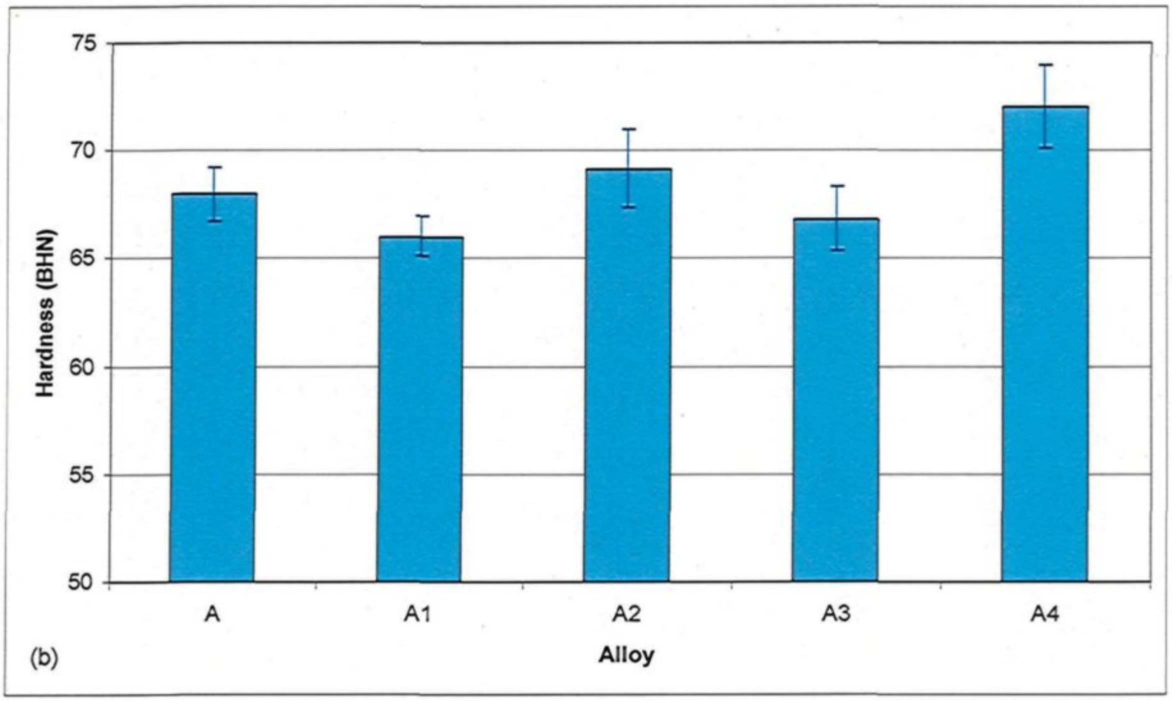

Figure 5.1 Variation in: (a) tensile properties (YS, UTS, and %El); and (b) hardness values of Alloying Group I in the as-cast condition.

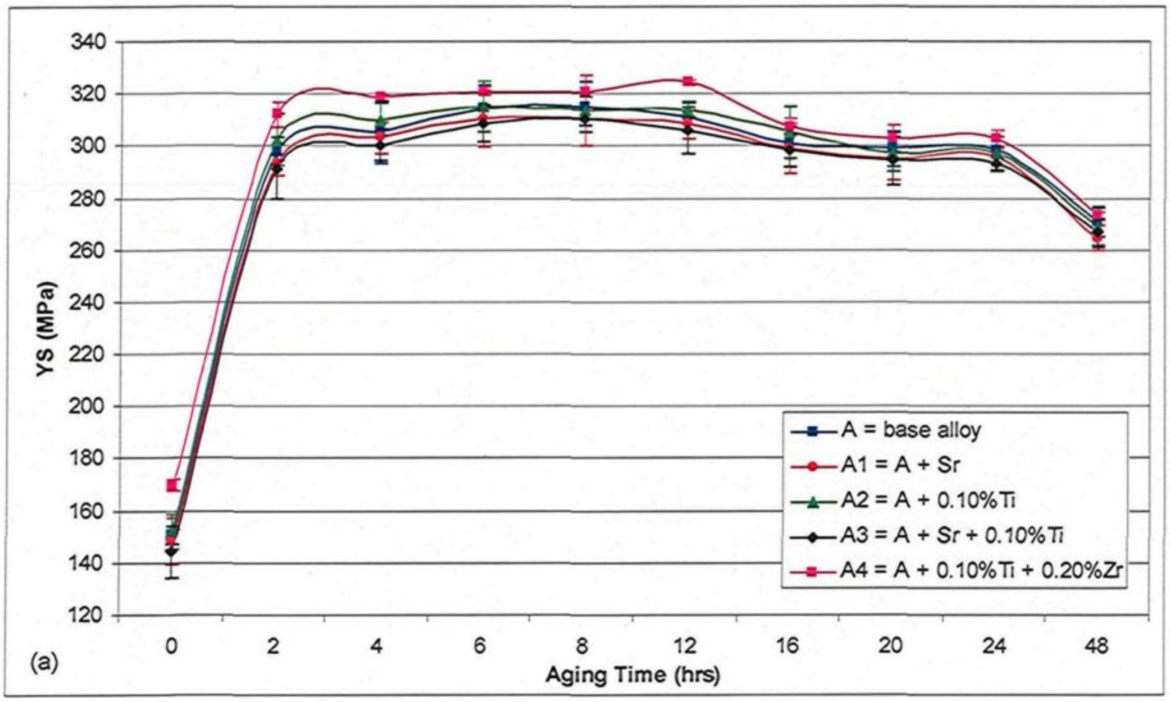

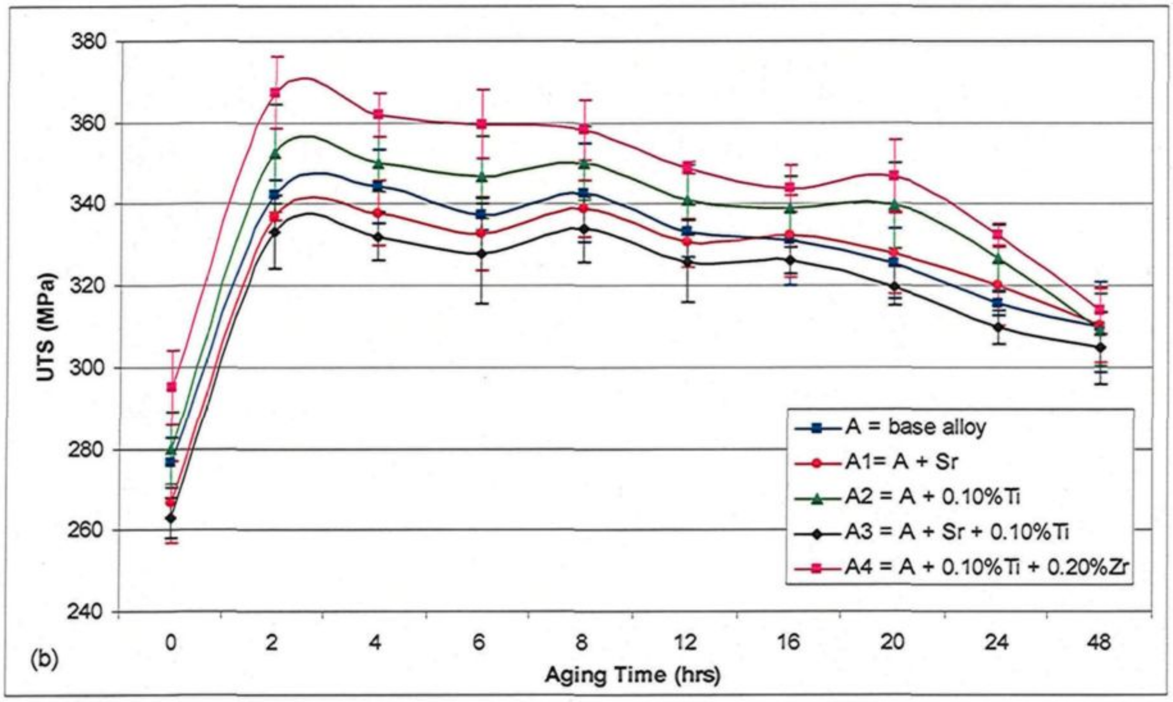

Figure 5.2 ⟶ **Continued**

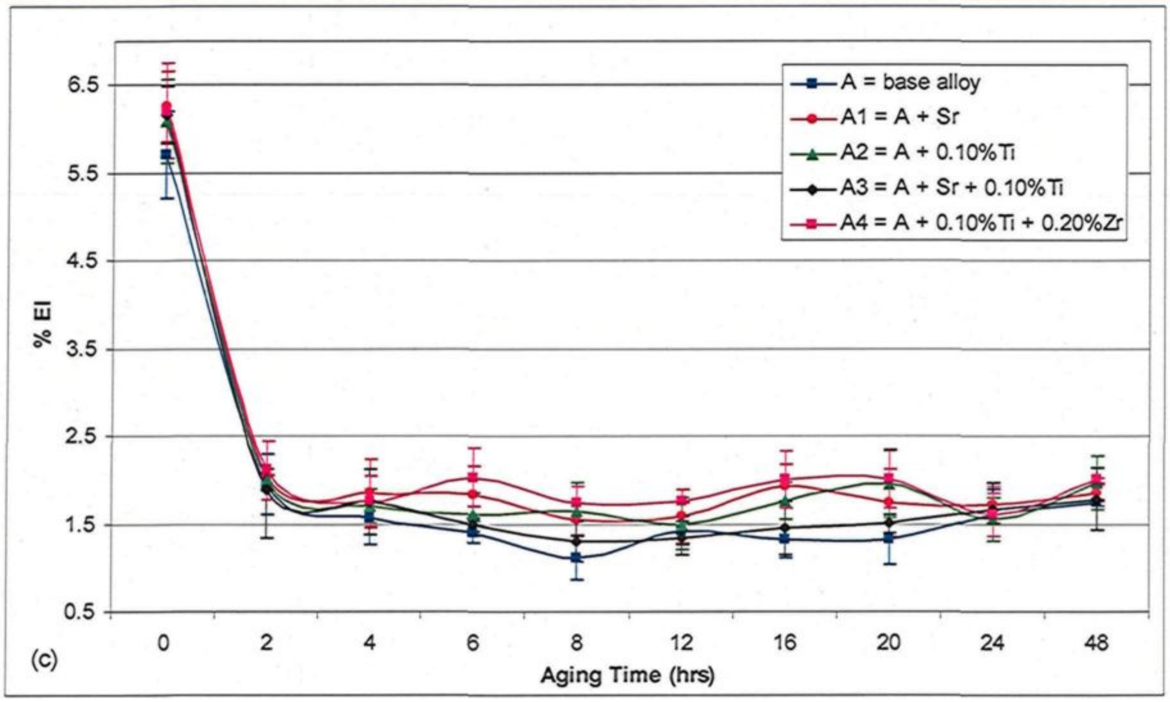

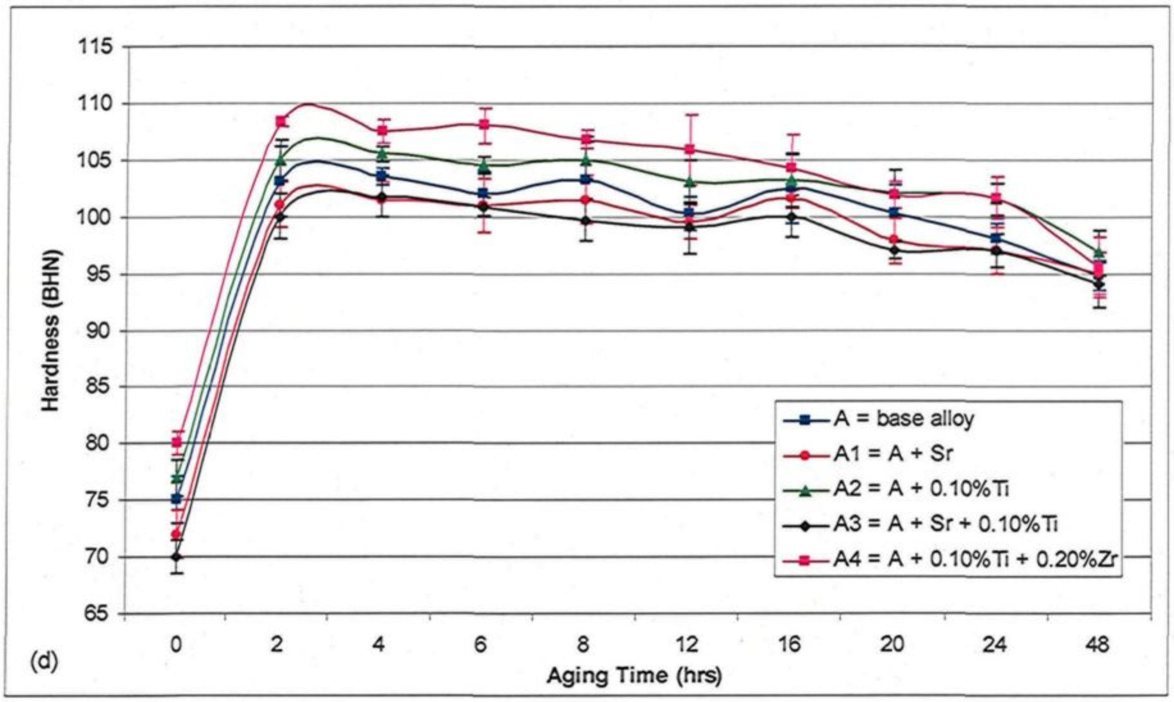

Figure 5.2 Variation in tensile properties and hardness values of Alloying Group I after aging at 180°C: (a) YS; (b) UTS; (c) %El; and (d) hardness values.

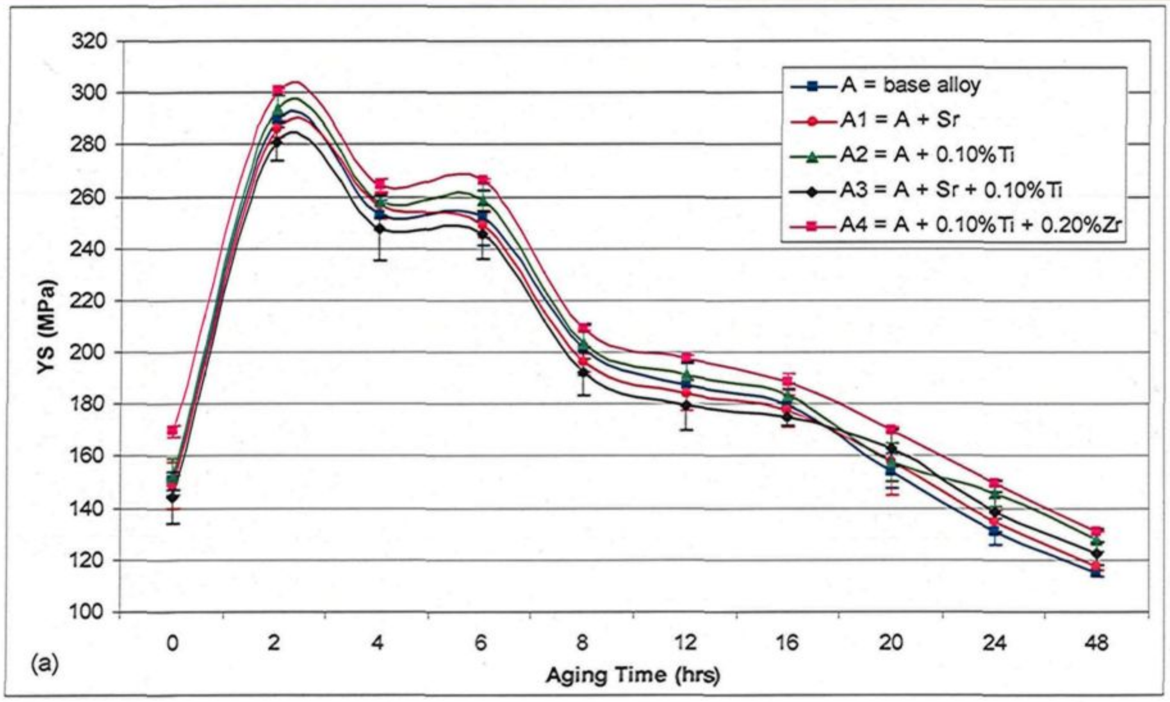

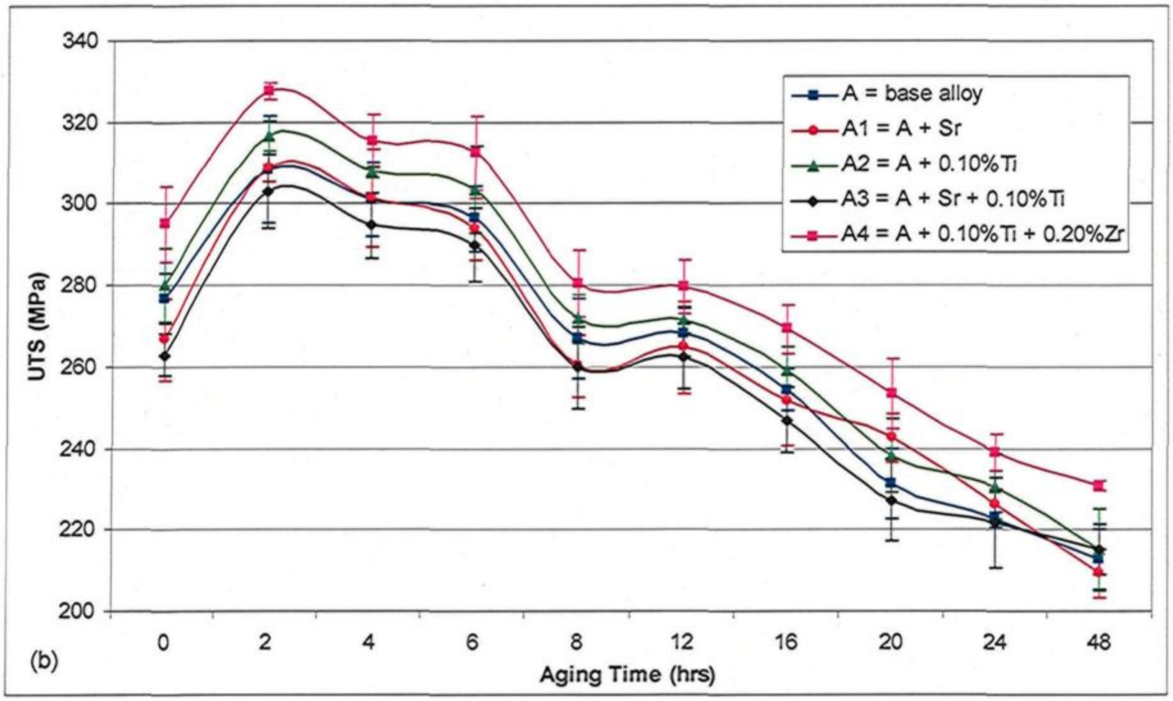

Figure 5.3 ⟶ **Continued**

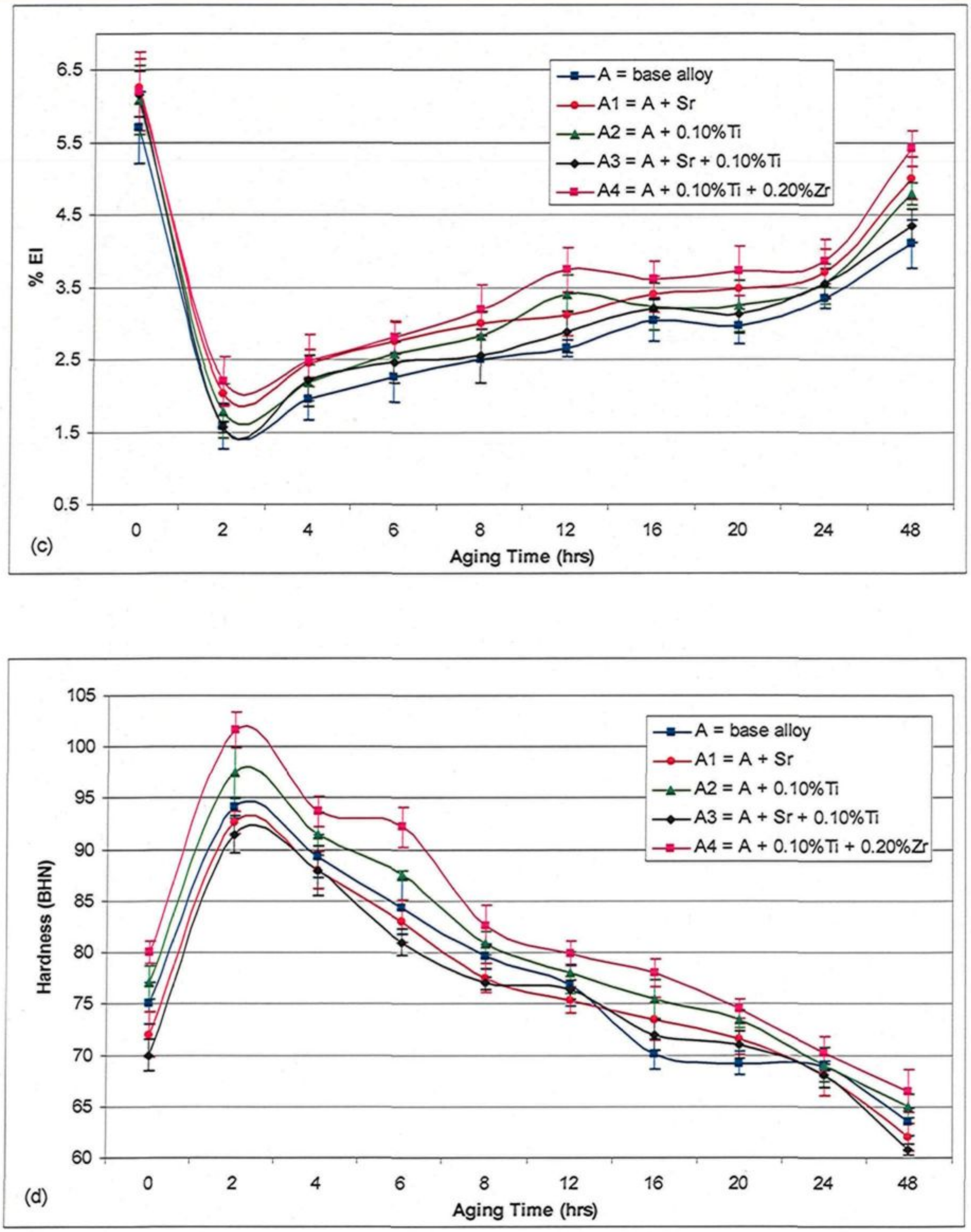

Figure 5.3 Variation in tensile properties and hardness values of Alloying Group I after aging at 220°C: (a) YS; (b) UTS; (c) %El; and (d) hardness values.

in the as-cast or heat-treated conditions. This absence of observable improvement in mechanical properties may be explained in terms of the interaction between Sr and B and/or Sr and Ti as reported by Liao *et al.*[131,132] These interactions have been known to cause mutual "poisoning" of the elements involved and consequently to suppress their modification and/or grain-refining effects.

The Zr-containing A4 alloy possesses the highest values for tensile properties and hardness of the alloys in Group I. This alloy displays significant increases in the YS and UTS together with a high level of ductility in the as-cast and heat-treated conditions. There is a distinct possibility that the higher strength increment produced in this alloy, particularly in the as-cast condition, may be attributed to the strengthening mechanism stimulated by the grain refining action of Zr through the formation of $Al_3(Zr,Ti)$ phase particles, as previously discussed in Chapter 4.

5.2.2 Effects of Iron Intermetallics and Silver: Alloying Group II

The effects of the addition of Fe, Fe + Mn, and Ag on the tensile properties and hardness of the Alloying Group II are shown in Figures 5.4(a) and 5.4(b), respectively, for the as-cast condition. These effects are also shown in Figures 5.5 and 5.6 for the T6 and T7 heat-treated conditions, respectively.

It appears that increasing the Fe content to 0.8% in the A31 alloy decreases the tensile properties, particularly ductility, but increases the hardness values in the as-cast and heat-treated conditions. These effects were predictable based on the increase in the volume fraction of iron intermetallic phases, mainly the α-Fe Chinese-script phase, caused by

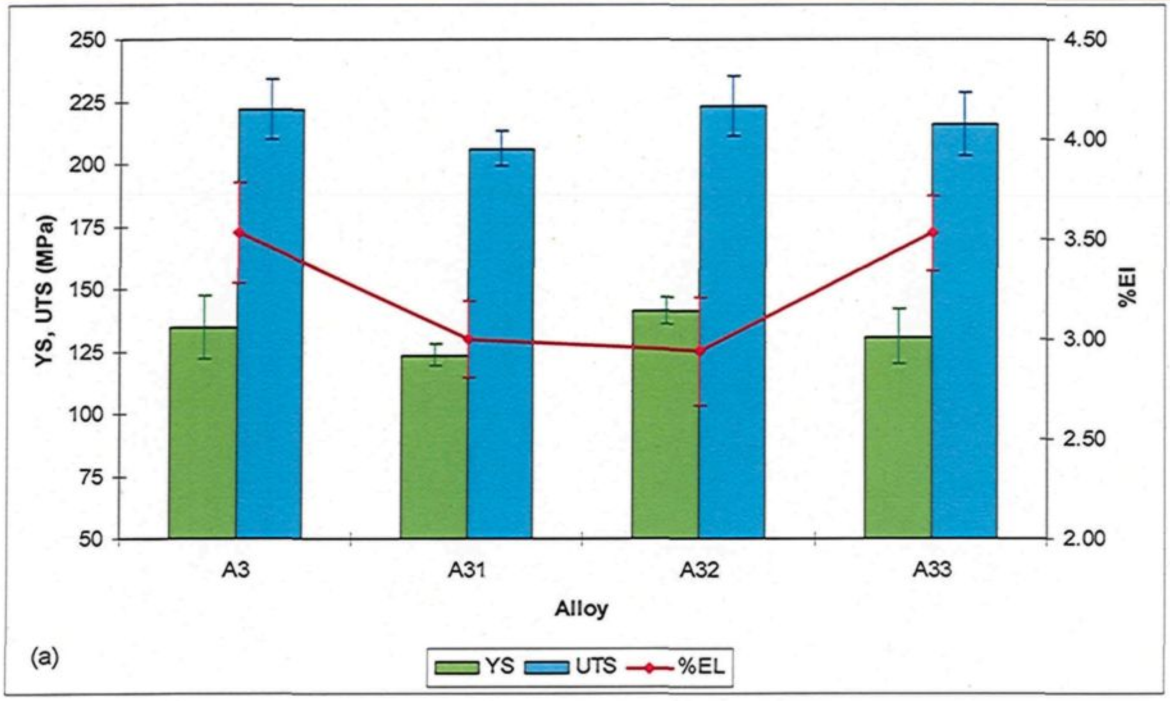

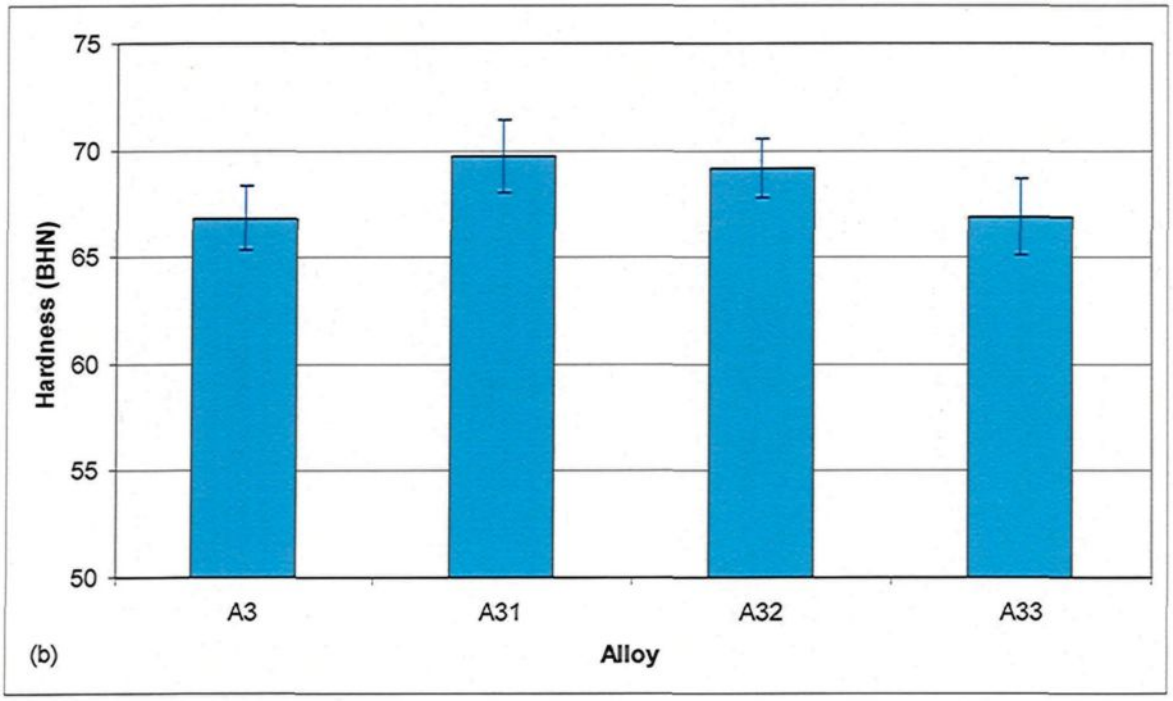

Figure 5.4 Variation in: (a) tensile properties (YS, UTS, and %El); and (b) hardness values of Alloying Group II in the as-cast condition.

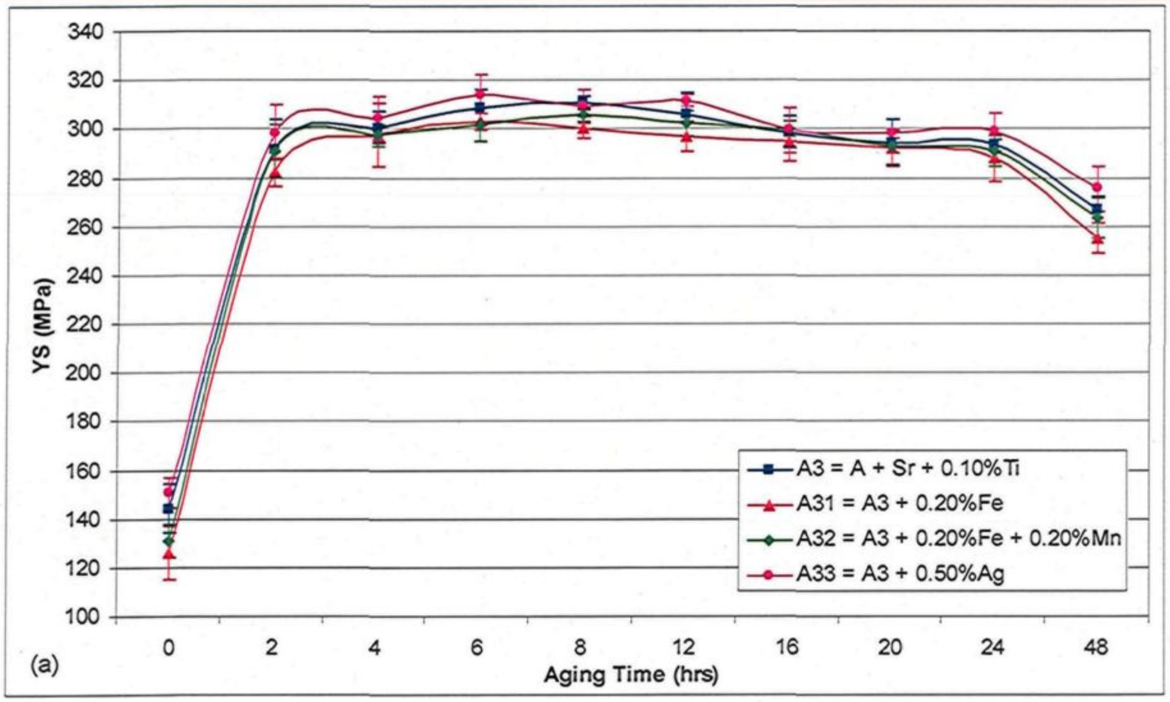

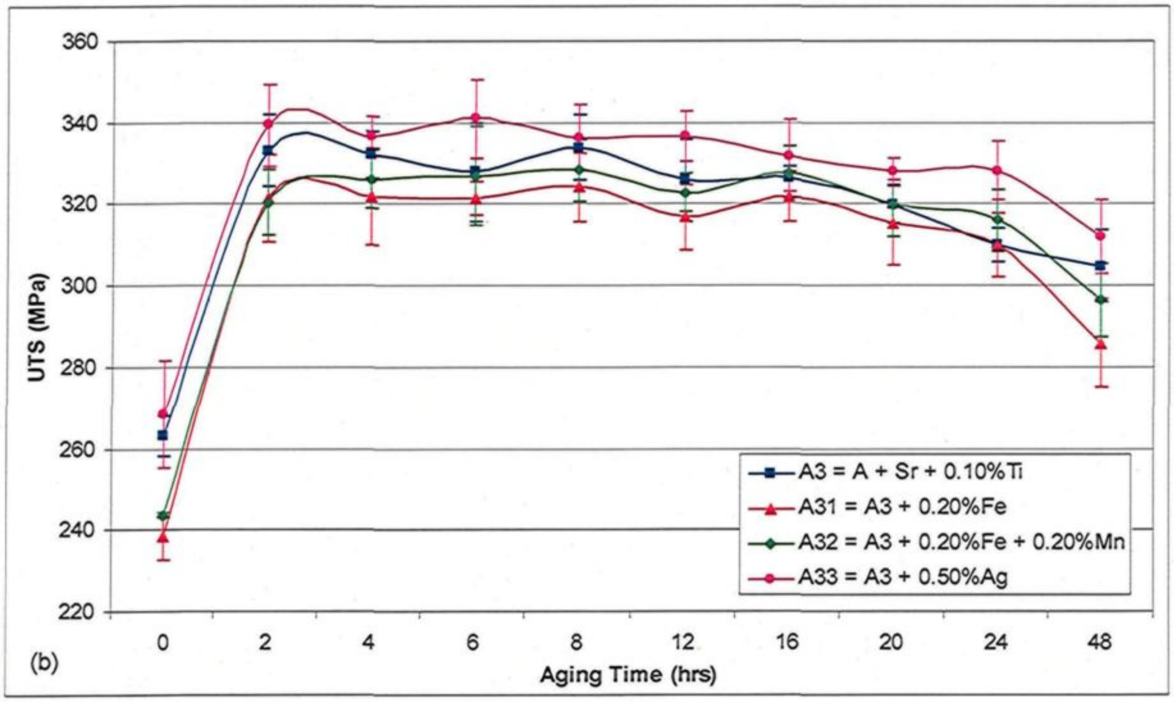

Figure 5.5 ⟶ **Continued**

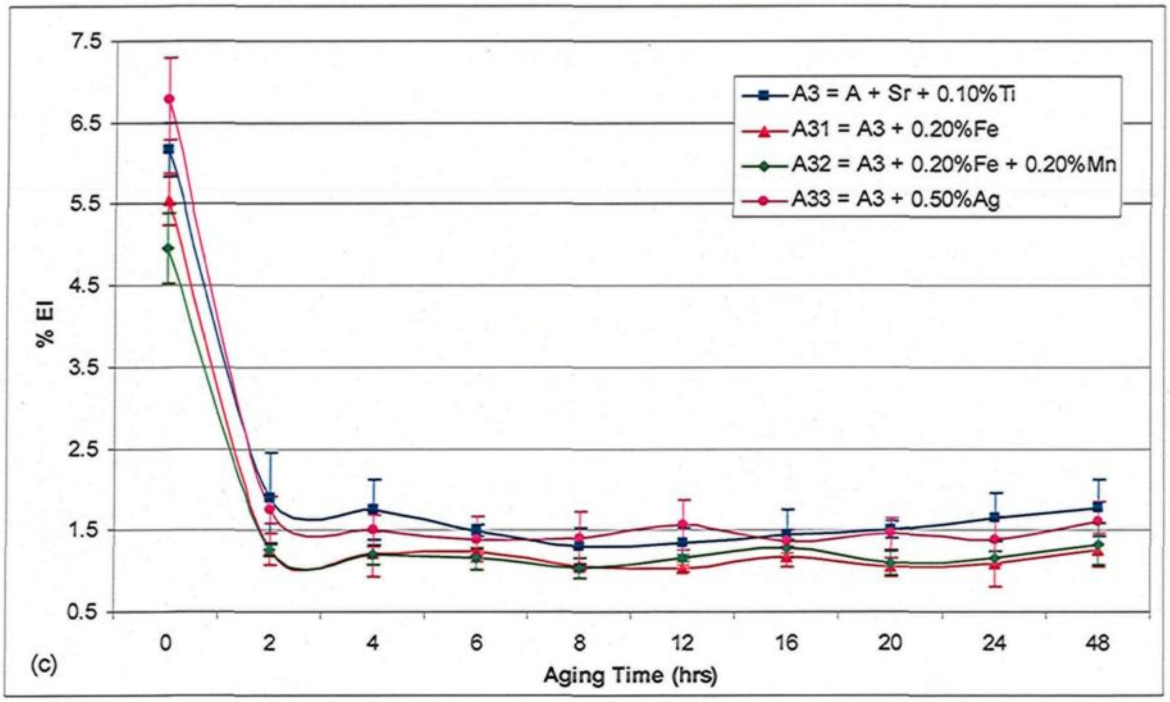

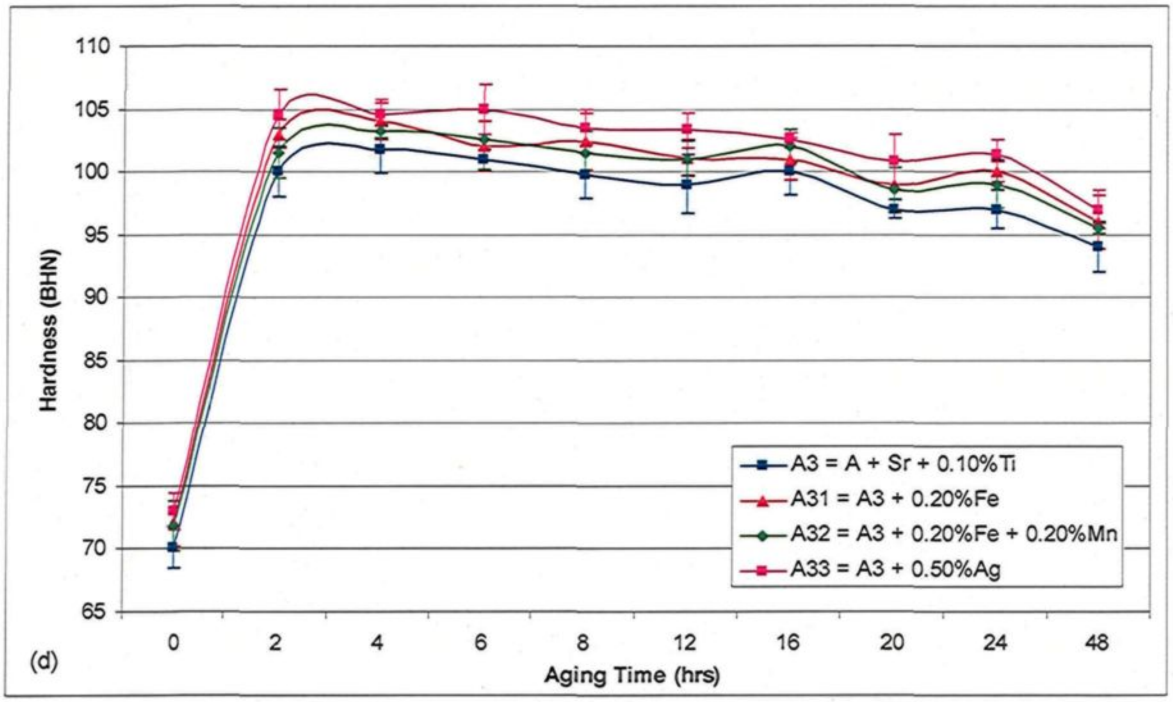

Figure 5.5 Variation in tensile properties and hardness values of Alloying Group II after aging at 180°C: (a) YS; (b) UTS; (c) %El; and (d) hardness values.

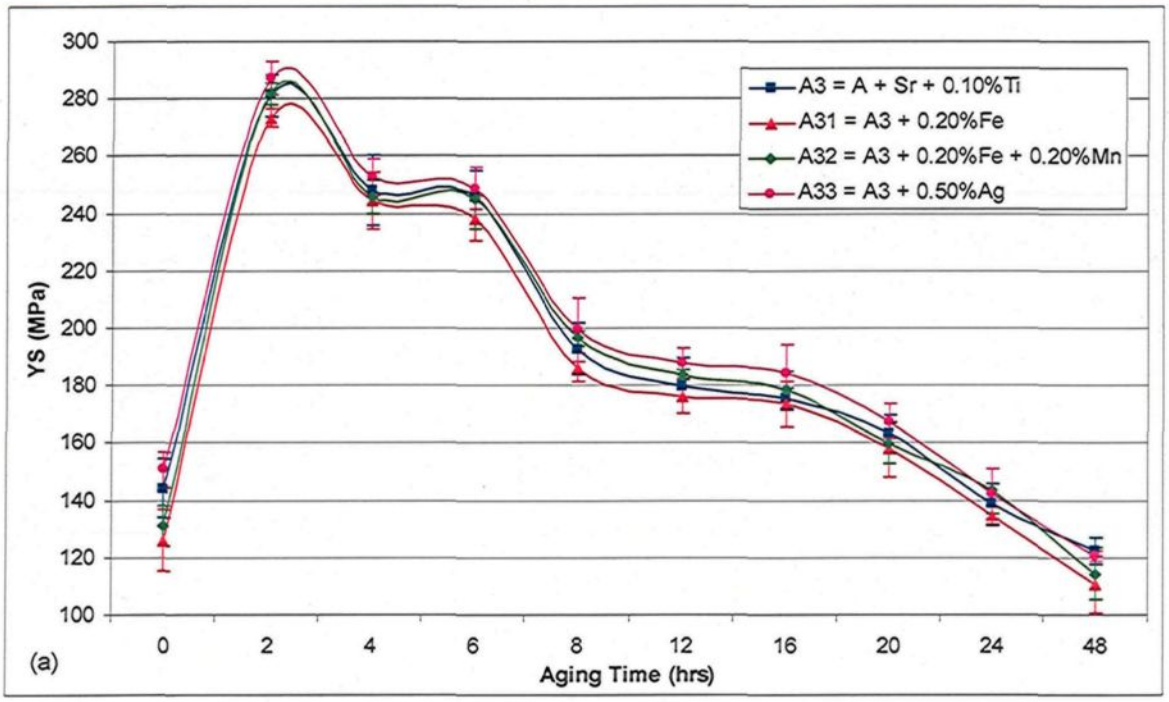

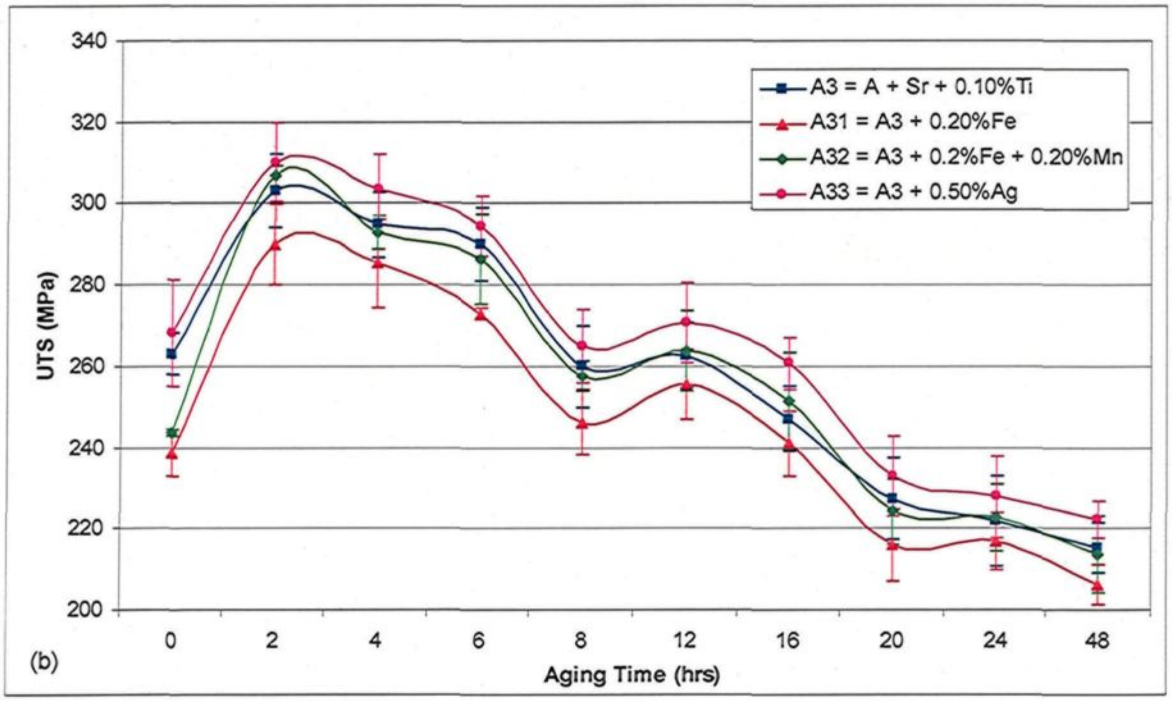

Figure 5.6 ⟶ Continued

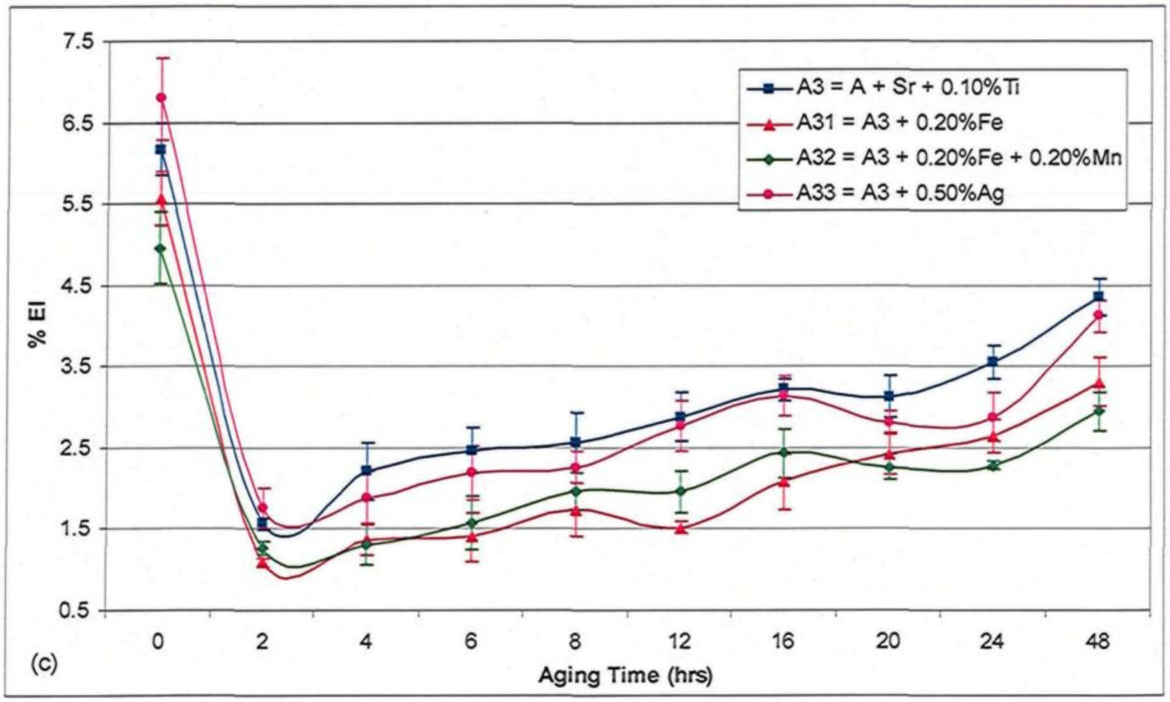

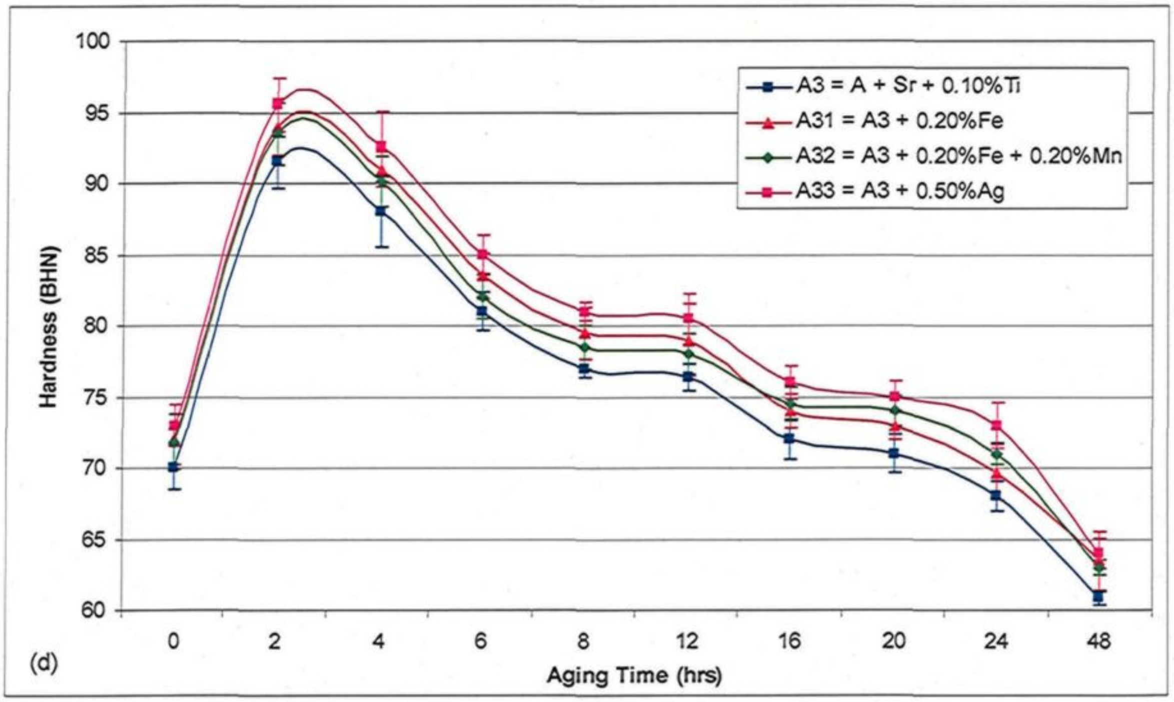

Figure 5.6 Variation in tensile properties and hardness values of Alloying Group II after aging at 220˚C: (a) YS; (b) UTS; (c) %El; and (d) hardness values.

increasing the iron content, as previously mentioned in the discussions on solution heat treatment and microstructure.

The subsequent addition of 0.2% Mn to the A31 alloy, producing the A32 alloy, seems to recover the YS and UTS values which were previously reduced by increasing the iron content in the A31 alloy. The %El and hardness values were not, however, markedly affected. The positive role of Mn in the promotion of the less harmful α-Fe Chinese-script phase instead of the brittle platelet-like β-Fe phase may explain the improvement caused in the YS and UTS values of the A32 alloy which was ascribable to the addition of Mn in spite of the preponderance of the former phase in the microstructure of the A31 alloy.

The addition of silver to the A3 alloy, producing the A33 alloy, did not in fact change the tensile properties or the hardness values in the as-cast condition. In the heat-treated conditions, however, the addition of silver did increase the strength properties and hardness values but not as originally expected. This situation may be attributed to the presence of Si in the base 220 alloy which favors the formation of the Mg-Si phases during the early stages of aging, in turn exhausting the supply of magnesium and reducing the number of Mg-Ag co-clusters known to act as nucleation sites for hardening precipitates, in particular, the Ω phase precipitates.[7,133]

Abis *et al.*[134] demonstrated that the addition of 0.15-0.5%Si to an Al-4.5%Cu-0.3%Mg-0.7%Ag alloy eliminates Ω precipitation at an aging temperature of 190°C. These researchers stated that the addition of Si inhibits the nucleation of Ω precursors which in turn leads to an enhancement in the precipitation of θ (Al_2Cu) and S (Al_2CuMg) phases. Gable *et al.*[135] showed that trace amounts of Si, depending on the Mg content, were responsible for limiting Ω precipitation in both Al-Cu-Mg and Al-Cu-Mg-Ag base alloys, and that a Mg/Si ratio of ~2.0 must be exceeded for Ω nucleation. It was also found that the addition of Ag to an Al-4.3%Cu-0.8Mg-0.7%Si, with a Mg/Si ratio of ~1.1, had little effect on age hardening.[73]

Matsuda *et al.*[78] found that the addition of Ag to the Al-Mg-Si alloy, containing Si content in excess of that required for Mg_2Si precipitates, did not produce any substantial improvement in age-hardening characteristics; the presence of Si was found to prevent the formation of Mg-Ag clusters which provide a large number of nucleation sites for fine and more dispersed β'' phase precipitates.[77] Mechanical testing at elevated temperatures may be recommended, so as to evaluate the mechanical properties of the A33 alloy; this should be carried out in view of the fact that the Ω phase, which favors precipitation at the expense of the θ (Al_2Cu) phase in the presence of Ag, was reported to improve the mechanical properties at higher temperatures.[136]

5.2.3 Effects of Free-Cutting Elements: Alloying Group III

The effects of the addition of free-cutting elements, namely Sn and Bi, as well as a combination of both, on the tensile properties and hardness of the Alloying Group III are shown in Figures 5.7(a) and 5.7(b), respectively, for the as-cast condition. These effects are also shown in Figures 5.8 and 5.9 for the T6 and T7 heat-treated conditions, respectively.

The addition of 0.15%Sn to the A4 alloy, producing the A41 alloy, causes a decrease in the strength properties and hardness values but increases the %El in the as-cast condition as a result of the softening effect of the soft Sn-bearing phases dispersed within

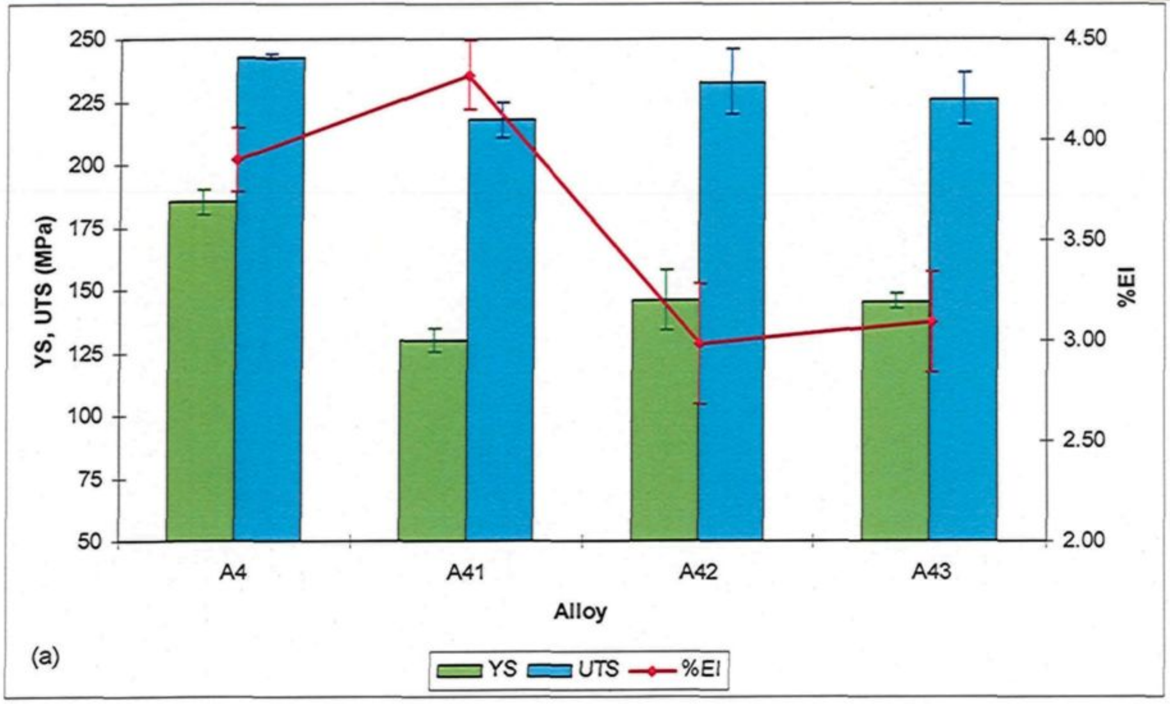

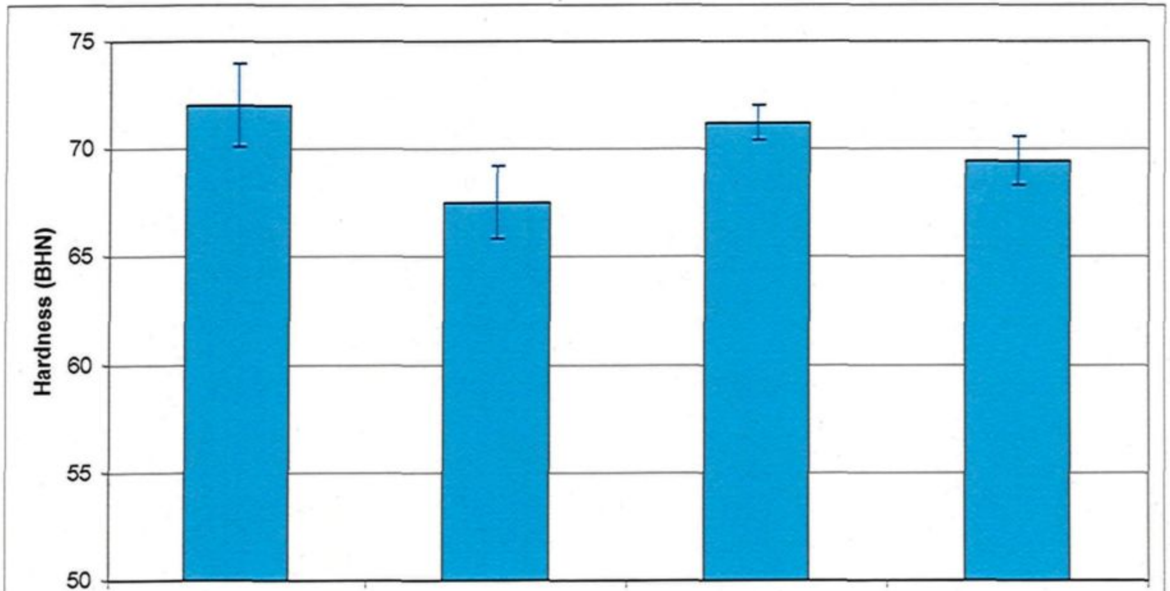

Figure 5.7 Variation in: (a) tensile properties (YS, UTS, and %El); and (b) hardness values of Alloying Group III in the as-cast condition.

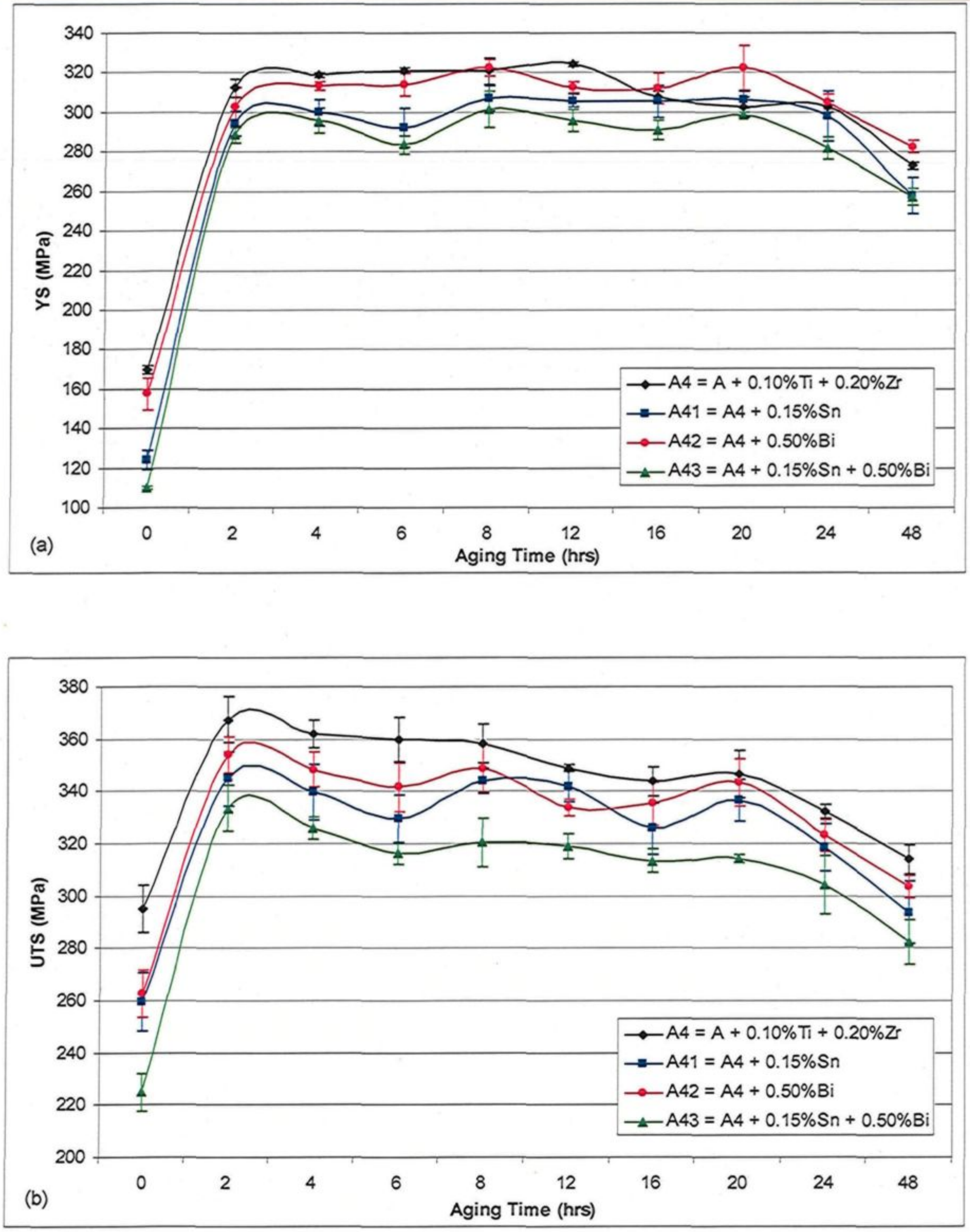

Figure 5.8 ⟶ **Continued**

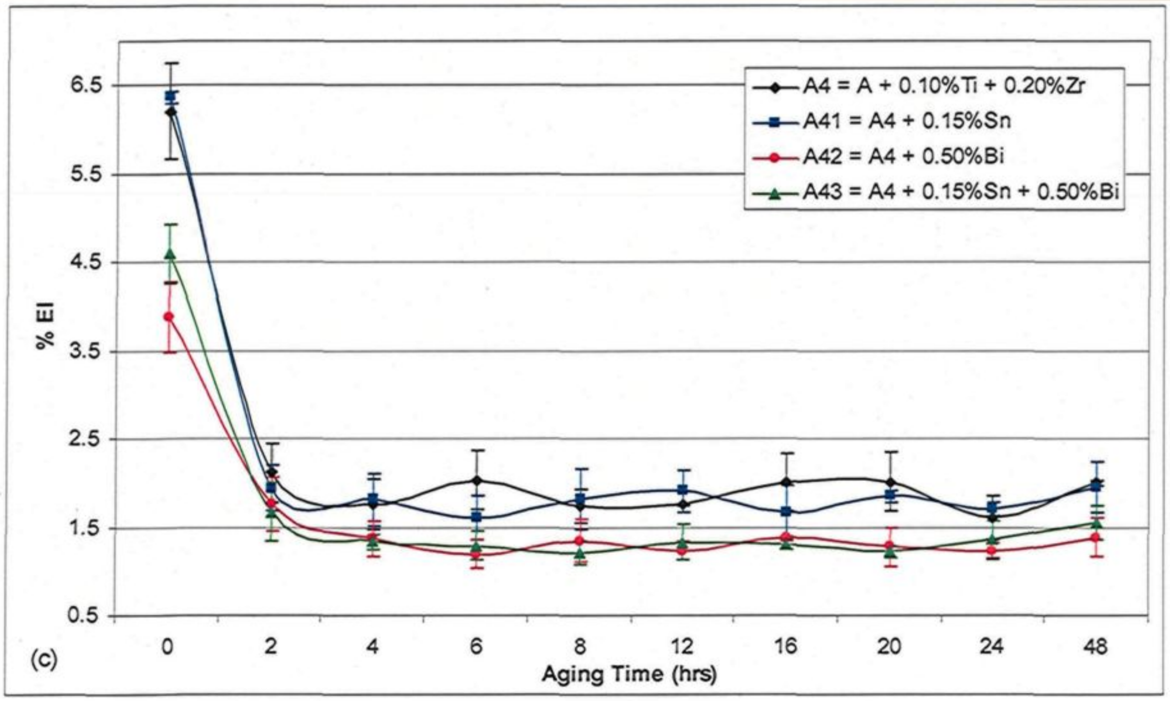

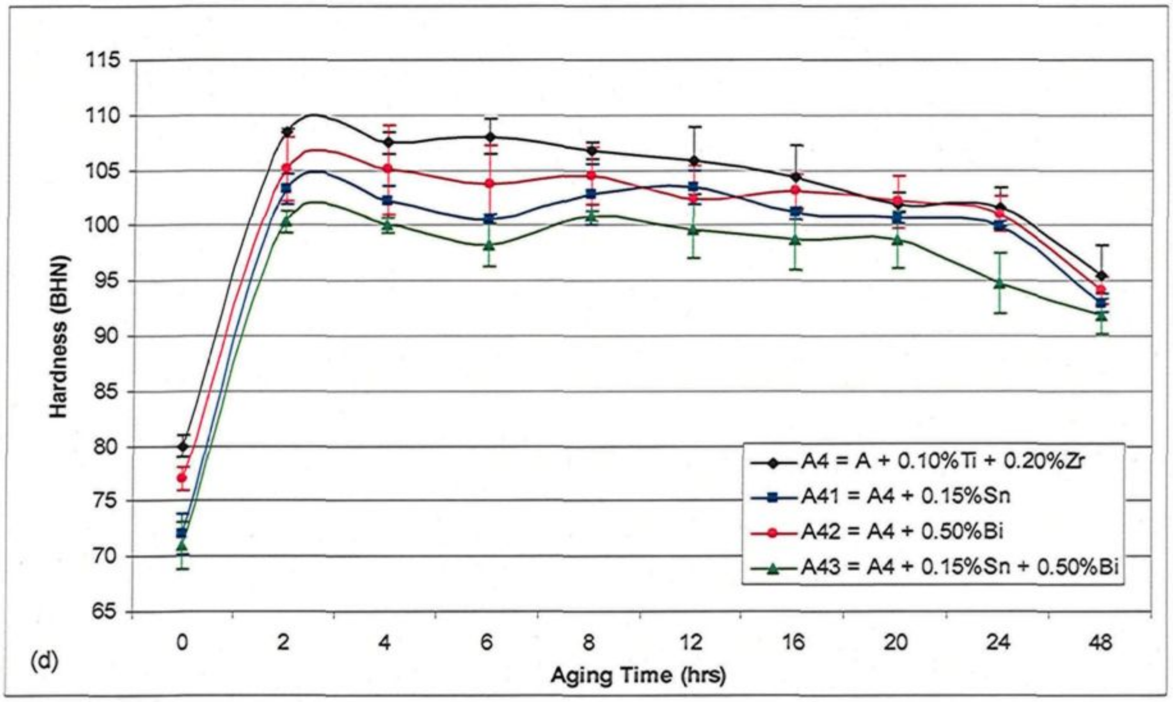

Figure 5.8 Variation in tensile properties and hardness values of Alloying Group III after aging at 180°C: (a) YS; (b) UTS; (c) %El; and (d) hardness values.

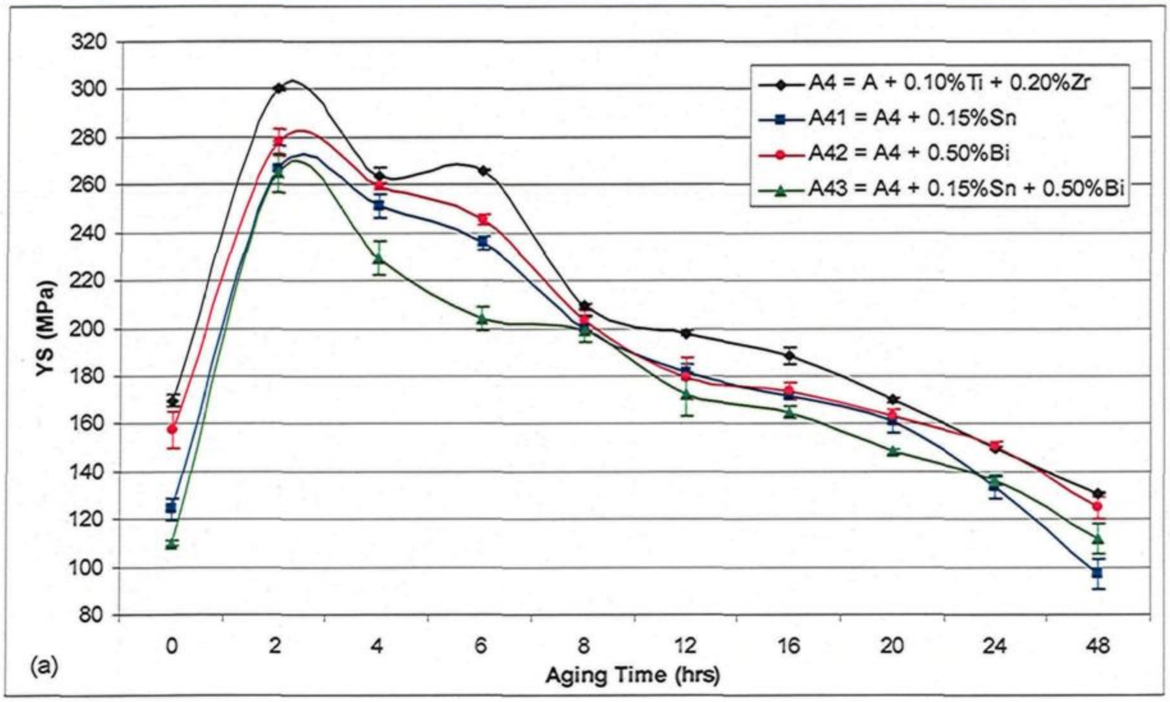

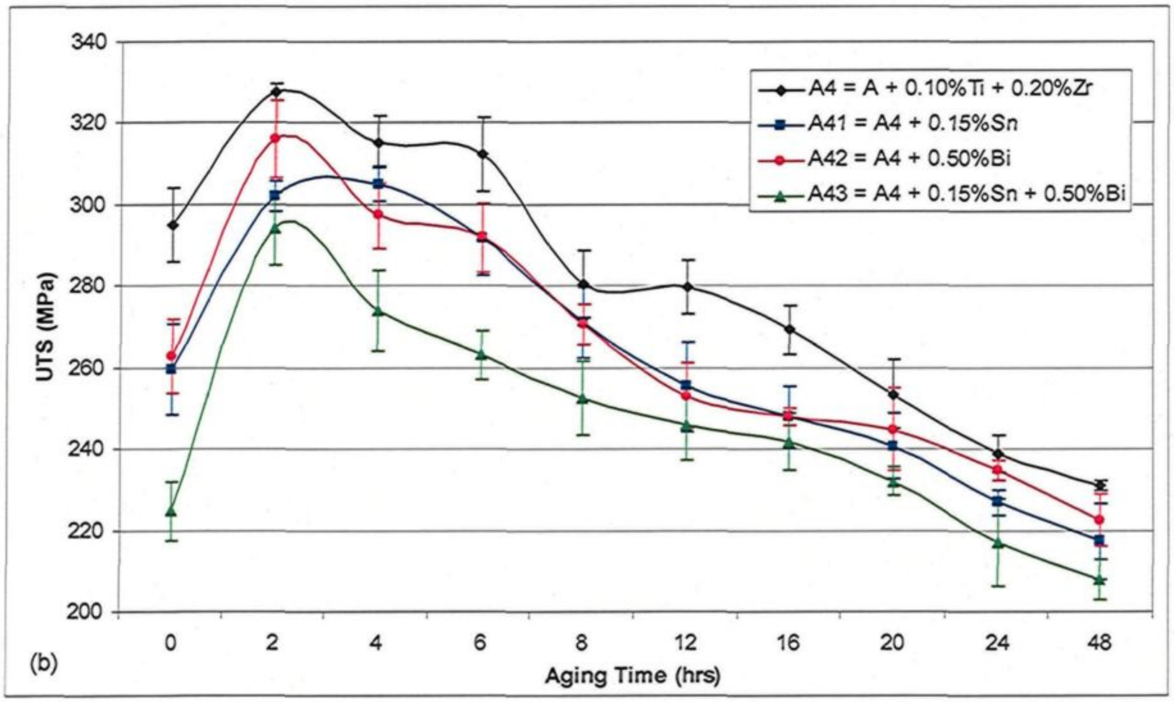

Figure 5.9 ⟶ **Continued**

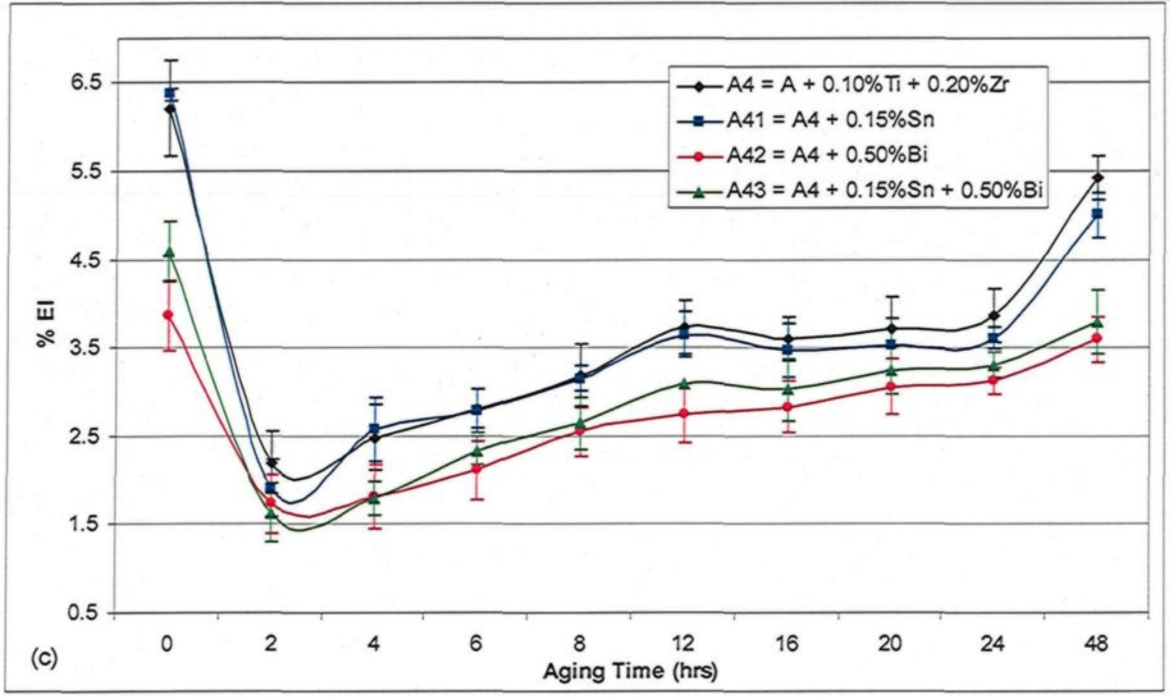

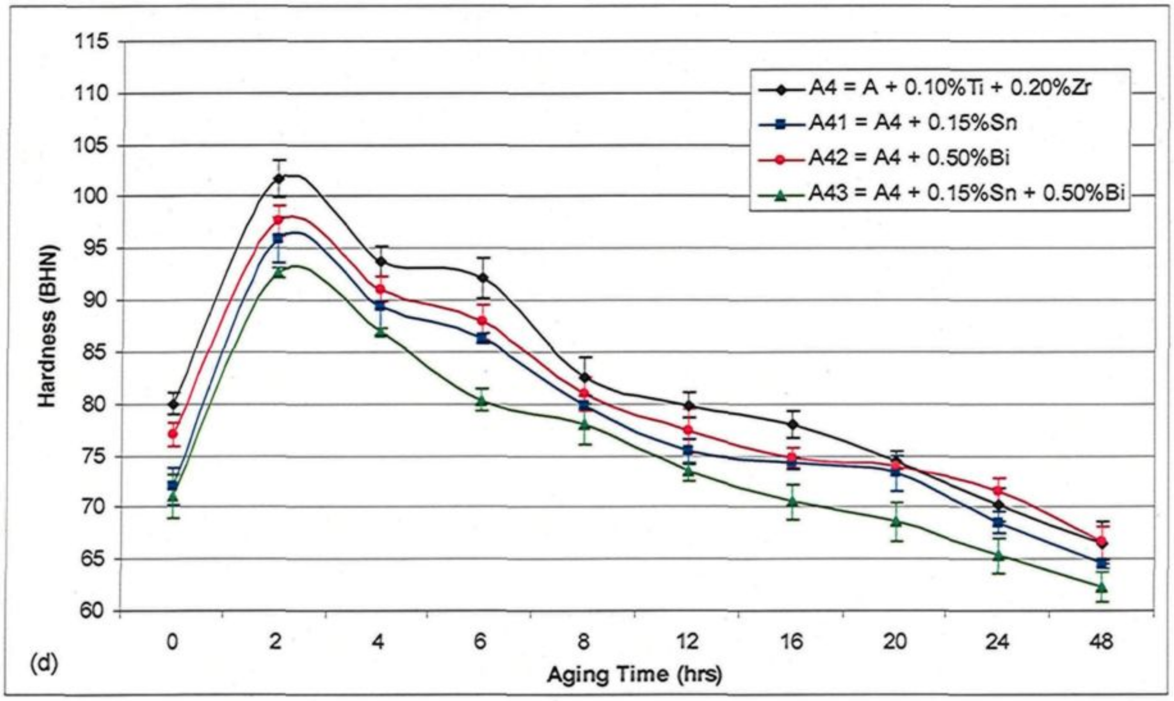

Figure 5.9 Variation in tensile properties and hardness values of Alloying Group III after aging at 220°C: (a) YS; (b) UTS; (c) %El; and (d) hardness values.

the alloy microstructure. In heat-treated conditions, the noticeable reduction occurring in the strength properties and hardness values of the Sn-containing A41 alloy may be explained in terms of the following effects, which were previously confirmed by an examination of the microstructure presented in Chapter 4: (i) the softening effect of the soft Sn-rich phases; (ii) the replacement of Si by Sn in Mg compounds, forming Mg_2Sn, which in turn diminishes the precipitation of the Mg_2Si and/or the $Al_5Mg_8Si_6Cu_2$ hardening phases; and (iii) the increase in the percentage porosity arising from the melting of the low melting point Sn-phases during solution heat treatment. It should be noted here that the increase in ductility resulting from the softening effect of the soft Sn-bearing phases may balance out the reduction caused by the increase in the percentage porosity, thus explaining why the ductility of the Sn-containing A41 alloy was not significantly affected by the addition of Sn in both T6- and T7-tempers for all the aging times applied.

The abovementioned effects were also confirmed by the work of Mohamed *et al.*,[137] who found that increasing the Sn content in B319.2 and A356.2 alloys decreases their mechanical properties in the heat-treated condition; this was ascribed to the increase in the percentage porosity resulting from the melting of β-Sn particles in the B319.2 alloy during solution heat treatment and the formation of Mg_2Sn in the A356.2 alloy which lessens the amount of Mg required for the formation of Mg hardening phases. Smolej *et al.*[125] demonstrated that the strength properties of AlCuMgSn alloys decreased with increasing Sn content and were lower in all cases in comparison with the standard AlCuMgPb alloy. These lower strength properties of the alloys containing Sn resulted from its distribution in the Al matrix and along the intermetallic phases thereby interrupting the homogeneity of the microstructure.

The bismuth-containing A42 alloy displays considerable deterioration in its tensile properties and hardness values in the as-cast and heat-treated conditions. The presence of Bi particles within the alloy microstructure reduces the tensile properties as reported by Hardy.[79] It is important to mention here that the effectiveness of Bi additions in improving the machinability of 6262 Al-Mg-Si alloys was found to be reduced by the loss of Bi in the formation of Bi_2Mg_3 particles.[138] The Bi-Mg-Sr interaction was also confirmed in research carried out by El Hadad.[90] Based on these preceding observations, it might be suggested that the reduction caused in the strength properties and hardness values of the A42 alloy in heat-treated conditions may be explained in terms of the Bi-Mg interaction which consumes the Mg available for the precipitation of Mg-hardening phases.

The deterioration occurring in the tensile properties and hardness values of the A43 alloy containing Sn and Bi in the as-cast and heat-treated conditions was fully expected in the light of the detrimental effects of the individual additions of Sn and Bi on the mechanical properties with regard to the A41 and A42 alloys, respectively. It may be concluded that the reductions caused in the values of the strength properties, YS and UTS, and the hardness as a result of the combined addition of Sn and Bi are approximately the sum of the reductions caused by the individual additions of these elements namely, the A41 and A42 alloys, respectively. Moreover, the %El values of the A43 alloy appear too close to those of the Bi-containing A42 alloy. This observation indicates that the %El of the A43 alloy was only reduced by the effects of Bi whereas Sn did not significantly affect the ductility for the same reason as that applied to the %El of the A41 alloy. The slight increase in the %El of the A43 alloy observed in the T7-tempered condition may be attributed to the fact that the detrimental effect of porosity arising from the melting of Sn was overridden by the beneficial softening effect of the soft Sn-rich phases.

5.3 EFFECTS OF HEAT TREATMENT

The precipitation-hardening characteristics of Al-Cu alloys containing Si and Mg often appear to be quite complex. This particularity may be attributed to the formation of several hardening phases including θ' (Al_2Cu), β'' (Mg_2Si), S' (Al_2CuMg) and the quaternary phase which is designated Q ($Al_5Mg_8Si_6Cu_2$) or λ ($Al_5Mg_8Si_5Cu_2$).[53,54] It may thus to be expected that the best combination of mechanical properties will be obtained when all these precipitates are present.

The precipitation-hardening characteristics of the alloys prepared in this study can be understood by investigating the curves representing the tensile properties and hardness values shown in Figures 5.2, 5.5 and 5.8, and in Figures 5.3, 5.6 and 5.9, corresponding to aging at 180°C and 220°C, respectively. It will be observed that all the alloys studied display almost the same hardening trend with the progress of aging time for both 180°C and 220°C tempers, regardless of the additives introduced. Age-hardening at 180°C results in alloy-hardening with aging for times ranging from 2 to 16 hours, whereas age-hardening at 220°C causes overaging and alloy-softening after 2 hours of aging. In the 180°C temper, the alloys attain the highest hardness peak after 2 hours of aging with a satisfactory age-hardening ability, *ΔBHN*, of 30 BHN calculated using the following equation:[139]

$$\Delta BHN = BHN_{\max} - BHN_{\mathrm{SHT}} \tag{5.1}$$

where $BHN_{\max}$ is peak hardness and BHN_{SHT} is the hardness value corresponding to the solution heat treated condition. It is important to note also that applying the 180°C temper for aging times ranging from 2 to 8 hours, may be a recommendable strategy for the new 220 based-alloys under investigation in order to maintain a satisfactory compromise between strength and ductility.

Field emission scanning electromicroscopy was carried out on A4 alloy samples cut from tensile test bars corresponding to different aging conditions with the aim of investigating the evolution in size, shape, and density of θ-Al_2Cu phase precipitates throughout the course of the aging process. Aging at 180°C for 2 hours resulted in densely dispersed fine precipitates approximately 25 to 100 nm in diameter, as shown in Figure 5.10(a). Increasing the aging time to 48 hours at 180°C did not significantly alter the size or the density of the precipitates, as may be seen from Figure 5.10(b). As will be observed, in this aging condition, the diameter of the precipitates ranges from 45 to 130 nm. Figure 5.10(c) reveals that aging at 220°C for 2 hours seems to have the same effect as aging at 180°C for 48 hours with regard to the characteristics of the precipitates; the precipitates are approximately 40 to 100 nm in diameter. Prolonged aging at 220°C for 48 hours coarsens the precipitates thereby increasing their diameter to a range of between 60 and 160 nm, as shown in Figure 5.10(d).

The presence of a number of hardening phases in the Al-Cu-Si-Mg alloy system, including θ (Al_2Cu), β (Mg_2Si), and Q ($Al_5Mg_8Si_6Cu_2$), which need not all yield to

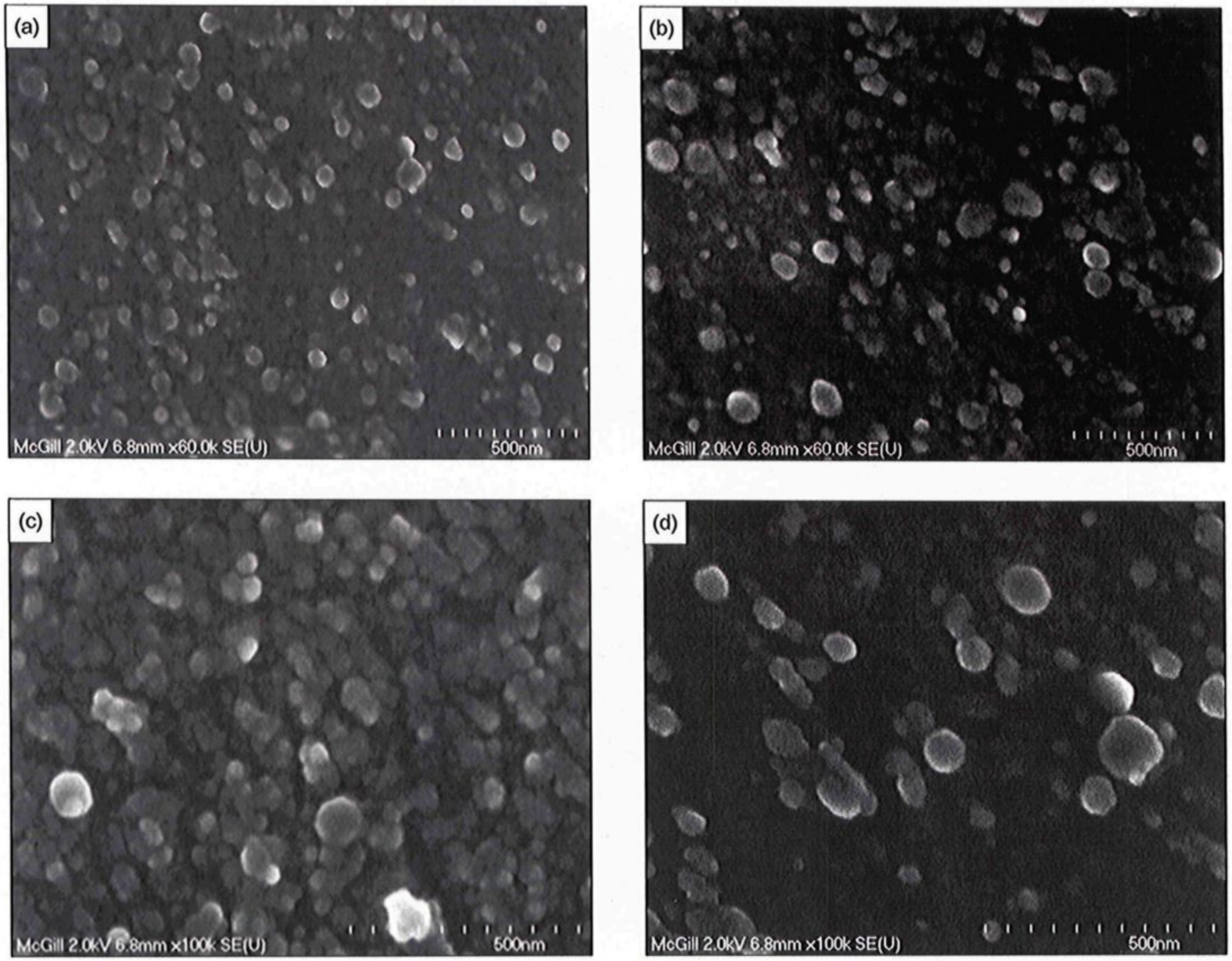

Figure 5.10 Field emission scanning electron micrographs obtained from A4 alloy samples: (a) aged at 180°C for 2 hours; (b) aged at 180°C for 48 hours; (c) aged at 220°C for 2 hours; (d) aged at 220°C for 48 hours.

coarsening simultaneously, may explain why the strength properties and hardness values of the 220 based-alloys remain at high levels without any significant decline for up to 16 hours of aging at 180°C. Kang *et al.*[139] observed that both the plate-like θ' (Al_2Cu) and the needle-like λ' ($Al_5Mg_8Si_5Cu_2$) precipitates were contained in the peak-aged specimens of Al-7.15%Si-2.8%Cu-0.43%Mg alloy. Moreover, the precipitation of the λ' phase was found to improve the age-hardening ability, since this phase precipitates homogeneously in α-Al contrary to the θ' phase which precipitates preferentially on the dislocations around eutectic Si particles. Wang *et al.*[140] demonstrated that, with regard to the Al-8%Si-1%Cu-0.4%Mg alloy, age-hardening was caused by the precipitation of the dot-shaped Q'' phase which is the precursor of the Q phase. For the Al-8%Si-3%Cu-0.4%Mg alloy, age-hardening resulted from the co-precipitation of the dot-shaped Q'' phase and the rod shaped θ' phase.

5.4 EVALUATION OF THE ALLOY QUALITY

The applicability of the quality index concept proposed by Drouzy *et al.*[93] for Al-7%Si-Mg alloys was examined by Din *et al.*[141] with regard to Al-Cu alloys, specifically A201 and A206 alloys. It was concluded that this concept did not apply to A201 and A206 alloys in any analogous manner, nor is it transferable at the present time. In another study, Cáceres *et al.*[142] demonstrated that when the A201 alloy is aged, a plot of tensile strength *versus* elongation to fracture follows a circular pattern; this is in contrast with Al-Si-Mg alloys, which show a linear relationship between these two parameters when aged. The latter observation is the basis for the quality index concept of Drouzy and co-workers which does not seem to be valid for alloy A201.

The plot of the tensile strength *versus* the elongation to fracture prepared for the alloys introduced in the present study as well did not show the linearity observed for Al-Si-Mg type alloys. This observation implies that the quality index (*Q*) proposed by Drouzy *et al.*[93] is not applicable to the 220 based-alloys under investigation. On the other hand, the universal applicability of Equations (2.8) and (2.11) which were used to draw the *"iso-YS"* lines and "*iso-q*" lines, respectively, of the quality map introduced by Cáceres[95-97] makes it possible to use this map to assess the quality of the 220 based-alloys. The alloy quality will be expressed by the relative ductility parameter, *q*, based on the correlation between the "*iso-q*" lines of Cáceres' map and the "*iso-Q"* lines of Drouzy's map, as previously explained in Subsection 2.3.2.

5.4.1 Methodology for Constructing the Quality Maps

The quality maps of the alloys prepared for this study which were constructed on the basis of Cáceres' model, are shown in Figure 5.11 to 5.16. As will be observed, each alloying group has two maps corresponding to both 180°C and 220°C tempered conditions. The methodology used to construct each of these maps is as follows:

1) Transforming the engineering stress-strain curves of each alloy composition studied into the equivalent true stress-strain curves. Each of these engineering stress-strain curves corresponds to the average of five curves obtained from the tensile testing of five tensile bars representing the alloy composition under consideration at one of the aging times of the abovementioned tempered conditions.

2) Calculating the parameters of the true stress-strain curves obtained in Step (1), namely, the strength coefficient of the material, K, and the strain-hardening exponent, n.
3) Determining K and n for each alloy composition as the mean values calculated over the respective values corresponding to the aging times of 180°C or 220°C tempers.
4) Calculating the K-value for each alloying group as the average of the K-values of the alloys involved in such group.
5) Substituting the K-value in Equation (2.8) and (2.11) to plot the families of the *"iso-YS"* lines and "*iso-q*" lines, respectively, of the quality map under construction for the given values of the strain-hardening exponent, n, engineering strain, s, and relative ductility, q.
6) Locating the data points of each alloy composition on the relevant quality map. Each point represents the UTS and %El values of that alloy composition at a specific aging time of a particular tempered condition. Note that some points were omitted from the map for the purpose of finding a certain trend which may describe the relationship between the UTS and %El in a common manner for all the alloy compositions studied.

5.4.2 Effects of Additives on Alloy Quality

As mentioned earlier, the quality of the alloys presented in this study will be expressed by the relative ductility parameter, q. The higher the q-value, the higher the combination of both UTS and %El, or, in Drouzy's terms, the higher the Q-value. High q-

value lines are close to the upper right hand corner of Cáceres' quality map, as previously shown in Figure 2.11.

The quality maps of the melt treatment group are shown in Figures 5.11 and 5.12 for the 180°C and 220°C tempers, respectively. It will be observed that the A4 alloy containing the combination of TiB_2 and Zr displays the best alloy quality of the alloys in the melt treatment group. This alloy possesses a q-value ranging from 0.60 to 0.27 in the 180°C tempered condition and from 0.65 to 0.29 in the 220°C tempered condition. The Sr-modified A1 alloy and the grain-refined A2 alloy display comparable alloy quality, particularly in the 220°C tempered case. This observation indicates that the increase in the %El caused by Sr addition, namely A1 alloy, may balance out the increase in the UTS caused by the addition of TiB_2, namely A2 alloy, with regard to the alloy quality so that both alloys end up having the same combination of strength and ductility. The base A alloy and the modified grain-refined A3 alloy also display comparable alloy quality. In spite of the fact that A alloy has higher UTS values compared to the A3 alloy, the slight improvement caused in the %El of the latter alloy raises its quality to approximately the same level as that of the A alloy. This observation may suggest the fact that the alloy quality is more susceptible to the changes occurring in the %El than those which occur in the UTS.

The quality maps of the iron intermetallics and hardening alloying elements group are shown in Figures 5.13 and 5.14 for the 180°C and 220°C tempers, respectively. It will be observed that the A31 and A32 alloys with higher Fe and Fe + Mn content, respectively, display the least desirable alloy quality of all the alloys studied. The A31 alloy has a

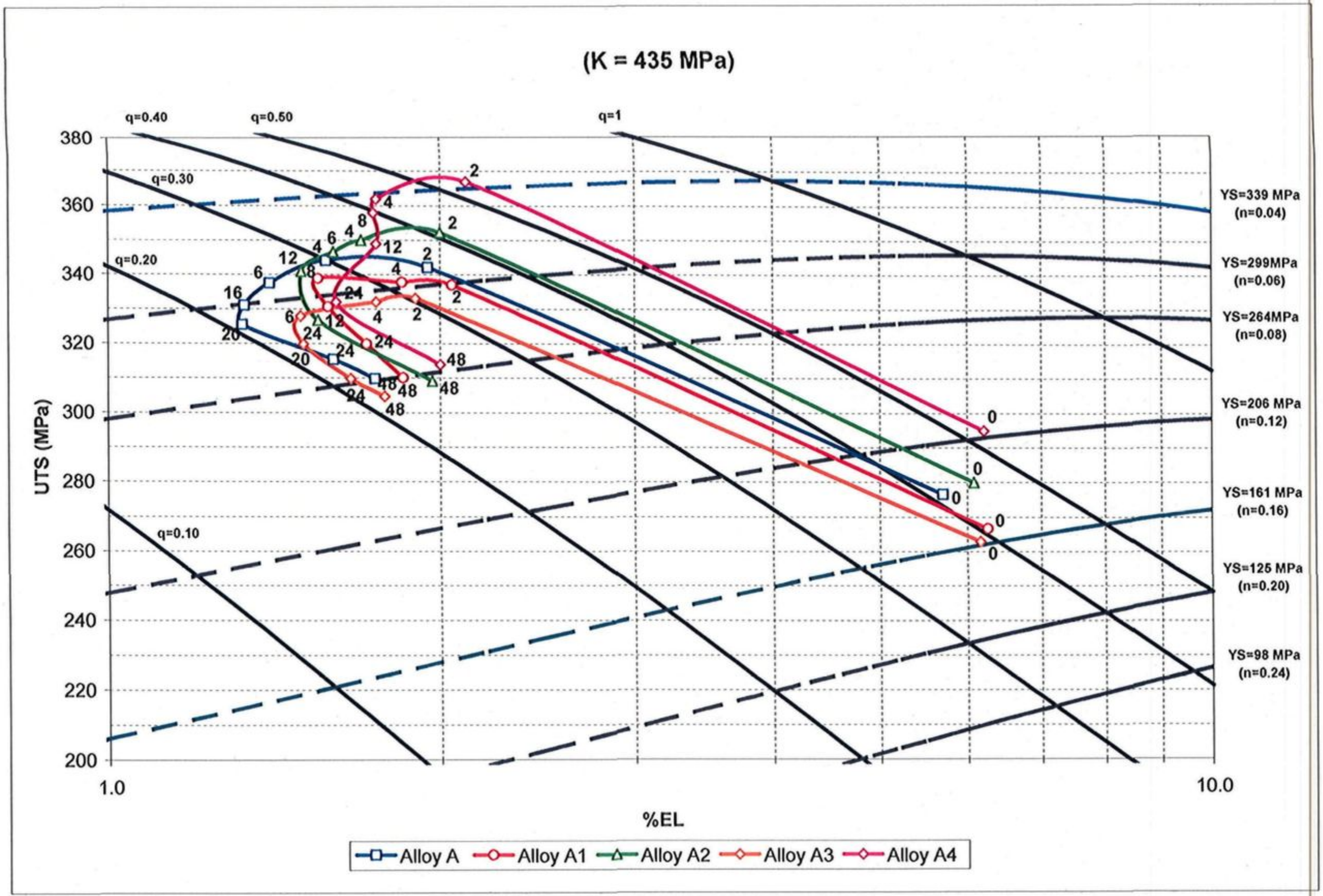

Figure 5.11 Quality map showing the relationship between UTS and %El for the alloys of Alloying Group I aged at 180°C for various aging times.

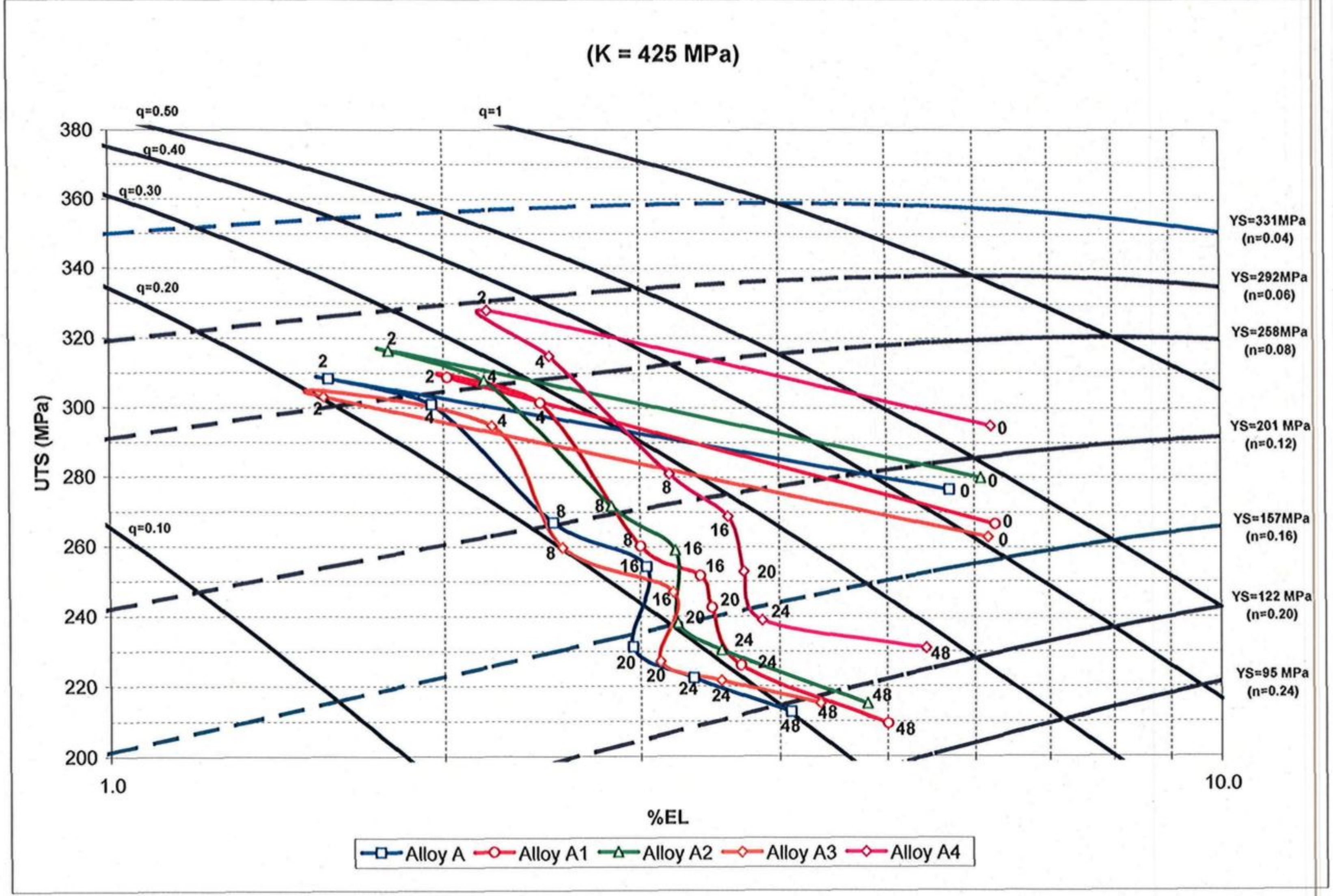

Figure 5.12 Quality map showing the relationship between UTS and %El for the alloys of Alloying Group I aged at 220°C for various aging times.

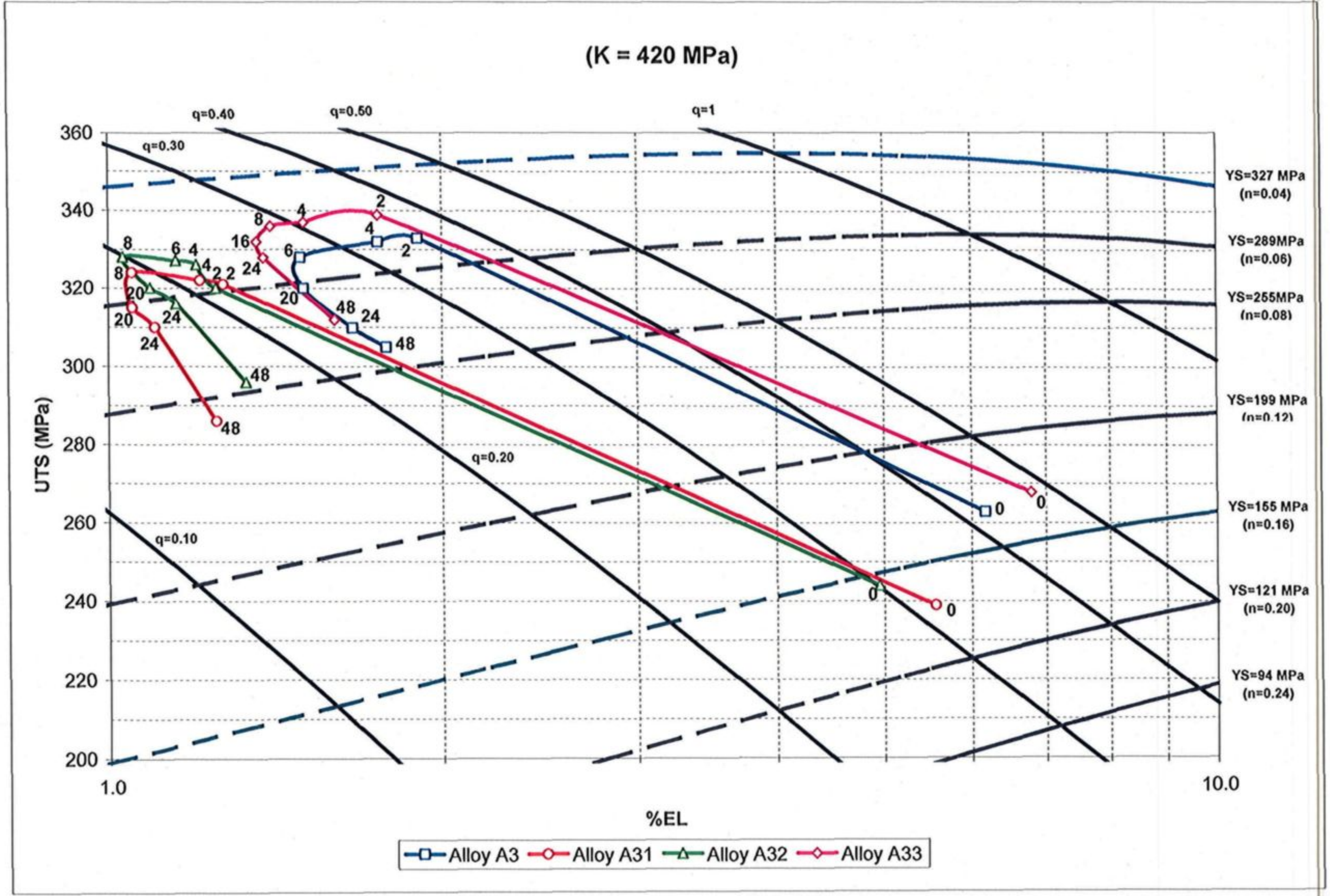

Figure 5.13 Quality map showing the relationship between UTS and %El for the alloys of Alloying Group II aged at 180°C for various aging times.

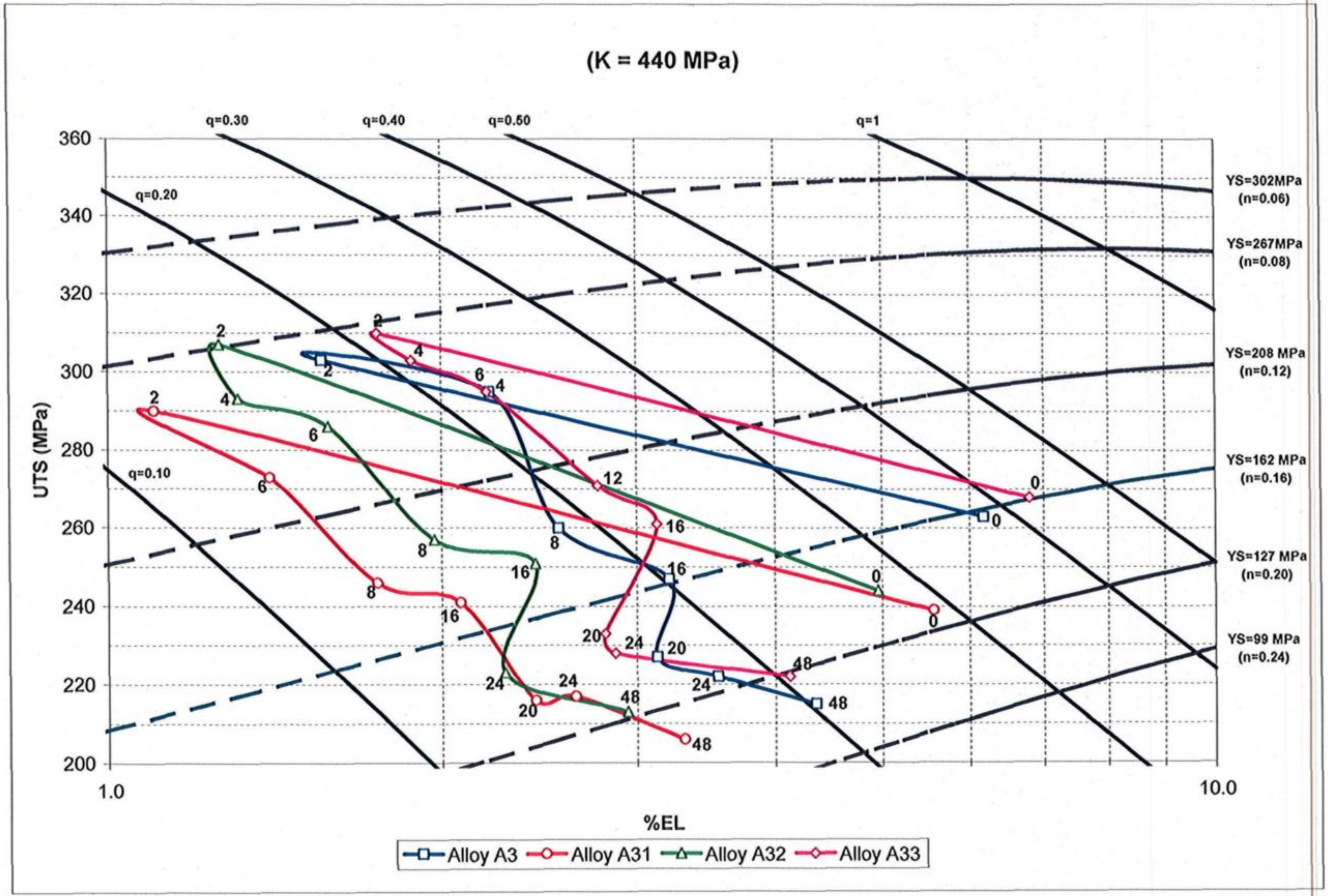

Figure 5.14 Quality map showing the relationship between UTS and %El for the alloys of Alloying Group II aged at 220°C for various aging times.

~~q-value ranging from 0.31 to 0.15 in the 180°C tempered condition and from 0.29 to 0.16 in~~ the 220°C tempered condition, whereas for the A32 alloy this value ranges from 0.30 to 0.18 and from 0.29 to 0.16 in the two respective conditions. The deterioration observed in the q-value of each of these alloys can undoubtedly be attributed to the negative effects of iron with respect to the tensile properties, particularly ductility. Addition of Ag, producing A33 alloy, did not bring about any considerable change in alloy quality. This finding may be interpreted in terms of the fact that the increase in the UTS caused by the addition of Ag was dampened by the associated reduction in the %EL and thus the alloy quality was ultimately not affected by this addition.

The quality maps for the free-cutting elements group are illustrated in Figures 5.15 and 5.16 for the 180°C and 220°C tempers, respectively. It will be observed that each of the A41 and A42 alloys displays an alloy quality which is lower than that of the reference A4 alloy; this can be ascribed to the reduction in the tensile properties of these alloys resulting from the addition of Sn and Bi, respectively. The A41 alloy in which the %El was not significantly affected by Sn addition, however, has a q-value which is higher than that of the Bi-containing A42 alloy. The aggregated deterioration previously observed in the tensile properties of the A43 alloy caused by the combined addition of Sn and Bi makes this alloy one of the least desirable of the alloys studied in terms of alloy quality. This alloy possesses a q-value ranging from 0.24 to 0.18, and from 0.23 to 0.19, in the 180°C and 220°C tempered conditions, respectively.

It is interesting to note, with regard to the quality maps discussed above, that the curves representing the UTS-%El relation have the tendency to follow a reversible path,

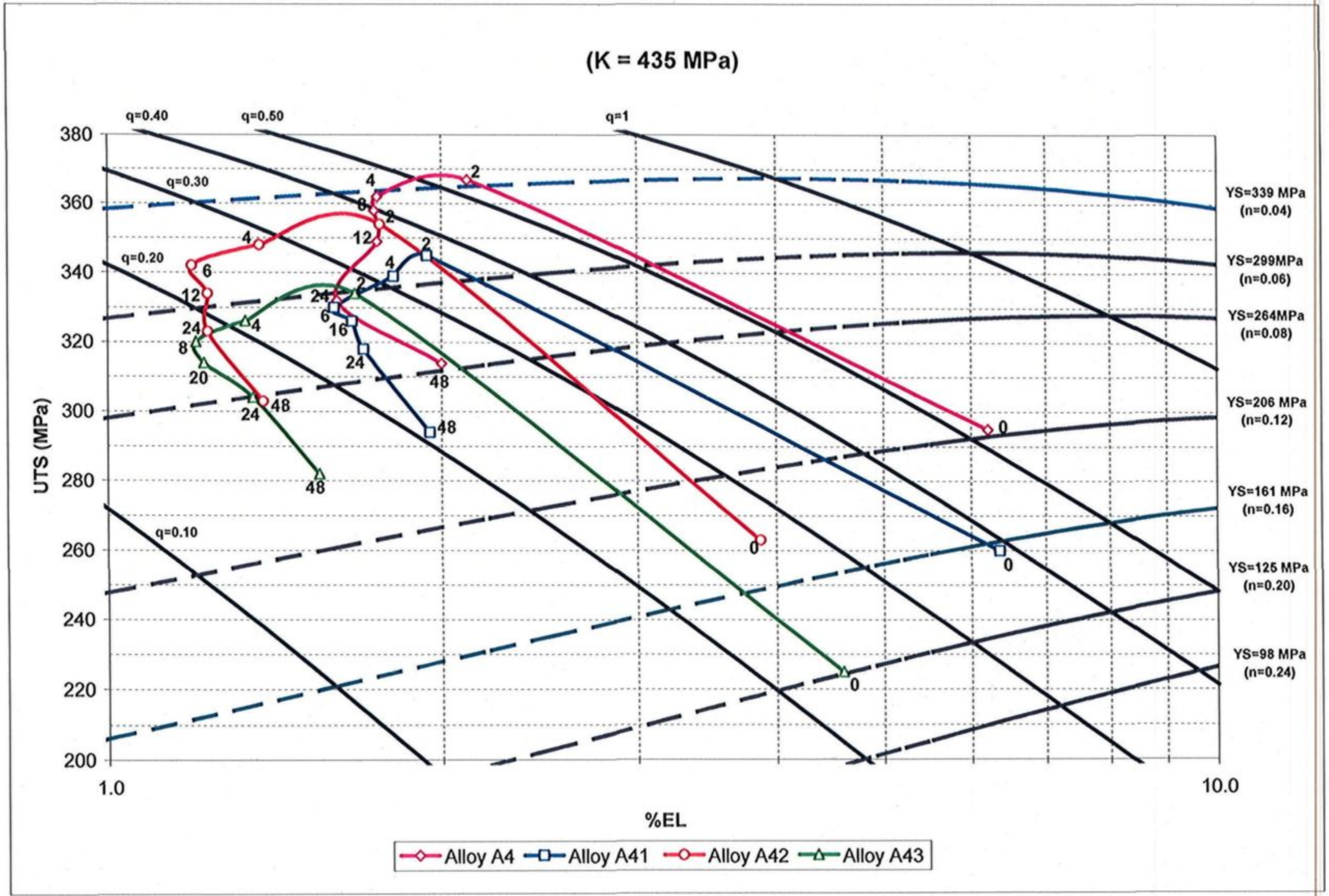
(K = 435 MPa)

Figure 5.15 Quality map showing the relationship between UTS and %El for the alloys of Alloying Group III aged at 180°C for various aging times.

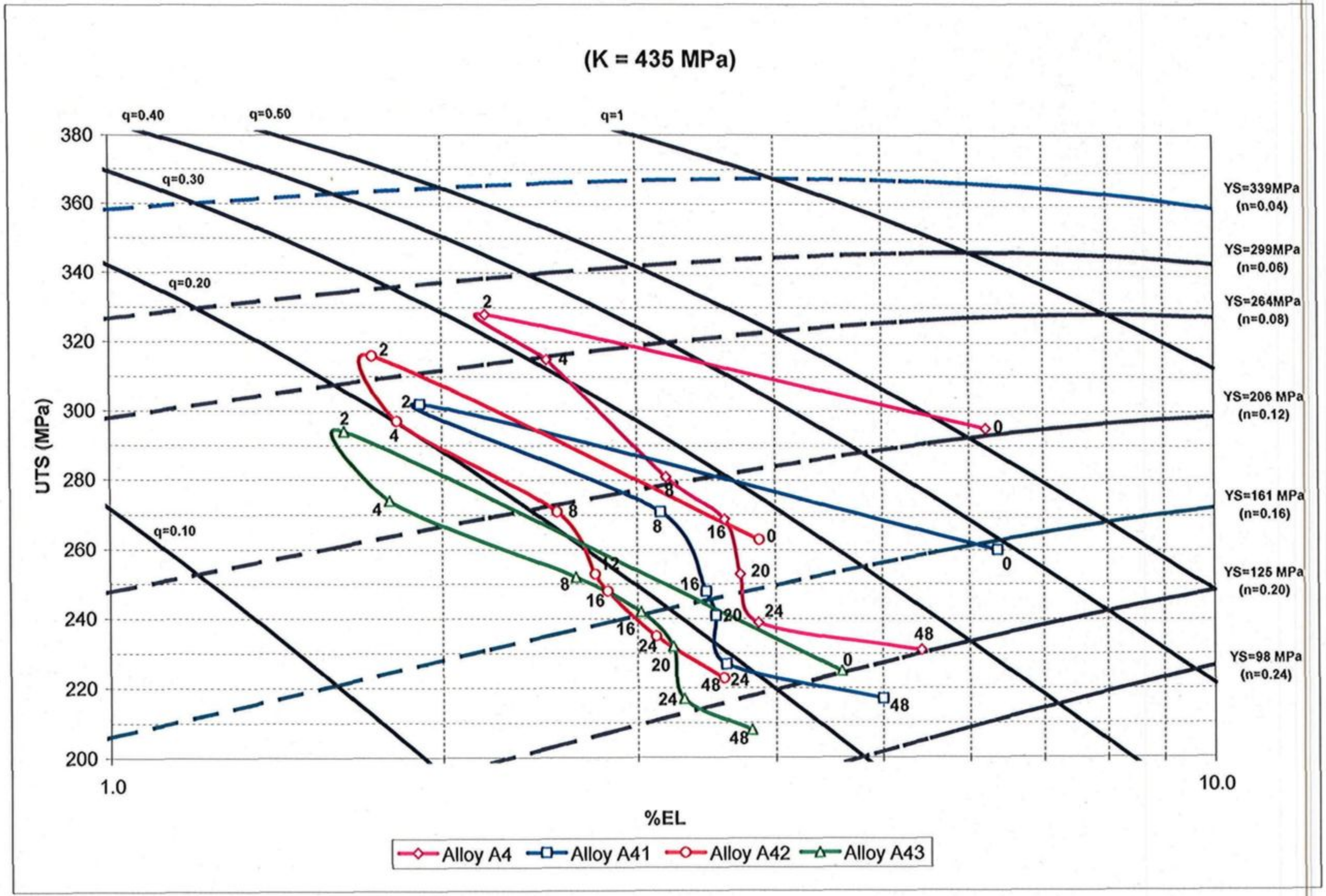

Figure 5.16 Quality map showing the relationship between UTS and %El for the alloys of Alloying Group III aged at 220°C for various aging times.

~~and thus the alloys may regain their as-cast properties after prolonged aging times. This~~ tendency results from the transition from the high q-value in the underaged and peak aged conditions to the lower q-value associated with the overaged condition. Din *et al.*[141] and Cáceres *et al.*[142] concluded for both A201 and A206 alloys that the plot of the tensile strength *versus* the elongation to fracture comes full circle after long aging times so that the property combination displayed by the original as-cast alloys is reproduced.

5.5 EFFECTS OF ADDITIVES ON THE IMPACT PROPERTIES

Toughness is a measure of the amount of energy a material can absorb before fracturing. It thus becomes important from an engineering point of view that the ability of a material to withstand an impact load without fracturing be considered. The broader applications of Al casting alloys may be impeded by their low fracture toughness which originates in the microstructure of these alloys, and is influenced by the α-Al dendrite arm spacing and grain size. Any improvement occurring in impact toughness will necessarily be dictated by type, shape, size, and distribution of second-phase particles present in the alloy microstructure.[143,144] This section will discuss the effects of additives which were introduced for the purposes of the current study regarding the relevant aspects of impact properties.

The effects of additives on the impact energies of the Alloying Groups I, II, and III are illustrated in Figures 5.17, 5.18, and 5.19, respectively, for both 180°C and 220°C tempers. The values for the crack initiation energy, E_i, and the total absorbed energy, E_t, were plotted simultaneously on the same graph in order to facilitate deducing the crack propagation energy E_p from their difference. The most common feature observed for all the alloy conditions studied is that the impact energies vary over aging time according to a similar trend to that displayed by the %El. Moreover, these impact energies are not significantly affected by aging time in the 180°C tempered condition. On the contrary, the softening effect associated with the 220°C tempered condition causes a proportional increase in the impact energy values in line with the progress of aging time.

With regard to the melt treatment group, it will be observed that the grain refining action resulting from the combined addition of TiB_2 and Zr, namely the A4 alloy, produces the highest values of impact energies in this alloying group. The improvement observed in the impact toughness of the Sr-containing A1 and A3 alloys is attributed to the positive role played by Sr in refining the morphology of α-Fe phase particles as previously explained for the effects of Sr addition on the %El; the improvement in this case, however, is more pronounced than that observed for %El. Richard[145] indicated that impact energy values of the Al-Si alloys are more sensitive to the minimal variations in the microstructure than the tensile properties. Calculating the difference between the total absorbed energy, E_t, and the crack initiation energy, E_i, for the alloys involved in the melt treatment group reveals that the crack propagation energy, E_p, is not significantly affected by the additives introduced.

Results obtained from the evaluation of the fracture toughness of the Alloying Group II shows that increasing the Fe content, either individually or in combination with Mn, producing A31 and A32 alloys, respectively, leads to a drastic reduction in the impact energies of these alloys. The crack initiation energy of the A31 alloy was reduced over aging time for the 180°C and 220°C tempered conditions by 29% and 33%,

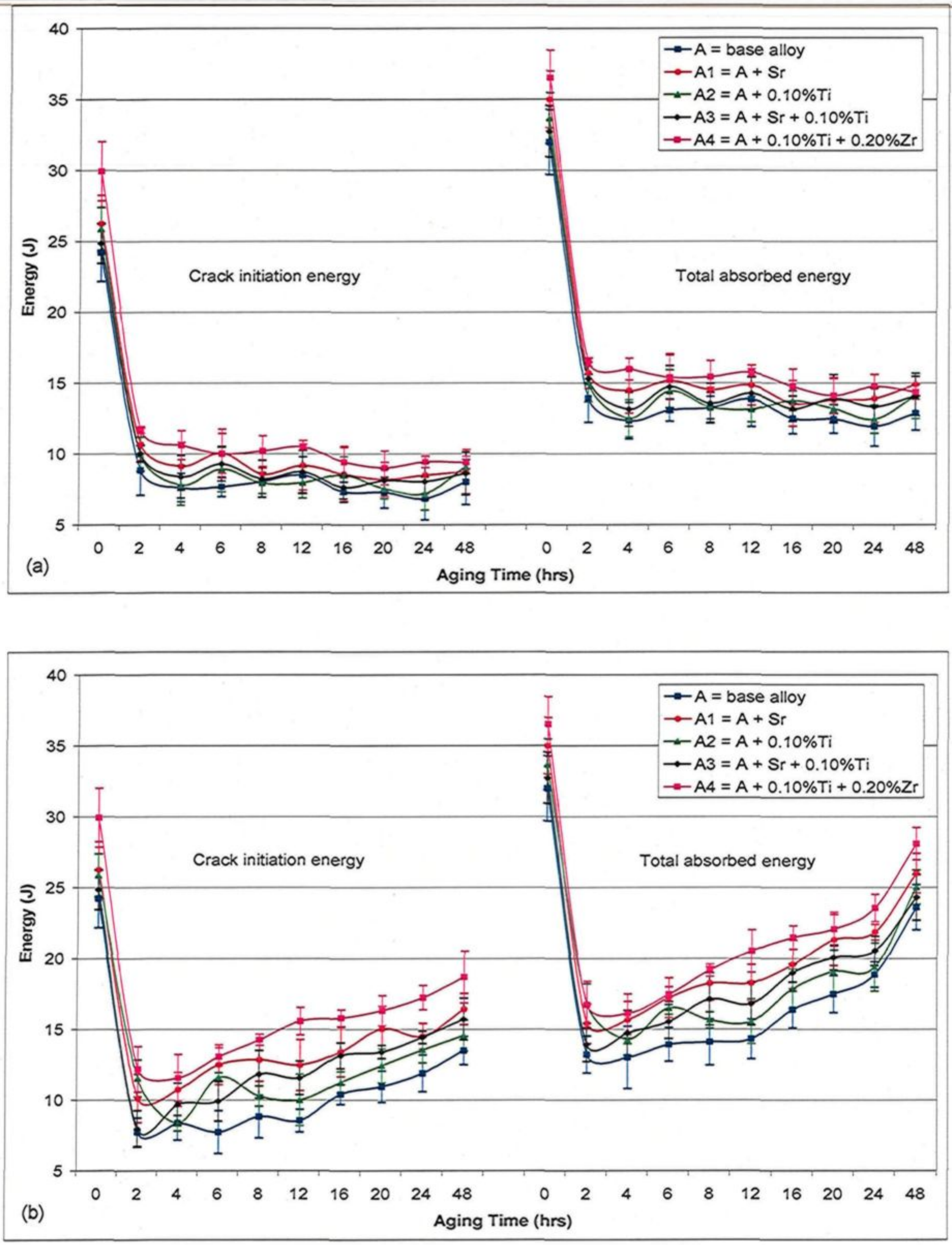

Figure 5.17 Variation in impact energies with aging time for Alloying Group I alloys aged at: (a) 180°C; and (b) 220°C.

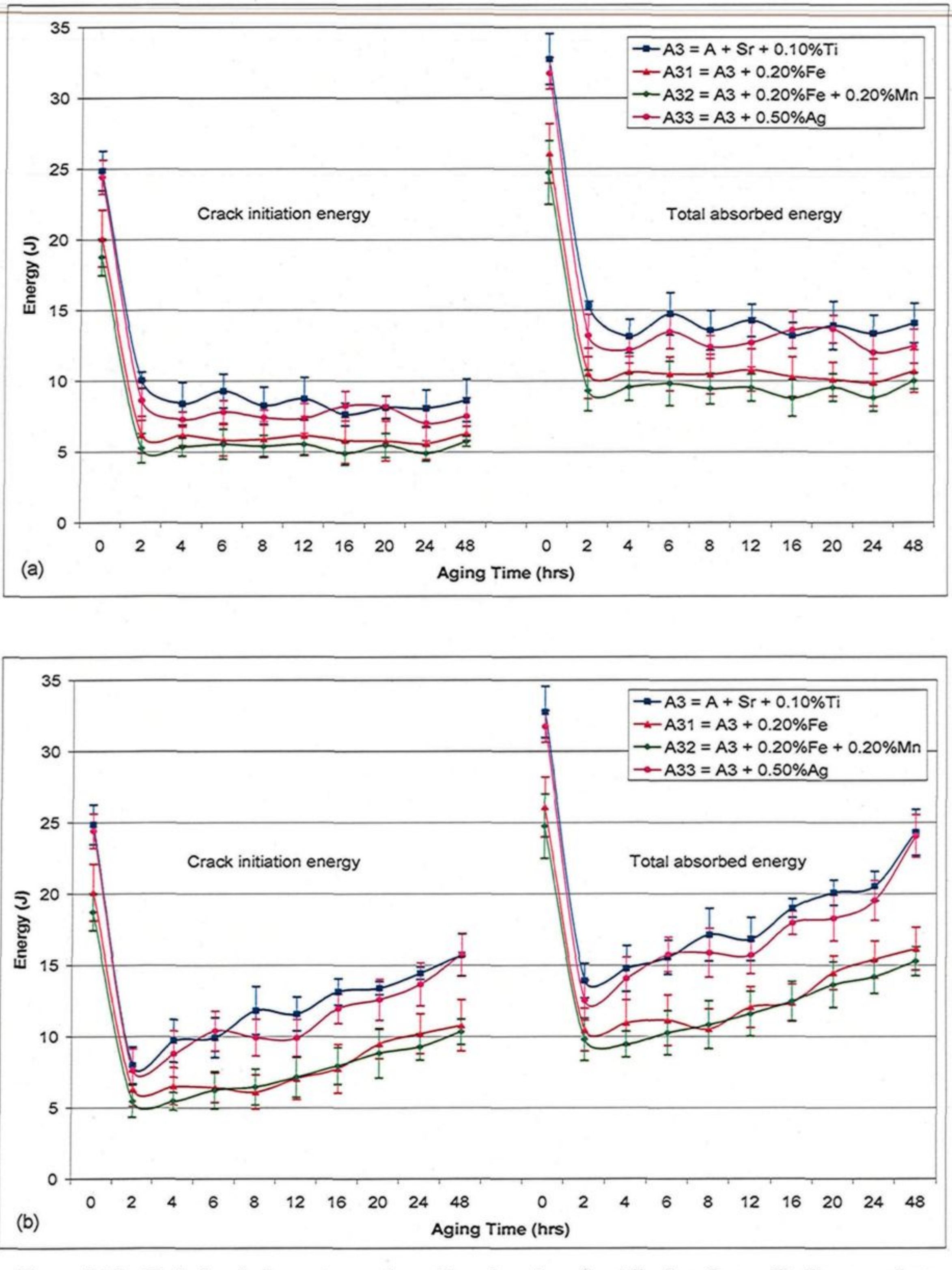

Figure 5.18 Variation in impact energies with aging time for Alloying Group II alloys aged at: (a) 180°C; and (b) 220°C.

respectively, compared to the reference A3 alloy. For the A32 alloy, the average reductions were calculated to be ~36% for both tempered conditions.

The increase in the fragility of the A31 and A32 alloys can also be manifested through the reduction caused in the crack propagation energy of these alloys. The crack propagation energy of the A31 alloy was reduced on average by 17% and 20% corresponding to the 180°C and 220°C tempered conditions, respectively, compared to the A3 alloy, whereas for the A32 alloy, the average reductions were found to be ~24% for both tempered conditions. The effects of iron on the mechanical properties of Al-Si casting alloys were investigated by Komastu *et al.*[146] Their results show that iron has a detrimental effect on the impact strength of such alloys because of the formation of Al-Si-Fe compounds.

The Ag-containing A33 alloy displays a slight reduction in impact energies compared to the reference A3 alloy. This reduction is consistent with the increase in the strength properties and hardness values of the A33 alloy produced by the hardening effect of Ag, as previously discussed in Subsection 5.2.2.

It will be seen with regard to the Alloying Group III that the addition of Sn, producing A41 alloy, does not bring about any substantial change in impact energies. This observation is interpreted in terms of the fact that the increase in impact toughness resulting from the softening effect of Sn may compensate for the reduction caused by the increase in the percentage porosity arising from the melting of the β-Sn phase particles during solution heat treatment. The impact toughness of both Bi-containing A42 and A43 alloys was observed to have become remarkably deteriorated. The free Bi particles which are brittle in

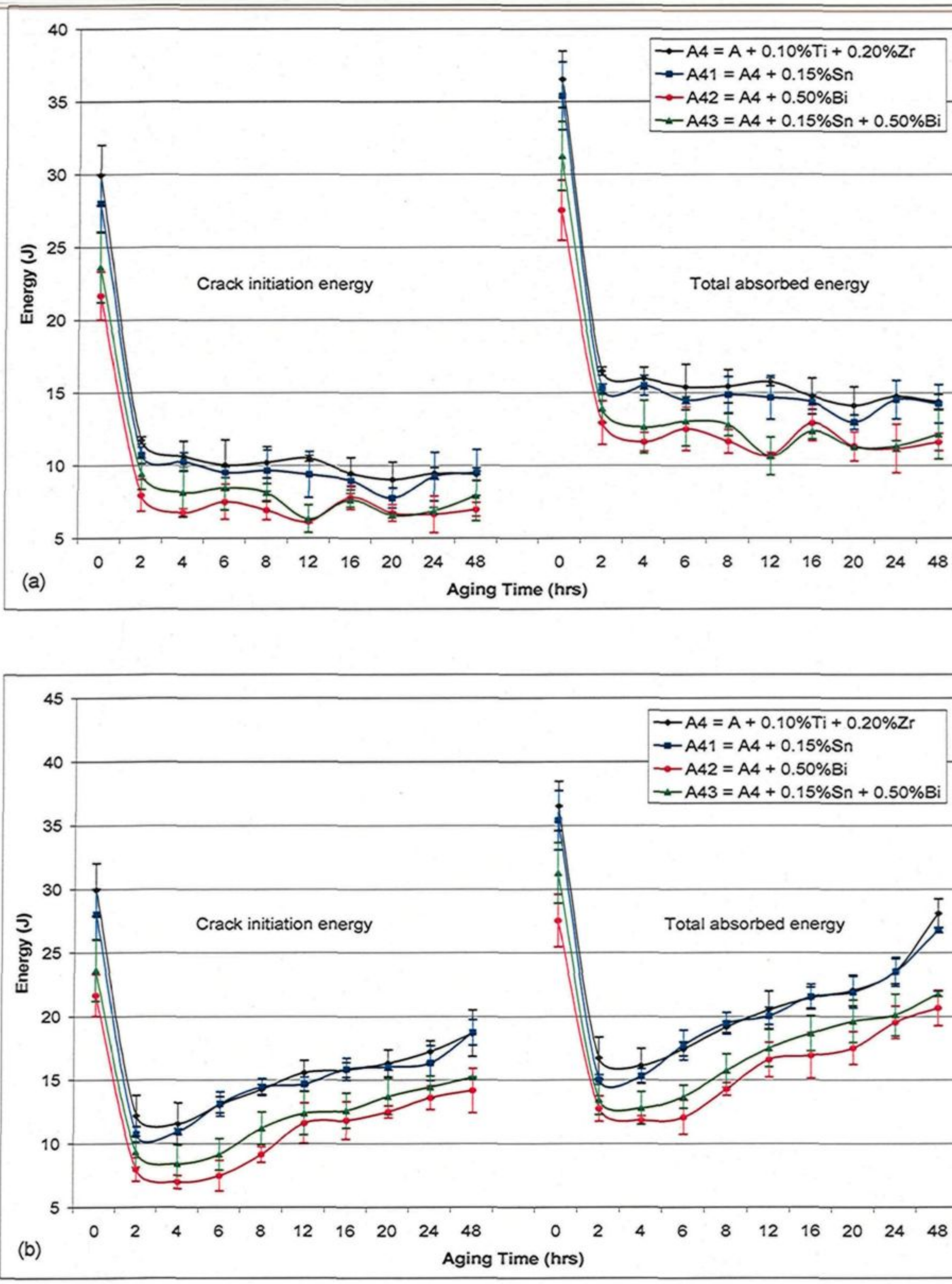

Figure 5.19 Variation in impact energies with aging time for Alloying Group III alloys aged at: (a) 180°C; and (b) 220°C.

nature act as internal stress risers in the alloy microstructure and provide an easy path to fracture. The total absorbed energy of the A42 and A43 alloys was reduced on average by 23% and 18%, respectively, for both 180°C and 220°C tempered conditions.

5.6 FRACTOGRAPHY

Fractography is generally used for upgrading material specifications, improving product design, and analyzing potential for failure with the intention of improving product reliability.[147] The fractographs presented in this section are backscattered electron images which were deemed suitable for highlighting the various features observed on the fracture surfaces of both the tensile-tested and impact-tested alloy samples.

5.6.1 Fractography of Tensile-Tested Samples

This subsection will study the fracture behavior of both the base A alloy and the Bi-containing A42 alloy in tensile testing. The fractographic investigation will cover the tensile-tested samples of the above alloys. For each alloy composition, four tensile-tested samples were used corresponding to: (i) the as-cast, (ii) the solution heat-treated, (iii) 180°C/4h aged, and (iv) 220°C/4h aged conditions.

Figure 5.20(a) shows the fracture surface of the as-cast base A alloy sample. This figure reveals the presence of two main intermetallic phases, namely θ-Al_2Cu and α-$Al_{15}(Fe,Mn)_3Si_2$, as confirmed by the corresponding EDX spectrums shown in Figures 5.20(b) and 5.20(c), respectively. Solution heat-treatment of this alloy resulted in the dissolution of the Al_2Cu phase as displayed in Figure 5.20(d).

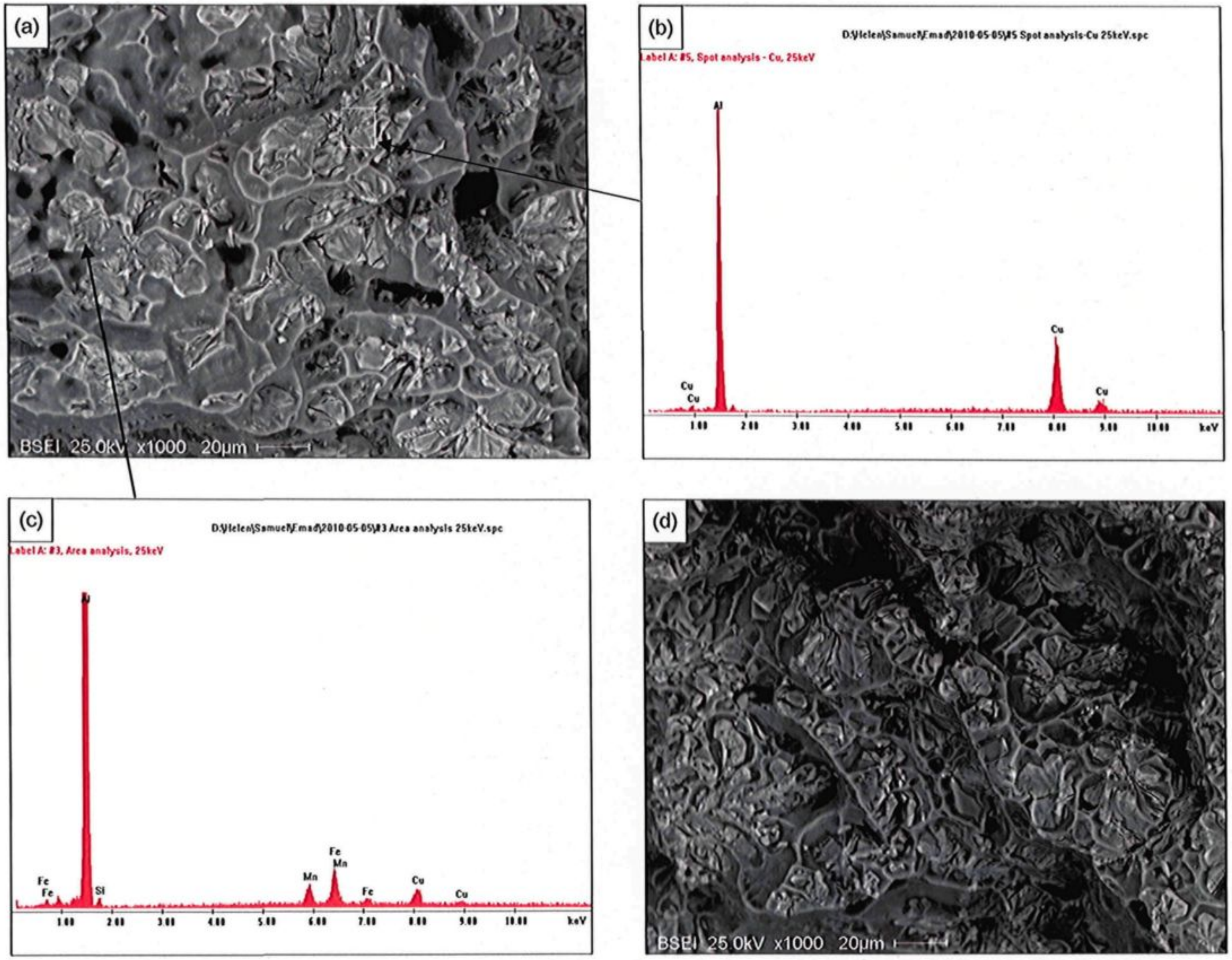

Figure 5.20 (a) Fracture surface of as-cast A alloy sample; (b) EDX-ray spectrum corresponding to Al_2Cu phase in (a); (c) EDX-ray spectrum corresponding to α-Fe phase in (a); and (d) fracture surface of solution heat-treated A alloy sample.

Figure 5.21 presents high magnification micrographs showing the fracture surface of the base A alloy samples corresponding to different conditions. The ultra-fine particles which precipitated after aging the alloy for 4 hours at 180°C and 220°C may be observed in the micrographs depicted in Figures 5.21(c) and 5.21(d), respectively, as indicated by the solid arrows. It should be noted here that the precipitation of these particles is associated with the formation of a network of dimples of less than a micron in diameter marked by the dashed arrows. In the as-cast and solution heat-treated conditions, represented by the micrographs shown in Figures 5.21(a) and 5.21(b), respectively, neither the ultra-fine particles nor the associated dimples may be observed.

The micrograph obtained from the fracture surface of the as-cast A42 alloy sample shown in Figure 5.22(a) reveals the presence of bright AlMgBi phase particles together with the Al_2Cu phase particles marked by solid and dashed arrows, respectively. The latter phase appears less luminous than the former because of the difference in their atomic numbers, 83 and 29, respectively. The composition of the AlMgBi phase was identified by the corresponding EDX-ray spectrum shown in Figure 5.22(b). Solution heat-treatment of A42 alloy at 495°C for 8 hours resulted in the dissolution of the Al_2Cu phase while both the AlMgBi and α-Fe intermetallics were not affected, as shown in Figure 5.22(c). The higher magnification backscattered image depicted in Figure 5.22(d) shows the Chinese-script morphology of the α-Fe phase circled in Figure 5.22(c).

Figures 5.23(a) and 5.23(b) are high magnification fractographs of two A42 alloy samples corresponding to 180°C and 220°C aging conditions, respectively. In these figures, the solid arrows refer to the presence of large AlMgBi particles inside the dimples, whereas

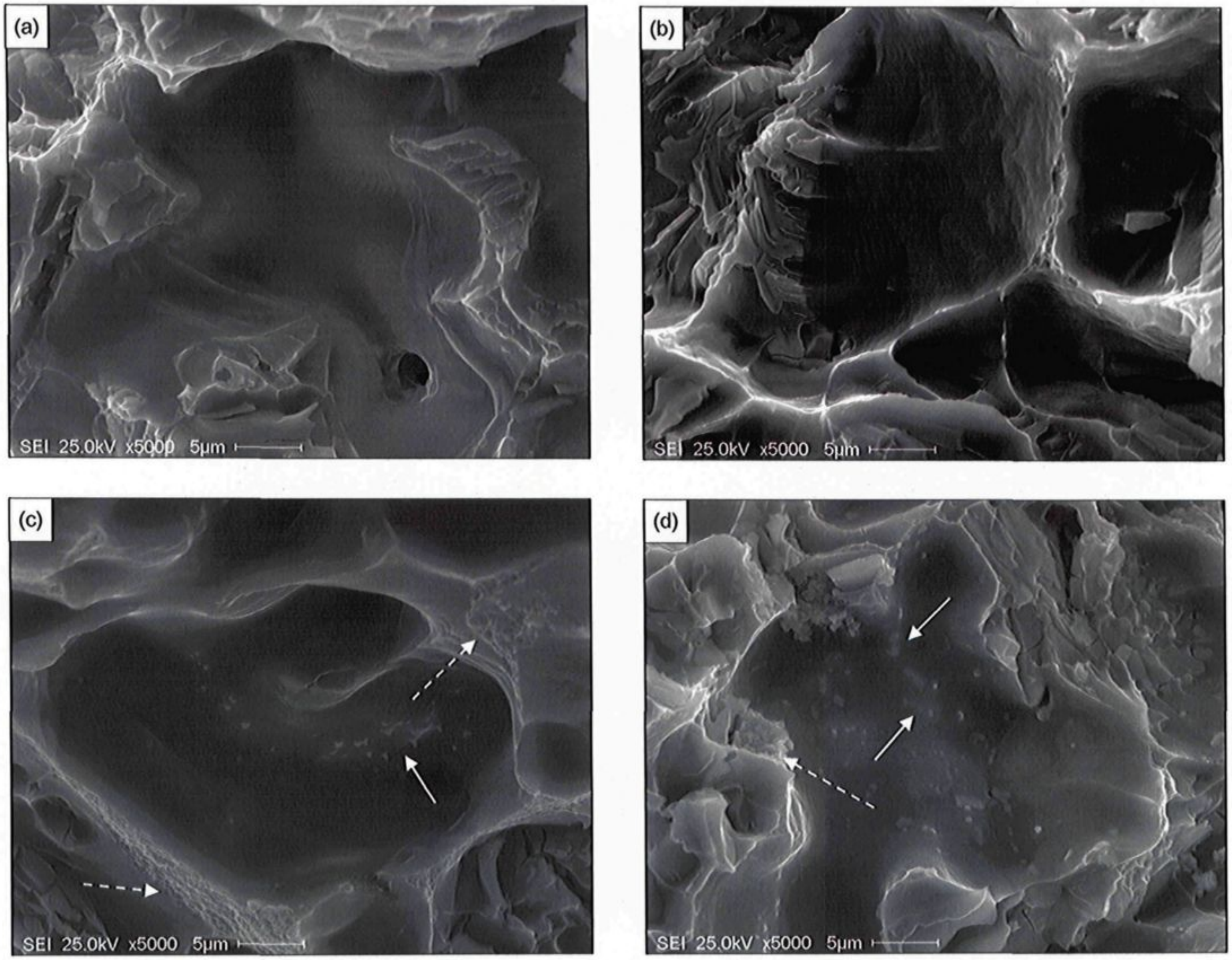

Figure 5.21 Fracture surface of A alloy samples in the: (a) as-cast; (b) 495°C for 8 hours solution heat-treated; (c) 180°C for 4 hours aged; and (d) 220°C for 4 hours aged conditions.

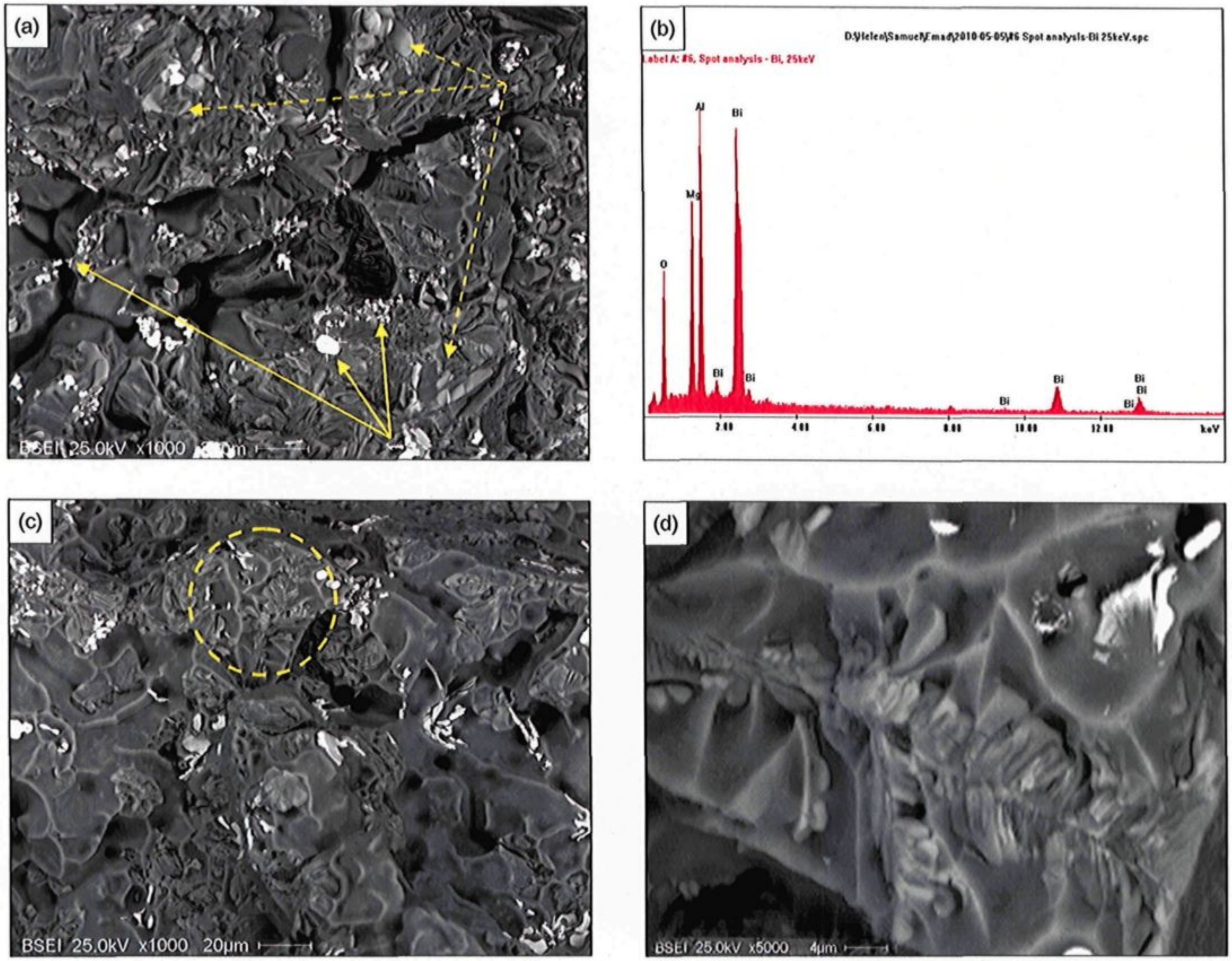

Figure 5.22 (a) Fracture surface of as-cast A42 alloy sample; (b) EDX-ray spectrum corresponding to AlMgBi phase in (a); (c) fracture surface of the solution heat-treated A42 alloy sample; and (d) higher magnification micrograph showing details of the α-Fe phase circled in (c).

the dashed arrows refer to the presence of networks of ultra-fine dimples. Figure 5.23(c) is a higher magnification micrograph of the area marked A in Figure 5.23(b), clearly showing the fineness of the dimples which are normally associated with the precipitation of fine particles similar to those shown previously.

5.6.2 Fractography of Impact-Tested Samples

This subsection will examine the fracture behavior of A1, A4, A32, and A41 alloys in impact testing. The fractographic investigation will cover the impact-tested samples corresponding to these alloy compositions. For each alloy, one impact-tested sample originally aged at 180°C for 4 hours was used. For each alloy sample, several backscattered images were taken from the edge and the centre of the fracture surface in order to discern crack initiation and crack propagation characteristics. In addition, interesting features appearing on the fracture surface will also be commented upon.

The fracture surface of the Sr-modified A1 alloy sample is shown in Figure 5.24. The area of fine dimples marked A in Figure 5.24(a) seems to be dominating the fractured surface. The arrow in Figure 5.24(b) refers to the fracture of the α-Fe intermetallic phase which can clearly be seen from the higher magnification fractograph shown in Figure 5.24(c). The crack was observed to propagate through the formation of secondary cracks marked by the arrows in Figure 5.24(d).

Figure 5.25(a) shows the crack initiation in the A4 alloy sample. The area marked A in this figure reveals the presence of fine bright particles. Figure 5.25(b) is a higher

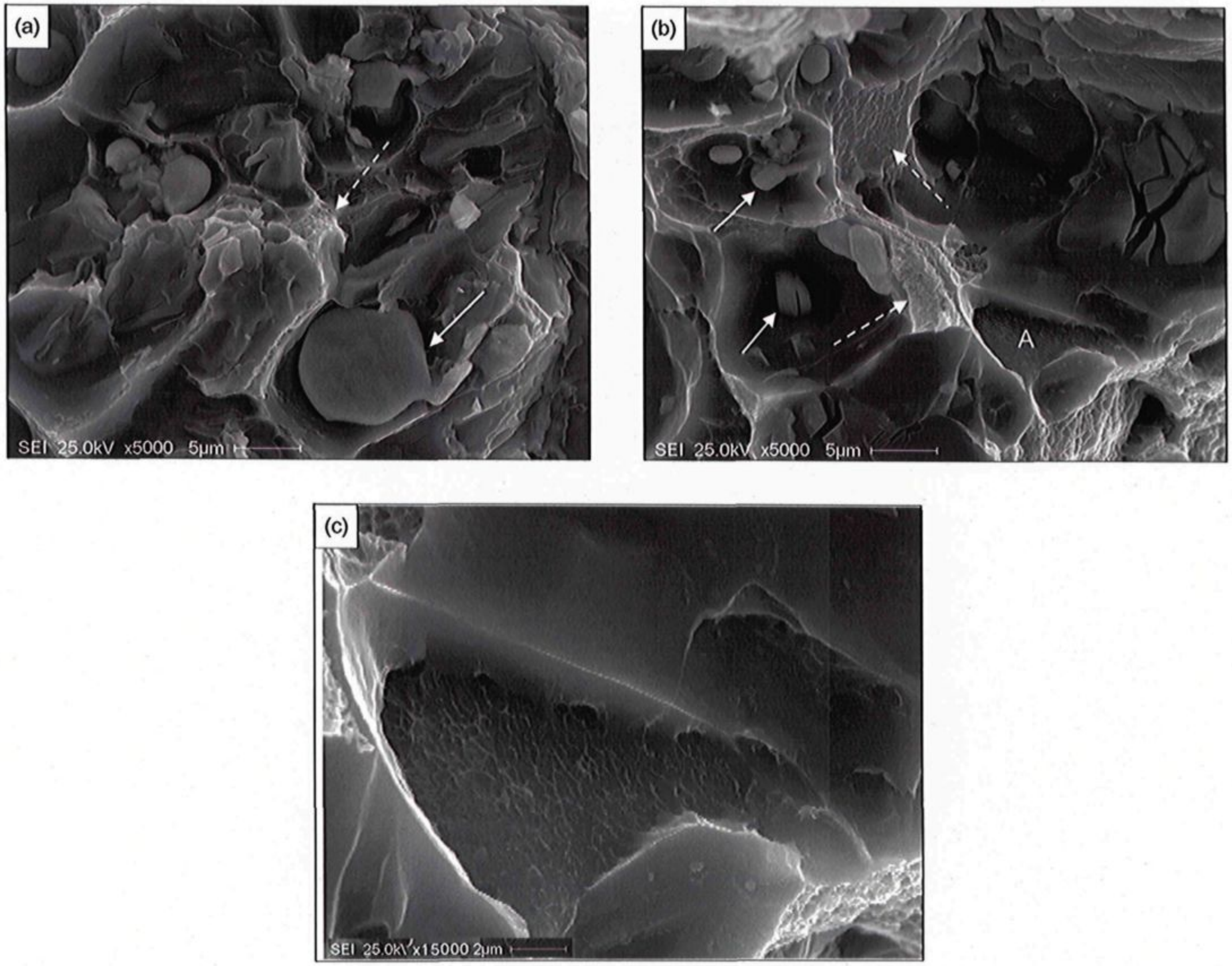

Figure 5.23 (a) Fracture surface of A42 alloy sample aged at 180°C for 4 hours; (b) fracture surface of A42 alloy sample aged at 220°C for 4 hours; and (c) higher magnification micrograph of area A shown in (b).

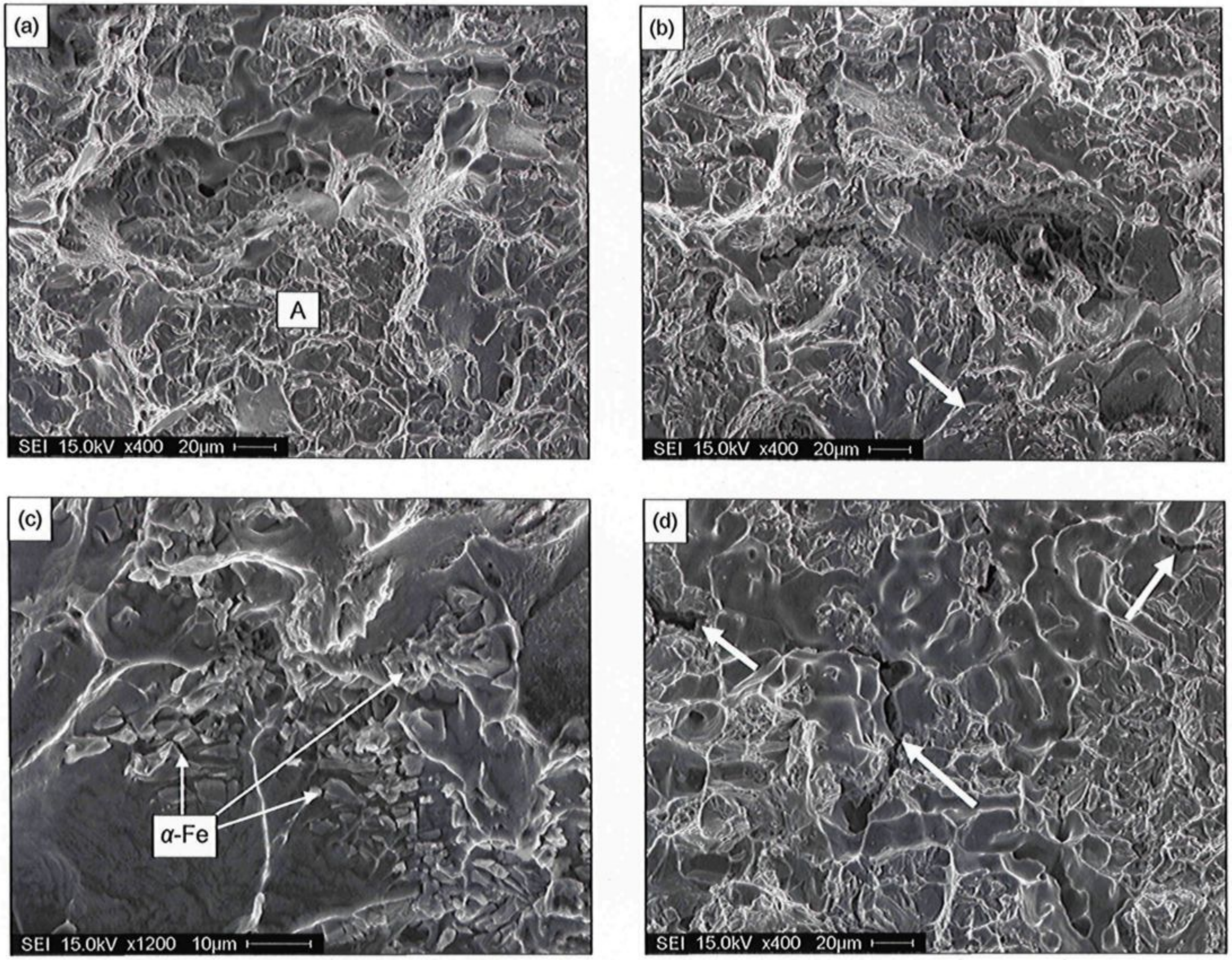

Figure 5.24 (a) Fracture surface of A1 alloy sample near the crack initiation side; (b) fracture of α-Fe phase; (c) higher magnification micrograph of the area below the arrow in (b); and (d) fracture surface of A1 alloy sample near the sample center.

magnification micrograph of this area showing the precipitation of Al_3Zr in the A4 alloy. Figure 5.25(c) is a higher magnification micrograph of the area marked by the arrow in Figure 5.25(a) displaying a deep secondary crack surrounded by fragments of the fractured α-Fe phase. The crack propagated through the formation of different sizes of dimples and fractured α-Fe phase, as indicated by the arrows shown in Figure 5.25(d).

Increasing both Fe and Mn in the A32 alloy resulted in an increase in the volume fraction of the α-Fe phase. Figure 5.26(a) shows the crack initiation in the sample of this alloy with the formation of several secondary cracks, as indicated by the arrows. The higher magnification micrograph depicted in Figure 5.26(b) is a good example showing the fracture of the α-Fe phase in A32 alloy. The crack continued to propagate through the fracturing of the intermetallics, as well as the formation of secondary cracks marked by the arrows in Figures 5.26(c) and 5.26(d).

The fracture of the A41 alloy sample initiated with formation of several deep secondary cracks marked by the arrows in Figure 5.27(a). The arrows in Figure 5.27(b) point to the presence of β-Sn inside the dimples. Figure 5.27(c) is a higher magnification fractograph showing the presence of a large number of β-Sn particles inside the coarse dimples, as confirmed by EDX analysis. The crack was observed to propagate in the usual manner, as mentioned above, through the formation of several secondary cracks. One of these cracks is indicated by the arrow in Figure 5.27(d).

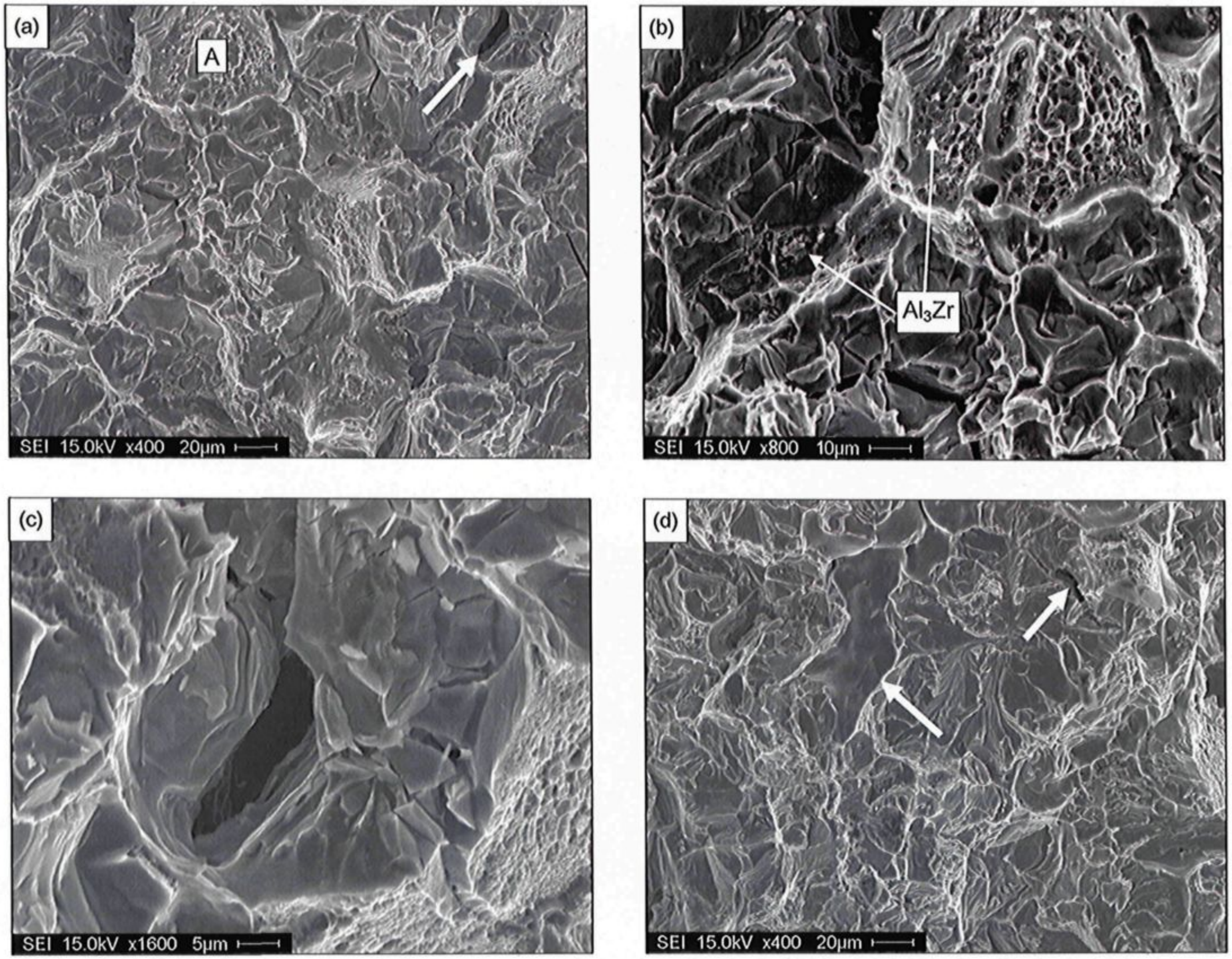

Figure 5.25 (a) Fracture surface of A4 alloy sample near the crack initiation side; (b) higher magnification micrograph of area A in (a); (c) higher magnification micrograph of the crack arrowed in (a); and (d) fracture surface of A4 alloy sample near the sample center.

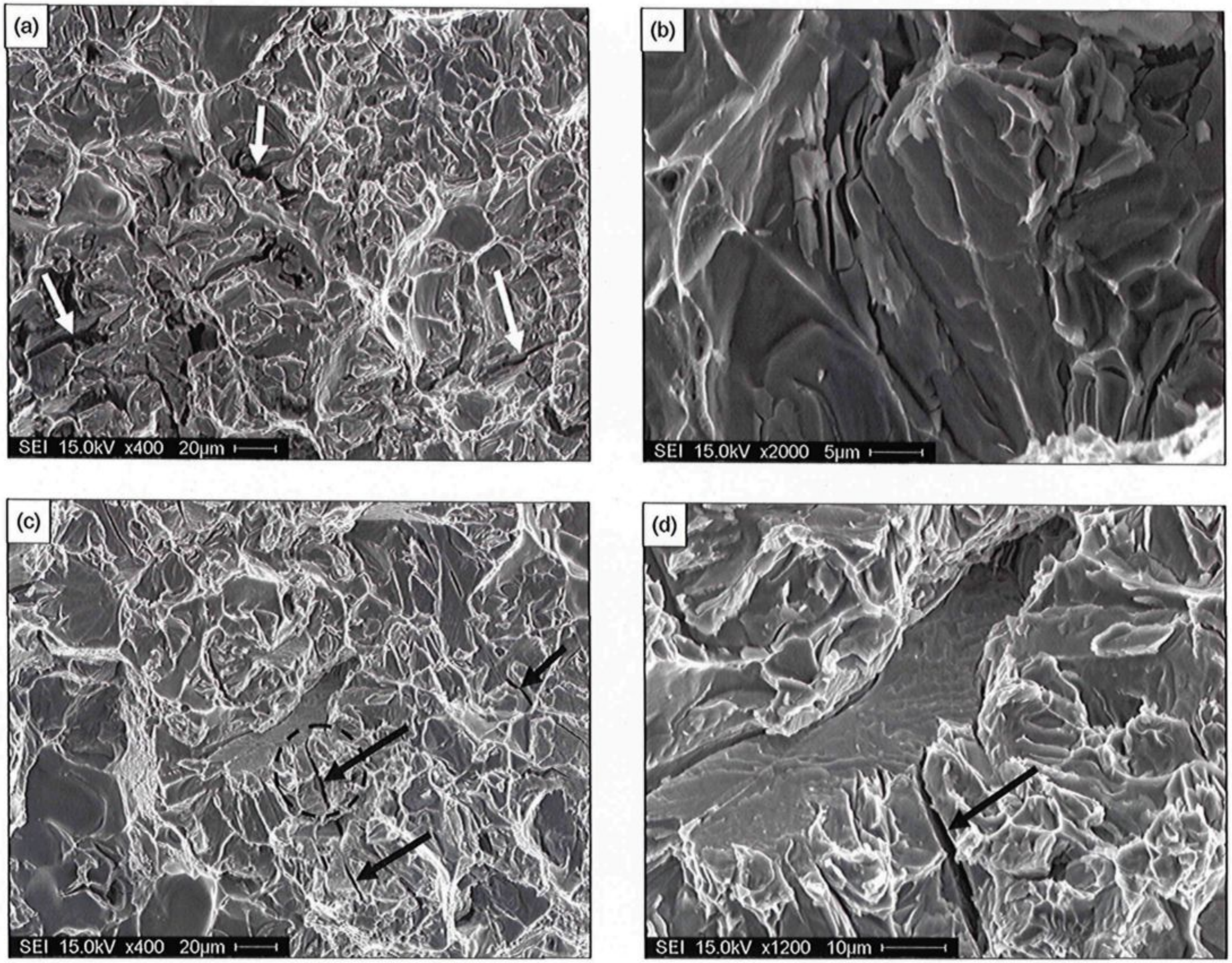

Figure 5.26 (a) Fracture surface of A32 alloy sample near the crack initiation side; (b) higher magnification micrograph showing the fractured α-Fe phase; (c) fracture surface of A32 alloy sample near the sample center showing the presence of several cracks; and (d) higher magnification micrograph of the crack circled in (c).

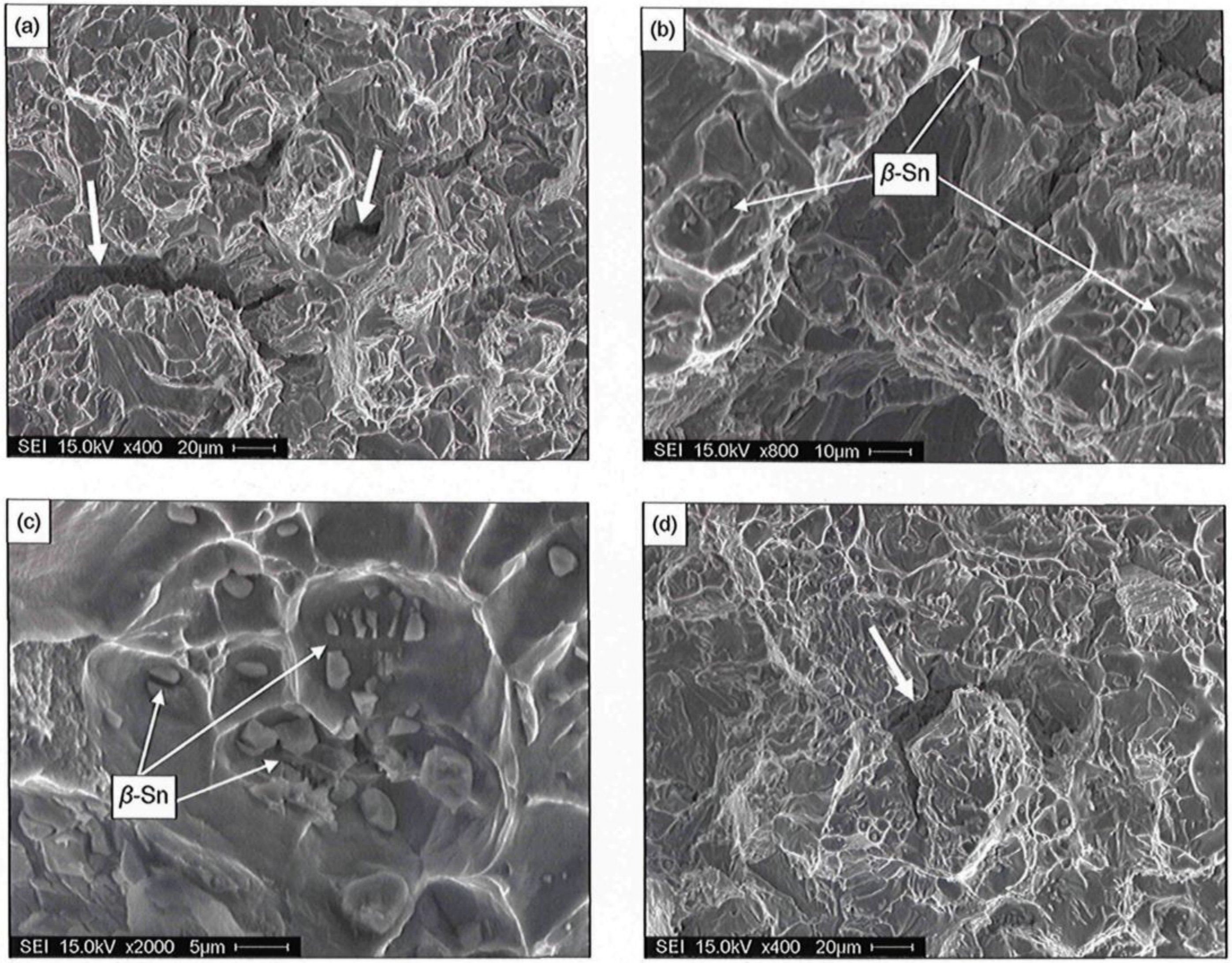

Figure 5.27 (a) Fracture surface of A41 alloy sample near the crack initiation side; (b) presence of *β*-Sn inside the dimples; (c) higher magnification micrograph showing a large number of *β*-Sn particles located within coarse dimples; and (d) fracture surface of A41 alloy sample near the sample center.

CHAPTER 6

MACHINABILITY EVALUATION

CHAPTER 6

MACHINABILITY EVALUATION

6.1 INTRODUCTION

This chapter is devoted to examining the drilling and tapping performance of four 220-based alloys, namely the A, A4, A41, and A42 alloys, as well as the A206 alloy. These alloys, having the chemical compositions listed in Table 3.3, were specifically selected for this machinability study based on the following considerations:

- The A alloy is the base 220 alloy and it is necessary to identify the machining characteristics of this new alloy, as it was received, without any metallurgical improvements.
- The A4 alloy is the best 220-based alloy studied from the point of view of mechanical properties; it should also be noted that the free-cutting alloys were prepared from this alloy.
- The A41 and A42 alloys, containing Sn and Bi, respectively, were selected to examine the effects of these free-cutting elements on machining performance. The A43 alloy containing a combination of both Sn and Bi was, however, excluded from the machinability study in the light of the deterioration in its mechanical properties, as previously explained in Subsection 5.2.3.

- Owing to its chemical composition, which is the closest to that of the 220 alloy among the well known Al-Cu alloys, the A206 alloy was selected for a comparative study on the machinability of this particular alloy and that of the 220 alloy.

The results reported here will focus on the machinability aspects of the abovementioned alloy conditions with respect to the cutting force and moment, tool life, chip characteristics, and built-up edge (BUE) formation. In addition, the machining behavior of the 220 alloy will also be compared with that of the A206, 356, B319, and A319 alloys currently used in industrial applications.

6.2 INVESTIGATION OF THE MICROSTRUCURE

The microstructure of the machinability test blocks of the alloys involved in the machinability study was investigated. This microstructural investigation was decided upon after taking into consideration the larger mass of the machinability test block casting compared to that of the sample used in the microstructure study presented in Chapter 4. The higher mass casting displays a lower cooling rate which may in turn affect the characteristics of the microstructure. The microstructures shown in Figure 6.1 were displayed by the samples cut from the heat-treated machinability test blocks prepared for the alloys studied. The rarity of the occurrence of Cu-rich intermetallic phases in the microstructures of the 220 based-alloys, including the A, A41, and A42 alloys, implies that the solution heat treatment caused these phases to become almost completely dissolved in

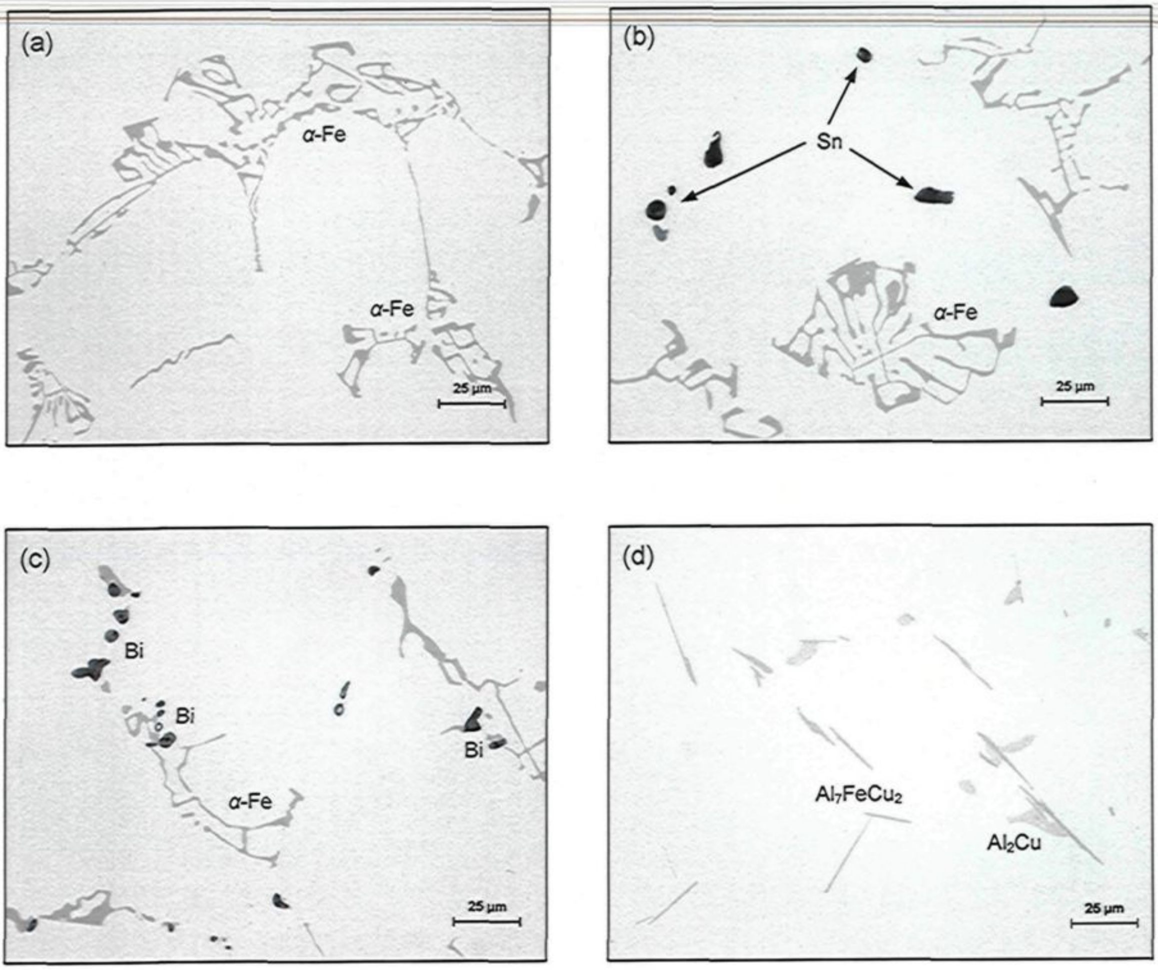

Figure 6.1 Microstructures obtained from the heat-treated machinability test blocks: (a) A alloy; (b) Sn-containing A41 alloy; (c) Bi-containing A42 alloy; and (d) 206 alloy.

the solid solution. On the other hand, the α-Fe Chinese-script phase particles, clearly seen in these microstructures, were not habitually affected by the solution heat treatment. The presence of Sn and Bi particles in the microstructures of the free-cutting A41 and A42 alloys, respectively, will also be clearly observed. Such a particularity supports the fact that Sn and Bi have no solubility in either liquid or solid aluminum, and do not form intermetallic compounds with aluminum and/or other alloying elements; all of which in turn fulfill the main requirements for obtaining the desired free-cutting action, as previously discussed in Subsection 2.4.6. The microstructure of the A206 alloy displays the presence of Al_7FeCu_2 phase particles and some Al_2Cu phase particles which had remained unaffected by the solution heat treatment. The presence of such Al_2Cu phase particles in the microstructure of the A206 alloy after heat treatment may be ascribed to the higher copper content of the alloy. This higher content increases the volume fraction of the Al_2Cu phase which may not be completely dissolved into the solid solution particularly in the light of the restricted temperature of the solution heat treatment of Al-Cu alloys. This observation suggests that such aluminum alloys containing high copper content, as in the case of A206 alloy, may show deteriorated machining characteristics since such undissolved Al_2Cu phase particles present in the microstructure may act as hard spots during machining.

6.3 HARDNESS VALUES

Hardness measurements were carried out on the heat-treated machinability test blocks to make sure that these blocks acquired the desired hardness levels of 100±10 HB. Table 6.1 provides the average hardness value for each set of eighteen heat-treated machinability test blocks prepared for each of the alloy compositions studied. It will be

Table 6.1 Average hardness of the machinability test blocks

Alloy	Average Hardness (BHN)
A (220)	101.0 ± 2.1
A4	103.2 ± 2.3
A41	99.2 ± 3.5
A42	102.0 ± 3.0
A206	103.0 ± 3.5

observed that the hardness values for the machinability test blocks of the 220 based-alloys are lower than those obtained from the hardness test blocks of these same alloys under the same aging condition, namely 180°C for 4 hrs, as shown in Figures 5.2(d) and 5.8(d). This reduction in the hardness values is to be expected in the light of the difference in mass between the larger machinability test block casting and the smaller hardness test block casting. The higher the casting mass, the lower the cooling rate and mechanical properties should prove to be. The hardness values of the machinability test blocks, however, are still within the desired range of 100±10 HB.

6.4 PROCESSING OF DATA FROM DRILLING AND TAPPING TESTS

The signal processing Matlab program developed by Tash[121] was used for processing the cutting data obtained during both drilling and tapping tests for all alloy conditions. The program determines the signals of the main components of the cutting force (Fx, Fy, and Fz) and moment (Mx, My, and Mz) for each test block from the force signals saved into the output files created by Cut Pro 8.0 software using the following set of equations:[148]

$$
\begin{gathered}
Fx = Fx_{1+2} + Fx_{3+4} \\
Fy = Fy_{1+4} + Fy_{2+3} \\
Fz = Fz_1 + Fz_2 + Fz_3 + Fz_4 \\
Mx = b(Fz_1 + Fz_2 - Fz_3 - Fz_4) \\
My = a(-Fz_1 + Fz_2 + Fz_3 - Fz_4) \\
Mz = b(-Fx_{1+2} + Fx_{3+4}) + a(Fy_{1+4} - Fy_{2+3}) \qquad (6.1)
\end{gathered}
$$

where a and b are the distances measured from the center of the dynamometer sensors to the x and y axes, respectively, as shown in Figure 3.19(a). According to the specifications of the Kistler 9255B-type dynamometer used for this work, each of these distances is equal to 80 mm. The force components on the right hand side of Equation 6.1 were previously defined in Subsection 3.1.6.

The signals obtained by applying Equation 6.1 were processed in such a way that the mean components of the cutting force (Fx_m, Fy_m, and Fz_m) and moment (Mx_m, My_m, and Mz_m), as well as their corresponding standard deviations (σ_{Fx_m}, σ_{Fy_m}, σ_{Fz_m}, σ_{Mx_m}, σ_{My_m}, and σ_{Mz_m}), were calculated for each hole. The program then determined the total mean cutting force (Ft_m) and moment (Mt_m) for each hole using the following set of equations:

$$Ft_m = [(Fx_m)^2 + (Fy_m)^2 + (Fz_m)^2]^{1/2}$$

$$Mt_m = [(Mx_m)^2 + (My_m)^2 + (Mz_m)^2]^{1/2} \qquad (6.2)$$

The standard deviations σ_{Ft_m} and σ_{Mt_m} of the total mean cutting force and moment, respectively, were calculated as follows:[149]

$$\sigma_{Ft_m} = [(Fx_m)^2 (\sigma_{Fx_m})^2 + (Fy_m)^2 (\sigma_{Fy_m})^2 + [(Fz_m)^2 (\sigma_{Fz_m})^2]^{1/2} / Ft_m$$

$$\sigma_{Mt_m} = [(Mx_m)^2 (\sigma_{Mx_m})^2 + (My_m)^2 (\sigma_{My_m})^2 + [(Mz_m)^2 (\sigma_{Mz_m})^2]^{1/2} / Mt_m \qquad (6.3)$$

Eventually, the drilling/tapping force and moment and their standard deviations were obtained for each test block as the mean values calculated over the respective values of 180 holes drilled/tapped in the same block.

6.5 EFFECTS OF ADDITIVES ON THE DRILLING FORCES AND MOMENTS

The effects of additives, namely TiB_2, Zr, Sn, and Bi, on the drilling force and moment are shown in Figures 6.2(a) and 6.2(b), respectively. It will be observed that the trend lines shown do not display a sharp increase in the drilling force and moment in line with the progress of the cutting process. This observation explains why the drill is capable of reaching the targeted tool life of 2520 holes without breakage with regard to all the alloy conditions investigated.

The combined addition of TiB_2 and Zr to the base A alloy, namely the A4 alloy, leads to a reduction of 6% and 4% in the drilling force and moment, respectively. Such a reduction may be ascribed to the improved distribution of second phase constituents and microporosity in the cast structure caused by the grain-refining action of TiB_2 and Zr, as previously discussed in Section 4.3.

The free-cutting A41 and A42 alloys containing Sn and Bi, respectively, display a considerable reduction in the drilling force and moment compared with the base A alloy. The drilling force was reduced over the evaluation extent of 2520 holes by 14%, ranging between 18% and 10%, in the A41 alloy and by 25%, ranging between 28% and 22%, in the A42 alloy. The drilling moment was reduced by almost the same percentages. It is clear

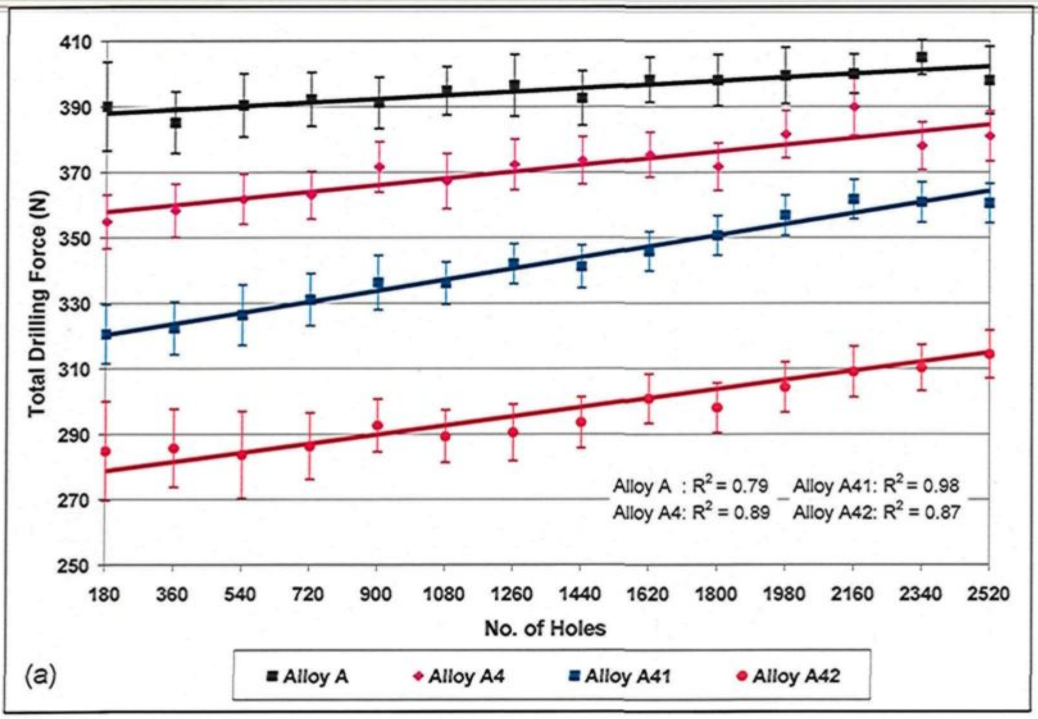

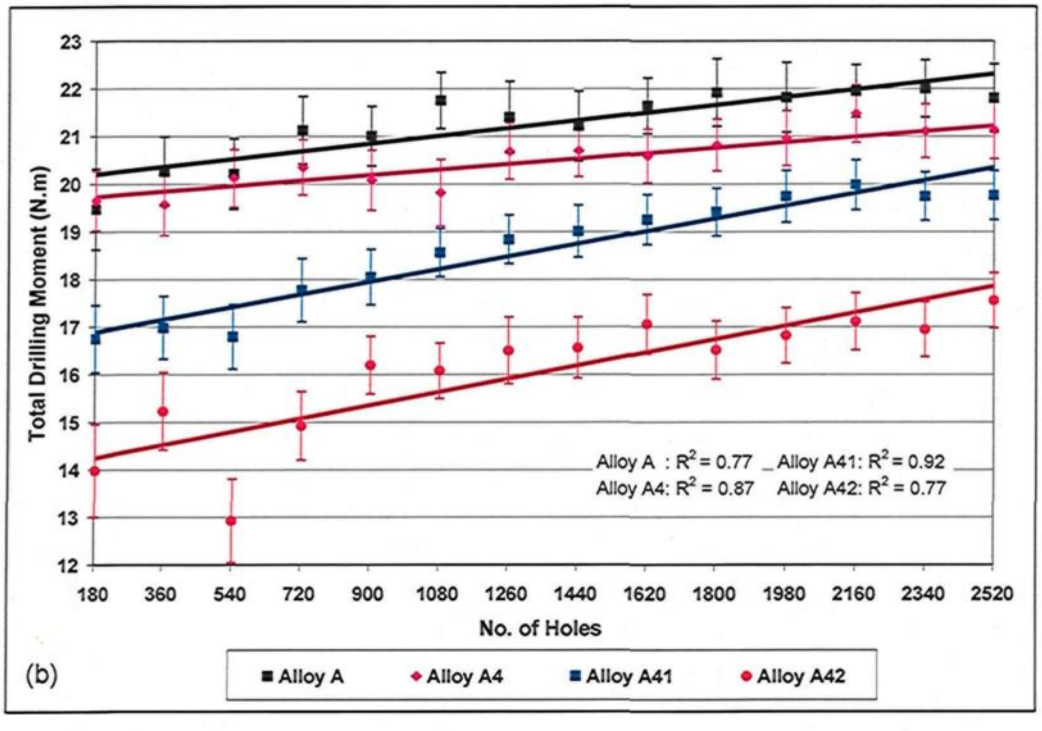

Figure 6.2 Effects of additives on: (a) drilling force; and (b) drilling moment.

that Bi is much more effective than Sn in reducing the drilling force and moment; such a fact may be understood in the light of the effect which both elements are observed to have on ductility, as demonstrated in Subsection 5.2.3. The lower ductility displayed by the Bi-containing A42 alloy compared to the Sn-containing A41 alloy decreases drill-chip friction which in turn decreases the cutting force and moment. It may therefore be concluded that Bi decreases the drilling force and moment not only through its lubricating effect during the cutting process as a free-cutting element but also through its role in decreasing alloy ductility.

6.6 EFFECTS OF ADDITIVES ON THE TAPPING FORCES AND MOMENTS

In the tapping test, each alloy condition was tested with two taps. The number of holes tapped by the first tap can be identified for each alloy condition from Figures 6.3(a) and 6.3(b) showing the effects of additives on the tapping force and moment, respectively. After the breakage of the first tap, the second one accomplished the tapping of the rest of the 2520 drilled holes without any breakage. In order to assure the reliability of the results, the data concerning the tap which machined the largest number of holes within the evaluation range of 2520 drilled holes, namely the first tap, was specifically taken into consideration in the plots shown in Figures 6.3(a) and 6.3(b). It appears from these figures that the additives have the same effect on the tapping force and moment as that observed in the drilling test. The tap, however, displays a shorter tool life compared to that of the drill for all the alloy conditions investigated. This shorter tool life may be ascribed to the high sensitivity of the high speed steel tap to the cutting force as compared to the carbide drill.

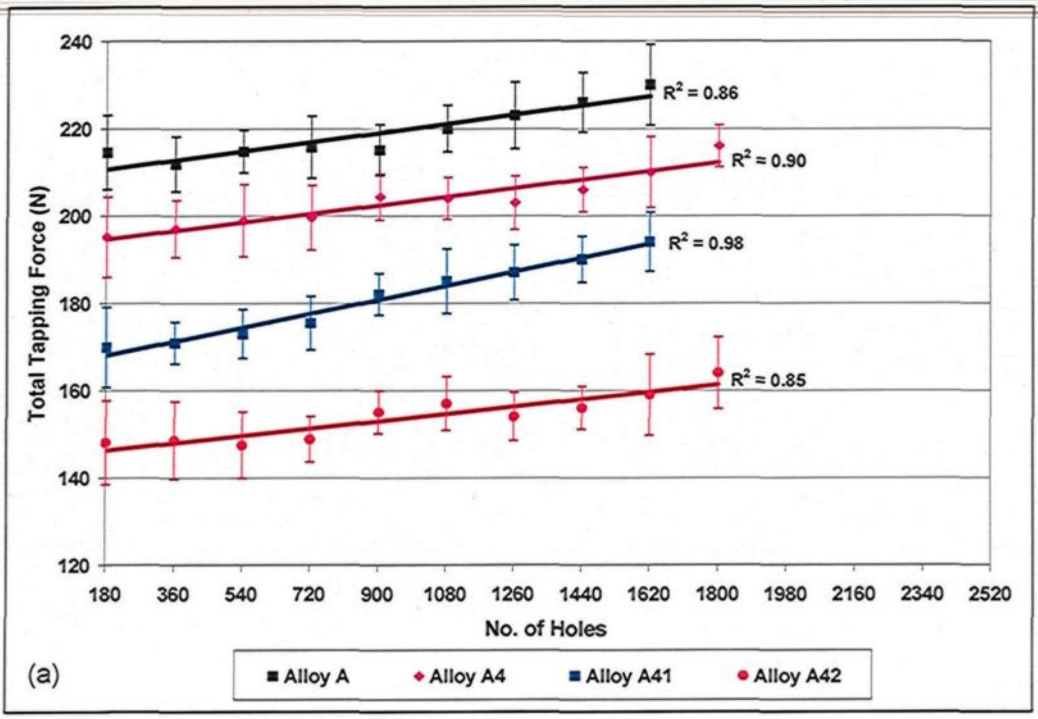

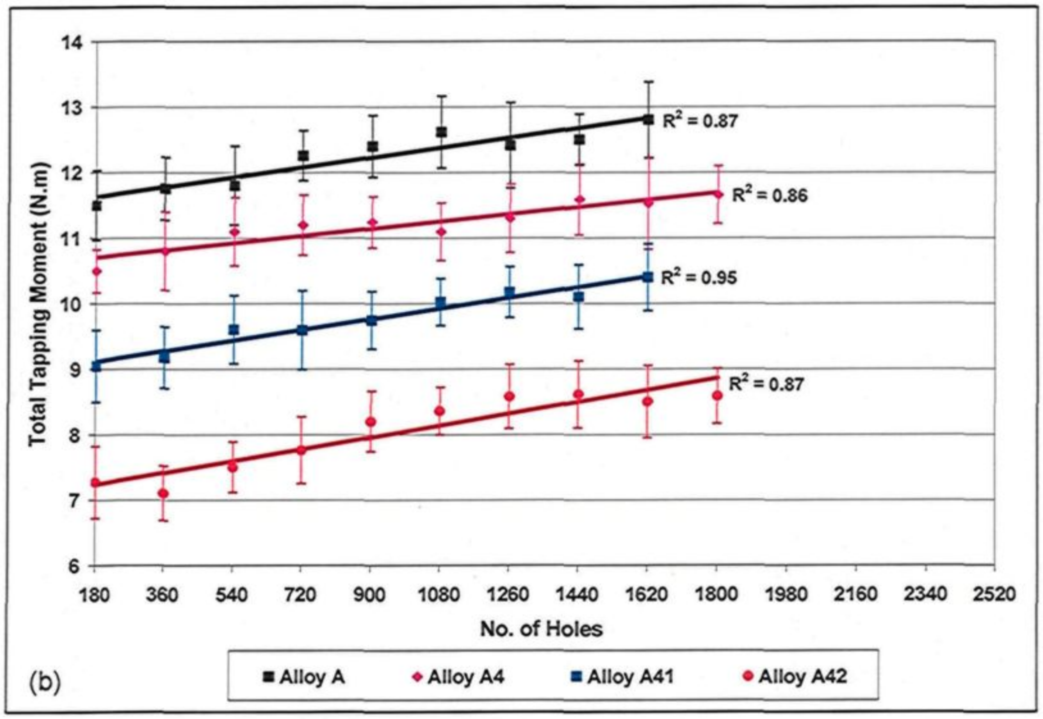

Figure 6.3 Effects of additives on: (a) tapping force; and (b) tapping moment.

In spite of the considerable reduction caused by the additives, particularly Sn and Bi, in the tapping force and moment, all the alloys display an approximate tool life ranging from 1620 to 1800 holes. This reduction may however be manifested by examining the breakage mode of the taps involved, as seen in the photographs shown in Figure 6.4. It will be found that the taps used in tapping the base A alloy and the A4 alloy are subject to abrupt breakage, as shown in Figures 6.4(b) and 6.4(c), respectively. On the other hand, the taps used in tapping the free-cutting A41 and A42 alloys, which display lower tapping force and moment, are subject to progressive tooth-breakage, as shown in Figures 6.4(d)

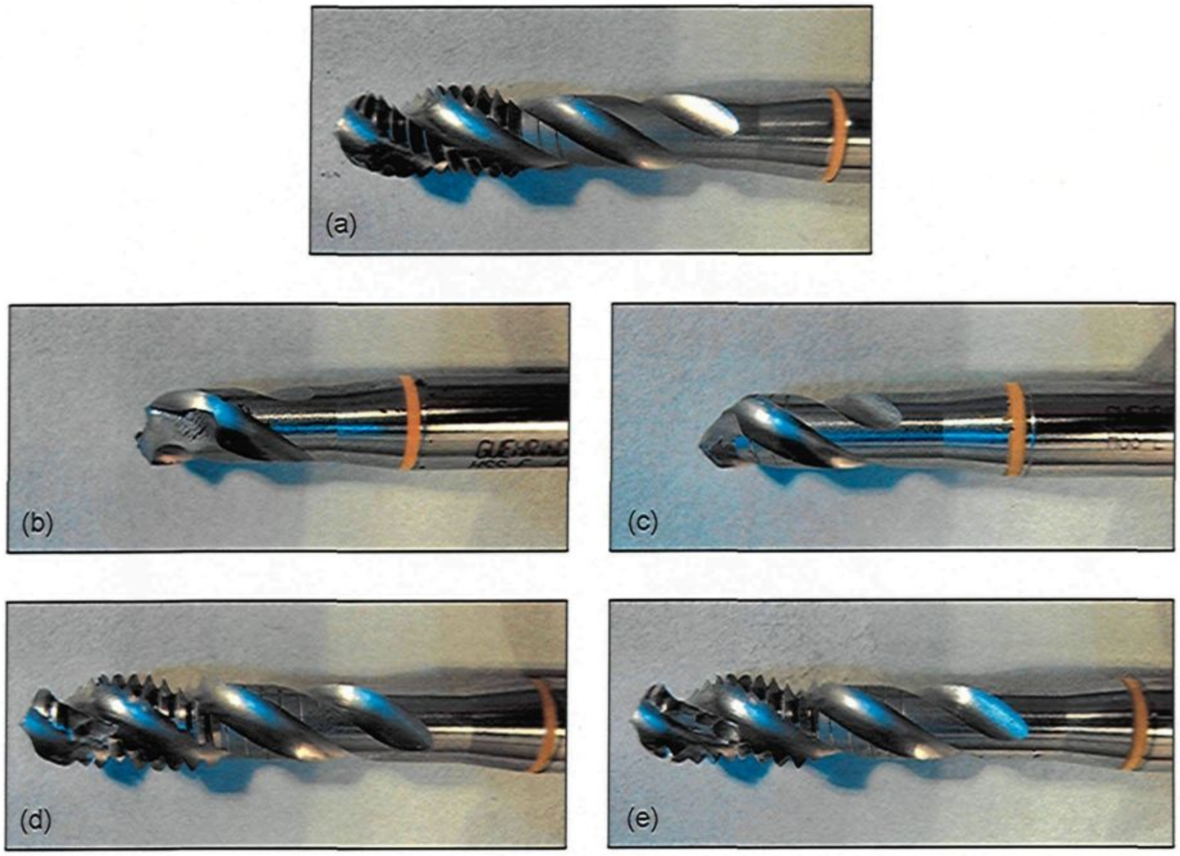

Figure 6.4 (a) New tap; (b) tap used in tapping A alloy (1620 holes); (c) tap used in tapping A4 alloy (1800 holes); (d) tap used in tapping A41 alloy (1620 holes); and (e) tap used in tapping A42 alloy (1800 holes).

and 6.4(e), respectively. It is important to mention here that the tooth-breakage evolves gradually and the breakage illustrated in the last-mentioned figures represents the worst-case situation in which the tap is no longer able to satisfy the dimensional accuracy of the holes as verified by the Go/No-Go gauge test.

6.7 ASSESSMENT OF HOLE QUALITY

An important assessment criterion during the drilling and tapping tests is the quality of the hole, that is to say, the precision of its dimensions and shape, as well as its surface finish. The Go/No-Go test is taken as an assessment characteristic for hole accuracy. The results relevant to this test are listed in Table 6.2 for all the alloy conditions investigated. These results show that the drill accomplishes the drilling of the targeted 2520 holes for each alloy condition within the allowable tolerance limits. For both the A and A1 alloys, the tap satisfies the hole accuracy up to 1620 and 1800 holes, respectively, where the abrupt tap breakage takes place. With regard to the free-cutting A11 and A12 alloys, the progressive tooth-breakage which occurred in the tap starts to cause the hole accuracy to deteriorate after up to 1620 and 1800 holes, respectively.

Table 6.2 Go/No-Go test results for hole accuracy

Alloy code	**Drilling Test**		**Tapping Test**	
	No. of holes	**Go/No-Go 6.5024/6.5278 mm**	**No. of holes**	**Go/No-Go 7.02056/7.15518 mm**
A	2520	OK	1620	OK
A1	2520	OK	1800	OK
A11	2520	OK	1620	OK
A12	2520	OK	1800	OK

6.8 CHIP CHARACTERISTICS

The qualitative inspection of drilling chips reveals that the form of the chips resulting from the 220 base A alloy closely approaches a fan-shaped form, as shown in Figure 6.5(a); this is considered the ideal chip form for most drilling applications. The addition of Bi, producing the A42 alloy, leads to a considerable refinement in chip morphology, as shown in Figure 6.5(b). It will also be observed that the chip produced by the Bi-containing A42 alloy tends to assume a needlelike form rather than the fan-shaped form displayed by the chips from the 220 base A alloy. The improvement in chip morphology caused by the addition of Bi may be attributed to the positive role played by this element, from the machinability point of view, in decreasing alloy ductility.

The A206 alloy is apt to produce long continuous conical chips, as shown in Figure 6.5(c), on account of the higher ductility of this alloy when compared to the 220 alloy. Long continuous conical chips are undesirable since they clog the drill flute and eventually lead to drill breakage. The difference in ductility between the 220 alloy and the A206 alloy can obviously be realized from Table 6.3. This table compares the tensile properties of both alloys in the same heat treatment conditions assigned to their machinability test blocks. As will be observed, the ductility of A206 is approximately five times that of the 220 alloy, once again explaining the evident difference found in the chip morphology of both these alloys. It should be mentioned that the tensile properties of the A206 alloy listed in Table 6.3 represent the respective mean values of 5 tensile test bars cast, heat-treated, and tested in the course of this work for the purposes of the abovementioned comparison which would, in its turn, contribute to an understanding of the machining characteristics of both the 220 alloy and the A206 alloy.

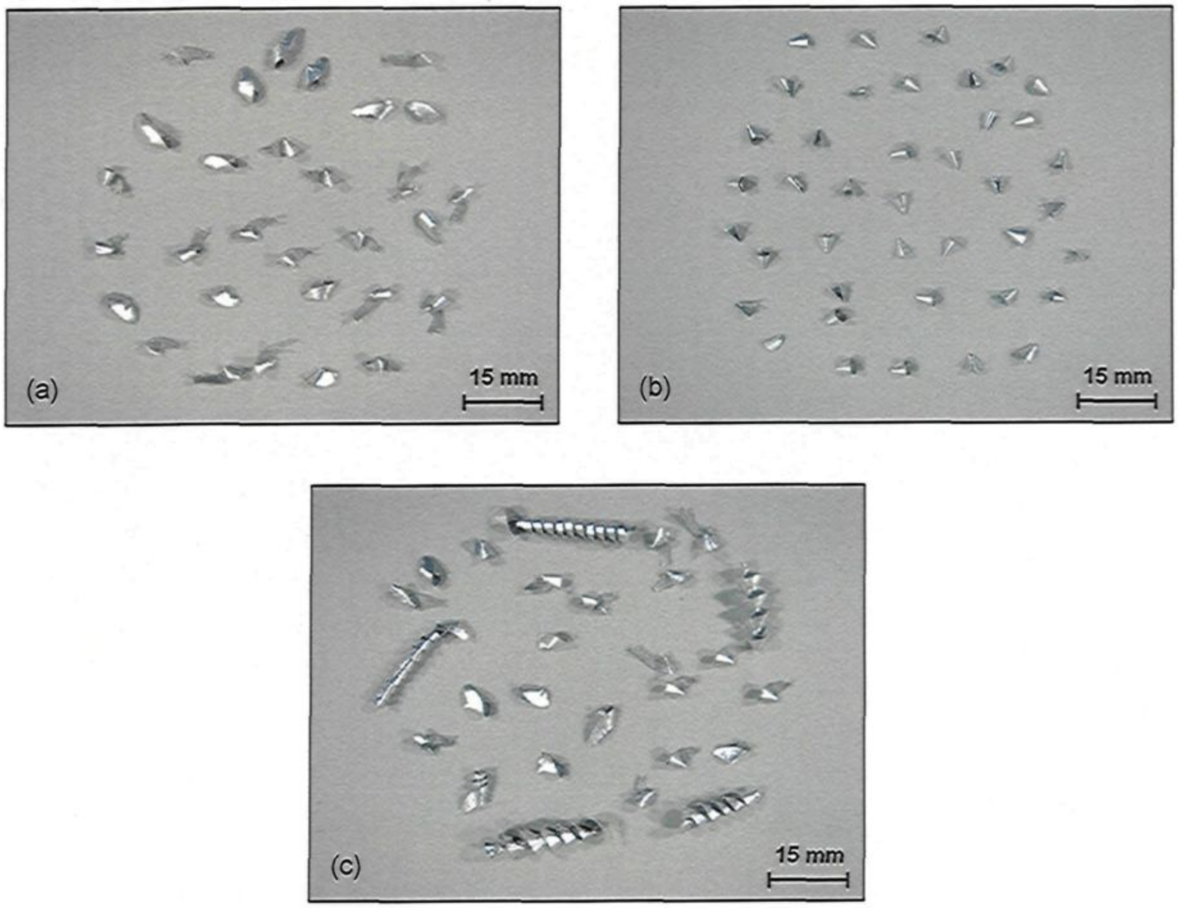

Figure 6.5 Chip morphology for (a) 220 base A alloy; (b) Bi-containing A42 alloy; and (c) A206 alloy.

Table 6.3 Comparing the tensile properties of the 220 and A206 alloys

Alloy	Tensile Properties		
	YS (MPa)	UTS (MPa)	El (%)
220	305±12	344±9	1.6±0.3
A206	340±8	411±5	7.8±0.8

The distinct difference in the chip morphologies illustrated in Figure 6.5 may be discerned from the histogram provided in Figure 6.6 which evaluates chip breakability for all the alloy conditions investigated in terms of the number of chips per gram. The combined addition of TiB_2 and Zr, producing the A4 alloy, did not in fact lead to any observable improvement in chip breakability. The addition of Sn, producing the A41 alloy, achieves up to 15% better chip breakability than the 220 base A alloy. The Bi-containing A42 alloy displays excellent chip breakability through an increase of about 70% in the number of chips per gram compared to the 220 base A alloy. In the light of its higher ductility, the A206 alloy displays a chip breakability of 32% less than does the 220 alloy.

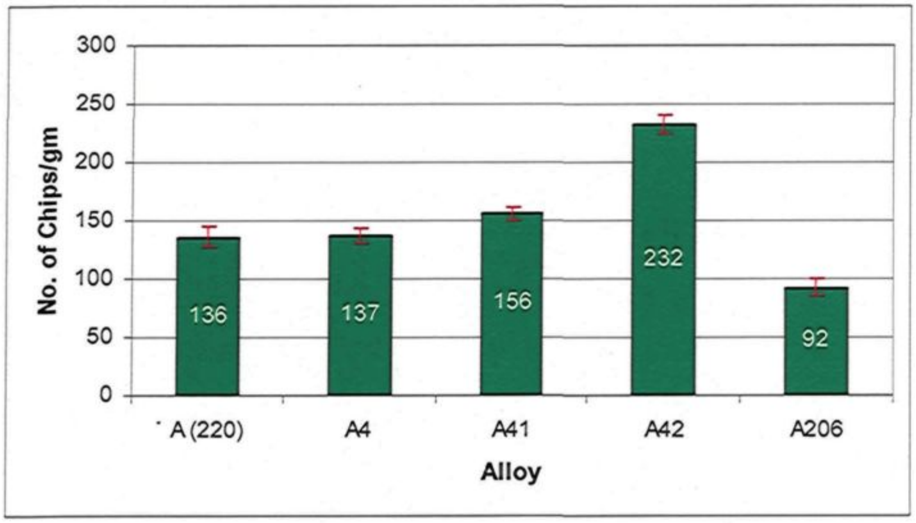

Figure 6.6 Number of chips per gram produced by the alloys studied.

6.9 EVOLUTION OF BUILT-UP-EDGE (BUE)

All of the alloys studied left a discernible deposit on the drill edge, as may be seen in Figure 6.7. The evolution in the width of this deposit, namely the width of the BUE, with the progress of the drilling process is listed in Table 6.4. It should be noted, however, that the results obtained from the A4 and A41 alloys are excluded since there was no substantial

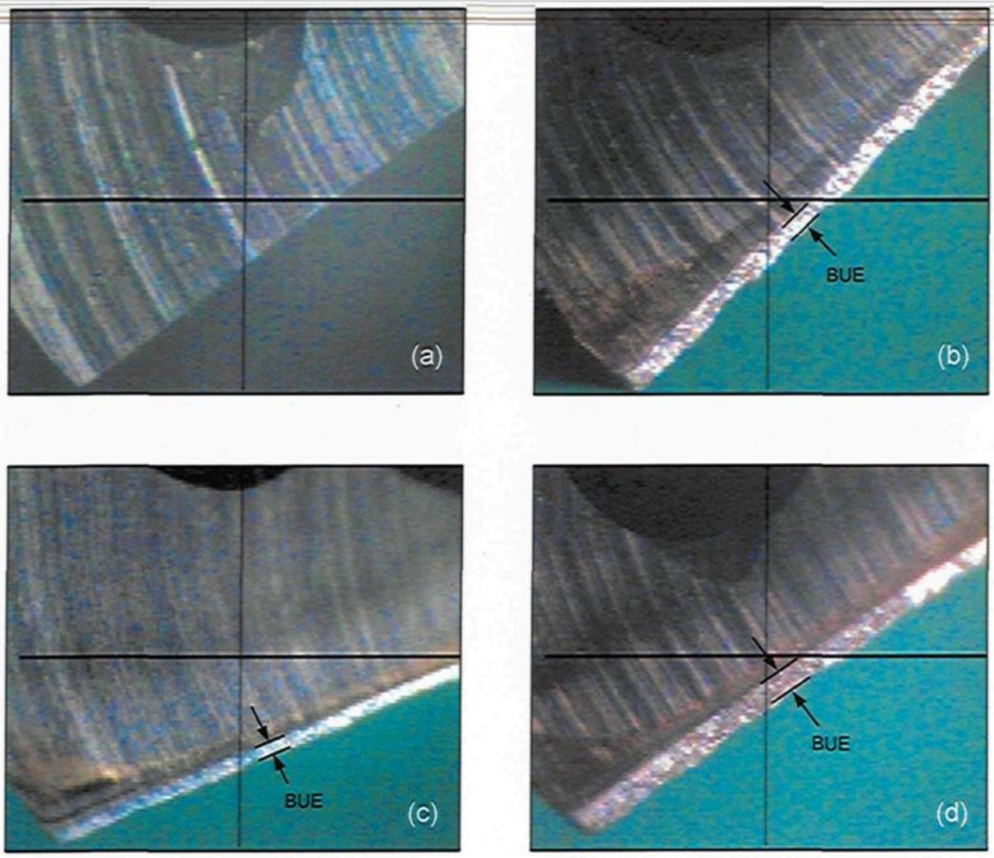

Figure 6.7 (a) New drill; (b) BUE formed by 220 base A alloy after 1620 holes; (c) BUE formed by Bi-containing A42 alloy after 1620 holes; and (d) BUE formed by A206 alloy after 1620 holes.

Table 6.4 Evolution of BUE width with the progress of the drilling process

No. of Holes	180	900	1620	2520	Average
Alloy	BUE width (mm)				(mm)
A (220)	0.172	0.169	0.177	0.181	0.175
A42	0.145	0.156	0.166	0.173	0.160
A206	0.194	0.208	0.196	0.223	0.205

difference to be observed in the width of BUE between these alloys and the base A alloy. It will be observed that, for all the alloys examined, there is no noticeable change in the width of the BUE during the course of the drilling process. Moreover, each alloy displays a width of BUE consistent with the quality of the chip produced by this same alloy. Such a conclusion is drawn from the observation that the Bi-containing A42 alloy, which possesses the best chip breakability of all the alloys used, displays a BUE width which is lower than the base A alloy by 9%. On the other hand, the higher ductility of the A206 alloy increases its BUE width by about 17% compared to the base A alloy.

6.10 RANKING THE MACHINABILITY OF THE 220 ALLOY

Ranking the machinability of the 220 alloy against that of the A206, A319, B319, and 356 alloys was carried out by comparing their drilling forces and moments, as shown in Figures 6.8(a) and 6.8(b), respectively. The values of the drilling force and moment of the A319, B319, and 356 alloys were obtained from work carried out by Tash[121] and Tash *et al.*,[122] then replotted for the purposes of the graphs shown below. The chemical compositions of the last mentioned three alloys are listed in Table 6.5. In order to support the following comparison, some typical microstructures showing the phases observed in the 319 and 356 alloys under different conditions are also illustrated in Figure 6.9.[122]

The pronounced convergence observed in the drilling results of the A206 and 220 alloys can be understood by ranking the machinability of both alloys taking into consideration the effects of their chemical composition and ductility. On the one hand, the machinability of the A206 alloy is better than that of the 220 alloy based on the fact that the higher content of Si, Mg, Fe, and Mn in the 220 alloy promotes the formation of the $Al_5Mg_8Si_xCu_2$ phase precipitates and the script-like α-$Al_{15}(Fe,Mn)_3Si_2$ phase particles within the alloy matrix, which in turn increase the cutting force and moment. On the other hand, the machinability of the 220 alloy is better than that of the A206 alloy since the

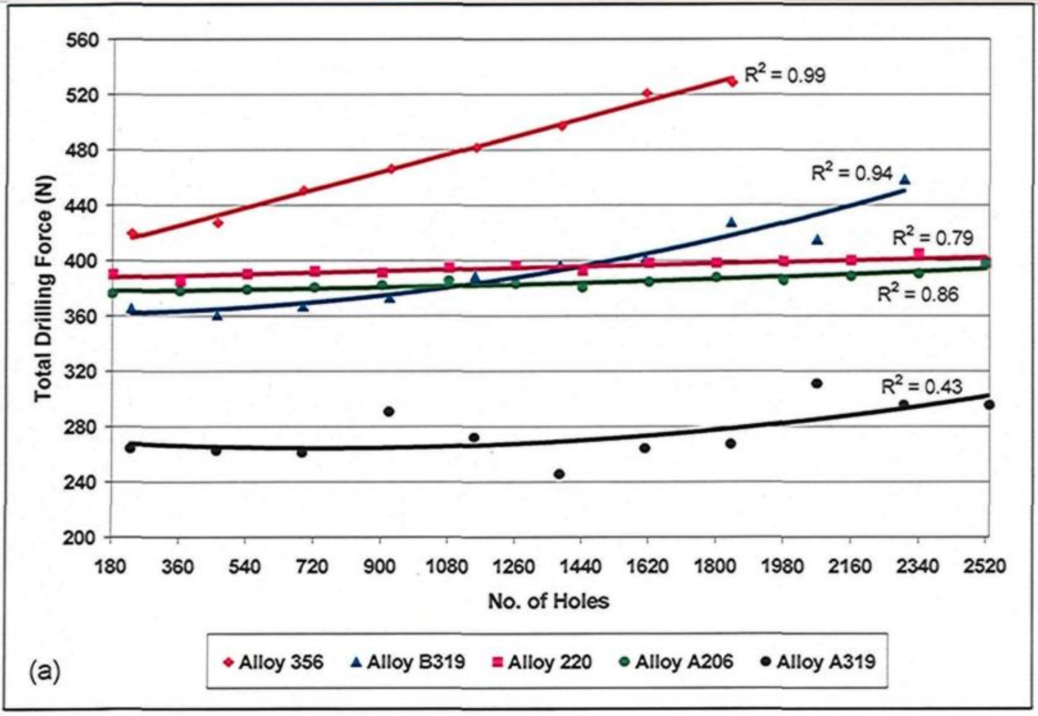

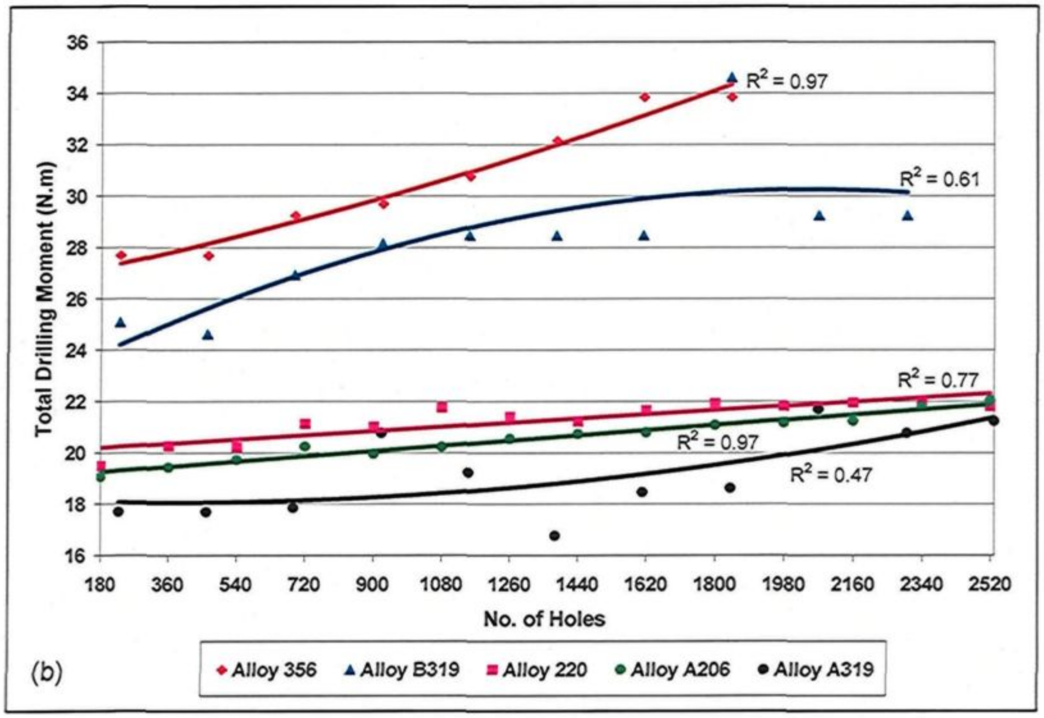

Figure 6.8 Ranking the machinability of 220 alloy against that of 206, A319, B319, and 356 alloys by comparing: (a) the cutting force, and (b) the cutting moment.

higher ductility of the latter leads to the formation of long continuous chips which clog the drill flute and increase the drill-chip friction thereby, in both cases, resulting in higher cutting force and moment. This contradiction implies, in other words, that the A206 and 220 alloys may attain the same rank of machinability which further explains the convergence observed in the drilling results of both these alloys.

Table 6.5 Chemical compositions of the 356, B319, and A319 alloys[122]

Alloy	**Chemical Composition (% wt)**							
	Cu	**Si**	**Mg**	**Fe**	**Mn**	**Ti**	**Sr**	**Al**
356	0.05	6.85	0.34	0.44	0.30	0.15	0.022	bal.
B319	3.40	6.30	0.29	1.02	0.39	0.15	0.026	bal.
A319	3.41	6.20	0.10	0.40	0.30	0.15	0.023	bal.

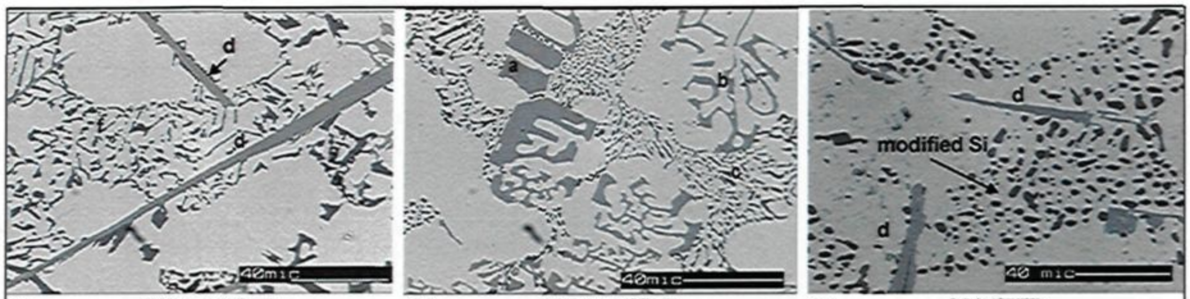

(a) 356 (modified) (b) 356 (modified) (c) 356 (SHT)

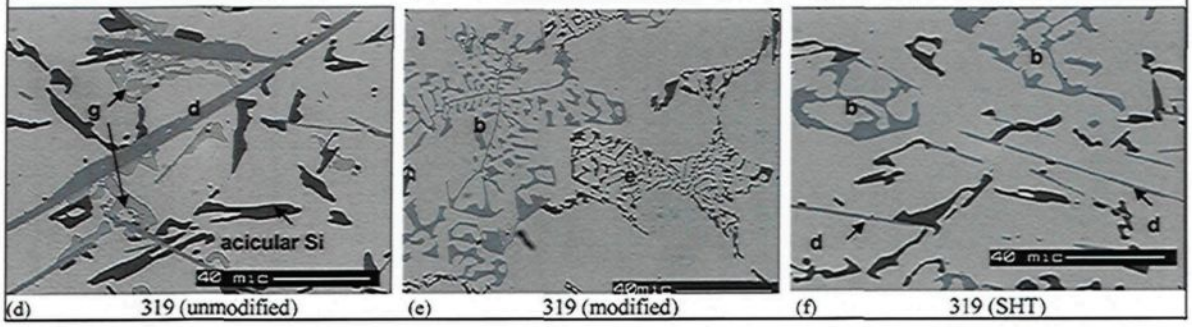

(d) 319 (unmodified) (e) 319 (modified) (f) 319 (SHT)

Figure 6.9 Optical micrographs showing the various phases observed in (a-c) 356 alloy and (d-f) 319 alloy under different conditions: (a) sludge particles; (b) script-like α-Fe phase; (c), (e), (f) modified eutectic Si; (d) plate/needle-like β-Fe phase; and (g) Al_2Cu phase; SHT: solution heat-treated.[122]

The drilling force and moment of the 220 alloy are noticeably lower than those of the 356 alloy; this may be attributed to: (i) the abrasiveness of the 356 alloy resulting from its higher Si content of 6.85% compared to only 1.3% in the 220 alloy; and (ii) the improvement in the homogeneity of the matrix hardness in the 220 alloy caused by the cooperative precipitation of Al_2Cu, Mg_2Si, and $Al_5Mg_8Si_6Cu_2$ hardening phases rather than the precipitation of only the Mg_2Si phase in the 356 alloy. The latter reasoning was confirmed by Tash[121] and Tash *et al.*[122] when explaining why the machinability of the B319 alloy is better than that of the 356 alloy.

The 220 alloy displays a higher drilling force and moment than the A319 alloy in spite of the higher Si content of the latter as a result of the low hardness level selected for the A319 alloy (90 HB) in the relevant study,[121] compared to that of the 220 alloy (101 HB). Moreover, the higher Mg content of the 220 alloy increases the volume fraction of Mg-precipitates within the alloy matrix resulting in higher cutting force and moment. This interpretation is consistent with the observation that the high Mg-content 319 alloy, namely the B319 alloy containing 0.29%Mg, produces cutting force and moment which are higher than those of the A319 alloy.

Although the Mg content of the 220 alloy (0.45%) is higher than that of the B319 alloy (0.29%), Mg may have the same hardening effect in both alloys. Such a possibility is based on the consideration that Mg additions beyond a certain level do not significantly change the precipitation characteristics of Al-Si-Cu alloys; defining this threshold level has become a controversial issue and depends to a large extent upon Cu/Mg and Mg/Si ratios.[46,150] This explanation may support the conclusion that the 220 alloy is more machinable than the B319 alloy due to the higher Si content of the latter alloy, regardless of the higher Mg content of the former. It is important to mention that the precipitation of the brittle platelet-like β-Fe phase and the extremely hard sludge particles in the 356 and 319 alloys (Figure 6.9) may further make these alloys less machinable than 220 alloy in which only the less harmful α-Fe Chinese script phase was precipitated.

CHAPTER 7

CONCLUSIONS AND RECOMMENDATIONS

CHAPTER 7

CONCLUSIONS AND RECOMMENDATIONS

7.1 CONCLUSIONS

An investigation was carried out of the effects of additives on the mechanical properties and machinability of 220 type Al-2%Cu-1.3%Si-0.4%Mg alloy. From the analysis and discussion of the results presented in Chapters 4, 5, and 6 of this dissertation, the following conclusions may be drawn.

Microstructure

1- The θ-Al_2Cu, *Q*-$Al_5Mg_8Si_6Cu_2$, and the Chinese script-like α-$Al_{15}(Fe,Mn)_3Si_2$ phases were identified as the main microstructural constituents of the 220 alloy.

2- Bismuth and β-Sn particles were found in the microstructures of their respective alloys. Neither of these particles dissolved in the Al-matrix, nor combined with other alloying elements, thereby making it possible to produce the desired free-cutting action of these additives during machining.

Mechanical Properties

3- The effects of Sr on the mechanical properties with respect to the modification of silicon eutectic do not come into play because of the low Si content of the 220 alloy.

~~The role of Sr in refining the morphology of the α-Fe Chinese script phase, however,~~ contributes to an improvement in ductility and impact toughness.

4- The addition of Zr increases the strength properties and hardness values as a result of its grain-refining action together with the dispersive strengthening caused by the precipitation of Al_3Zr phase particles. However, both the ductility and impact toughness remain at a high level.

5- Increasing the Fe content, individually or in combination with Mn, also increases the precipitation of α-Fe Chinese script particles which, in turn, reduces the tensile and impact properties.

6- Contrary to expectations, the addition of silver does not produce any considerable increase in the strength properties or in the hardness values for the heat-treated conditions. Such results may be ascribed to the presence of Si which suppresses the vital role of silver in the precipitation-hardening of Al-Cu-Mg-(Ag) alloys.

7- The deterioration observed in the strength properties and hardness values of the Sn-containing alloys in the heat-treated conditions may be attributed mainly to the formation of porosity associated with the melting of Sn during solution heat treatment and the replacement of Si by Sn in Mg compounds; this in turn hinders the precipitation of Mg-hardening phases such as β-Mg_2Si and Q-$Al_5Mg_8Si_6Cu_2$. The ductility and impact toughness, however, remained unaffected by the addition of Sn.

8- The Bi-Mg interaction, which consumes the amount of Mg required to form the Mg-hardening phases, is responsible for the reduction caused in the strength properties and hardness values of Bi-containing alloys in heat-treated conditions. In addition, the presence of free Bi particles in the Al-matrix, which being brittle in nature, reduces both the ductility and impact toughness.

Aging Characteristics

9- Aging characteristics reveal that age-hardening at 180°C results in alloy-hardening with aging for times ranging from 2 to 16 hours, whereas age-hardening at 220°C causes overaging and alloy-softening after 2 hours of aging.

10- The presence of a number of hardening phases in the Al-Cu-Si-Mg alloy system, including θ-Al_2Cu, β-Mg_2Si, and Q-$Al_5Mg_8Si_6Cu_2$, which may not all coarsen simultaneously, maintains the strength and hardness of the alloys at high levels, without any significant decline for up to 16 hours of aging at 180°C.

Fractography

11- With regard to the fracture mechanism of the impact-tested samples, crack initiation occurs through the fragmentation of the α-$Al_{15}(Fe,Mn)_3Si_2$ phase and the formation of several secondary cracks. The crack propagates through the formation of a mixture of fine and coarse dimples, as well as through the fracturing of such insoluble intermetallics as α-Fe, Al_3Zr, and AlMgBi.

12- The fracture surface of the tensile-tested Bi-containing alloy sample reveals the presence of large AlMgBi particles inside the coarse dimples as well as particles of θ-Al_2Cu and α-$Al_{15}(Fe,Mn)_3Si_2$ phases. Solution heat-treatment results in the dissolution of the Al_2Cu phase, whereas neither the AlMgBi nor the α-Fe intermetallics are affected.

Machining Characteristics

13- All the alloys involved in the machinability study attained a superior rate of machinability with respect to the drill life which may exceed 2520 holes. This record of tool life is consistent with the fact that there is no sharp increase in the drilling force and moment observed with the progress of the cutting process.

14- The addition of Sn and Bi improves machinability through a decrease in the total drilling force over the evaluation range by 14% and 25%, respectively, compared to the base 220 alloy. The total drilling moment was reduced by almost the same percentages.

15- All 220-based alloys display a fan-shaped chip which is considered to be the ideal chip for most drilling applications. The addition of Bi increases the fragility of the chip considerably by 70% compared to the base 220 alloy, whereas no distinct change in chip characteristics is observed with the addition of Sn.

16- The 220 alloy may be proposed as a promising cheaper and lighter alternative for the machining applications of A206 alloy, based on (i) the close similarity of the cutting forces and moments observed from machining tests carried out for the two alloys, and (ii) the relatively improved chip characteristics displayed by the 220 alloy.

17- The machinability of the 220 alloy may be deemed an acceptable compromise between that of 356/B319 alloys and that of A319 alloy.

7.2 SUGGESTIONS FOR FUTURE WORK

The following areas may be recommended for further research on the 220 type alloy:

1- A detailed study on the role of addition of such transition elements as Cr, Sc, Zr, and Ag in preserving alloy strength at higher working temperatures over fairly long periods of service.

2- Investigating the thermal resistance of the newly-developed alloy compared to that of the commonly used A206 alloys taking into consideration the corrosive effect produced when the alloy is soaked in E85 fuel (a mixture of 85% ethanol and 15% gasoline, as an alternative fuel) for different periods of time.

3- The effects, on alloy yield strength, of the thermal expansion which occurs during cycling at different working temperatures; this in turn determines the alloy resistance to thermal fatigue.

4- Investigating the possibility of producing castings made of the present alloy using a variety of casting technologies such as lost foam, precision sand, and low pressure die casting.

REFERENCES

REFERENCES

1 Samuel, A.M., Samuel, F.H., Doty, H.W., "Observations on the Formation of β-Al_5FeSi Phase in 319 Type Al-Si Alloys," *Journal of Materials Science*, 1996, vol. 31(20), pp. 5529-5539.

2 Espinoza-Cuadra, J., Gallegos-Acevedo, P., Mancha-Molinar, H., Picado, A., "Effect of Sr and Solidification Conditions on Characteristics of Intermetallic in Al-Si 319 Industrial Alloys," *Materials and Design*, 2010, vol. 31(1), pp. 343-356.

3 Shabestari, S.G., Gruzleski, J.E., "Modification of Iron Containing Precipitates in AlSi12 Alloys with Strontium," Giesserei-Praxis (Germany), 1997, vol. 17, pp. 385-394.

4 Ryum, N., "Precipitation and Recrystallization in an Al-0.5wt Percent Zr Alloy," *Acta Metallurgica*, 1969, vol. 17, pp. 269-278.

5 Rystad, S., Ryum, R., "A Metallographical Investigation of the Precipitation and Recrystallization Process in an Al-Zr Alloy," *Aluminium*, 1977, vol. 53(3), pp. 193-195.

6 Ringer, S.P., Hono, K., Polmear, I.J., Sakurai, T., "Nucleation of Precipitates in Aged Al-Cu-Mg-(Ag) Alloys with High Cu:Mg Ratios," *Acta Materialia*, 1996, vol. 44(5), pp. 1883-1898.

7 Zhu, A., Gable, B.M., Shiflet, G.J., Strake Jr., E.A., "Trace Element Effect on Precipitation in Al-Cu-Mg-(Ag, Si) Alloys: A Computational Analysis," *Acta Materialia*, 2004, vol. 52, pp. 3671-3679.

8 Chang, Y.C., Howe, J.M., "Composition and Stability of Ω phase in an Al-Cu-Mg-Ag Alloy," *Metallurgical and Materials Transactions A*, 1993, vol. 24(7), pp. 1461-1470.

9 Qing-kun, X., Zhi-yi, L., Yun-tao, L., "Microstructure and Properties of Al-Cu-Mg-Ag Alloy Exposed at 200°C With and Without Stress," *Transactions of Nonferrous Metals Society of China*, 2008, vol. 18(4), pp. 789-794.

10 Crepeau, P.N., "Effect of Iron in Al-Si Casting Alloys: A Critical Review," *AFS Transactions*, 1995, vol. 103, pp. 361-366.

11 Couture, A., "Iron in Aluminum Casting Alloys," *AFS International Cast Metals Journal*, 1984, vol. 6(6), pp. 9-17.

12 Bonsack, W., "Discussion on the Effect of Minor Alloying Elements on Aluminum

Casting Alloys," *ASTM Bulletin*, 1942, pp 45-51.

[13] ASM Handbook, *Properties and Selection: Nonferrous Alloys and Special Purpose Materials*, vol. 2, ASM International, Materials Park, OH, 1990.

[14] Lakshmanan, A.N., Shabestari, S.G., Gruzleski, J.E., "Microstructure Control of Iron Intermetallics in Al-Si Casting Alloys," *Zeitschrift für Metallkunde*, 1995, vol. 86(7), pp. 457-464.

[15] Kim, H.Y., Han, S.W., Lee, H.M., "The Influence of Mn and Cr on the Tensile Properties of A356-0.20Fe Alloy," *Materials Letters*, 2006, vol. 60, pp. 1880-1883.

[16] Sigworth, G.K., "Controlling Tensile Strength in Aluminum Castings," Private Communication, *Alcoa Primary Metals*, Rockdale, TX, 2006.

[17] Jorstad , J.L., *Aluminum Casting Technology*, 2nd Edition, American Foundrymen's Society, Des Plaines, IL, 1993.

[18] Hatch, J.E. (Ed.), *Aluminum Properties and Physical Metallurgy*, 1st Edition, ASM, Metals Park, OH, 1988.

[19] Barth, C.F., "Turning," In: King, R.I. (Ed.), *Handbook of High Speed Machining Technology*, Chapman and Hall, New York, NY, 1985.

[20] Drozda, T.J., Wick, C. (Eds.), *Tool and Manufacturing Engineers Handbook*, 4th Edition, vol.1, SME, Dearborn, MI, 1983.

[21] Cook, N.H., *What is the machinability? Influence of metallurgy on machinability*, ASM, Metals Park, OH, 1975.

[22] Smolej, A., Breskvar, B., Sokovic, M., Ljubljana, Dragojevic, V., Slacek, E., Smolar, T., Bistrica, S., "Properties of Aluminum Free-Cutting Alloys with Tin, Part I," *Aluminum Dusseldorf*, 2002, vol. 78(4), pp. 284-288.

[23] Davis, J.R. (Ed.), *ASM Speciality Handbook: Aluminum and Aluminum Alloys*, ASM International, Materials Park, OH, 1993.

[24] Totten, G.E. and MacKenize, D.S. (Eds.), *Handbook of Aluminum - vol. 1: Physical Metallurgy and Process*, Marcel Dekker Inc., New York, NY, 2003.

[25] Brick, R.M., Gordon, R.B., Phillips, A., *Structure and Properties of Alloys*, 3rd Edition, McGraw-Hill, 1965.

[26] Shivkumar, S., Apelian, D., Brucher, H., "Melt Cleanliness in Die Cast Al Alloys,"

Transaction of the 16th International Die Casting Congress and Exposition, 1991, Detroit, MI, pp. 143-152.

27 Neff, D.V., Cooper, P.V., "Clean Metal for Aluminum Foundries: New Technology Using a Rotor Degasser and Filter Pump," *AFS Transactions*, 1990, vol. 98, Paper 90-138, pp. 579-584.

28 Sigworth G.K., "Theoretical and Practical Aspects of the Modification of Al-Si Alloys," *AFS Transactions*, 1983, vol. 91, pp. 7-16.

29 Lu, S.Z., Hellawell, A. "The Mechanism of Silicon Modification in Aluminum Silicon Alloys: Impurity Induced Twinning," *Metallurgical Transactions*, 1987, vol. 18A, pp. 1721-1733.

30 Gruzleski, J., Closset, B., *The Treatment of Liquid Aluminum-Silicon Alloys*, American Foundrymen's Society Inc., Des Plaines, IL, 1990, pp. 25-55.

31 Dahle, A.K., Nogita, K., McDonald S., Dinnis, C., Lu, L., "Eutectic modification and microstructure development in Al-Si Alloys," *Materials Science and Engineering A*, 2005, vol. 413-414, pp. 243-248.

32 Hafiz, M., Kobayashi, T., "Mechanical Properties of Modified and Non-modified Eutectic Al-Si Alloys," *Journal of Japan Institute of Light Metals*, 1994, vol. 44(1), pp. 28-34.

33 Fat-Halla, N., "Structural Modification of Al-Si Eutectic Alloy by Sr and its Effect on Tensile and Fracture Characteristics," *Journal of Materials Science*, 1989, vol. 27, pp. 2488-2490.

34 Nogita, K., Schaffer, P.L., McDonald, S.D., Lu, L., Dahle, A.K., "Modification of Al-Si Alloys," *Aluminum Dusseldorf*, 2005, vol. 81(4), pp. 330-335.

35 McDonald, S.D., Dahle, A.K, Taylor, J.A., StJohn, D.H., "Modification-Related Porosity Formation in Hypoeutectic Aluminum-Silicon Alloys," *Metallurgical and Materials Transactions B*, 2004, vol. 35B, pp. 1097-1106.

36 Lee, Y.C., Dahle, A.K., StJohn, D.H., Hutt, J.E.C., "The Effect of Grain Refinement and Silicon Content on Grain Formation in Hypoeutectic Al-Si Alloys," *Materials Science and Engineering A*, 1999, vol. 259, pp. 43-52.

37 Cibula, A., "The Grain Refinement of Al Alloy Castings by Addition of Ti and B," *Journal of the Institute of Metals*, 1951-52, vol. 90, pp. 1-16.

38 McCartney, D.G., "Grain Refining of Aluminum and its Alloys Using Inoculants,"

International Materials Reviews, 1989, vol. 34(5), pp. 247-260.

39 Gruzleski, J.E., *Microstructure Development During Metal Casting*, American Foundry Society, Des Plaines, IL, 2000.

40 Mondolfo, L.F., Farooq, S., Tse, C., "Grain Refinement of Aluminum Alloys by Titanium and Boron," *Solidification Processing*, 1987, pp. 133-136.

41 Guzowski, M.M., Sigworth, G.K., Sentner, D.A., "The Role of Boron in the Grain Refinement of Aluminum with Titanium," *Metallurgical and Materials Transactions A*, 1987, vol. 18A, pp. 603-620.

42 Mohanty, P.S., Samuel, F.H., Gruzleski, J.E., "Studies on Addition of Inclusions to Molten Aluminum Using a Novel Technique," *Metallurgical and Materials Transactions B*, 1995, vol. 26(1), pp. 103-109.

43 Sigworth, G.K., Guzowski, M.M., "Grain Refining of Hypoeutectic Al-Si Alloys," *AFS Transactions*, 1985, vol. 93, pp. 907-912.

44 Bäckerud, L., Chai, G., Tamminen, J., *Solidification Characteristics of Aluminum Alloys, vol. 2: Foundry Alloys*, AFS/SKANALUMINUM, Des Plaines, IL, 1990.

45 Fuoco, R., Correa, E.R., "Incipient Melting During Solution Heat Treatment of Al-Si-Mg and Al-Si-Cu-Mg Alloys," *AFS Transactions*, 2002, vol. 110, pp. 417-433.

46 Ouellet, P., Samuel, F.H., "Effect of Mg on the Ageing Behavior of Al-Si-Cu 319 Type Aluminum Casting Alloys," *Journal of Materials Science*, 1999, vol. 34, pp. 4671-4697.

47 Mondolfo, L.F., *Aluminum Alloys: Structure and Properties*, Butterworths, London-Boston, 1976.

48 Wang, G., Bian, X., Wang, W., Zhang, J., "Influence of Cu and Minor Elements on Solution Treatment of Al-Si-Cu-Mg Cast Alloys," *Materials Letters*, 2003, vol. 57, pp. 4083-4087.

49 Crowell, N., Shivkumar, S., "Solution Treatment Effects in Cast Al-Si-Cu Alloys," *AFS Transactions*, 1995, vol. 103, pp. 721-726.

50 ASTM Standard B917/B917M-2001, Standard Practice for Heat Treatment of Aluminum-Alloys Castings from All Processes.

51 Martin, J.W., *Precipitation Hardening*, 2nd Edition, Butterworth-Heinemann, Oxford, 1998.

[52] Stanley, J.T., "Quench Factor Analysis of Aluminum Alloys," *Materials Science and Technology*, 1987, vol. 3, pp. 923-935.

[53] Reif, W., Yu, S., Dutkiewicz, J., Ciach, R., Krol, J., "Pre-Ageing of AlSiCuMg Alloys in Relation to Structure and Mechanical Properties," *Materials and Design*, 1997, vol. 18(4), pp. 253-256.

[54] Mishra, R.K., Smith, G.W., Baxter, W.J., Sachdev, A.K., Franetovic, V., "The Sequence of Precipitation in 339 Aluminum Castings," *Journal of Materials Science*, 2001, vol. 36(2), pp. 461-468.

[55] Suzuki, H., Arai, I., Kanno, M., Itoi, K., "Effect of Silicon Addition on the Aging Behavior of an Al-2%Cu-0.9%Mg Alloy," *Journal of the Japan Institute of Metals*, 1977, vol. 27(5), pp. 239-245.

[56] Yao, J-Y., Edwards, G.A., Graham, D.A., "Precipitation and Age-Hardening in Al-Si-Cu-Mg-Fe Casting Alloys," *Materials Science Forum*, 1996, vol. 217, pp. 777-782.

[57] Sagalowicz, L., Hug, G., Bechet, D. (Eds.), *Aluminum Alloys: Their Physical and Mechanical Properties,* ICAA4, Georgia Institute of Technology, Atlanta, GA, 1994.

[58] Dumolt, S.D., Laughlin, D.E., Williams, J.C., "Formation of a Modified Beta Prime Phase in Aluminum Alloy 6061," *Scripta Metallurgica*, 1984, vol. 18(12), pp. 1347-1350.

[59] Li, Y.J., Brusethaug, S., Olsen, A., "Influence of Cu on the Mechanical Properties and Precipitation Behavior of AlSi7Mg0.5 Alloy During Aging Treatment," *Scripta Materialia*, 2006, vol. 54(1), pp. 99-103.

[60] Li, R.X., Li, R.D., Zhao, Y.H., He, L.Z., Li, C.X., Guan, H.R., Hu, Z.Q., "Age-Hardening Behavior of Cast Al-Si Base Alloy," *Materials Letters*, 2004, vol. 58(15), pp. 2096-2101.

[61] Triveno Rios, C., Caram, R., Bolfarini, C., Botta F., W.J., Kiminami, C.S., "Intermetallic Compounds in the Al-Si-Cu System," *Acta Microscopica*, 2003, vol. 12(1), pp. 77-81.

[62] Tash, M., Samuel, F.H., Mucciardi, F., Doty, H.W., "Effect of Metallurgical Parameters on the Hardness and Microstructural Characterization of As-Cast and Heat-Treated 356 and 319 Aluminum Alloys," *Materials Science and Engineering A*, 2007, vol. 443, pp. 185-201.

[63] Dinnis, C.M., Taylor, J.A., Dahle, A.K., "Iron-Related Porosity in Al-Si-(Cu) Foundry Alloys," *Materials Science and Engineering A*, 2006, vol. 425, pp. 286-296.

64 Taylor, J.A., Schaffer, G.B., StJohn, D.H., "The Role of Iron in the Formation of Porosity in Al-Si-Cu-Based Casting Alloys: Part I. Initial Experimental Observations," *Metallurgical and Materials Transactions A*, 1999, vol. 30(6), pp. 1643-1650.

65 Lakshmanan, A.N., Samuel, F.H., Gruzleski, J.E., "Crystallization Behavior of Iron-Containg Intermetallic Compounds in 319 Aluminum Alloy," *Metallurgical and Materials Transactions*, 1994, vol. 25(8), pp. 1761-1774.

66 Gobrecht, J., "Ségrégation par Gravité du Fer, du Manganèse et du Chrome dans les Alliages Al-Si de Fonderie," *Fonderie*, 1977, No. 367, pp. 171-173.

67 Jorstad, J.L., Understanding "Sludge", *Die Casting Engineer*, Nov-Dec 1986, pp. 30-36.

68 Nes, E., "Precipitation of the Metastable Cubic Al_3Zr-Phase in Subperitectic Al-Zr Alloys," *Acta Metallurgia*, 1972, vol. 20(4), pp. 499-506.

69 Robson, J.D., Prangnell, P.B., "Modelling Al_3Zr Dispersoid Precipitation in Multicomponent Aluminum Alloys," *Materials Science and Engineering A*, 2003, vol. 352, pp. 240-250.

70 Mahmudi, R., Sepehrband, P., Ghasemi, H.M., "Improved Properties of A319 Aluminum Casting Alloy Modified with Zr," *Materials Letters*, 2006, vol. 60, pp. 2606-2610.

71 Sepehrband, P., Mahmudi, R., Khomamizadeh, F., "Effect of Zr Addition on the Ageing Behavior of A319 Aluminum Cast Alloy," *Scripta Materialia*, 2005, vol. 52(4), pp 253-257.

72 Yin, Z., Pan, Q., Zhang, Y., Jiang, F., "Effect of Minor Sc and Zr on the Microstructure and Mechanical Properties of Al-Mg Based Alloys," *Materials Science and Engineering,* 2000, vol. A280, pp. 151-155.

73 Polmear, I.J., "The Effects of Small Additions of Silver on the Ageing of Some Aluminium Alloys," *Transactions of Metals Society*, 1964, vol. A230, pp. 1331-1339.

74 Vietz, J.T., Polmear, I.J., "The Influence of Small Additions of Silver on the Ageing of Aluminum Alloys: Observations on Al-Cu-Mg Alloys," *Journal of the Institute of Metals*, 1966, vol. 94(12), pp. 410-416.

75 Garg, A., Chang, Y.C., Howe, J.M., "Precipitation of the Omega Phase in an Al-4.0Cu-0.5Mg Alloy," *Scripta Metallugica et Materialia,* 1990, vol. 24(4), pp. 677-680.

76 Reich, L., Murayama, M., Hono, K., "Evolution of Ω Phase in an Al-Cu-Mg-Ag Alloy

– A Three-Dimensional Atom Probe Study," *Acta Materialia*, 1998, vol. 46(17), pp. 6053-6062.

77 Zou, Y., Matsuda, K., Kawabata, T., Himuro, Y., Ikeno, S., "Effects of Ag on Age-Hardening Behavior of Al-Mg-Si Alloys," *Materials Forum - Institute of Materials Engineering Australasia Ltd*, 2004, vol. 28, pp. 539-544.

78 Matsuda, K., Fukaya, K., Young, Z., Kawabata, T., Uetani, Y., Ikeno, S., "Effect of Copper, Silver and Gold on Tensile Behavior in Al-Mg-Si Alloy," *Materials Forum - Institute of Materials Engineering Australasia Ltd*, 2004, vol. 28, pp. 424-428.

79 Hardy, H.K, "The Effect of Small Quantities of Cd, In, Sn, Sb, Ti, Pb, or Bi on the Aging Characteristics of Cast and Heat-Treated Al-4%Cu-0.15%Ti Alloy," *Journal of the Institute of Metals*, 1950, vol. 78, pp. 169-194.

80 Silcock, J.M., Heal, T.J., Hardy, H.K., "The Structural Aging Characteristics of Ternary Al-Cu Alloys with Cd, In, or Sn," *Journal of the Institute of Metals*, 1955, vol. 84(1), pp. 23-31.

81 Cizek, J., Melikhovo, O., Prochazka, I., Kuriplach, J., Stulikova, I., Vostry, P., "Annealing Process in Quenched Al-Sn Alloys: A Positron Annihilation Study," *Physical Review B*, 2005, vol. 71, pp. 1-13.

82 Ringer, S.P., Hono, K., Sakurai, T., "The Effect of Trace Additions of Sn on Precipitation in Al-Cu Alloys: An Atom Probe Field Ion Microscopy Study," *Metallurgical and Materials Transactions A*, 1995, vol. 26A, pp. 2207-2217.

83 Bourgeois, L., Garg, P., Nie, J.F., Muddle, B.C., "Vacancies and the Tin-assisted Nucleation of θ' in Al-Cu-Sn," *Materials Forum*, 2004, vol. 28, pp. 1341-1346.

84 Silcock, J.M., Flower, H.M., "Comments on a Comparison of Early and Recent Work on the Effect of Trace Additions of Cd, In, or Sn on Nucleation and Growth of *θ'* in Al-Cu Alloys," *Scripta Materialia*, 2002, vol. 46, pp. 389-394.

85 Grebenkin, V.S., Sil'chenko, T.V., Gorshkov, A.A., Dzykovich, I.Y., "Effect of Magnesium on the Distribution of Tin and Lead in Al-Si Alloys," *Metallovedenie i Termicheskaya Obrabotka Metallov. (Metals Science & Heat Treatment)*, 1972, vol. 3, pp. 50-54.

86 Salnikov, V.P., Zaigraikin, A.G., "Effect of Bismuth Addition on Properties of Aluminum-Silicon Alloys," *The Bulletin of the Bismuth Institute*, 1978, No. 19.

87 Pillai, N.P., Anatharaman, T.R., "Elements of V Group as Modifiers of Aluminum-Silicon Alloys," *Transactions of the Metallurgical Society of AIME*, 1968, vol. 242, pp. 2025-2027.

88 Thai, L.T., "The Effects of Bismuth, Strontium and Antimony Additions on the Microstructure and Mechanical Properties of A356 Aluminium Casting Alloy," M.Sc. Thesis, Universiti Teknologi Malaysia, 2006.

89 Cho, J.I., Loper, C.R., "Limitation of Bismuth Residual in A356.2 Al," *AFS Transactions*, 2000, vol. 108, pp. 359-367.

90 El Hadad, S., "Effect of Trace Elements on the Microstructure and Porosity Formation in 319 Type Al-Si-Cu Alloys," M.Sc. Thesis, Université du Québec à Chicoutimi, Canada, 2003.

91 Feikus, F.J., "Einflub von Bismut auf Die Gefugeausbildung und Die Mechanischem Eigenschaften der Sekundargublegierung G-AlSi12(Cu)," *Unpublished Report*, VAW Aluminum AG, Germany, 1993.

92 Fiorini, P., Giordano, G., "Effect of Zn and Bi Addition on Precipitation Process after Quenching," *Metals Technology*, 1983, vol. 10(2), pp. 52-56.

93 Drouzy, M., Jacob, S., Richard, M., "Interpretation of Tensile Results by Means of Quality Index and Probable Yield Strength," *International Cast Metals Journal*, 1980, vol. 5, pp. 43-50.

94 Barat, A., Drouzy, M., "Relation de la Limite d'Elasticite avec la Charge de Rupture et l'Allongement dans les Alliages d'Aluminium de Fonderie. Application au Contrôle," *Revue de Metallurgie*, 1967, vol. 64(6), pp. 585-592.

95 Cáceres, C.H., "A Rationale for the Quality Index of Al-Si-Mg Casting Alloys," *International Journal of Cast Metals Research*, 2000, vol. 12(6), pp. 385-391.

96 Cáceres, C.H., "A Phenomenological Approach to the Quality Index of Al-Si-Mg Casting Alloys," *International Journal of Cast Metals Research*, 2000, vol. 12(6), pp. 367-375.

97 Cáceres, C.H., "Material Properties and Quality Index in Al-Si-Mg Alloys," *AFS Transactions*, 1998, vol. 106, pp. 601-604.

98 Stephenson, D.A., Agapiou, J.S., *Metal Cutting Theory and Practice*, 2nd Edition, Taylor and Francis Group, Boca Raton, FL, 2006.

99 Trent, E.M., Wright, P.K., *Metal Cutting*, 4th Edition, Butterworth-Heinemann, Woburn, MA, 2000.

100 Taps-Cut and Ground Threads, ASME/ANSI Standard B94.9, 1987.

101 Groover, M.P., "A Survey on the Machinability of Metals," *SME Technical Paper*,

1976, MR76-269.

[102] Wright, P.K., Bagchi, A., "Wear Mechanisms Which Dominate Tool Life in Machining," *Journal of Applied Metalworking*, 1981, vol. 1, pp. 15-23.

[103] http://www.toolingandproduction.com, G. Schneider, *Cutting Tool Applications*, 2002.

[104] Cook, N.H., "Tool Wear and Tool Life," *ASME, Journal of Engineering for Industry*, 1973, vol. 95, pp. 931-938.

[105] Kurimoto, T., Barrow, G., "The Influence of Aqueous Fluids on the Wear Characteristics and Life of Carbide Cutting Tools," *CIRP Annals*, 1982, vol. 31(1) , pp. 19-23.

[106] Galloway, D.F., "Some Experiments on the influence of Various Factors on Drill Performance," *ASME Transactions*, 1957, vol. 79, pp. 191-231.

[107] Sonderberg, S., Vingsbo, O., Nissle, M., *Performance and Failure of High Speed Steel Drills Related to Wear, Wear of Materials-1981*, ASME, New York, NY, 1981.

[108] Subramanian, K., Cook, N.H., "Sensing of Drill Wear and Prediction of Drill Life," *ASME, Journal of Engineering for Industry*, 1977, vol. 99, pp. 295-301.

[109] Henderer, W.E., "Relationship Between Alloy Composition and Tool-Life of High Speed Steel Twist Drills," *ASME, Journal of Engineering Materials and Technology*, 1992, vol. 114, pp. 459-464.

[110] Alverio, J., Agapiou, J.S., Shen, C.H., "High Speed Drilling of 390 Aluminum," *Transactions of the North American Manufacturing Research Institution of SME*, 1990, vol. 18, pp. 209-215.

[111] Ernst, H., *Physics of Metal Cutting, Machining of Metals*, vol. 24, ASM, Metals Park, OH, 1938.

[112] Merchant, M.E., "Mechanics of the Metal Cutting Process. I. Orthogonal Cutting and a Type 2 Chip," *Journal of Applied Physics*, 1945, vol. 16, pp. 267-275.

[113] Heginbotham, W.B., Gogia, S.L., "Metal Cutting and the Built-Up Nose," *Proceedings of the Institution of Mechanical Engineers*, 1961, vol. 175, pp. 892-917.

[114] Nakayama, K., Ogawa, M., "Basic Rules on the Form of Chip in Metal Cutting," *CIRP Annals*, 1978, vol. 27(1), pp. 17-21.

[115] Kahng, C.H., Koegler, W.C., "A Study of Chip Curl Formation During Twist

Drilling," *Proceedings-Third North American Metalworking Research Conference*, 1975, pp. 575-588.

116 Batzer, S.A., Hann, D.M., Rao, P.D., Olson, W.W., Sutherland, J.W., "Chip Morphology and Hole Surface Texture in the Drilling of Cast Aluminum Alloys," *Journal of Materials Processing Technology*, 1998, vol. 79, pp. 72-78.

117 Kahng, C.H., Koegler, W.C., "A Study of Chip Breaking During Twist Drilling," *SME Technical Paper*, 1976, MR76-267, pp. 8-12.

118 Oxford, C.J., "On the Drilling of Metals: 1-Basic Mechanics of the Process," *Transactions of ASME, Journal of Engineering for Industry*, 1955, vol. 77, pp. 103-114.

119 Ogawa, M., Nakayama, K., "Effects of Chip Splitting Nicks in Drilling," *CIRP Annals*, 1985, vol. 34(1), pp. 101-104.

120 Jorstad, J.L., "Machinability of 380 Alloy: Effect of Minor Elements and Impurities," *Transactions of the Society of Die Casting Engineers*, 1979, G-T79-072.

121 Tash, M., "Effect of Metallurgical Parameters on Machining Behavior of 356 and 319 Alloys (Drilling and Tapping Study)," Ph.D. Thesis, Université du Québec à Chicoutimi, Canada, 2005.

122 Tash, M., Samuel, F.H., Mucciardi, F., Doty, H.W., Valtierra, S., "Effect of metallurgical parameters on the machinability of heat-treated 356 and 319 aluminum alloys," *Materials Science and Engineering A*, 2006, vol. 434, pp. 207-217.

123 Bichsel, H., "Bismuth as an Alloying Element in Aluminum Alloys," *Bulletin-Bismuth Institute*, 1978, vol. 19.

124 Kim, K.H., Chung, I.S., "Effect of Lead and Bismuth Element on the Cutting Characteristics in Al-Cu Alloys," *Journal of the Korean Institute of Metals*, 1990, vol. 28(3), pp. 244-251.

125 Smolej, A., Breskvar, B., Sokovic, M., Ljubljana, Dragojevic, V., Slacek, E., Smolar, T., Bistrica, S., "Properties of Aluminum Free-Cutting Alloys with Tin, Part II," *Aluminum Dusseldorf*, 2002, vol. 78(5), pp. 388-391.

126 Sircar, S., "X6030, A New Lead-Free Machining Alloy," *Materials Science Forum*, 1996, vols. 217-222, pp. 1795-1800.

127 Faltus, J., Stulikova, I., Hajek, M., Madl, J., Koutny, V., "Aluminum alloys on the basis of Al-Cu-Mg, lead-free, intended for cutting," *Materials Science Forum*, 2002,

vols. 396-402(3), pp. 1641-11646.

128 Royset, J., Saeter, J.A., Ustad, T., Reiso, O., "Effects of Sn Addition on Microstructure, Extrudability, Mechanical Properties and Machinability of a 6082 Alloy," *Materials Science Forum*, 2002, vols. 396-402(2), pp. 1205-1210.

129 AMS 4235A, SAE, 1987, Warrendale, PA.

130 http://www.gordonengland.co.uk/hardness/brinell.htm

131 Liao, H., Sun, G., "Mutual Poisoning Effect Between Sr and B in Al-Si Casting Alloys," *Scripta Materialia*, 2003, vol. 48, pp. 1035-1039.

132 Liao, H., Sun, Y., Sun, G., "Effect of Al-5Ti-1B on the Microstructure of Near-Eutectic Al-13.0%Si Alloys Modified with Sr," *Materials Science*, 2002, vol. 37, pp. 3489-3495.

133 Muddle, B.C., Ringer, S.P., Polmear, I.J., "High Strength Microalloyed Aluminium Alloys," *Advanced Materials'93 VI/Frontiers in Materials Science and Engineering*, 1994, pp. 999-1023.

134 Abis, S., Mengucci, P., Riontino, G., "Influence of Si Additions on the Ageing Process of an Al-Cu-Mg-Ag Alloys," *Philosophical Magazine A*, 1994, vol. 70(5), pp. 851-868.

135 Gable, B.M., Shiflet, G.J., Starke Jr., E.A., "The Effect of Si Additions on Ω Precipitation in Al-Cu-Mg-(Ag) Alloys," *Scripta Materialia*, 2004, vol. 50, pp. 149-153.

136 Polmear, I.J., Pons, G., Octor, H., Sanchez, C., Morton, A., Borbidge, W., Rogers, S., "After Concorde: Evaluation of an Al-Cu-Mg-Ag alloy for use in the proposed European SST," *Materials Science Forum*, 1996, vols. 217-222(3), pp. 1759-1764.

137 Mohamed, A.M.A., Samuel, F.H., Samuel, A.M., Doty, H.W., Valtierra, S., "Influence of Tin Addition on the Microstructure and Mechanical Properties of Al-Si-Cu-Mg and Al-Si-Mg Casting Alloys," *Metallurgical and Materials Transactions A*, 2008, vol. 39A, pp. 490-501.

138 Couper, M.J., "6XXX Series Aluminum Alloy," U.S. Patent No. 6,364,969B1, 2002.

139 Kang, H.G., Kida, M., Miyahara, H., Ogi, K., "Hoyt Memorial Lecture: Age-Hardening Characteristics of Al-Si-Cu-Base Cast Alloys," *AFS Transactions*, 1999, vol. 107, pp. 507-515.

140 Wang, G., Sun, Q., Feng, L., Hui, L., Jing, C., "Influence of Cu Content on Ageing

Behavior of AlSiMgCu Cast Alloys," *Materials and Design*, 2007, vol. 28(3), pp. 1001-1005.

141 Din, T., Rashid, A.K.M.B., Campbell, J., "High Strength Aerospace Casting Alloys: Quality Factor Assessment," *Materials Science and Technology*, 1996, vol. 12(3), pp. 269-273.

142 Cáceres, C.H., Din, T., "Effect of Ageing on the Quality Index of an Al-Cu Alloy," Materials Science and Technology, 1999, vol. 15, pp. 711-716.

143 Brechet, Y., Embury, J.D., Tao, S., Luo, L., "Damage initiation in metal matrix composites," *Acta Metallurgica et Materialia*, 1991, vol. 39(8), pp. 1781-1786.

144 Sonsino, C.M., Ziese, J., "Fatigue Strength and Application of Cast Aluminum Alloys with Different Degrees of Porosity," *International Journal of Fatigue,* 1993, vol. 15(2), pp. 75-84.

145 Richard, M., "Impact Strngth of Aluminum Alloy Casting," *Fonderie*, 1980, vol. 35(404), pp. 397-400.

146 Komastu, N., Nakamura, M., Yamamoto, Y., "Metallurgical Structure and Impact Strength of Al-Si Alloys," Technical Report of Toyota R&D Center, TR-11, 1975, pp. 1-46.

147 Gerberich, W.W., *Metals Handbook*, 9th Edition, vol. 8, ASM, Metals Park, OH, 1985.

148 http://www.kistler.com

149 Taylor, J.R., *An Introduction to Error Analysis: The Study of Uncertainties in Physical Measurements*, University Science Books, Mill Valley, California, 1982.

150 Moustafa, M.A., Samuel, F.H., Doty, H.W., Valtierra, S., "Effect of Mg and Cu additions on the microstructural characteristics and tensile properties of Sr-modified Al-Si eutectic alloys," *International Journal of Cast Metals Research*, 2002, vol. 14, pp. 235-253.